NASA Contractor Report 191089

An Experimental Investigation of High Temperature Superconducting Microstrip Antennas at K- and Ka-Band Frequencies

Mark A. Richard
Case Western Reserve University
Cleveland, Ohio

March 1993

Prepared for
Lewis Research Center
Under Cooperative Agreement NCC3-99

National Aeronautics and Space Administration

AN EXPERIMENTAL INVESTIGATION OF HIGH TEMPERATURE SUPERCONDUCTING MICROSTRIP ANTENNAS AT K- AND Ka-BAND FREQUENCIES

Abstract

by

MARK ADRIAN RICHARD

The recent discovery of high temperature superconductors (HTS) has generated a substantial amount of interest in microstrip antenna applications. However, the high permittivity of substrates compatible with HTS results in narrow bandwidths and high patch edge impedances of such antennas. To investigate the performance of superconducting microstrip antennas, three antenna architectures at K and Ka-band frequencies are examined. Superconducting microstrip antennas that are directly coupled, gap coupled, and electromagnetically coupled to a microstrip transmission line have been designed and fabricated on lanthanum aluminate substrates using $YBa_2Cu_3O_7$ superconducting thin films. For each architecture, a single patch antenna and a four element array were fabricated. Measurements from these antennas, including input impedance, bandwidth, patterns, efficiency, and gain are presented. The measured results show useable antennas can be constructed using any of the architectures. All architectures show excellent gain characteristics, with less than 2 dB of total loss in the four element arrays. Although the direct and gap

coupled antennas are the simplest antennas to design and fabricate, they suffer from narrow bandwidths. The elecromagnetically coupled antenna, on the other hand, allows the flexibility of using a low permittivity substrate for the patch radiator while using HTS for the feed network, thus increasing the bandwidth while effectively utilizing the low loss properties of HTS. Each antenna investigated in this research is the first of its kind reported.

TABLE OF CONTENTS

List of Figures

List of Tables

CHAPTER I.

INTRODUCTION AND BACKGROUND

1.1 Background: Communication System Requirements

In the world today, wireless communication has become very important. Commercial broadcasting services, such as television and radio, military communication networks, and personal communication all play important roles in our daily activity. All of these communication services have proliferated in recent years. With the increase of radio-wave activity, the electromagnetic spectrum has become quite crowded, forcing users to reduce bandwidth or move to higher, unoccupied frequency bands. Traditionally, the microwave spectrum, especially the C and X band frequencies, has been used for space satellite communication. However, because of band crowding, newer generation satellites have begun to use Ku (12-18 GHz), K (18-26.5 GHz), and even Ka (26.5 - 40 GHz) band frequencies. For instance, NASA's Advanced Communication Technology Satellite, to be launched in 1994, will use a 20 GHz downlink and a 30 GHz uplink. In the commercial sector, products for wireless computer networks which use an 18 GHz carrier are being marketed [1], as are truly global cellular telephones which communicate directly with orbiting satellites using K-

band frequencies[2]. Inter-satellite communication links using a 60 GHz carrier frequency are also being considered for satellite networks. This trend towards higher frequency communication is quite pronounced and is expected to continue into the future as personal communication and other forms of wireless communication increase in popularity.

Traditionally, waveguide or coaxial components along with parabolic dish antennas have been employed for microwave communication circuitry. However, for satellite applications, these components are less than ideal because of their heavy weight and bulky structure. Although the size and thus weight of waveguide components decreases with increasing frequency, components also become exceedingly expensive because of the tight machining tolerances that must be employed when fabricating high frequency components.

Size and weight, though, do not tell the whole story. Today's communication circuitry require the use of solid state components such as transistors and diodes which are not easily incorporated into waveguide circuitry. In fact, another unmistakable trend in the communication area is a trend towards increased integration. Over the past decade, monolithic microwave integrated circuits (MMIC's) have become available. It is because of such circuits that microwave personal communication systems have become affordable. In the drive towards higher frequencies, smaller size components, and integratability, one area that has been given particular attention is the antenna.

In this research, the application of a promising new technology, high temperature superconductivity, was investigated for use in antenna systems. The focus of this research was, first, to find practical ways of using superconductors in high frequency microstrip antennas and, secondly, to investigate experimentally the performance advantages of HTS antennas over antennas fabricated using conventional metals. For this research, several different types of superconducting antennas were designed and fabricated. Each one was the first of its kind reported.

1.2 Microstrip Antennas

Since the days when antennas were first used to transmit electromagnetic energy, the search has been on for low profile radiators. One of the first such antennas was invented by Booker[3], who investigated a low profile slot antenna. Since that time, a new class of low profile antennas, called microstrip antennas, has been discovered and thoroughly investigated. The microstrip antenna in its basic form is shown in Figure 1-1. A metal patch, printed on a dielectric substrate, forms a resonant cavity with the ground plane on the backside of the dielectric substrate. This cavity radiates a portion of its energy from the open sides. It is this radiation which causes the microstrip patch to act like an antenna.

The invention of the printed circuit antenna is generally attributed to DesChamps as early as 1953[4]. Although the unwanted radiation from printed circuit transmission lines (stripline) was well known[5], there was little interest in exploiting this radiation to form an antenna. Thus, the microstrip antenna

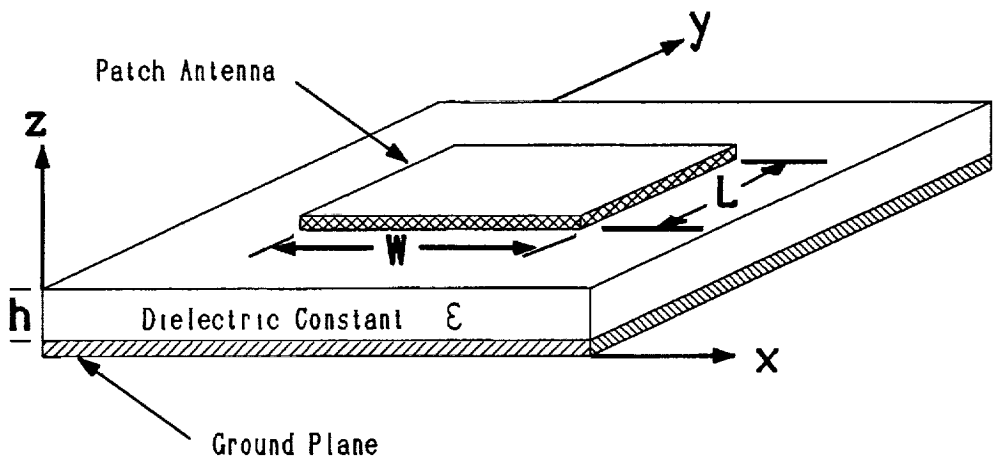

Figure 1-1: The geometry of a microstrip patch antenna.

concept was largely ignored until the early 1970's. A special conference on the topic of microstrip antennas, convened at Las Cruces, New Mexico in 1979[6], represented the beginning of the flood of research done on the topic. The proceedings from this conference were published in a special issue of the *IEEE Transactions on Antennas and Propagation*[7]. One of the main reasons that the field of microstrip antennas remained dormant for so long was because of manufacturing concerns. Until the early 1980's, low cost, low permittivity substrates with uniform properties were unavailable. Only then did manufacturers begin to offer substrates with tighter tolerances and greater resistance to thermal stresses.

The microstrip antenna is desirable because it can be easily integrated with existing solid state circuits such as amplifiers and oscillators, so that integrated receivers or transmitters can be fabricated. The microstrip antenna, being a low profile radiator, has the additional advantage of being rugged, light weight, low

cost, and can be mounted around a conformal surface. One of the drawbacks of the microstrip antenna, however, is its relatively narrow bandwidth and low gain. In its simple form, it usually has a bandwidth of less than 3 %, and often lower than 1 %, while the gain is often between 5 and 7 dB.

Since the early 1980's, the field of printed circuit antennas has exploded, with numerous books and research papers being published. Although the field of microstrip antenna research is now quite broad and varied, much of the research effort has been focused either upon analytical modeling, or experimentally, upon bandwidth extension techniques and gain improvements. A multitude of radiator shapes has been examined. Although the rectangular and circular patches are by far the most common, shapes such as elliptical[8], triangular[9], annular rings[10] and sectors[11], and pentagonal[12] have also been examined. The shape of the microstrip patch antenna has no substantial effect upon the antenna's performance characteristics. The annular ring antennas tend to have a larger bandwidth when excited in a higher order modes, but also become physically larger[13].

1.2.1 Theoretical Antenna Research

The published work in modeling and characterization of microstrip antennas can be divided mainly into four categories: cavity models, transmission line models, wire grid models, and models utilizing Green's function analysis. Each of these is explained briefly below.

Cavity Models: The simple cavity model has been proposed by Lo *et. al.*[14,15]. This model is based upon the following assumptions:

1). Underneath the patch the **E** field has only a z-component while the **H** field has only xy components (Figure 1-1).

2). The fields under the patch have no z-dependence.

3). The cavity formed by the patch and ground plane have perfect magnetic walls (no tangential component of **H** along the edge of the patch).

With these assumptions, the fields of the antenna may be assumed to be the fields in the cavity. Using this knowledge, the input impedance, radiation patterns, and radiated power may be found. A cavity model quite similar to the simple cavity model is the Modal Expansion Model advanced by Carver[16]. This model differs from the simple cavity model in that the four open walls of the cavity are given complex wall impedances instead of being treated as perfect magnetic walls.

Transmission Line Models: The transmission line models are applicable only to rectangular patch antennas. These models[17,18,19] treat the patch as a low impedance microstrip transmission line with two open ends which act as slot radiators (Figure 1-2). Each slot is assumed to have a constant magnetic current **M**. From this magnetic current, the field in the slot and the field radiated by each slot may be found. The radiated fields, then, are found by the pattern multiplication principle. The radiated power may be found by integrating the radiated field, while the input impedance at any point may be found by transforming the slot impedances to the feed point. Improvements upon the

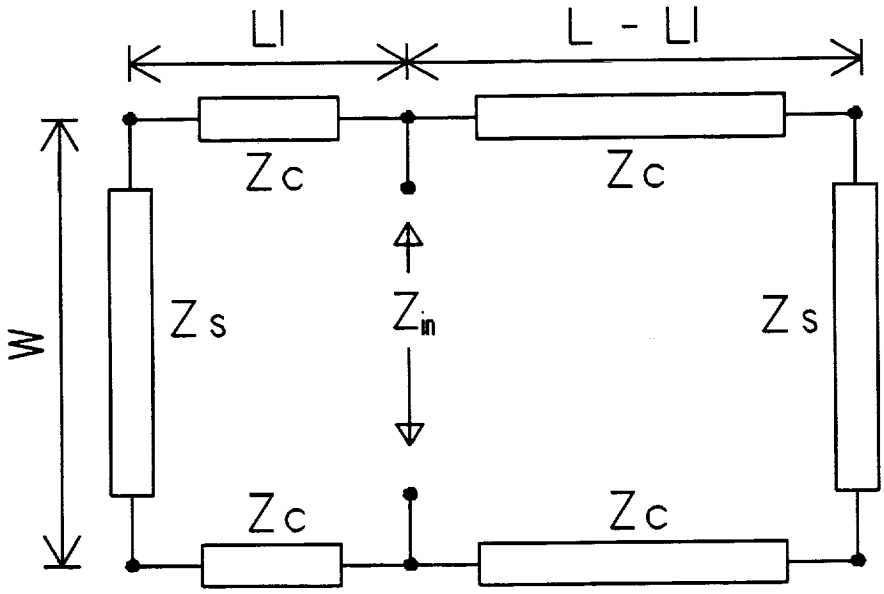

Figure 1-2: Equivalent circuit used for the transmission line model, fed at an arbitrary point L1. Zs is the equivalent slot impedance and Zc is the characteristic impedance of the patch treated as a transmission line.

transmission line model account for mutual coupling between the two slots and radiation from the side walls.

Wire Grid Model: The wire grid model, advanced by Agrawal and Bailey[20] approximates the patch by a fine wire grid and replaces the ground plane by a mirror image of the patch (Figure 1-3). Using Rumsey's Reaction theorem[21], the currents in these wires are calculated. From these currents, the characteristics of the antenna can be calculated.

Green's Function Analysis: To model a microstrip patch using Green's Function analysis, the dyadic Green's Function must first be found. Once this is know, a superposition integral is used to calculate the field from an arbitrary source

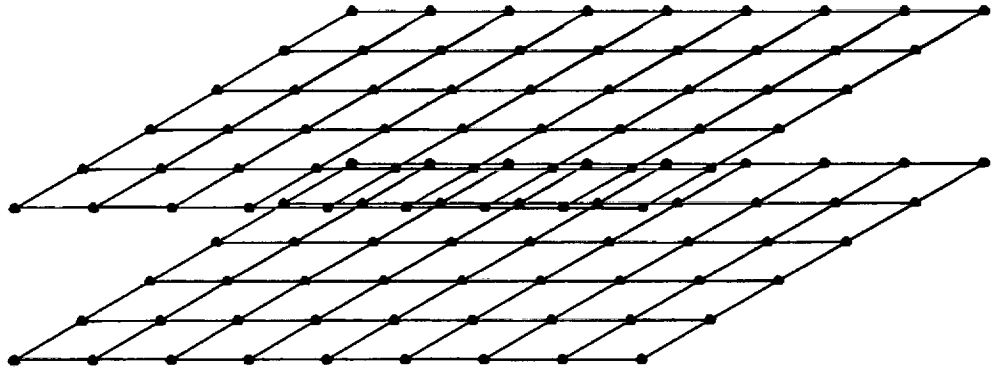

Figure 1-3: A rectangular microstrip patch modeled using the wire grid model. The patch and its mirror image are replaced by a grid of wires on which the currents are calculated.

distribution. Although this method is exact, it is difficult to set up and computationally intensive.

1.2.2 Experimental Antenna Research

On the experimental side of the research, wider bandwidth has been sought after. One simple method of realizing a wide bandwidth microstrip antenna is to use a thick, low permittivity substrate. This increases the bandwidth since the bandwidth is directly proportional to the dielectric thickness, h, and inversely proportional to the permittivity. However, this also causes an increase in surface wave generation and dielectric losses. Other methods of increasing the bandwidth that have been proposed include the addition of matching networks[22] and the use of multilayer structures such as aperture coupling[23] or electromagnetic coupling[24]. Multilayer structures have also exhibited increased gain, particularly when an air gap is used between the feed substrate and the patch substrate[25].

In recent years, two areas of research interest have been component integration with microstrip antennas, and microstrip array design. In the former, an annular ring antenna and a rectangular patch with Gunn diodes integrated to form active antennas have been reported[26,27] as have active antennas which utilize integrated FET oscillators[28]. Passive microstrip arrays have been investigated both theoretically[29,30,31,32] and experimentally[33,34]. The challenge facing antenna designers today, though, is not just the integration of one or two devices with a microstrip antenna or simple passive arrays but, rather, the integration of entire circuits such as phase shifters, oscillators, and power amplifiers to form active phased array antennas. Although a few such phased array antennas have been reported, they tend to suffer from poor yield factors in the fabrication of the active devices. Additionally, microstrip transmission lines are quite lossy. Thus, as the array size and complexity increases, the gain of the array becomes limited by the losses in the feed network.

1.3 Superconductors: History and Applications

A superconductor is a substance which has zero resistance when cooled to temperatures below a certain temperature known as its critical temperature T_c. Superconductivity was first discovered by Onnes in 1911 when a mercury sample was cooled below 4.2 Kelvin (K)[35]. In 1933, Meissner and Oschenfeld discovered that a superconductor in its superconducting state (cooled below T_c) expels magnetic flux from its interior when exposed to a magnetic field[36]. These two properties, namely zero resistance and the Meissner effect, are the two

necessary conditions for superconductivity. Since Onnes' discovery in 1911, many compounds have been found to exhibit superconductivity. Until 1986, (Nb_3Ge) was the superconducting material with the highest T_c at 23.2 K. In 1986, Bednorz and Muller demonstrated the existence of a new class of superconductors by discovering that $La_{2-x}Ba_xCu_4O_9$ had a critical temperature of 40 K[37]. Soon afterwards, $YBa_2Cu_3O_{7-x}$ (YBCO) was discovered to have a critical temperature of 92 K[38]. This discovery was of paramount importance in the field of superconductivity because for the first time it raised the critical temperature above the boiling point of liquid nitrogen. In practical terms, this meant that now the relatively cheap liquid nitrogen could be used as a cryogen for superconducting devices as opposed to the expensive liquid helium. Since the discovery of superconductivity in $YBa_2Cu_3O_{7-x}$, two other higher transition temperature materials have been discovered: $Bi_2Sr_2Ca_2Cu_3O_x$ with a T_c of 105 K[39], and $Tl_2Ba_2Ca_2Cu_3O_x$ with a T_c of 120 K[40]. This new class of superconductors is referred to as high temperature superconductors, or HTS.

Although superconductors have zero resistance at DC, they do have AC losses resulting from the inertia of the electrons of the superconductor. Using the two-fluid model advanced by Gorter and Casimir[41], the complex impedance of a thin film superconductor is given by

$$Z=\sqrt{\frac{j\omega\mu_0}{\sigma}} \qquad \textbf{(1-1)}$$

where ω is the angular frequency, μ_0 is the permeability of free space, and σ is the complex conductivity of the superconductor given by $\sigma_1 - j\sigma_2$. The conductivities σ_1 and σ_2 are given by (assuming frequencies below $1x10^{11}$ Hz)

$$\sigma_1=\frac{n_N e^2\tau}{m} \qquad \textbf{(1-2)}$$

and

$$\sigma_2=\frac{n_S e^2}{m\omega} \qquad \textbf{(1-3)}$$

Here n_N and n_s are the densities of the normal and superconducting electrons, respectively, e is the electronic charge, τ is the mean carrier scattering time, and m is the electron mass. Substituting Eq. (1-2) and (1-3) into (1-1), the complex impedance can be written as

$$Z=(\omega^2\mu_0{}^2\lambda^3 n_N\sigma_N/2n)+j\omega\mu_0\lambda_p=R_s+j\omega L_s \qquad \textbf{(1-4)}$$

where R_s and L_s are the surface resistance and inductive reactance of the superconductor, respectively, and λ_p is the magnetic penetration depth given by

$$\lambda_p(T) = \lambda_{p0} \frac{1}{\sqrt{1-(T/T_c)^4}} \qquad (1\text{-}5)$$

In Eq. (1-5), λ_{p0} is the magnetic penetration depth at absolute zero temperature (T = 0 K) and T_c is the critical temperature of the superconductor. From (4), it may be seen that superconductors exhibit not only a surface resistance, but also an inductance.

1.3.1 Substrates

For practical microwave use, superconductors must be available on a dielectric substrate. Although YBCO films with the best DC characteristics have been grown on strontium titanate ($SrTiO_3$), this substrate is not a practical one from a microwave standpoint. $SrTiO_3$ has a dielectric constant (ϵ_r) of 300 at room temperature and over 1000 at liquid nitrogen temperatures[42,43]. In addition, it has a dielectric loss tangent that is very high (0.06 at 77 K).

Magnesium oxide (MgO) is an excellent substrate from a microwave point of view. It has a permittivity of 9.6 and a loss tangent of 3×10^{-4} at room temperature. However, it has a rather large lattice mismatch of 6.7 % with the epitaxially grown YBCO thin films. This mismatch makes the growth of high quality thin films difficult, and in addition, causes an increase in the surface resistance of the superconductor.

Lanthanum aluminate ($LaAlO_3$) substrates have qualities that are favorable both from the HTS film grower's point of view and the microwave designer's

point of view. It has a low loss tangent of less than 8.5 x 10^{-4} at 77 K[44]. The dielectric constant has been reported to be as low as 21.9[45] and as high as 24.0[46]. One of the reasons that the permittivity of $LaAlO_3$ substrates is not known accurately is that the substrates have crystal structure boundaries, or twinning, which cause at least a 2 % uncertainty in the permittivity[47], and it is also slightly anisotropic. Lanthanum aluminate has a very good lattice match with YBCO, having a mismatch of only 0.99%.

In recent months, YBCO films on sapphire (Al_2O_3) substrates have been demonstrated[48], but the HTS deposition process onto a sapphire substrate is complicated by the need for a buffer layer. In addition, sapphire has an anisotropic permittivity of 9.4 along the c-axis and 11.6 perpendicular to the c-axis, complicating the microwave design process.

1.3.2 HTS Thin Films

Thin films of YBCO on lanthanum aluminate have shown surface resistance, R_s, values of 0.3 to 0.4 mΩ at 77 K and 10 GHz[49,50]. These values can be compared with bulk copper, which has a R_s of 26 mΩ at room temperature. At other frequencies, the R_s of HTS films can be scaled approximately by using the equation

$$R_s = R_{s_{10GHz}} \frac{f^2}{100} \qquad \textbf{(1-6)}$$

where f is the frequency in GHz.

In addition to YBCO, various other HTS thin films have recently been developed. Of particular interest are the thallium-based compounds, $Tl_2Ba_2CaCu_2O_x$ with a T_c of 110 K, and $Tl_2Ba_2Ca_2Cu_3O_x$ with a T_c of 125 K. At 77 K, the surface resistance of these materials has been reported to be similar to that of YBCO. Despite the higher T_c values of the thallium-based compounds, YBCO was used for the main portion of this work. This was because YBCO was more commonly available and in-house fabrication procedures had been developed for YBCO but not for the thallium compounds.

It is clear that HTS offers a substantial reduction in resistive losses for electrical circuits. To date, many passive microstrip circuits which effectively utilize the low loss properties of HTS have been reported. These circuits include transmission lines and delay lines[51], multiple-pole filters[52,53,54], and resonators[55,56,57]. Experimental work with Ka-band superconducting ring resonators has shown a factor of 3 improvement in circuit "Q" at 35 GHz over an identical circuit fabricated with evaporated gold[55]. Such results have encouraged the investigation of potential HTS applications in microstrip antenna systems.

1.4 Superconducting Antennas

The use of superconductors in antenna systems began long before the discovery of HTS. In 1966, Walker and Haden[58] reported on the performance of a 400 MHz electrically short superconducting antenna. In the 1970's and early 1980's, several other groups reported on electrically short superconducting antennas and superdirective arrays[59,60,61]. However, the practicality of such

antennas was severely limited because of the need to operate them at liquid helium temperatures. This situation changed with the discovery of HTS compounds. In 1988, Khamas *et. al.*[62] reported an electrically short superconducting dipole antenna, operating at 550 MHz. The superconducting antenna was found to have a radiated field strength 12 dB higher than that of a copper antenna having identical dimensions. This antenna was made from bulk YBCO material as opposed to a thin film.

More recently, Hansen[63] and Dinger[64] have analyzed the potential applications of HTS in antenna systems. Hansen analyzed the potential benefits of using superconductors in superdirective arrays, millimeter-wave arrays, electrically small antennas, and in matching networks for electrically small and superdirective antennas. It is shown that an HTS superdirective array would be impractical for three reasons. First, the Q of a superdirective array increases rapidly as the directivity increases[65]. This places a fundamental limit on the applicability of superdirective arrays since the bandwidth (VSWR < 2) is given by

$$B.W. = \frac{1}{\sqrt{2}Q} \tag{1-7}$$

Secondly, the input resistance of the elements decreases with increasing directivity. This in turn makes the matching of the feed network to the elements difficult. Finally, with increasing directivity the tolerances required on the excitation currents of individual elements to produce superdirectivity increases.

In practice it would be difficult to control the excitation current in the elements to the precision required.

Electrically small antennas likewise suffer from high Q and thus low bandwidth. In fact, Chu[66] and Harrington[67] showed that the Q is proportional to the inverse cube of the antenna size. In both of these cases, the application of HTS to the radiating element would not produce substantial benefit, but the use of HTS in the matching network would. The reason for this is that losses in the matching show up as a much higher apparent loss. This apparent loss is given by[68]

$$L_a = \frac{(V+1)^2 L^2 - (V-1)^2}{4VL} \tag{1-8}$$

where V is the antenna VSWR and L is the loss in the matching network.

In large microwave and millimeter wave microstrip arrays, the feed losses become large enough so that at some point the gain of the antenna begins to decrease as the number of array elements increases. Because of the low loss properties of HTS microstrip transmission lines, these feed losses could be reduced so that larger arrays with higher directivities could be made using HTS than with the use of conventional metals. As an example, Figure 1-3 shows calculated gains as a function of frequency for a two-dimensional, one meter square microstrip array using both HTS and copper metallization. In this plot, the elements are assumed to be spaced at one half the free space wavelength ($\lambda_0/2$), so that for a given frequency f, the number of elements is given by

$$n=\left[\frac{2f}{c}+1\right]^2 \tag{1-9}$$

where c is the speed of light. For higher frequencies the losses in the feed network become large enough so that even though the directivity increases, the gain actually begins to decrease. Dinger has shown that a HTS 100 element linear array at 35 GHz could experience a gain increase of 8 to 10 dB over an identical copper array. Thus, it is clear that HTS can reduce the feed losses in a microstrip array. It is noteworthy that the losses in the actual radiating element are quite small. For the patches used in this work, the loss was less than 1 dB.

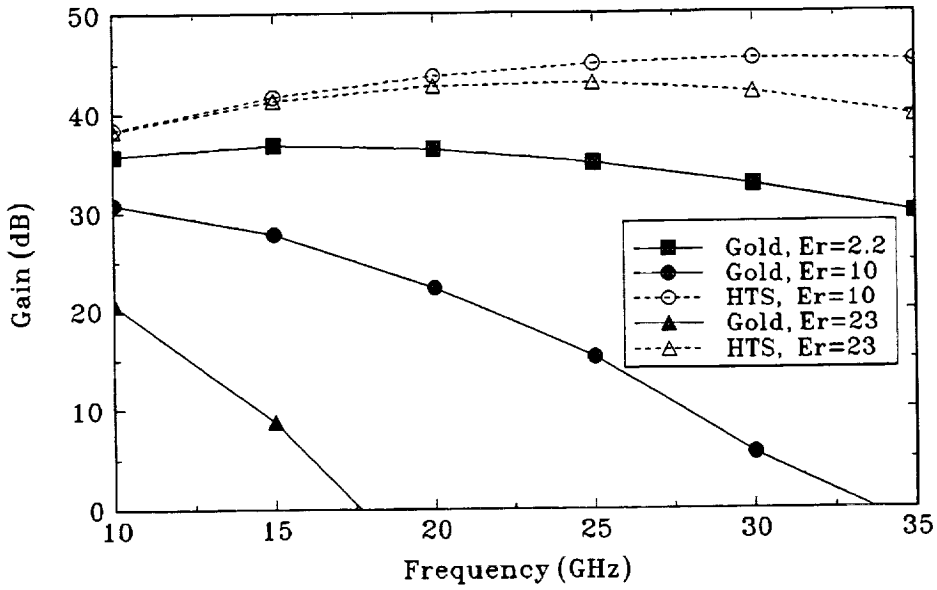

Figure 1-4: Gain of a 1 meter square microstrip array as a function of frequency.

Despite these advantages, the design and implementation of a practical HTS antenna or array is difficult due to two problems. First, the antenna must be

cooled. Because the antenna must radiate, cooling equipment such as shrouds, insulation, and cryogen must be carefully designed and placed to avoid interference with the performance of the antenna. Secondly, substrates compatible with the epitaxially grown HTS films have high permittivities. To date, lanthanum aluminate has been the substrate of choice because of its good lattice match with HTS, resulting in YBCO films with high (90 K) transition temperatures and low surface resistance. However, this substrate is less than ideal as an antenna substrate because of its high permittivity (ϵ_r~23). Films on sapphire (Al_2O_3) have recently been demonstrated[48], but the HTS deposition process onto a sapphire substrate is complicated by the need for a buffer layer and by sapphire's anisotropy, which complicates the antenna design process. These substrates can be compared with typical substrate such as Duroid 5880[69] which has a permittivity of 2.2 and a dielectric loss tangent of 0.001. HTS compatible substrates and their parameters are shown in Table 1, together with common microstrip antenna substrates.

The use of high permittivity substrates results in microstrip antennas with small patch sizes, narrow bandwidths, and high patch edge impedances. The high permittivity substrates make traditional feed methods quite difficult, even for planar architectures. In particular, coaxial feeding is difficult even at low frequencies because of the fragile nature of the crystalline HTS-compatible substrates, and impossible at K-band and higher frequencies because of the very small patch sizes. The traditional microstrip edge feed is possible, but the

Table 1-1: Substrate Materials and Properties				
Material	ϵ_r	Tan δ	HTS ?	Comment
$LaAlO_3$	23	$5x10^{-5}$	Yes	Twinning
MgO	9.7	$1x10^{-4}$	Yes	Latt. mismatch
Al_2O_3 (Sapphire)	≈10	$1x10_{-6}$	Yes	Anisotropic
Al_2O_3 (Alumina)	9.9	$1x10^{-4}$	No	
Quartz	3.8	$1x10^{-4}$	No	
Duroid (5880)	2.2	$1x10^{-3}$	No	

feedline must be inset into the patch edge substantially to match a 50 ohm transmission line. Multilayer structures alleviate some of the above difficulties, but they introduce a new dimension of complexity in the antenna architecture.

The experimental work done to date in the area of HTS antennas has been quite limited. Several groups have fabricated and tested electrically small antennas. Chaloupka, *et. al.*[70], have reported a 2.4 GHz miniaturized microstrip antenna fabricated using YBCO on $LaAlO_3$. This antenna showed an efficiency between 35% and 65%, while identical copper antennas showed radiation efficiencies between 1% and 6%. Dinger *et. al.*[71] have demonstrated a 500 MHz electrically small HTS dipole antenna with a matching network. This antenna showed an efficiency of 16% to 37% compared to 7% for an identical copper antenna. He *et. al.*[72] demonstrated a 6 GHz microstrip patch antenna which showed a gain enhancement of 5.5 dB over a copper patch. More recently, Herd

et. al.[73] have reported on the construction of a 16 element microstrip array at 12 GHz using a HTS feed network. In this array, the authors use a YBCO microstrip array fabricated on $LaAlO_3$. Rectangular microstrip patches printed on a quartz substrate placed above this array are electromagnetically coupled to the feed array. Performance improvements of this array over conventional metals have not been reported.

1.5 Research Objectives

The objective of this research was two fold. One objective was to first find practical ways of implementing superconducting microstrip antennas at high frequencies. Because HTS can only be deposited on high permittivity substrates, three distinct methods of coupling a microstrip feed line to a superconducting patch were investigated to accomplish this objective. The second objective was to investigate experimentally the performance advantages of HTS antennas over antennas fabricated using conventional metals. To accomplish this objective, the performance of superconducting single patch and four element array antennas were compared to both modeled data and identical antennas fabricated using normal metals. This research demonstrated several types of superconducting antennas for the first time.

Chapter 2 presents some of the theoretical aspects of the research. This chapter begins with design rules for microstrip transmission lines. Expressions for characteristic impedance and the effective dielectric constant are presented. Following this, the quarter-wave transformer is analyzed with and without losses.

From this point, loss mechanisms in microstrip transmission lines are individually examined and accepted expressions quantifying these losses are presented. The method for obtaining the Q of a circuit from S-parameter measurements is given, and finally, the mathematical basis for antenna arrays is presented.

Chapter 3 is a description of the experimental setup and procedures used in this research. The methods of thin film circuit fabrication and patterning are first discussed. Following this, the test fixtures, and cryogenic equipment are described. Finally, the methods used to measure the properties of the antennas are discussed.

In Chapters 4, 5, and 6, each of the three antenna architectures investigated is in turn described. In Chapter 4 the direct coupled antenna is discussed, in Chapter 5 the gap coupled antenna, and in Chapter 6 the electromagnetically coupled antenna is discussed. Each of these three chapters begins with a description of the particular antenna architecture and the motivations for investigating it. Experimental results for the antennas include patterns, input impedance, bandwidth, and efficiency for the single patch antennas, and patterns, VSWR, and gain for the four element arrays.

Chapter 7 presents an application of the technology developed in this dissertation. A 10 GHz superconducting active patch antenna is described.

Chapter 8 presents conclusions drawn from the experimental work. Some potential applications of the technology developed, and suggestions for future research are also presented.

1.6 References

1. Thomas A. Freeburg, "ALTAIR - True Wireless In-Building Networking," *IEEE Antennas and Propag. Symposium Digest*, p. 1269, 1992.

2. Raymond Leopold, "Motorola's IRIDIUM System: Low-Earth Orbit Global Cellular Communication Network," *IEEE Antennas and Propag. Symposium Digest*, p. 1270, 1992.

3. H. G. Booker, "Slot aerials and their relation to complementary wire aerials," *Journal of the IEE*, Pt. III A, vol. 93, p. 620, 1946.

4. G.A. Deschamps, "Microstrip Microwave Antennas," 3rd USAF Symposium on Antennas, 1953.

5. L. Lewin, "Radiation from discontinuities in stripline," *Proc. IEE*, vol. 107C, pp. 163-170, 1960.

6. *Proc. of the Workshop on Printed Circuit Antenna Technology*, October 17-19, 1979, New Mexico State University, Las Cruces, New Mexico.

7. *IEEE Trans. Antennas and Propag.*, Special Issue on Microstrip Antennas, vol. AP-29, no. 1, 1981.

8. L.C. Shen, "The elliptical microstrip antenna with circular polarization," *IEEE Trans. on Antennas and Propag.*, vol. AP-29, no. 1, pp. 90-94, Jan. 1981.

9. K. Luk, K.F. Lee, and J.S. Dahele, "Theory and experiment on equilateral triangular microstrip antenna," *Proc. 16th European Microwave Conference*, 1986.

10. Weng Cho Chew, "A Broad-Band Annular Ring Microstrip Antenna," *IEEE Trans. Antennas and Propagat.*, vol. AP-30, no. 5, pp. 918-922, Sep. 1982.

11. William F. Richards, Jai-Dong Ou, and Stuart A. Long, "A Theoretical and Experimental Investigation of Annular, Annular Sector, and Circular Sector Microstrip Antennas," *IEEE Trans. Antennas and Propagat.*, vol. AP-32, no. 8, pp. 864-867, Aug. 1984.

12. H.D. Weinschel, "Cyclindrical Array of Circularly Polarized Microstrip Antenna," *IEEE AP-S Int. Symposium Digest*, pp. 177-180, 1975.

13. Weng Cho Chew, "A Broad-Band Annular Ring Microstrip Antenna," *IEEE Trans. Antennas and Propagat.*, vol. AP-30, no. 5, pp. 918-922, Sep. 1982.

14. Y.T. Lo, D. Solomon, and W.F. Richards, "Theory and Experiment on Microstrip Antennas," *IEEE Trans. Antennas and Propagat.*, vol. AP-27, no. 2, pp. 137-145, Mar. 1979.

15. William F. Richards, Y.T. Lo, and Daniel D. Harrison, "An Improved Theory for Microstrip Antennas and Applications," *IEEE Trans. Antennas and Propagat.*, vol. AP-29, no. 1, pp. 38-46, Jan. 1981.

16. K.R. Carver, "Practical Analytical Techniques for the Microstrip Antenna," *Proc. Workshop on Printed Circuit Antennas*, New Mexico State University, Las Cruces, Oct. 1979, pp. 7.1-7.20.

17. Robert E. Munson, "Conformal Microstrip Antennas and Microstrip Phased Arrays," *IEEE Trans. Antennas and Propagat.*, vol. AP-22, no. 1, pp. 74-78, 1974.

18. A.G. Derneryd, "A Theoretical Investigation of the Rectangular Microstrip Antenna Element," *IEEE Trans. Antennas Propagat.*, vol. AP-26, no. 4, pp. 532-535, July 1978.

19. H. Pues and A. Van de Capelle, "Accurate Transmission-line Model for the Rectangular Microstrip Antenna," *IEE Proc.*, vol 131, pt. H, no. 6, pp. 334-340, Dec. 1984.

20. Pradeep K. Agrawal and M.C. Bailey, "An Analysis Technique for Microstrip Antennas," *IEEE Trans. Antennas and Propagat.*, vol. AP-25, no. 6, pp. 756-759, Nov. 1977.

21. V.H. Rumsey, "Reaction Concept in Electromagnetic Theory, *Physical Review*, vol. 94, pp. 1483-1491, June 15, 1954.

22. D.R. Poddar and J.S. Chatterjee, and S.K. Chowdhury, "On Some Broadband Microstrip Resonators," *IEEE Trans. on Antennas and Propag.* vol. AP-31, no. 1, Jan. 1983.

23. David M. Pozar, "Microstrip Antenna Aperture-Coupled to a Microstripline," *Elec. Letters,* vol. 21, no. 2, pp. 49-50, Jan. 17, 1985.

24. H. George Oltman and Donald A. Huebner, "Electromagnetically Coupled Microstrip Dipoles," *IEEE Trans. Antennas and Propagat.*, vol. AP-29, no. 1, pp. 151-157, Jan. 1981.

25. R.Q. Lee, K.F. Lee, and J. Bobinchak, "Characteristics of a Two-Layer Electromagnetically Coupled Rectangular Patch Antenna," *Electon. Letters*, vol. 23 no. 20, pp. 1070-1072, Sep. 24, 1987.

26. Richard E. Miller and Kai Chang, "Integrated Active Antenna Using Annular Ring Microstrip Antenna and Gunn Diode," *Microwave and Optical Technology Letters*, vol. 4, no. 2, pp. 72-75, Jan. 20 1991.

27. H.J. Thomas, D.L. Fudge, and G. Morris, "Gunn Source Integrated with a Microstrip Patch," *Microwaves and RF*, vol. 24, pp. 87-88, Feb. 1985.

28. J. Birkeland and T. Itoh, "Planar FET Oscillators Using Periodic Microstrip Patch Antennas," *IEEE Trans. Microwave Theory Tech.*, vol. MTT-37, no. 8, pp. 1232-1236, Aug. 1989.

29. E. H. Newman and J. E. Tehan, "Analysis of a Microstrip Array and Feed Network," *IEEE Trans. Antennas and Propagat.*, vol. AP-33, No. 4, pp. 397-403, Apr 1985.

30. David M. Pozar and Daniel H. Schaubert, "Comparison of Architectures for Monolithic Phased Array Antennas," *Microwave Journal*, pp. 93-104, Mar. 1986.

31. Barry J. Forman, "Directivity Characteristics of Scannable Planar Arrays, *IEEE Trans. Antennas and Propagat.*, vol. AP-20, no. 3, pp. 245-252, May 1972.

32. J.H. Cloete, and L.J. du Toit, "Linear Patch Array Pattern Degradation due to Corporate Feed Radiation," *IEEE Int. AP-S Symposium Digest*, pp. 466-469, 1988.

33. J. Ashkenazy, P. Perlmutter, and David Treves, "A Modular Approach for the Design of Microstrip Array Antennas," *IEEE Trans. Antennas and Propagat.*, vol. AP-31, No. 1, pp. 190-193, Jan. 1983.

34. Ely Levine, Gabi Malamud, Shmuel Shtrikman, and David Treves, "A Study of Microstrip Array Antennas with the Feed Network," *IEEE Trans. Antennas and Propagat.*, vol. AP-37, no. 4, pp. 426-434, Apr. 1989.

35. H.K. Onnes, "Disappearance of the Electrical Resistance of Mercury at Helium Temperatures," *Leiden Comm. Suppl.*, vol. 34, no. 122b, pp. 657-658, 1911.

36. W. Meissner and R. Ochsenfeld, *Naturwiss.*, vol. 21, p. 787, 1933.

37. J.G. Bednorz and K.A. Mueller, "Possible High-T_c Superconductivity in the Ba-La-Cu-O System," *Z. Physics B* vol. 64, pp. 189-193, 1986.

38. M.K. Wu, J.R. Ashburn, C.J. Torng, P.H. Hor, R.L. Meng, L. Gao, Z.J. Huang, Y.Q. Wang, and C.W. Chu, "Superconductivity at 93 K in a New Mixed-Phase Y-Ba-O Compound System at Ambient Pressure," *Phys. Rev. Lett.*, vol. 58, pp. 908-910, 1987.

39. H. Maeda, Y. Tanaka, N. Fukutomi, and T. Asano, *Jap. Journ. Appl. Phys. Lett.*, vol. 27, 1988.

40. S.S.P. Parkin, V.Y. Lee, E.M. Engler, A.I. Nazzal, T.C. Huang, G. Gorman, R. Savoy, and R. Beyers, *Phys. Rev. Lett.*, vol. 58, p. 908, 1987.

41. J.C. Gorter and H.B.G. Casimir, "The Thermodynamics of the Superconducting State," *Physik. Z.* vol. 35, pp. 963-966, 1934.

42. G.A. Samara and A.A. Giardini, "Pressure Dependence of the Dielectric Constant of Strontium Titanite," *Phys. Rev.* vol 140, p. A954-A957, 1965.

43. H.E. Weaver, "Dielectric Properties of Single Crystals of $SrTiO_3$ at Low Temperatures," *Pys. Chem. Solids*, vol. 11, pp. 274-277, 1959.

44. R.W. Simon, C.E. Platt, A.E. Lee, G.S. Lee, K.P. Daly, M.S. Wire, J.A. Luine, and M. Urbanik, *Appl. Phys. Lett.*, vol. 53, p. 2677, 1988.

45. F.A. Miranda, W.L. Gordon, V.O. Heinen, B.T. Ebihara, and K.B. Bhasin, "Measurements of Complex Permittivity of Microwave Substrates in the 20 to 300K Temperature Range from 26.5 GHz to 40.0 GHz," NASA TM-102123, 1989.

46. Tsuneo Konaka, Makoto Sato, Hidefumi Asano, and Shugo Kubo, "Relative Permittivity and Dielectric Loss Tangent of Substrate Materials for High-Tc Superconducting Film," *J. Superconductivity*, vol. 4, no. 4, pp. 283-288, 1991.

47. K.H. Young, G.V. Negrete, M.M. Eddy, J.Z. Sun, T.W. James, McD. Robinson, and E.J. Smith, "Comparisons of HTSC Thin films on various Substrates for Microwave Applications," Proc. ICFMCTF-91, San Diego, CA, 1991.

48. G.C. Liang, R.S. Withers, B.F. Cole, and W.G. Lyons, "High Temperature Superconductive Delay Lines and Filters on Sapphire and Thinned

$LaAlO_3$ Substrates," Presented at the 1992 Applied Superconductivity Conference, Aug. 1992.

49. N.Newman, B. Cole, S. Garrison, K. Char, and R.C. Taber, "Double Gun Off-Axis Sputtering of Large Area $YBa_2Cu_3O_{7-\delta}$ Superconducting Films for Microwave Applications," *IEEE Trans. Magn.*, vol. 27, pp. 1276 - 1279, 1991.

50. D. Oates, A. Anderson, D. Sheen, and S. Ali, "Stripline Resonator Measurements of Z_s versus H_{rf} in $YBa_2Cu_3O_{7-x}$ Thin Films," *IEEE Trans. Microwave Theory and Tech.*, vol. 39, no. 9, pp. 1522-1529, 1991.

51. Erik Ekholm and Stephen McKnight, "Attenuation and Dispersion for High-Tc Superconducting Microstrip Lines," *IEEE Trans. Microwave Theory and Tech.*, vol. MTT-38, no. 4, pp. 387-394, Apr. 1990.

52. W.G. Lyons, R.R. Bonetti, A.E. Williams, P.M. Mankiewich, M.L. O'Malley, J.M. Hamm, Alfredo C. Anderson, R.S. Withers, A. Meulenberg, and R.E. Howard, "High-Tc Superconductive Microwave Filters," *IEEE Trans. on Magnetics*, vol. 27, no. 2, pp. 2537-2539, March 1991.

53. S.H. Talisa, M.A. Janocko, c. Moskowitz, J. Talvaccio, J.F. Billing, R. Brown, D.C. Buck, C.K. Jones, B.R. McAvoy, G.R. Wagner, and D.H. Watt, "Low and High-Temperature Superconducting Microwave Filters," *IEEE Trans. Microwave Theory and Tech.*, vol. 39, no. 9, pp. 1448-1454, Sept. 1991.

54. W. Chew, A.L. Riley, D.L. Rascoe, B.D. Hunt, M.C. Foote, T.W. Cooley, and L.J. Bajuk, "Design and Performance of a High-T_c Superconductor Coplanar Waveguide Filter," *IEEE Trans. Microwave Theory and Tech.*, vol. 39, no. 9, pp. 1455 - 2461, Sept. 1991.

55. J.H. Takemoto, F.K. Oshita, H.R. Fetterman, P. Korbin, and E. Sovoro, "Microstrip Ring Resonator Technique for Measuring Microwave Attenuation in High-T_c Superconducting Thin Films," *IEEE Trans. Microwave Theory and Tech.*, vol. 37, no. 10, pp. 1650-1652, Oct. 1989.

56. C.M. Chorey, Keon-Shik Kong, K.B. Bhasin, J.D. Warner, and Tatsuo Itoh, "YBCO Superconducting Ring Resonators at Millimeter-wave Frequencies," *IEEE Trans. on Microwave Theory and Tech.*, vol 39, no. 9, pp. 1480-1486, Sept. 1991.

57. C. Wilker, Z.Y. Shen, P. Pang, D.W. Face, W.L. Holstein, A.L. Matthews, and D.B. Laubacher, "5 GHz High-Temperature Superconductor Resonators with High Q and Low Power Dependence to 90 K," *IEEE Trans. Microwave Theory and Tech.*, vol. 39, no. 9, pp. 1462-1468, Sept. 1991.

58. G.B. Walker and C.R. Haden, "Superconducting Antennas," *Journal of Applied Physics*, vol. 40, no. 5, pp. 2035-2039, Apr. 1969.

59. V.A. Pavlyuk, E.F. Krivosheev, V.I. Mikhailov, A.V. Tarasov, "Superconducting Antenna," *Soviet Physics Technical Physics*, vol 4, no. 2, p. 80, Feb. 1978.

60. Saburo Adachi, Kazuhide Ashida, and Shigeo Ohnuki, "Superconducting Dipole Array Antenna," *Transactions of the IECE of Japan*, vol E 63, no. 9, pp. 683-684, Sep. 1980.

61. G.B. Walker, Clovis R. Haden, and O.G. Ramer, "Superconducting Superdirectional Antenna Arrays," *IEEE Trans. Antennas and Propagat.*, vol. AP-25, no. 6, pp. 885-887, Nov. 1977.

62. S.K. Khamas, M.J. Mehler, T.S. Maclean, C.E. Gough, "High Tc Superconducting Short Dipole Antenna," *Electron. Letters*, vol.24, no. 8, pp. 460-461, 1988.

63. R.C. Hansen, "Superconducting Antennas," *IEEE Trans. Aerospace and Electronic Systems*, vol 26, no. 2, pp. 345-354, Mar. 1990.

64. Robert J.Dinger, "Some Potential Antenna Applications of High Temperature Superconductors," *Journal of Superconductivity*, vol. 3, no. 3, pp. 287-296, Sep. 1990.

65. R.C. Hansen, "Fundamental Limitations in Antennas," *Proceedings of the IEEE*, vol. 69, pp. 170-182, Feb. 1981.

66. L.J. Chu, "Physical Limitations of Omni-Directional Antennas," *Journal of Applied Physics*, vol. 19, pp. 1163-1175, Dec. 1948.

67. R.F. Harrington, "Effects of Antenna Size on Gain, Bandwidth, and Efficiency," *Journal of Research of the National Bureau of Standards*, vol. 64D, pp. 1-12, Jan./Feb. 1960.

68. T. Moreno, *Microwave Transmission Design Data*, New York: Dover, 1948, Ch. 2.

69. Rogers Corp., Microwave Materials Division, 100 S. Roosevelt Ave., Chandler, AZ 85226.

70. Heinz Chaloupka, Norbert Klein, Michael Peiniger, Helmut Piel, Arndt Pischke, and Georg Splitt, "Miniaturized High-Temperature Superconductor Microstrip Patch Antenna," *IEEE Trans. Microwave Theory and Tech.*, vol. 39, no. 9, pp. 1513-1521, Sept 1991.

71. Robert J. Dinger, Donald R. Bowling, and Anna M. Martin, "A Survey of Possible Passive Antenna Applications of High-Temperature Superconductors," *IEEE Trans. Microwave Theory and Tech.*, vol. 39, no. 9, pp. 1498-1507, Sept. 1991.

72. Y.S. He, A.S. He, X.X. Zhang, C.S. Shi, N. Lu, B. Tian, D.R. Lu, M.L. Zhou, and W.G. Wang., "Progress in High Tc Superconducting Ceramic Antennas," *Superconductor Science Technology*, vol. 4 p. S124-S126, 1991.

73. J.S. Herd, J.P. Kenney, K.G. Herd, W.G. Lyons, Alfredo Anderson, P. M. Mankiewich, and M.L. O'Malley, "Experimental Results on a 12 GHz 16-Element Multilayer Microstrip Array with a High-T_c Superconducting Feed Network," *IEEE Antennas and Propag. Symposium Digest*, pp. 974-977, 1992.

CHAPTER II.

THEORETICAL MICROWAVE CONSIDERATIONS

2.1 Introduction

Microstrip patch antennas are an outgrowth of the microstrip transmission line, where an electromagnetic wave is supported between metallization on the top and bottom of a dielectric sheet. However, the design and analysis of microstrip transmission lines and antennas is not simple due to several factors. First, the dielectric constant seen by the electromagnetic wave is not purely the dielectric constant of the substrate. This is because the electromagnetic fields are not wholly contained within the substrate. Thus, some type of effective permittivity must be used to account for the fields outside of the substrate. Secondly, the effect of fringing fields at the ends of the microstrip circuit must be considered. This effect, known as the open end effect, is especially important in microstrip antennas as the fringing fields are the most important radiation mechanism. Finally, because current tends to flow along the edges of microstrip circuits, the dielectric and metallization losses of microstrip circuits are difficult to analyze accurately.

The aim of this chapter is not to comprehensively analyze microstrip circuits. Rather, it is to achieve a level of understanding of their functioning and to present some of the theoretical issues that were considered in this research. To this end, the microstrip transmission line is first considered. Expressions for the effective dielectric constant and impedance of the lines are given. Because superconductors exhibit a complex conductivity, the modifications in these expressions necessary to model superconducting transmission lines and antennas are also considered. From this point, the attenuation mechanisms in microstrip circuits are explained and modeled. Finally, expressions necessary to design microstrip antenna arrays are given. The analysis of the individual antenna architectures are presented in Chapters 4, 5, and 6.

2.2 Microstrip Transmission Lines

To describe microstrip transmission lines analytically, two of the most important parameters are the effective dielectric constant (ϵ_{eff}) and the line impedance (Z_0). Analytic expressions for these parameters are presented. These expressions allow one to find ϵ_{eff} and Z_0 based upon the physical geometry of the circuit, and vise versa. The quarter-wave transformer is then analyzed with and without losses.

2.2.1 Effective Dielectric Constant

The microstrip transmission line is shown in Figure 2-1. Although the substrate has a dielectric constant ϵ_r, the propagating wave sees an effective dielectric constant, ϵ_{eff}, that is substantially less than ϵ_r because the propagating

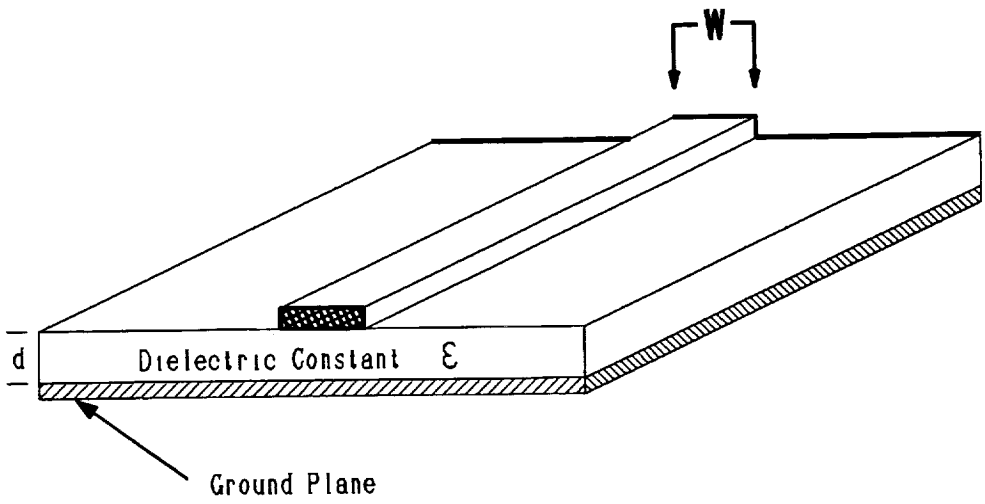

Figure 2-1: Microstrip transmission line.

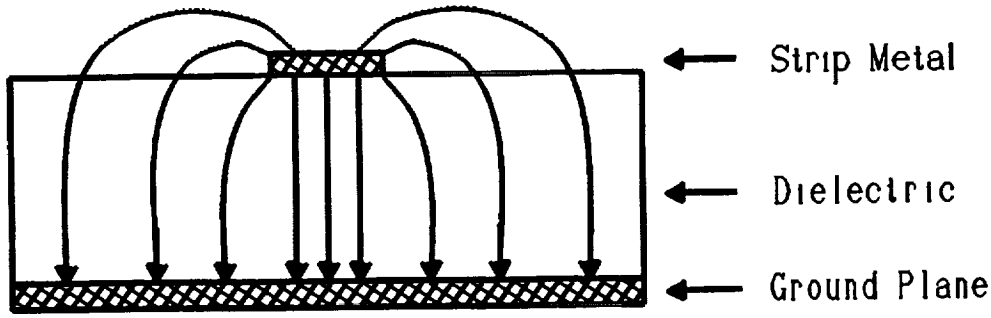

Figure 2-2: Electric field pattern for a microstrip transmission line. Not all of the field is contained within the substrate.

wave is not entirely contained within the substrate, as shown in Figure 2-2. The most commonly used expression for the effective dielectric constant, ϵ_{eff}, is the one developed by Wheeler[1] and by Schneider[2],

$$\epsilon_{eff} = \frac{\epsilon_r+1}{2}+\frac{\epsilon_r-1}{2}\left(1+12\frac{h}{W}\right)^{-1/2} \qquad (2\text{-}1)$$

where h and W are the dielectric height and width of the transmission line, respectively. This expression is a quasi-static approximation, and thus its accuracy

declines with increasing frequency. As this dissertation concerns work at very high frequencies (above 20 GHz), an expression which takes into account variations with frequency was deemed necessary. Such an equation has been reported by Kirschning and Jansen as

$$\epsilon_{eff}(f) = \epsilon_r - \frac{\epsilon_r - \epsilon_{eff}(f=0)}{1 + P(f)} \tag{2-2}$$

Here, $\epsilon_{eff}(f=0)$ is given by Eqn. (2-1), and the frequency dependent term P(f) is given by

$$P(f) = P_1 P_2 \left[\left(0.1844 + P_3 P_4 \right) 10fh \right]^{1.5763} \tag{2-3}$$

with

$$P_1 = 0.2749 + \left[0.6315 + \frac{0.525}{(1 + 0.157fh)^{20}} \right] u - 0.06568e^{(-8.751u)} \tag{2-4}$$

$$P_2 = 0.3362\left[1 - e^{-0.03442\epsilon_r}\right] \tag{2-5}$$

$$P_3 = 0.0363e^{-4.6u}\left[1 - e^{-(fh/3.87)^{4.97}}\right] \tag{2-6}$$

$$P_4 = 1 + 2.751\left[1 - e^{-(\epsilon_r/15.916)^8}\right] \tag{2-7}$$

In these equations, *fh* is the normalized frequency in GHz-cm. Kirschning and Jansen[3] claim accuracy within 0.6% when $0.1 \le w/h \le 100$, $1 \le \epsilon_r \le 20$, and $0 \le h/\lambda_0 \le 0.13$.

2.2.2 Transmission Line Impedance

An expression for the impedance of a microstrip transmission line has also been given by Wheeler[4] and by Schneider[2] as

$$Z_0 = \frac{\eta}{2\pi\sqrt{\epsilon_{eff}}} \ln\left(\frac{8h}{W}+\frac{W}{4h}\right) \qquad (2\text{-}8)$$

for W/h ≤ 1 and

$$Z_0 = \frac{\eta}{\sqrt{\epsilon_{eff}}} \left[\frac{W}{h}+1.393+0.667\ \ln\left(\frac{W}{h}+1.444\right)\right]^{-1} \qquad (2\text{-}9)$$

for W/h > 1. In these expressions, $\eta = 120\,\pi$ ohm and ϵ_{eff} is given by Eqn. (2-1). To find Z_0 based from given values of W and h, these equations may be manipulated to give

$$W/h = \frac{8\exp(A)}{\exp(2A)-2} \qquad (2\text{-}10)$$

in the case that A > 1.52, and

$$W/h = \frac{2}{\pi}\left(B-1-\ln(2B-1)+\frac{\epsilon_r-1}{2\epsilon_r}\left[\ln(B-1)+0.39-0.\frac{61}{\epsilon_r}\right]\right) \qquad (2\text{-}11)$$

for A ≤ 1.52. In Eqns. (2-10) and (2-11) A and B are defined as

$$A = \frac{Z_0}{60}\left(\frac{\epsilon_r+1}{2}\right)^{1/2} + \frac{\epsilon_r-1}{\epsilon_r+1}\left(0.23+\frac{0.11}{\epsilon_r}\right) \qquad (2\text{-}12)$$

and

$$B = \frac{60\pi^2}{Z_0\sqrt{\epsilon_r}} \qquad (2\text{-}13)$$

These equations have a stated accuracy of better than 2% when compared to rigorous conformal mapping methods. For this work, because the thickness of the metallization was very small when compared to the dielectric thickness, the effect of strip thickness upon the impedance and effective dielectric constant was neglected.

The above equations were applied to the materials used in this study. Unless stated otherwise, the permittivity of $LaAlO_3$ is assumed to be 23 throughout this study. For a 50 ohm transmission line on $LaAlO_3$ Eqn. (2-12) gives A = 3.10, and Eqn. (2-10) results in a line width of 92 μm. In this study, a width of 100 μm was used which, using Eqn. (2-8), gives an impedance of 48.6 Ω. For a $LaAlO_3$ substrate that is 254 μm thick, Eqn. (2-1) gives a value for ϵ_{eff} of 14.1 while Eqns. (2-2) through (2-7) give 14.7. Thus, a wave propagating along a microstrip transmission line with a strip width of 100 μm will have a guided wavelength that is reduced by a factor of $14.7^{-1/2}$, or 0.26, from the freespace wavelength.

2.2.3 Quarter-wave Transformer

In microstrip circuitry it is often necessary to connect lines of differing impedance. To maintain a low reflection coefficient at the input of the circuit, some type of transformer must be used for impedance matching. One of the simplest and most common transformers is the quarter-wave transformer.

Consider a case where the load impedance, Z_L, is to be fed by a lossless line having characteristic impedance Z_c, propagation constant β and length l. At the input of this ideal line, the impedance of the load will appear as

$$Z_{in} = Z_c \frac{Z_L + jZ_c \tan(\beta l)}{Z_c + jZ_L \tan(\beta l)} \qquad \textbf{(2-14)}$$

If βl is made to be $\pi/4$, Eqn. (2-14) reduces to

$$Z_{in} = \frac{Z_c^2}{Z_L} \qquad \textbf{(2-15)}$$

Thus, when Z_c is made to be $(50Z_L)^{1/2}$ and $\lambda/4$ in length, the load impedance appears as 50 ohms. When the transforming section is lossy a perfect match will no longer occur, but the reflection coefficient will still be quite small, as shown in Figure 2-3.

2.3 Loss Mechanisms in Microstrip Circuits

One of the major shortcomings of microstrip transmission lines is their high attenuation when compared to other transmission media such as coaxial cable or rectangular waveguides. There are four main forms of microstrip transmission line losses: conductor losses, dielectric losses, radiation losses, and surface wave losses. Radiation losses are desirable in microstrip antennas since the function of an antenna is to radiate. However, radiation from the antenna feedline must be kept to a minimum. In this section, each of the above loss mechanisms is examined for microstrip transmission lines and, in a general sense, for microstrip antennas, although the specific equations presented may not necessarily be

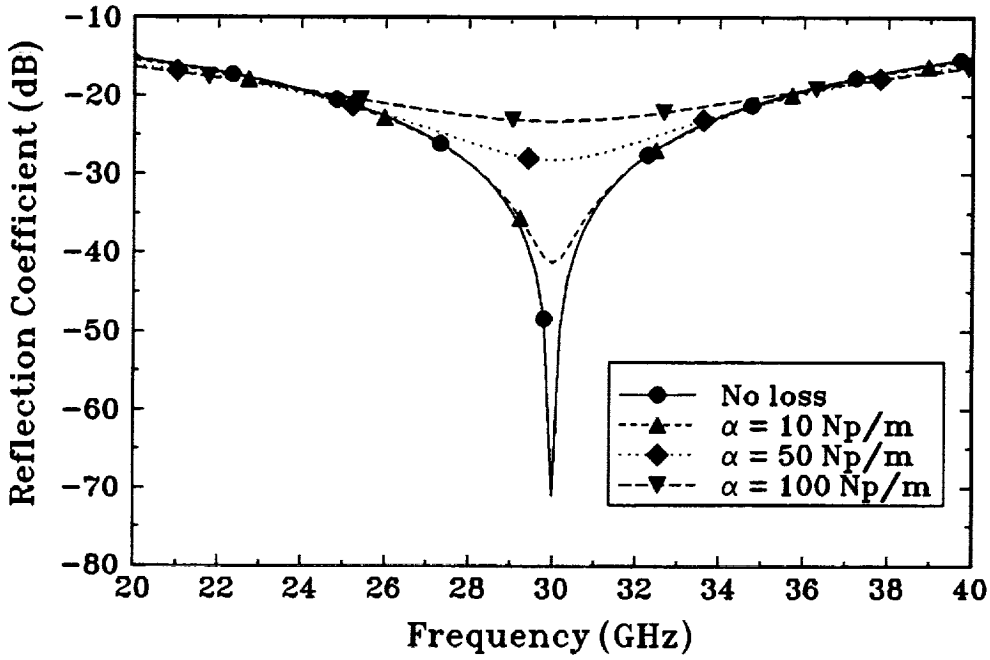

Figure 2-3: Reflection coefficient of quarter wave transformers including losses. A TEM wave is assumed on a transmission line with an air dielectric and a 2.5 mm line length.

applicable to microstrip antennas. Equations specific to microstrip antennas are given in Chapters 4,5, and 6.

2.3.1 Conductor Losses: Normal Metals

A plane wave incident upon a metal will decrease exponentially in amplitude as it travels further into the metal. For a normal metal, the wave amplitude will decreases according to

$$E(x) = E_0 e^{-x/\delta_s} \tag{2-16}$$

where E_0 is the wave amplitude at the air-metal boundary and x is the direction into the metal. The quantity δ_s is known as the skin depth, and is the distance at which the field intensity has decreased by 1/e. The skin depth is given by

$$\delta_s = \frac{1}{\sqrt{f\pi\mu\sigma}} \tag{2-17}$$

where f is the frequency, σ is the DC conductivity of the metal, and μ is the permeability of the metal. The surface resistance of the metal, R_s is related to the skin depth by

$$R_s = \frac{1}{\sigma\delta_s} = \sqrt{\frac{f\pi\mu}{\sigma}} \tag{2-18}$$

Closed form expressions for the attenuation in microstrip lines with conductor width and dielectric height of W and h, respectively, due to the conductor losses have been reported by Pucel *et. al.*[5,6] as

$$\alpha_c(dB/m) = 1.38A \frac{R_s}{hZ_0} \frac{32-(W_e/h)^2}{32+(W_e/h)^2} \tag{2-19}$$

for W/h ≤ 1, and

$$\alpha_c(dB/m) = 6.1x10^{-5}A \frac{R_s Z_0 \epsilon_{eff}}{h} \left[W_e/h + \frac{0.667 W_e/h}{W_e/h+1.444}\right] \tag{2-20}$$

for W/h ≥ 1. In these equations,

$$\frac{W_e}{h} = \frac{W}{h} + \frac{\Delta W}{h} \tag{2-21}$$

and

$$\frac{\Delta W}{h} = \frac{1.25}{\pi}\frac{t}{h}\left(1+\ln\frac{4\pi W}{t}\right) \tag{2-22}$$

for W/h ≤ $1/2\pi$ and

$$\frac{\Delta W}{h} = \frac{1.25}{\pi}\frac{t}{h}\left(1+\ln\frac{2h}{t}\right) \qquad (2\text{-}23)$$

for W/h ≥ $1/2\pi$. A is defined by

$$A = 1+\frac{h}{W_e}\left(1+\frac{1}{\pi}\ln\frac{2B}{t}\right) \qquad (2\text{-}24)$$

while B = h for W/h ≥ $1/2\pi$ and B = 2πW for W/h ≤ $1/2\pi$. The metallization thickness of the strip is represented by t.

2.3.2 Conductor Losses: Superconductors

As explained in Section 1.3, superconductors are not without a surface resistance for frequencies above DC. This surface resistance is given by

$$R_s = R_N \frac{\sqrt{\sigma_1^2+\sigma_2^2}-\sigma_2}{\sqrt{\sigma_1^2+\sigma_2^2}} \qquad (2\text{-}25)$$

In this equation, R_N is the surface resistance at T_c,

$$\sigma_1 = \frac{\omega\mu_0}{2R_N^2}\left(\frac{T}{T_c}\right)^4 \qquad (2\text{-}26)$$

$\sigma_2 = (1/\mu_0\omega\lambda_p^2)$, and λ_p is the penetration depth given by

$$\lambda_p = \frac{\lambda_0}{\sqrt{1-(T/T_c)^4}} \qquad (2\text{-}27)$$

according to the two-fluid model. Miranda *et. al.* have measured the complex conductivities of HTS thin films on $LaAlO_3$ and found typical values for R_N to be between 0.6 Ω and 0.8 Ω [7]. The agreement between Eqn. (2-27) and measured surface resistance values is quite poor, especially at lower temperatures. Even if the surface resistance were to be well characterized analytically, the previously

presented expressions for α_c are not accurate for superconductors. This is both because superconductors have a different current distribution than normal metals and because the thickness of an HTS film is generally no more than one or two penetration depths. Although several authors have reported methods for calculating the attenuation of HTS microstrip lines[8,9], these methods remain cumbersome and inaccurate. For this work, losses in HTS lines were assumed to be similar to those found experimentally from 35 GHz ring resonators by Chorey *et. al.*[10]

2.3.3 Dielectric Losses

The losses due to the dielectric are described by the loss tangent of the dielectric, tan δ. According to Pucel *et. al.*[5,6], the dielectric loss in a microstrip line on a substrate of permittivity ϵ_r and loss tangent tan δ is given by

$$\alpha_d\,(dB/m) = 27.3\frac{\epsilon_r}{\epsilon_r - 1}\frac{\epsilon_{eff} - 1}{\sqrt{\epsilon_{eff}}}\frac{\tan\delta}{\lambda_0} \qquad \textbf{(2-28)}$$

In general, dielectric losses are quite small when compared to conductor losses. The loss tangent of $LaAlO_3$ is approximately 5×10^{-5}. For a 50 Ω line operating at 30 GHz, Eqn. (2-25) gives a dielectric loss of 0.51 dB/m. Duroid has a dielectric loss tangent of 1×10^{-3}. Using Eqn. (2-28), a dielectric loss of 3.3 dB/m would result for a 50 Ω line on this substrate operating at 30 GHz.

2.3.4 Radiation Losses

Microstrip transmission lines radiate some of their energy as space waves. This occurs mainly at discontinuities such as gaps, open end, and bends. Lewin[11] has derived expressions for the power radiated due to discontinuities as

$$P = 60\left(\frac{\omega_0 h}{c}\right)^2 F(\epsilon_r) \tag{2-29}$$

In this expression, the $F(\epsilon_r)$ are given by:

Open circuit

$$F(\epsilon) = \frac{\epsilon+1}{\epsilon} - \frac{(\epsilon-1)^2}{2\epsilon\sqrt{\epsilon}}\ln\frac{\sqrt{\epsilon+1}}{\sqrt{\epsilon-1}} \tag{2-30}$$

Short circuit

$$F(\epsilon) = 3 - \frac{1}{\epsilon} - \left(3+\frac{1}{\epsilon}\right)\frac{\epsilon-1}{2\epsilon\sqrt{\epsilon}}\ln\frac{\sqrt{\epsilon+1}}{\sqrt{\epsilon-1}} \tag{2-31}$$

Matched termination

$$F(\epsilon) = 1 - \frac{\epsilon-1}{2\sqrt{\epsilon}}\ln\frac{\sqrt{\epsilon+1}}{\sqrt{\epsilon-1}} \tag{2-32}$$

Right-angle bend

$$F(\epsilon) = \frac{\epsilon+1}{\epsilon}\ln\frac{\sqrt{\epsilon+1}}{\sqrt{\epsilon-1}} - \frac{2\epsilon}{\sqrt{2\epsilon-1}}\ln\frac{\sqrt{2\epsilon}}{\sqrt{2\epsilon-2}} \tag{2-33}$$

It is important to note that the radiated power from microstrip circuits increases as the square of the dielectric thickness. In practical terms, this means that it is desirable to construct microstrip antennas on thick substrates, since a rectangular microstrip antenna can be thought of as two open ends separated by a low

impedance transmission line. On the other hand, the feed network would ideally be placed on a thin substrate so as to minimize radiation from the feed network.

2.3.5 Surface Wave Losses

Surface waves are waves that are trapped by total internal reflection within the dielectric substrate. These waves travel along the two dimensional substrate surface. For a finite dielectric, these waves eventually come to the edge of the dielectric and radiate out as space waves. Surface waves are undesirable in microstrip antennas for two reasons. First, they represent power which is lost, and thus they reduce the efficiency of antennas. Secondly, when they are diffracted from the edge of the dielectric to become space waves, they interfere with the radiation pattern of the antenna to degrade both the main beam and side lobe response[12]. In large arrays, surface waves can cause scan blindness when a surface wave mode and a Floquet (periodic) mode of the structure have identical propagation constants[13].

Surface waves occur in both TE and TM modes. The cutoff frequencies are given by[14]

$$f_{co} = \frac{nc}{4h\sqrt{\varepsilon_r - 1}} \qquad (2\text{-}34)$$

where n is the mode number and h is the substrate thickness. Surface waves will always exist because the lowest order TM mode, TM_0 has a zero cutoff frequency. For the substrate and dimensions used in this study (254 μm thick $LaAlO_3$), the next higher modes, TM_1 and TE_1, have cutoff frequencies of 62 GHz.

There are several ways of calculating surface wave efficiencies for patch antennas. The most accurate is to use a method of moments analysis such as Pozar[12] has done. However, this method is a long and cumbersome process, so several closed-form approximations have been published[15,16,17]. Perlmutter *et. al.*[15] use an electric surface current model for rectangular patches which assumes uniform current under microstrip metallization. Nauwelaers *et. al.*[16] have done curve fitting on data from Perlmutter *et. al.* and from Pozar[12] to obtain closed form expressions. Pozar[17] claims a closed-form approximation for the propagation constant of the surface waves that is more accurate than that of Perlmutter *et. al.* or that of Nauwelaers *et. al.*, thus giving an accuracy improvement in the expressions for surface wave efficiency. His expressions are

$$P_{sw} = \frac{Z_0 k_0^2}{4} \frac{\epsilon_r (x_0^2-1)}{\epsilon_r \left[\frac{1}{\sqrt{x_0^2-1}} + \frac{\sqrt{x_0^2-1}}{\epsilon_r - x_0^2} \right] + \left[1 + \frac{\epsilon^2_r (x_0^2-1)}{\epsilon_r - x_0^2} \right] (k_0 h)} \tag{2-35}$$

where

$$x_0 = 1 + \frac{-\epsilon^2_r + \alpha_0\alpha_1 + \epsilon_r \sqrt{\epsilon^2_r - 2\alpha_0\alpha_1 + \alpha^2_0}}{\epsilon^2_r - \alpha^2_1} \tag{2-36}$$

$$\alpha_0 = s \tan(k_0 hs) \tag{2-37}$$

$$\alpha_1 = \frac{-1}{s} \left[\tan(k_0 ds) + \frac{k_0 ds}{\cos^2(k_0 ds)} \right] \tag{2-38}$$

and

$$s = \sqrt{\epsilon_r - 1} \tag{2-39}$$

In the above equations, k_0 is the free space propagation constant, given by $2\pi/\lambda_0$. The author claims an agreement with method of moments solutions within 5% for $\sqrt{\epsilon_r} < \lambda_0/8h$. Since the materials used in this study fall within this criteria, Eqn. (2-35) is used. Surface wave efficiencies, $P_{rad}/(P_{rad}+P_{sw})$, calculated using the above relations for three different substrate permittivities are shown in Figure 2-4. This figure illustrates the dramatic increase in surface wave generation with an increase in frequency or in substrate permittivity. In an antenna array, however, surface wave efficiency is much more difficult to calculate because of the interaction between waves generated at each element.

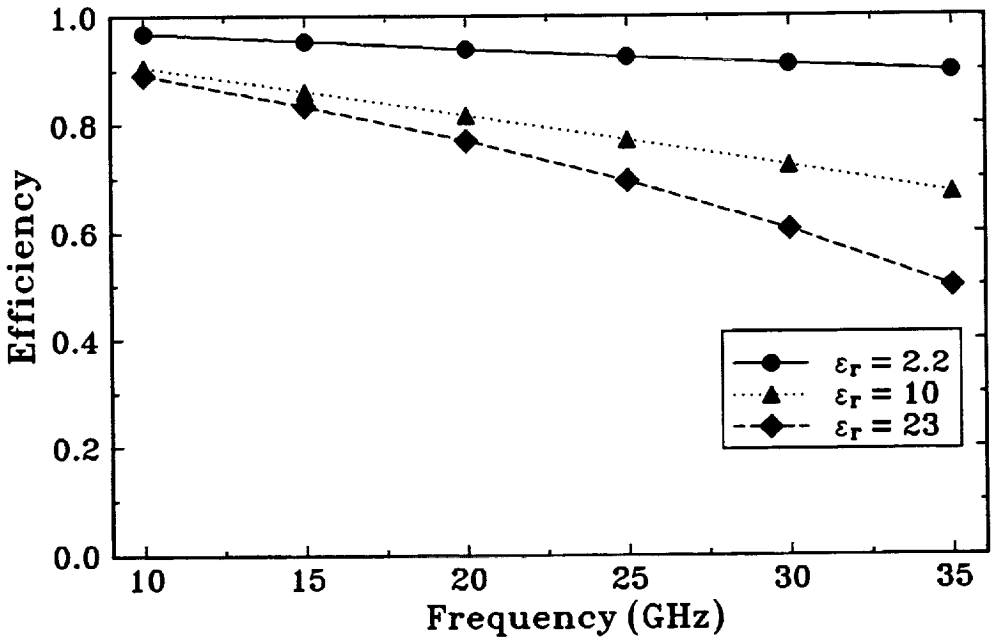

Figure 2-4: Surface wave efficiency using Pozar's closed form expressions.

2.3.6 Other Loss Mechanisms

The remaining causes of losses in microstrip circuits are substrate surface roughness and the resistivity of the thin layer of adhesion metal. The effects of surface roughness were first studied by Morgan[18]. Hammerstad and Bekkadal[19] proposed the formula

$$\alpha_{cr} = \alpha_c \left[1+\frac{2}{\pi}\arctan\ 1.4\left(\frac{\Delta}{\delta}\right)^2\right] \qquad \textbf{(2-40)}$$

to include the effects of surface roughness in the conductor loss. In the above equation, Δ is the RMS surface roughness, and δ is the skin depth. The surface roughness of $LaAlO_3$ varies from sample to sample and depends upon amount and quality of substrate polishing that is done. Some research has indicated that these substrates roughen considerably upon high temperature (above 500 °C) thermal cycling necessary in pulsed laser deposition processes[20].

For the circuits used in this study, adhesion of gold or copper to $LaAlO_3$ was achieved by evaporating a thin layer (less than 200 Å) of chromium before the gold or copper. The effect of such adhesion layers upon microstrip losses has been investigated by Sobol[21]. He found that a thin adhesion layer produced negligible losses well into the millimeter wave region.

2.4 Calculation of Q from the Reflection Coefficient

Since microstrip antennas are narrow band resonant devices, their quality factor, or Q, can be found from microwave measurements. The Q of a resonant circuit is important because it allows a quantitative description of the losses

present in a resonant circuit. This section will describe the calculations necessary to find the Q of a microstrip antenna.

In general, the Q of a resonant circuit is defined as

$$Q = \omega_r \frac{\textit{Energy Stored in System}}{\textit{Energy Lost Per Second}} \qquad \textbf{(2-41)}$$

The transmission line and matching network which feed the resonator contains both reactive and resistive parts. These components load the resonant circuit so that what one measures is not the Q of the resonator, but the Q loaded by the coupling network and transmission line. This loaded Q is denoted as Q_L, while the Q of the unloaded resonator is denoted as Q_0. For typical microstrip resonators, a narrow coupling gap is used to couple energy from a transmission line into the resonator. For this work, three types of coupling were used: gap coupling, direct coupling, and electromagnetic coupling. Each of these architectures is described in detail in subsequent chapters. This section is based upon work published by Romanofsky[22].

A resonator can be modeled by a parallel RLC network, while the coupling network can be described by an ideal transformer and a series resistive loss, R_i, which represents the coupling loss (Figure 2-5). The input impedance of the circuit to the right of the transformer is

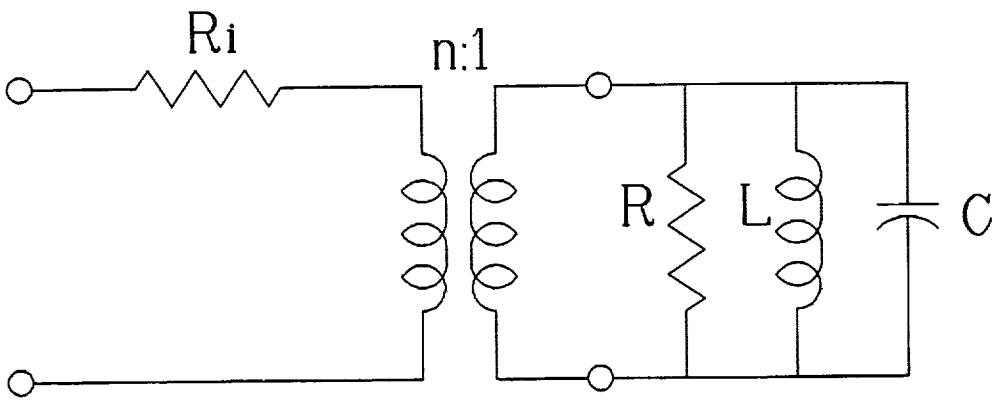

Figure 2-5: Equivalent circuit of resonator and coupling network.

$$Z_{res} = \frac{1}{\frac{1}{R} + j\left(\omega C - \frac{1}{\omega L}\right)} \tag{2-42}$$

and the $Q = \omega_0 RC$, where ω_0 is the resonant angular frequency. When the coupling network is included, the input impedance is modified and becomes

$$Z_{in} = \frac{1}{\frac{n^2}{(Z_0 + R_i)} + \frac{1}{R} + j\left(\omega C - \frac{1}{\omega L}\right)} \tag{2-43}$$

where Z_0 is the characteristic impedance of the transmission line. The Q of this circuit is the loaded Q, and is given by

$$Q_L = \frac{\omega_0 CR\left(1 + \frac{R_i}{Z_0}\right)}{\left(1 + \frac{R_i}{Z_0} + \frac{Rn^2}{Z_0}\right)} \tag{2-44}$$

Letting $\sigma = R_i/Z_0$ and $\kappa = Rn^2/Z_0$ and writing $\omega_0 RC$ as Q_0, Q_L can be written as

$$Q_L = \frac{Q_0(1+\sigma)}{(1+\sigma+\kappa)} \qquad (2\text{-}45)$$

where σ is the coupling loss while κ is the coupling coefficient. If $\kappa < 1$, the resonator is undercoupled, while if $\kappa > 1$ the resonator is overcoupled. The resonator is said to be critically coupled when $\kappa = 1$. In this final case, the impedance of the resonator is matched to that of the source.

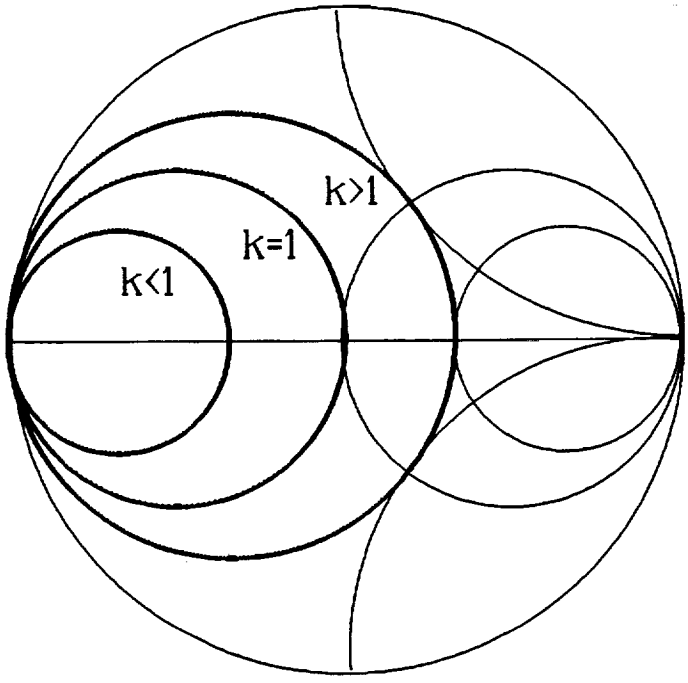

Figure 2-6: Smith chart showing coupling of resonators.

At frequencies far from resonance very little power is coupled into the resonator so that the reflection coefficient is

$$\Gamma_f = \frac{R_L - Z_0}{R_L + Z_0} = \frac{R_L/Z_0 - 1}{R_L/Z_0 + 1} = \frac{\sigma - 1}{\sigma + 1} \qquad (2\text{-}46)$$

At resonance, the reflection coefficient is given by

$$\Gamma_r = \frac{Z_{in}-Z_0}{Z_{in}+Z_0} = \frac{R_i+Rn^2-Z_0}{R_i+Rn^2+Z_0} = \frac{(\sigma+\kappa-1)}{(\sigma+\kappa+1)} \tag{2-47}$$

Using Eqns (2-46), σ can be found as

$$\sigma = \frac{1-\Gamma_i}{1+\Gamma_i} \tag{2-48}$$

From the above three equations, κ can be found. When the resonator is undercoupled,

$$\kappa = \frac{1-\Gamma_r}{1+\Gamma_r}-\sigma \tag{2-49}$$

When the resonator is overcoupled,

$$\kappa = \frac{1+\Gamma_r}{1-\Gamma_r}-\sigma \tag{2-50}$$

The loaded Q is related to the bandwidth and resonant frequency as

$$Q_L = \frac{f_r}{f_1-f_2} \tag{2-51}$$

where f_1 and f_2 are the half-power frequencies, which have reflection coefficients given by

$$p_{half} = \frac{1}{2}\left(\left[\frac{\sigma+\kappa-1}{\sigma+\kappa+1}\right]^2+\left[\frac{\sigma-1}{\sigma+1}\right]^2\right) \tag{2-52}$$

Thus to find the loaded Q, the reflection coefficients at resonance and far from resonance are measured and used to find σ and κ. Then, the resonant frequency and half-power frequencies are found and substituted into Eqn. (2-51). Once the loaded Q is known, the unloaded Q may be found using Eqn. (2-45).

2.5 Antenna Arrays

When several antenna elements are placed in close proximity of each other an antenna array is formed. Antenna arrays follow the pattern multiplication theorem, which states that the pattern of an array is given by the pattern of an individual element multiplied by a quantity known as the array factor. This theorem allows one to calculate relatively easily the radiation pattern which an array will produce. In this section, the mathematical basis for the array factor is presented, based upon the work of Collin[23].

A single antenna element radiates with a field given by

$$E(r) = f(\theta,\phi)\frac{e^{-jk_0 r}}{4\pi r} \tag{2-53}$$

where $\mathbf{f}(\theta,\phi)$ is the far-field pattern of the element. When an array is formed, the excitation amplitude and phase of each element and the relative position of each element are accounted for to obtain the radiated field as

$$E(r) = \sum_{i=1}^{N} C_i e^{j\alpha_i} f(\theta,\phi) e^{-jk_0 r + jk_0 \mathbf{a}_r \cdot \mathbf{r}_i} \tag{2-54}$$

Eqn. (2-54) can then be written in the form

$$E(r) = f(\theta,\phi)F(\theta,\phi) \tag{2-55}$$

where the array factor F is given by

$$F(\theta,\phi) = \sum_{i=1}^{N} C_i e^{j\alpha_i + jk_0 \mathbf{a}_r \cdot \mathbf{r}_i} \tag{2-56}$$

In the above equations, C_i is the relative excitation coefficient of the i'th element, α_i is the phase of the i'th element, and $\mathbf{a}_r \cdot \mathbf{r}_i$ is the relative propagation delay. In

the case of a one-dimensional array positioned along the x-axis and fed in-phase with equal amplitudes I_0, the array factor reduces to

$$| F | = I_0 \left| \frac{\sin(nk_0 d \cos\phi)}{\sin(k_0 d \cos\phi)} \right| \qquad (2\text{-}57)$$

In this equation, n is the number of elements and d is the element spacing. The array factor is a function of element spacing. As can be seen in Figure 2-8, a wider element spacing narrows the main beam. However, element spacing greater than one wavelength brings secondary main lobes into the array radiation pattern (visible space).

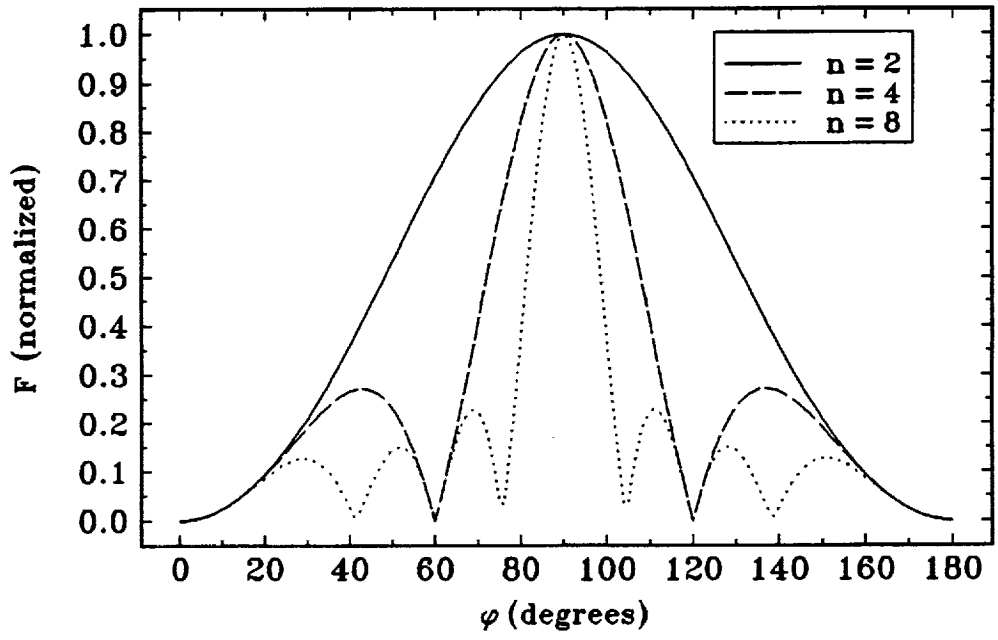

Figure 2-7: Array factor for one-dimensional array with 2, 4, and 8 elements.

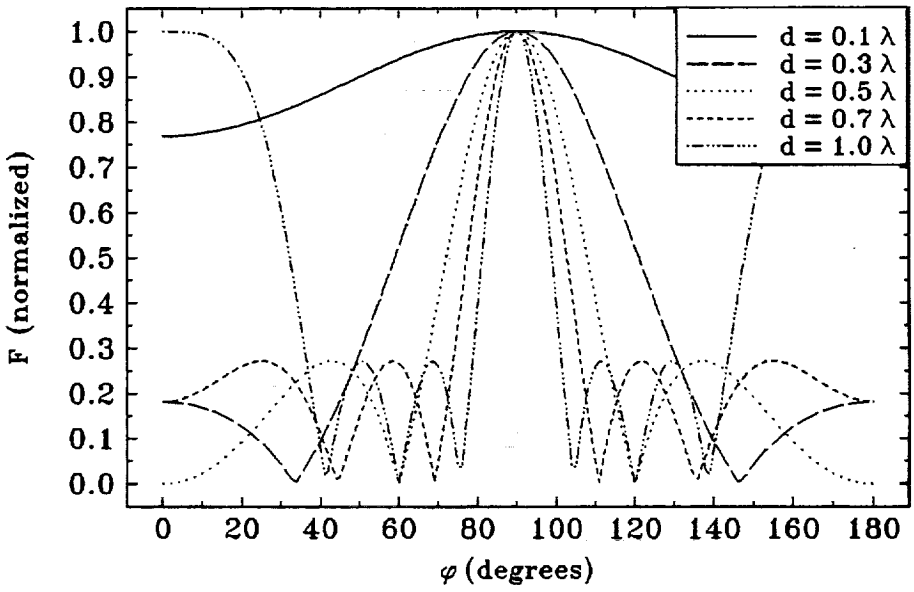

Figure 2-8: Array factor for a four element one-dimensional array with various spacings.

In the case of a two-dimensional uniform array fed in-phase with n elements along the x-axis and m elements along the y-axis ($n*m$ total elements), the array factor becomes

$$|F| = I_0 \left| \frac{\sin\left[\frac{n}{2}k_0 d \sin\theta\cos\phi\right] \sin\left[\frac{m}{2}k_0 d \cos\theta\right]}{\sin(k_0 \sin\theta\cos\phi) \sin(k_0 d \cos\theta)} \right| \qquad \text{(2-58)}$$

This is plotted for the case of a 16 element (4 x 4) array in Figure 2-9. For a two-dimensional array, the directivity can be estimated from the number of elements as

$$D \approx \frac{8.83nmd^2}{\lambda_0^2} \qquad \text{(2-59)}$$

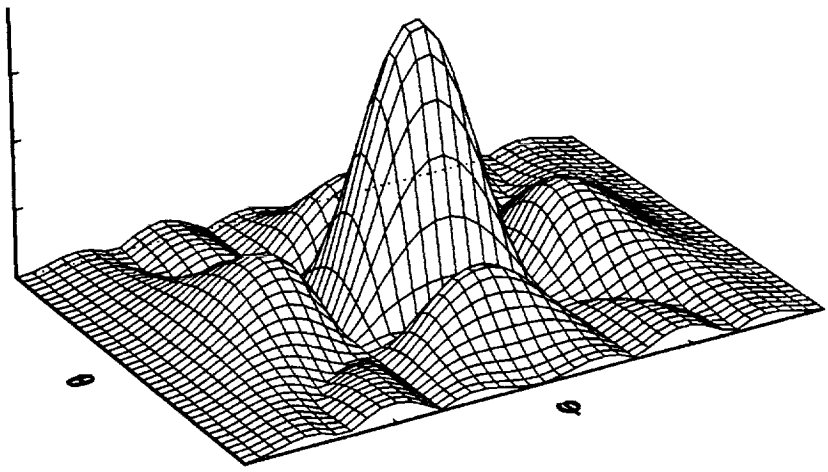

Figure 2-9: Two-dimensional array factor for a 16 element array.

2.6 Summary

Some of the theoretical aspects of the research have been presented in this chapter. Expressions necessary to design and analyze microstrip transmission lines and impedance transformers have been given, as well as equations to account for the complex conductivity of superconductors. The mathematical basis for antenna arrays was also presented. In Chapter 3, the experimental apparatus and techniques will be described.

2.6 References

1. Harold A. Wheeler, "Transmission-Line Properties of a Strip on a Dielectric Sheet on a Plane, *IEEE Trans. Microwave Theory and Tech.*, vol. MTT-25, no. 8, p. 631-647, Aug. 1977.

2. M.V. Schneider, "Microstrip Lines for Microwave Integrated Circuits," *Bell System Tech. Journal*, vol. 48, pp. 1421-1444, May 1969.

3. M. Kirschning and R.H. Jansen, "Accurate Model for Effective Dielectric Constant of Microstrip with Validity up to Millimetre-wave Frequencies," *Electron. Letters*, vol. 18, no. 6, pp. 272-273, Mar. 18, 1982.

4. H.A. Wheeler, "Transmission-line Properties of Parallel Strips Separated by a Dielectric Sheet," *IEEE Trans. Microwave Theory Tech.*, vol. MTT-13, pp. 172-185, 1965.

5 Robert A. "Pucel, Daniel J. Masse, and Curtis P. Hartwig, "Losses in microstrip," *IEEE Trans. Microwave Theory and Tech.*, vol. MTT-16, no. 6, pp. 342-350, June 1968.

6. Robert A. "Pucel, Daniel J. Masse, and Curtis P. Hartwig, "Correction to 'Losses in microstrip,'" *IEEE Trans. Microwave Theory and Tech.*, vol. MTT-16, no. 12, pp. 1064, Dec. 1968.

7. F.A. Miranda, W.L. Gordon, K.B. Bhasin, V.O. Heinen, and J.D. Warner, "Microwave properties of $YBa_2Cu_3O_{7-\delta}$ high-transition-temperature superconducting thin films measured by the power transmission method," *J. Appl. Phys.*, vol. 70, no. 10, pp. 5450-5462, 15 Nov. 1991.

8. Hai-Young Lee and Tatsuo Itoh, "Phenomenological Loss Equivalence Model for Planar Quasi-TEM Transmission Lines with a Thin Normal Conductor or Superconductor," *IEEE Trans. Microwave Theory and Tech.*, vol. MTT-37, no. 12, pp. 1904-1909, Dec. 1989.

9. Erik Ekholm and Stephen McKnight, "Attenuation and Dispersion for High-Tc Superconducting Microstrip Lines," *IEEE Trans. Microwave Theory and Tech.*, vol. MTT-38, no. 4, pp. 387-394, Apr. 1990.

10. C.M. Chorey, Keon-Shik Kong, K.B. Bhasin, J.D. Warner, and Tatsuo Itoh, "YBCO Superconducting Ring Resonators at Millimeter-wave Frequencies," *IEEE Trans. on Microwave Theory and Tech.*, vol 39, no. 9, pp. 1480-1486, Sept. 1991.

11. L. Lewin, "Spurious radiation from microstrip," *IEE Proc.*, vol. 125, pp. 633-642, 1978.

12. David M. Pozar, "Considerations for Millimeter Wave Printed Antennas," *IEEE Trans. Antennas and Propagat.*, vol. AP-31, no. 5, pp. 740-747, Sept. 1983.

13. David M. Pozar and Daniel H. Schaubert, "Comparison of Architectures for Monolithic Phased Array Antennas," *Microwave Journal*, pp. 93-104, Mar. 1986.

14. R.E. Collin, *Field Theory of Guided Waves*, IEEE Press, New York, 1991, p. 713.

15. P. Perlmutter, S. Shtrikman, and David Treves, "Electric Surface Current Model for the Analysis of Microstrip Antennas with Application to Rectangular Elements," *IEEE Trans. Antennas and Propagat.*, vol. AP-33, No. 3, pp. 301-311, Mar, 1985.

16. B. Nauwelaers and A. Van de Capelle, "Surface Wave Losses of Rectangular Microstrip Antennas," *Electron. Letters*, vol. 25, no. 11, pp. 696-697, May 25, 1989.

17. David M. Pozar, "Rigorous Closed-Form Expressions for the Surface Wave Loss of Printed Antennas," *Elecron. Letters*, vol. 26, no. 13, pp. 954-956, Jun 21, 1990.

18. S.P. Morgan, ""Effect of Surface Roughness on Eddy Current Losses at Microwave Frequencies," *J. Applied Physics*, vol. 20, pp. 352-362, Apr. 1949.

19. E.O. Hammerstad and F. Bekkadal, "Microstrip Handbook," ELAB report STF 44 A74169, The University of Trondheim, The Norwegian Institute of Technology.

20. Felix A. Miranda, "Microwave Response of High Transition Temperature Superconducting Thin Films," Ph.D. Dissertation, Case Western Reserve University, May 1991.

21. H. Sobol, "Technology and design of hybrid microwave integrated circuits," *Solid State Technol.*, pp. 49-57, Feb. 1970.

22. Robert R. Romanofsky, "Analytical and Experimental Procedures for Determining Propagation Characterisitics of Millimeter-Wave Gallium Arsenide Microstrip Lines," NASA Technical Paper 2899, 1989.

23. R.E. Collin, *Antennas and Radiowave Propagation*, McGraw-Hill, New York 1985.

CHAPTER III.

EXPERIMENTAL ARRANGEMENTS AND PROCEDURES

3.1 Introduction

This chapter presents the experimental procedures used in the course of this research and describe some of the laboratory apparatus that was utilized. The chapter is divided into four basic sections: circuit fabrication, test fixture design, cryostat design, and microwave measurements.

3.2 Circuit Fabrication

The $YBa_2Cu_3O_{7-x}$ HTS films used in this study were, for the most part, obtained commercially from Conductus, Inc[1]. These films were deposited by off-axis sputtering onto 1 cm x 1 cm, 254 μm thick (10 mil) $LaAlO_3$. Larger area films were not available from any vendor at the time because of the brittle nature of the substrate material. Conductus specified the films to have a transition temperature (T_c) of at least 88 K, a thickness of 350 nm, and a surface resistance at 77 K and 10 GHz of not more than 800 $\mu\Omega$. DC transition temperature measurements on films from this vendor showed the transition temperature to range between 87 K to 91 K. A few of the HTS films used were deposited by pulsed laser deposition (PLD) at the NASA Lewis Research Center or at The

Ohio State University[2]. The films deposited using PLD had slightly lower transition temperatures. Patterning was done using standard photolithographic techniques and "wet" chemical etching. Complete details on the patterning methods used for both the thin films and gold circuits are given in Appendix A.

3.3 Test Fixture Design

To test microstrip circuits, it is necessary to mount them in a test fixture which provides both mechanical support and electrical grounding. In addition, since microwave instrumentation provides input/output ports that are either coaxial or waveguide, a transition from coax or waveguide to microstrip must be provided. For antennas, it is essential that the test fixture interfere with the radiation properties of the antenna as little as possible. For this research two basic fixtures were used.

Fixture A, shown in Figure 3-1, was fabricated using brass. The fixture is 2 inches long by 1 inch wide and was made as thin as practically possible to reduce the thermal loading of the cryostat, thereby hastening the cool-down and warm-up times involved. A coax-to-microstrip transition (Wiltron V-connector) is built into the end of the fixture, and a length of 50 Ω curved microstrip feed line separates the transition from the antenna. The feedline was fabricated on an alumina substrate. The antenna to be tested was fastened to the test fixture using silver paint and then wirebonded to the end of the curved feedline using a gold ribbon bond. A tapped hole in the corner of the fixture allows a temperature sensing diode to be mounted.

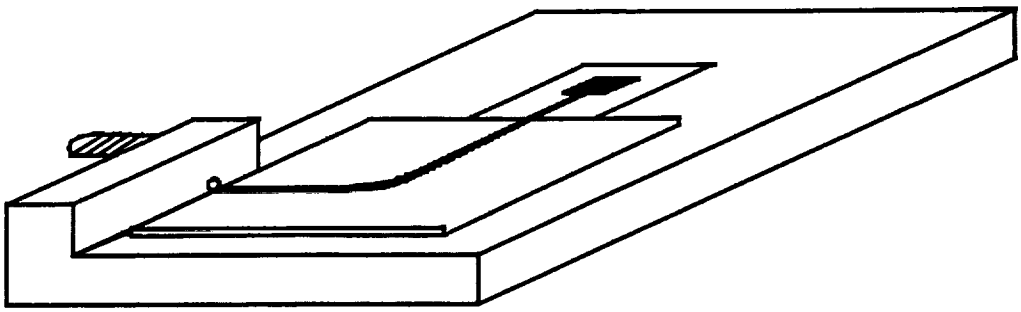

Figure 3-1: Brass test fixture used primarily for pattern measurements. A V-sparkplug launcher serves as the microstrip to coax transition, and a curved microstrip feeds on an alumina substrate feeds the antenna.

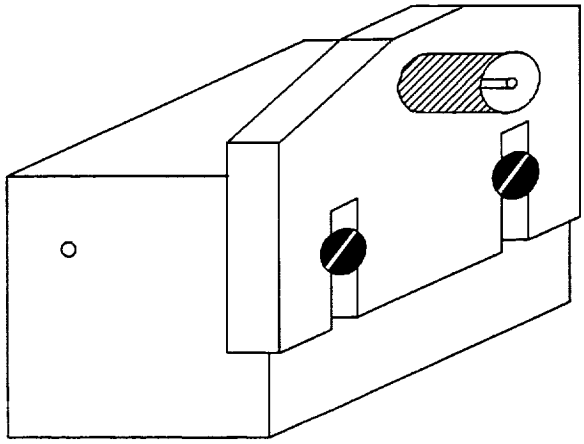

Figure 3-2: Copper test fixture with detachable launching flange. The connector is a K-sparkplug launcher.

Fixture B, shown in Figure 3-2, consists of two parts: a copper block and a launching flange. The copper block is a square piece of copper, 1.25 inches wide and 1 inch high and 1 inch long. Holes are drilled for mounting to the cryostat and for temperature sensor mounting. In addition, two holes allow the

launching flange to be fastened. The launching flange is constructed from brass and has a coax-to-microstrip transition (Wiltron K-connector) installed. The microstrip circuit to be tested is fastened to the block using silver paint. The launching pin protrudes from the end of the flange and is positioned to contact the microstrip circuit. For pattern or efficiency measurements a 50 Ω transmission line fabricated on $LaAlO_3$ separated the connector from the antenna. Wire bonds were then used to make RF connections. No transmission lines were used when measuring the reflection coefficient so that the performance of just the antenna was measured as opposed to the antenna performance transformed by the transmission line.

3.4 Cryostat Design

To measure superconducting circuits it is necessary to cool them to cryogenic temperatures. Traditionally this is done by immersion in a cryogen such as liquid nitrogen or liquid helium. In general such an arrangement allows performance measurements at two temperatures: room temperature and the boiling point of the cryogen. To immerse circuits directly into a cryogen, researchers usually seal the device into a metallic test chamber to prevent condensation of moisture upon warmup. This is necessary because water is detrimental to HTS thin films. However, devices which radiate, such as antennas, cannot be enclosed within a metallic cavity. Thus, cryogenic immersion was not a viable alternative for this research. A gas refrigerator, on the other hand, has the advantage that the temperature can be set to any value within its range.

However, a vacuum must be maintained, which necessitates the use of some type of radio-transparent vacuum jacket.

For this research, a two stage, closed-cycle helium refrigerator was used. The unit consists of a compressor unit and a cold head attached by two flexible metal hoses. The cold head has a cold finger where the sample to be cooled is mounted. The cold finger is wrapped with a heater wire and temperature sensor for temperature monitoring and control. Temperature control is achieved through the use of a Lakeshore Cryogenics temperature controller. This unit monitors the temperature and provides sufficient current through the heater element to maintain a set temperature. The cold finger is enclosed by a stainless steel tube, capped with a lid machined from high-density polyethylene (HPDE). This enclosure serves as a vacuum jacket (Figure 3-2). Although the permittivity of HPDE ($\epsilon_r = 2.34$)[3] is slightly higher than that of teflon ($\epsilon_r = 2.1$), it is substantially less expensive. The lid is a hemispheric shell which prevents distortion of the antenna radiation patterns. The lid is 0.66 cm thick, or approximately one wavelength at 30 GHz. This dimension was chosen to minimize reflections of the electromagnetic signals impinging upon it. The antennas were positioned at the center of the hemisphere. When using test fixture B, a spacer was inserted between the stainless steel tube and the HPDE radome so that the antenna was positioned at the center of the radome hemisphere. In addition to being able to operate at any temperature between 300 K and 20 K, this refrigeration system was small, relatively light weight, and could be operated in any physical position.

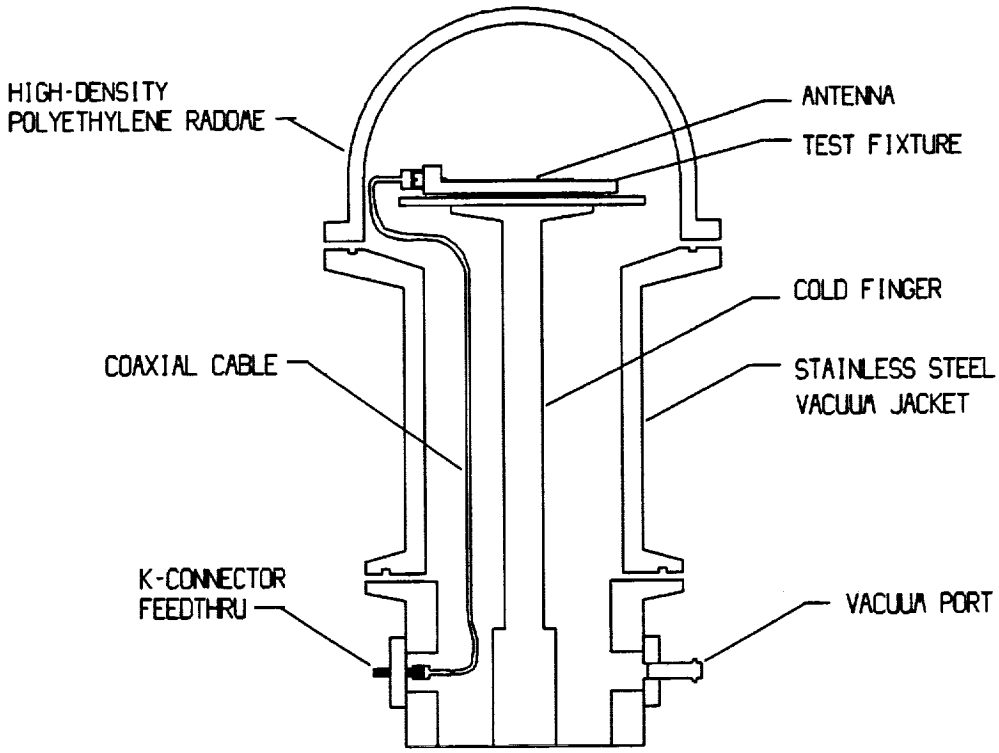

Figure 3-3: Cryogenic antenna test unit.

To connect the antennas under test (AUT) to the instrumentation, a hermetically sealed coaxial feedthrough was used. This feedthrough was made by mounting two Wiltron "K" sparkplug launchers back to back, sharing the same glass bead. A short length of flexible coaxial cable inside the test chamber connected the feedthrough to the antenna test fixture.

3.5 Microwave Measurements

The primary measurements made on the antennas were measurements of the reflection coefficient (S_{11}), pattern measurements, efficiency measurements of the single patch antennas, absolute gain measurements of the gold antennas, and the gain of the HTS antennas relative to the gold antennas. The procedures

for each of these measurements are described in detail below. All of the measurements except the pattern and absolute gain measurements were made using a Hewlett Packard 8510B Automatic Network Analyzer. The analyzer was capable of measurements from 45 MHz to 40 GHz in the coaxial mode.

3.5.1 Reflection Coefficient

To measure the reflection coefficient of a device using an automatic network analyzer (ANA), it is necessary to establish a reference plane and calibrate the analyzer. The reference plane defines the zero-phase point, while the calibration accounts for systematic errors such as reflections and losses in the cables. Although several types of calibration are available, the most common type of coaxial calibration is the Open-Short-Load, or OSL calibration. For a one port calibration, the OSL calibration requires a precision open circuit, short circuit, and a sliding load. Each of these standards is in turn connected to the network analyzer. From the measurement of these devices the parameters of the error model[4] can be found.

For a two port calibration, the open, short and sliding load circuits are connnected to each port and measured. In addition, an isolation measurement is performed, and the two ports are connected together to perform a "through" measurement. The parameters of the 12-term error model are found from these measurements.

When measuring the performance of microstrip circuits, the shortcoming of the OSL calibration is that it does not take into account the effects of the coax-

to-microstrip connector. To do so requires the use of a different calibration, such as the Through-Reflect-Line, or TRL calibration. The TRL calibration is inherently a 2-port calibration, and requires two transmission lines (THRU and LINE) and some type of highly reflective circuit (REFLECT), such as an open or a short. The transmission lines must differ in length by approximately $\lambda/4$. The phase reference may be set by the reflective circuit if the phase response of the circuit is ideal or well known. Alternatively, the electrical length of the THRU circuit may be specified to set the reference planes. By nature, a TRL calibration is customized. It has a limited frequency range determined by the $\lambda/4$ difference between the lengths of the LINE and THRU circuits. Because the capacitances and inductances of the coax-to-microstrip transition will vary with the width of the microstrip line, the THRU and LINE circuits must be fabricated on the same substrates material as the device under test (DUT).

For this work, network analyzer calibration was done using coaxial standards at the end of the coaxial cable inside of the cryostat. This method was chosen because of the extreme difficulties in implementing a TRL calibration at the frequencies involved (K and Ka-bands). At these frequencies, an ideal microstrip short circuit is nearly impossible to realize, and non-ideal ones are difficult to characterize. Thus, the REFLECT could not be used for phase reference. Because the permittivity of lanthanum aluminate is not known precisely, the electrical length of a THRU or LINE circuit could not be known precisely, meaning that these could not be used for phase reference either. Even if a phase

reference could be established, because of the high permittivity of $LaAlO_3$ the difference in length between a THRU and LINE circuit would be 1 mm or less. Thus, a small misalignment during the measurement could wipe out the $\lambda/4$ difference between the two circuits. In addition, for short (less than 2 cm) lengths of microstrip transmission lines, standing waves can easily be setup between the two coax-to-microstrip transitions, causing spurious coupling between the ports which in turn affect the measurements. Finally, for the substrate material and height used, a 50 Ω line is only 100 μm wide. Thus, repeatable connections of the connector launching pin to the microstrip line could not be guaranteed.

The combination of the above difficulties made a coaxial calibration much more accurate, reliable, and repeatable than a TRL calibration. To account for the phase delay of the sparkplug launcher, the reference plane was then shifted after performing the coaxial calibration. It should be noted that a calibration at low-temperature could not be performed for practical reasons: with each cool-down cycle taking approximately two hours, a minimum of 8 hours would elapse before any antenna measurements could begin. Instrument drift within this period of time would make the calibration worthless.

Once the calibration was completed, the antenna to be tested was mounted in test fixture B, the launching flange was carefully positioned and fastened, and the test fixture was bolted to the cold finger. A temperature sensor was mounted on the side of the test fixture for accurate temperature measurements. With the coaxial cable connected, the chamber was sealed and evacuated so that the cool

down cycle could begin. The reflection coefficient measurements were then taken periodically as the temperature decreased.

3.5.2 Pattern Measurements

Antennas are characterized by their radiation patterns. Thus, pattern measurements of the two principle radiation planes were carried out in the two principle planes, the E- and H-plane. Initally, pattern measurements were done at the Far Field Antenna Range of the NASA Lewis Research Center. However, as availability of this testing site was limited, a simpler measurement facility was established. For testing at room temperature, the antenna to be tested (AUT) was connected to a microwave detector and rotated over a 180° span in the presence of a radiating horn antenna. As the AUT rotated, a linear potentiometer rotated with it so that by passing a constant current through the potentiometer and reading the voltage, the angle could be determined. A computer was programmed to continually read the angle and the voltage across the microwave detector to determine the received power. Radar absorbing material (Eccosorb AN-72) placed around the setup helped to minimize spurious reflections. This setup is shown in Figure 3-4.

For pattern measurements of cryogenic antennas, the radiating horn was mounted on a pivoting arm and moved in a constant radius arc (Figure 3-5). The presence of the cryostat was found to disturb the patterns very little, while no difference was noted in the patterns measured with and without the HPDE radome.

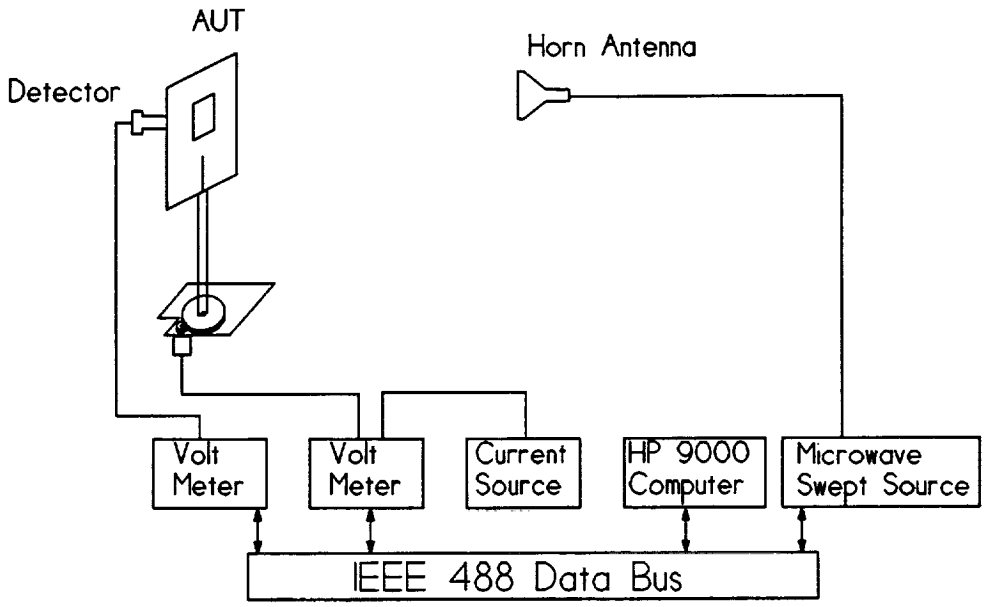

Figure 3-4: Far field antenna measurement setup. The entire setup is computer controlled for ease of use.

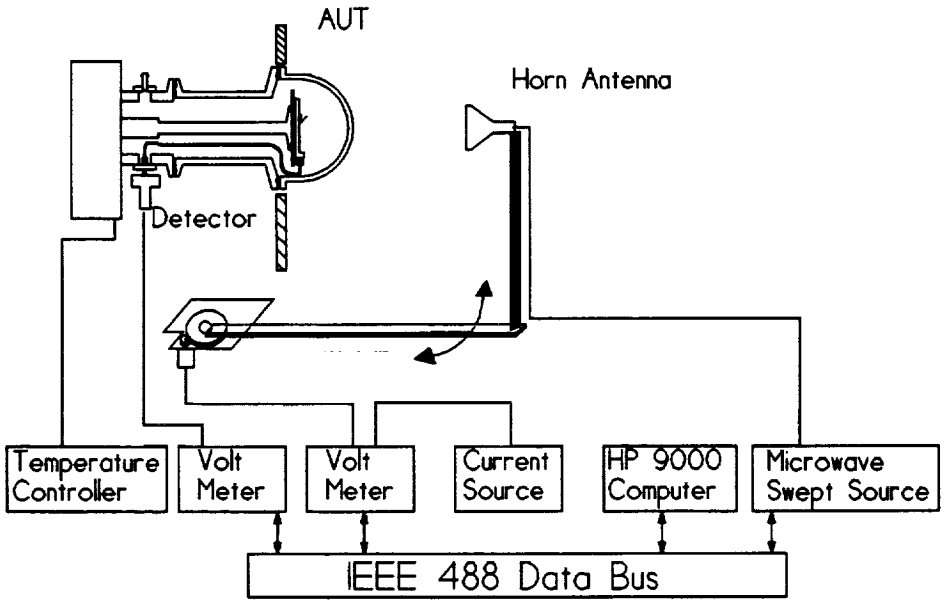

Figure 3-5: Far field pattern measurement setup for cryogenic antennas.

3.5.3 Efficiency

There are several ways to measure the efficiency of a single patch antenna, including the horn substitution method, the radiometric method[5], and the Wheeler cap method[6]. The Wheeler cap method was selected because it is simple to implement and has been reported to be one of the most accurate methods[7]. This method assumes the antenna to be modeled by a parallel RLC equivalent circuit as shown in Figure 2-5, with a series resistance representing the losses. The input impedance of the antenna at resonance is measured with and without a radiation shield. The radiation shield is assumed to short out the radiation resistance so that the efficiency (η) may be calculated as

$$\eta = 1 - \frac{R_w}{R_{wo}} \qquad (3\text{-}1)$$

where R_W and R_{wo} are the input resistances with and without the radiation shield, respectively. Work by Newman, Bohley, and Walter[8] and by Pozar and Kaufman[9] has shown that the size and conductivity of the radiation shield is not important, but good contact to electrical ground is. To implement this method, an aluminum cap with inner dimensions of 12 mm wide by 12 mm deep by 6.8 mm high was used. Electrical contact to the grounded copper test fixture was ensured with both silver paint and copper tape. The input resistance of each antenna was measured from room temperature down to 20 K with and without the radiation shield.

3.5.4 Gain

The gain of each gold four element array was measured at room temperature using a horn substitution method with a standard gain horn. To do this, a transmission link was established using a radiating horn antenna and the AUT, and the power received by the AUT was measured. The AUT was then replaced by a horn antenna with a known gain, and the power received by the horn is measured. By comparing these measured powers with the known gain of the horn antenna, the gain of the AUT may be found from the Friis transmission formula[10],

$$P_{rec} = (1 - |\Gamma_r|^2)\frac{\lambda^2_0}{4\pi}G_r(1 - |\Gamma_t|^2)\frac{P_{in}}{4\pi r^2}G_t \qquad (3\text{-}2)$$

In this equation, Γ_r and Γ_t are the reflection coefficients of the receive and transmit antennas, respectively, and G_r and G_t are the gains of the receive and transmit antennas, respectively. P_{in} is the transmit power while P_{rec} is the received power.

Assuming that the reflection coefficient Γ_r is small and writing Eqn. (3-2) as

$$\frac{P_r}{G_r} = \frac{\lambda_0{}^2 P_{in}}{(4\pi)^2 r^2}G_t\left(1 - |\Gamma_t|^2\right) \qquad (3\text{-}3)$$

we see that the right hand side of Eq. (3-3) remains unchanged when the AUT is substituted for the horn antenna of known gain, $G_r = G_{horn}$. Thus,

$$\frac{P_{r,AUT}}{G_{AUT}} = \frac{P_{r,horn}}{G_{horn}} \tag{3-4}$$

and G_{AUT} may be found as

$$G_{AUT} = \frac{P_{r,AUT}\, G_{horn}}{P_{r,horn}} \tag{3-5}$$

This method could not be used for the cryogenic antennas because a horn could not be placed properly in the cryostat. To find the gain of each HTS array, the gain relative to its identical gold array was found by measuring the power received at boresight and applying the Friis transmission formula. The AUT was used in the receive mode and a transmitting horn antenna was used as the source. The transmission coefficient of this link, S_{21}, and the reflection coefficient of the AUT, S_{11}, were measured at various temperatures (Figure 3-6) using an automatic network analyzer. The gain of the HTS antenna relative to the gold antenna may then be found as

$$\frac{G_{HTS}}{G_{Au}} = \frac{\dfrac{|S_{21}|^2_{HTS}}{1-|S_{11}|^2_{HTS}}}{\dfrac{|S_{21}|^2_{Au}}{1-|S_{11}|^2_{Au}}} \tag{3-6}$$

Knowing the gain of the HTS antenna relative to the gold antenna, the absolute gain of the HTS antenna may then be found.

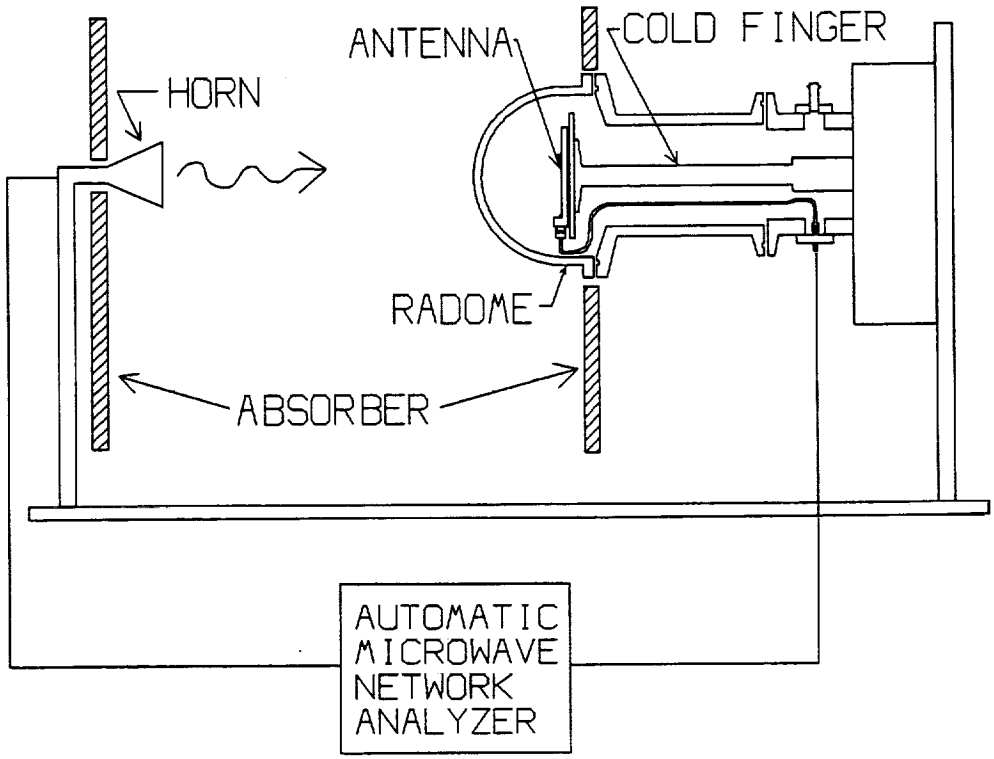

Figure 3-6: Experimental setup for measuring the gain of a HTS antenna relative to the gain of a gold antenna.

3.6 Summary

Experimental procedures and apparatus for measuring superconducting antennas have been presented. These methods were used to measure antenna return loss, patterns, efficiency, and gain. In next three chapters, the design and performance of three microstrip antenna architectures will be discussed.

3.7 References

1. Conductus, Inc., 969 West Maude Ave., Sunnyvale, CA 94086.

2. J.D. Warner, K.B. Bhasin, N.C. Varaljay, D.Y. Bohman, and C.M. Chorey, "Growth and Patterning of the Laser Ablated Superconducting YBaCuO Films on $LaAlO_3$ Substrates," NASA TM #102346, 1989.

3. Karlheinz Seeger, "Microwave Measurement of the Dielectric Constant of High-Density Polyethylene," *IEEE Trans. Microwave Theory and Tech.*, vol. 39, no. 2, pp. 352-354, Feb. 1991.

4. Edward A. Wolff and Roger Kaul, *Microwave Engineering and Systems Applications*," John Wiley & Sons, New York, 1988.

5. J. Ashkenazy, E. Levine, and D. Treves, "Radiometric measurement of Antenna Efficiency," *Electron. Lett.*, vol. 21, no. 3, Jan. 31, 1985.

6. Harold A. Wheeler, "The radiansphere around a small antenna," *Proceedings of the IRE*, vol 47, pp. 1325-1331, Aug. 1959.

7. David M. Pozar, Barry Kaufman, "Comparison of Three Methods for the Measurement of Printed Antenna Efficiency," *IEEE Trans. Antennas and Propagat.*, vol. AP-36, no. 1, pp. 136-139 Jan. 1988.

8. E.H. Newman, Peter Bohley, and C.H. Walter, "Two methods for the measurement of antenna efficiency," *IEEE Trans. Antennas and Propagat.*, vol. AP-23, no. 4, pp. 457-461, July 1975.

9. David M. Pozar, Barry Kaufman, "Comparison of Three Methods for the Measurement of Printed Antenna Efficiency," *IEEE Trans. Antennas and Propagat.*, vol. AP-36, no. 1, pp. 136-139 Jan. 1988.

10. H.T. Friis, "A Note on a Simple Transmission Formula," *Proc. IRE*, vol. 34, pp. 254-256, May 1946.

CHAPTER IV.

DIRECT COUPLED ANTENNA

4.1 Introduction

One of the simplest and most common ways to feed a microstrip antenna is to feed the patch directly by a microstrip transmission line. In this chapter, the performance of a 30 GHz HTS rectangular microstrip antenna that is directly coupled by a microstrip transmission line is discussed. The chapter begins with the motivations for using such an architecture, and then presents the design and performance of an HTS single patch antenna. Performance parameters include patterns, input impedance, bandwidth, and efficiency. These results are compared with results that are expected from the cavity model. Following this, the performance of a four element array is presented, and finally, the design and performance of a 64 element array. In each case, the results are compared to those of an identical antenna fabricated using gold metallization.

4.2 Motivation

The directly coupled microstrip antenna was chosen for performance evaluation mainly because it is simple to fabricate and is commonly used. In terms of fabrication, it is a planar architecture and all that is required is a feed

line intersecting the patch area. Thus, all the microstrip circuitry including the feed network can be printed on one side of the antenna substrate. In addition, the planar microstrip antenna is relatively simple to analyze both conceptually and numerically.

For this work, a rectangular patch was chosen. Although many patch shapes have been investigated, the most commonly used shapes are the circular disk and the rectangular patch. The rectangular patch was chosen because its input impedance can be decreased by increasing the width of the patch.

4.3 Single Element Antennas

4.3.1 Design

The direct coupled antenna design used in this study is shown in Figure 4-1. It is a rectangular patch with a resonant length, L, of 935 μm and a width, W, of 1630 μm. The length was selected to be one-half wavelength at the desired resonant frequency of 30 GHz, while the width was made to be 1.75L. Narrow widths cause the radiation efficiency to decrease and the input impedance to increase, while widths greater than 2L cause the generation of higher-order modes.

As will be discussed in Section 4.5, the high permittivity of the substrate causes a very high edge impedance. To match this edge impedance requires the use of both an impedance transformer and an inset into the patch. Thus, an inset of 400 μm or 43 % was used to obtain an input resistance of 100 Ω for the patch at the inset point. Matching to the 100 μm wide 50 Ω feed line was done via a

28 μm wide, 71 Ω quarter-wave transformer. The antenna is designed for a lanthanum aluminate substrate 1 cm x 1 cm square by 254 μm (10 mil) thick. The dielectric thickness used is the minimum practical substrate thickness and was chosen to reduce the generation of surface waves, while the size was chosen because larger area HTS films were not available. A YBCO superconducting thin film was used for the circuit metallization, while an evaporated copper ground plane of at least 1.2 μm in thickness was used. The HTS film used for this antenna was deposited using an off-axis sputtering technique and was obtained commercially. The film had a transition temperature (T_c) of 89 K.

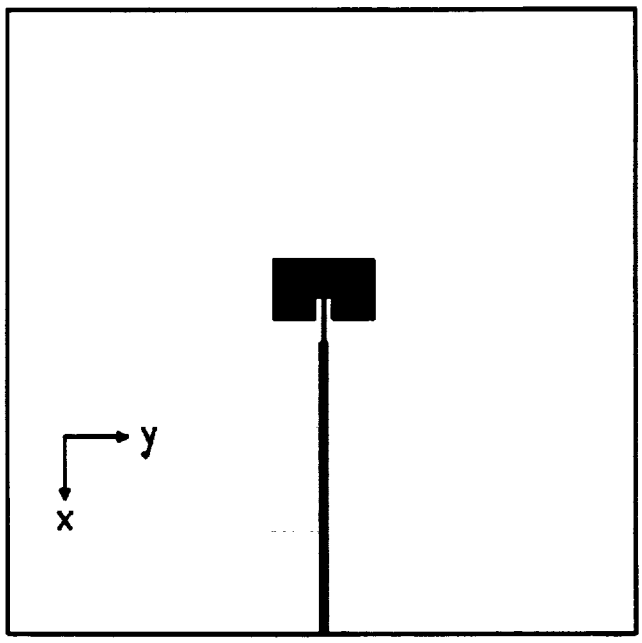

Figure 4-1: Physical layout of the direct coupled microstrip antenna on a 1 cm x 1 cm $LaAlO_3$ substrate.

4.3.2 Resonant Frequency

The measured resonant frequencies for both the gold and HTS direct coupled patches are shown in Figure 4-2 as a function of temperature. Using the cavity model, the resonant frequency of the rectangular patch can be found from the dimensions of the cavity. The electric field of a given mode in a rectangular cavity of size a by b is given by

$$E_z = E_0 \cos(m\pi x/a)\cos(n\pi y/b) \tag{4-1}$$

where m and n are integers representing the mode number. Here the electric field is assumed to have only a z-component with no z-dependance in accordance with the cavity model[1,2]. The resonant frequency is then given by

$$f_{mn} = \frac{c}{2\pi\sqrt{\epsilon_r}}\sqrt{\left(\frac{m}{a}\right)^2 + \left(\frac{n}{b}\right)^2} \tag{4-2}$$

where ϵ_r is the permittivity of the dielectric inside the cavity. For a patch antenna, a represents the width W while b represents the length L, and the dielectric inside the cavity is the substrate. Thus, for the lowest order (TM_{01}) mode the resonant frequency is given by

$$f_r = \frac{c}{2L\sqrt{\epsilon_r}} \tag{4-3}$$

However, this expression predicts frequencies substantially higher than measured frequencies. This is because the cavity model, in its purest form, assumes perfect magnetic walls and thus does not account for the fringing fields. Several

empirical expressions have been proposed to compensate for this deficiency. One such expression, suggested by James *et. al.*[3] is

$$f_{rI} = f_{r0}\frac{\epsilon_r}{\sqrt{\epsilon_e(W)\epsilon_e(L)}}\frac{1}{(1+\Delta)} \tag{4-4}$$

where

$$\Delta = \frac{h}{W}\left[0.882+\frac{0.164(\epsilon_r-1)}{\epsilon_r^2}+\frac{(\epsilon_r+1)}{\pi\epsilon_r}\left(0.758+\ln\left(\frac{W}{h}+1.88\right)\right)\right] \tag{4-5}$$

$$\epsilon_e(u) = \frac{\epsilon_r+1}{2}+\frac{\epsilon_r-1}{2}\left[1+10\frac{h}{W}\right]^{-1/2} \tag{4-6}$$

and f_{r0} is the resonant frequency given by Eqn. (4-3).

Bahl and Bhartia[4] have suggested modifying the length of the patch by adding on a term ΔL for analysis, where ΔL is given by

$$\Delta L = 0.412h\frac{(\epsilon_e+0.3)(W/h+0.264)}{(\epsilon_e-0.258)(W/h+0.8)} \tag{4-7}$$

and ϵ_e is given by

$$\epsilon_e = \frac{\epsilon_r+1}{2}+\frac{\epsilon_r-1}{2}\left(1+\frac{12h}{W}\right)^{-1/2} \tag{4-8}$$

The simplest expression to account for the fringing fields, though, is to use the effective dimensions[1]

$$L_e = L + h/2 \quad \textbf{(4-9a)}$$
$$W_e = W + h/2. \quad \textbf{(4-9b)}$$

The gold antenna had a measured resonant frequency of 28.96 GHz at room temperature. Using a value of 23 for the permittivity of lanthanum aluminate, Eqn. (4-3) gives a resonant frequency of 33.45 GHz (15.5 % error), Eqns. (4-4) through (4-6) give 32.69 GHz (12.9 % error), Eqns. (4-7) and (4-8) give 30.22 GHz (4.35 % error), while Eqn. (4-9) give a resonant frequency of 29.45 GHz (1.7 % error). Thus, for resonant frequency analysis, Eqn. (4-9) was used and the length and width of the antenna were extended by one-half the substrate height, *h* to an effective length and width.

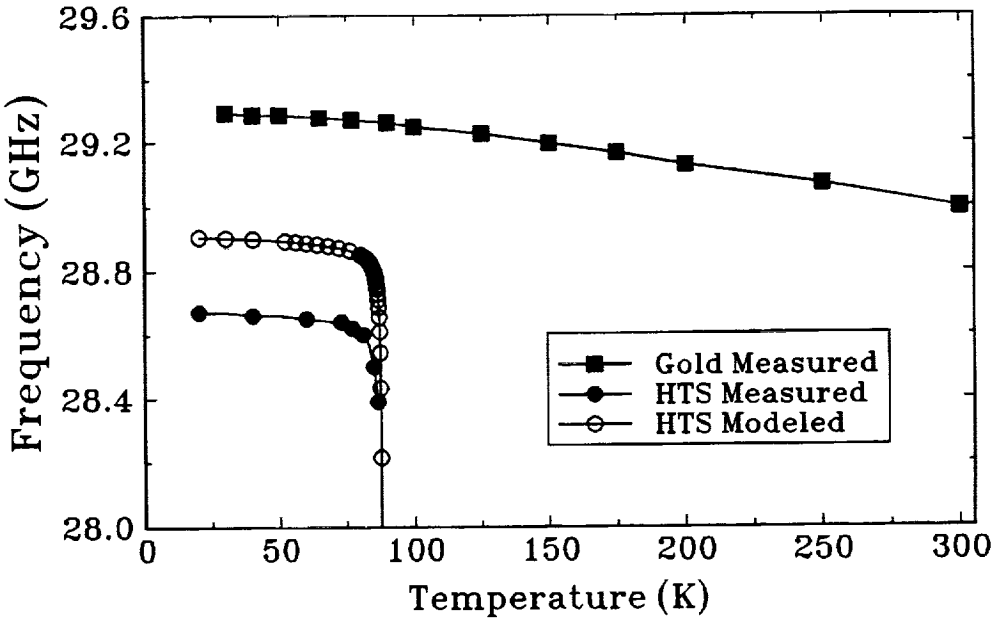

Figure 4-2: Resonant frequencies of the single patch antennas. HTS modeled data uses the permittivity extracted from the gold antenna data and HTS film parameters of T_c = 88 K, λ_{p0} = 200 nm, and t = 350 nm.

As discussed in Chapter 1, the room temperature permittivity of lanthanum aluminate has been reported over a range of values from 21.9 up to 24.0 and higher, and it is becoming increasingly clear that there are variations in permittivity between samples. A recent report[5] has put the value at 24.0, decreasing by 2 % to 23.52 at 30 K. Because of this uncertainty in the permittivity, the measured resonant frequencies of the gold antenna were used to extract the permittivity using Eqn. (4-3) modified by Eqn. (4-9). Using these expressions, the permittivity was found to be 23.81 at 300 K, decreasing by 2 % to 23.33 at 30 K, as shown in Figure 4-3. It is important to note the slope of the extracted permittivity curve matches exactly the permittivity curve as reported by Konaka *et. al.*[5]. Thus it is reasonable to attribute the change of the gold antenna's resonant frequency with temperature to a slight decrease in permittivity with temperature. The curve reported by Konaka *et. al.*[5] and by *Miranda et. al.*[6] are also shown in Figure 4-3 for comparison.

The steep change in the HTS antenna's resonant frequency at temperatures near T_c, on the other hand, can be attributed to a change in the magnetic penetration depth of the YBCO. To model the resonant frequency of the HTS antenna, it is necessary to consider the effective dielectric constant, $\epsilon_{r,eff}$, given by[7]

$$\epsilon_{r_{eff}} = \epsilon_r \left[1 + \frac{\lambda_p}{h} \coth\left(\frac{t}{\lambda_p} \right) \right] \qquad \textbf{(4-9)}$$

for a HTS film with thickness t and substrate with relative permittivity ϵ_r. The magnetic penetration depth of the film, λ_p, is related to the temperature of the

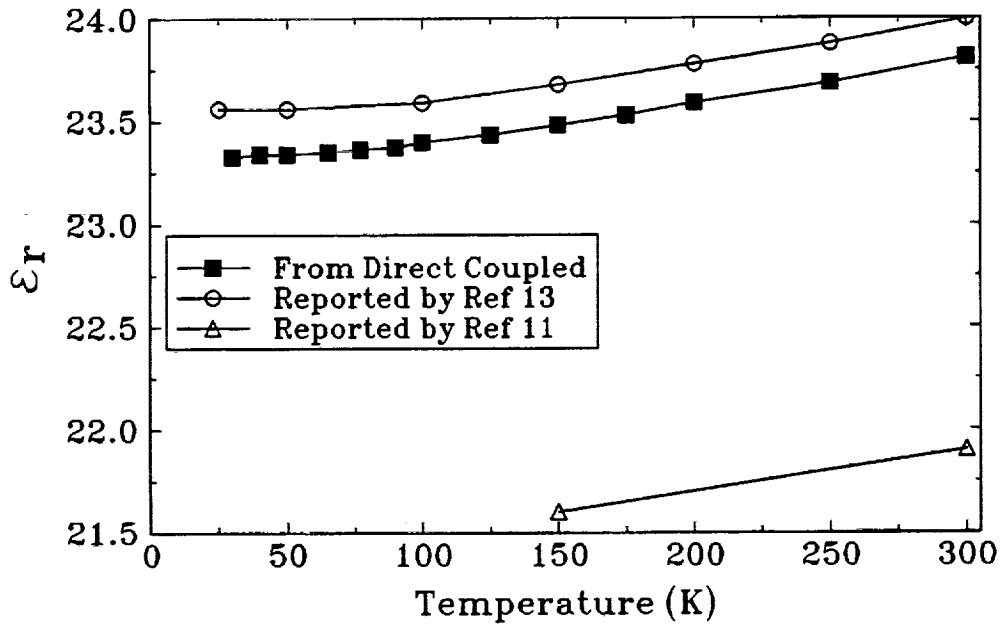

Figure 4-3: Permittivity of lanthanum aluminate extracted from resonant frequency data of gold antennas. Values reported by other researchers are also shown.

film and can be modeled by the Gorter-Casimir two fluid model as

$$\lambda_p = \lambda_{p0}\left[1 - \left[\frac{T}{T_c}\right]^4\right]^{-1/2} \qquad \textbf{(4-10)}$$

where T is the temperature and T_c is the transition temperature of the superconductor. For this antenna, the HTS film had a T_c of 88 K, and a thickness of 350 nm. The zero-temperature penetration depth, λ_{p0}, was assumed to be 200 nm, a value typical for good quality films[8]. Using the temperature versus permittivity curve extracted from the gold antenna resonant frequency data and Eqns. (4-9) through (4-11), the predicted resonant frequencies for the HTS antenna were found and are also plotted in Figure 4-2. At temperatures

significantly below T_c, the slope of the modeled curve matches that of the experimental curve within 1 %, indicating the same change in permittivity with temperature as the gold antenna. The difference in resonant frequency between the gold and HTS antennas can be attributed to a number of factors including a slight (6 %) difference in the dielectric height between the samples, fabrication tolerances, and variations in substrate permittivities.

4.3.3 Antenna Patterns

The radiated fields from a rectangular patch can be evaluated from the fields under the patch and for the TM_{01} mode are[3]

$$|E_\theta| = 8V_0 \sin\left(\frac{k_0 W}{2}\cos\phi\,\sin\theta\right)\cos\left(\frac{k_0 L}{2}\sin\phi\,\sin\theta\right) k_0 \sin\phi\,\cos\phi\,\sin\theta \left[\frac{1}{k_0^2\cos^2\phi\,\sin^2\theta} - \frac{1}{k_0^2\sin^2\phi\,\sin^2\theta - \frac{\pi^2}{L^2}}\right] \quad (4\text{-}11)$$

and

$$|E_\phi| = 8V_0 \sin\left(\frac{k_0 W}{2}\cos\phi\,\sin\theta\right)\cos\left(\frac{k_0 L}{2}\sin\phi\,\sin\theta\right) k_0 \sin\theta\,\cos\theta \left[\frac{1}{k_0^2\sin^2\theta} - \frac{\sin^2\phi}{k_0^2\sin^2\phi\,\sin^2\theta - \frac{\pi^2}{L^2}}\right] \quad (4\text{-}12)$$

The radiation pattern in the E-plane, or the plane perpendicular to the antenna substrate and parallel to the microstrip feed line, is given by

$$\left| E_\theta(\phi=90^\circ) \right| = \cos\left(\frac{k_0 L}{2}\sin\theta\right) \tag{4-13}$$

The radiation pattern in the H-plane, or the plane perpendicular to the substrate and to the microstrip feed line, is given by

$$\left| E_\phi(\phi=0^\circ) \right| = \cos\theta \, \frac{\sin\left(\frac{k_0 W}{2}\sin\theta\right)}{\frac{k_0 W}{2}\sin\theta} \tag{4-14}$$

The measured E- and H-plane patterns for the antennas are shown in Figures 4-4 and 4-5. The H-plane data shows good agreement with the cavity model while dramatic deviations from the model result in the E-plane. This is agreement with data from Schaubert *et. al.*[9], who found that the E-plane patterns of high-permittivity antennas are affected substantially by surface waves while the H-plane is affected very little. Surface wave power that is generated should radiate from the substrate at the substrate edges. However, attempts to suppress this radiated power using radar absorbing material or to shield the substrate edges using grounded conducting tape produced no improvement in the measured E-plane patterns.

4.3.4 Input Impedance

The measured return loss data for the direct-coupled single patch antennas are shown in Figure 4-6. The VSWR is less than 1.36 (2.3 % reflected power) for all temperatures for the gold single patch, and 1.17 (0.6 % reflected power)

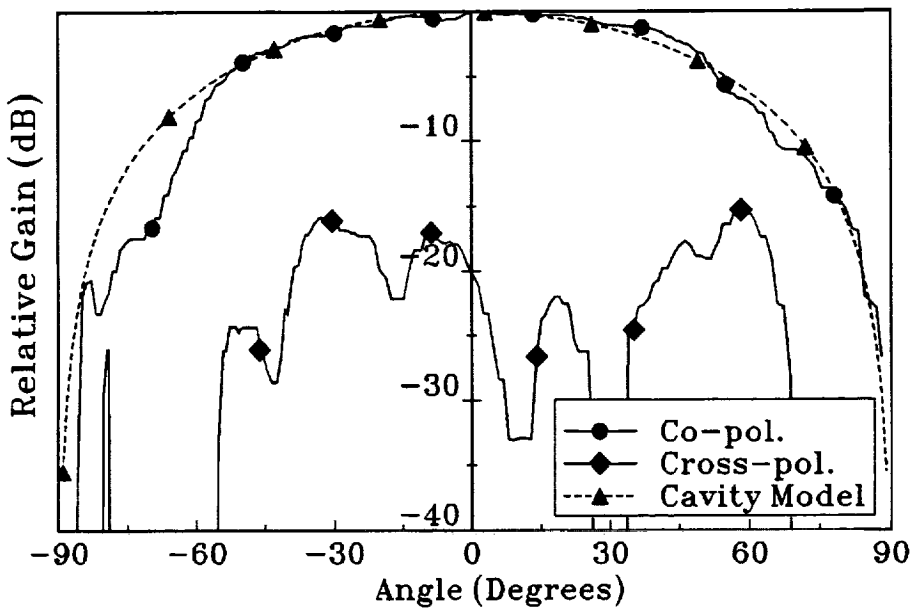

Figure 4-4: H-plane patterns of the direct coupled antenna showing co- and cross-polarizations. The cavity model prediction is also shown.

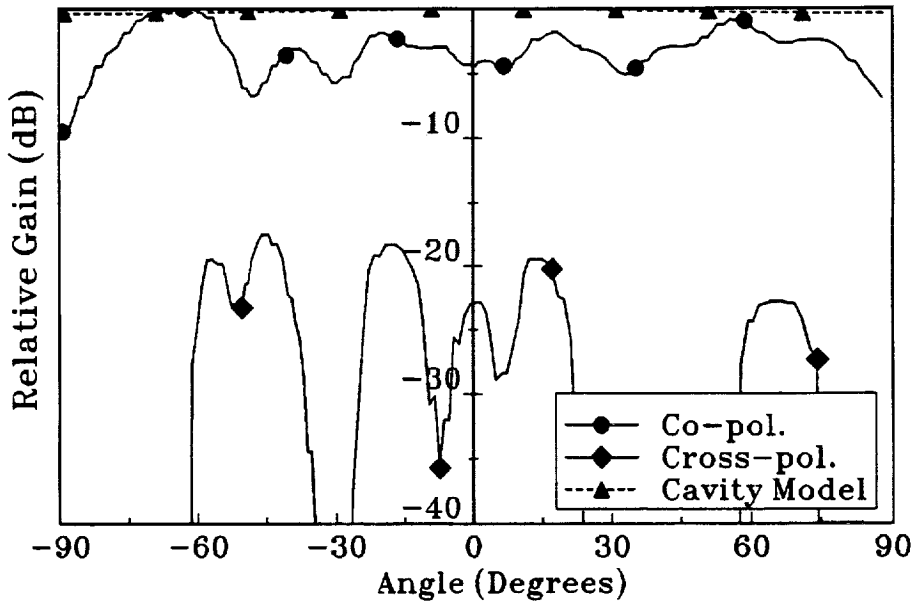

Figure 4-5: E-plane patterns of the direct couple d antenna showing co- and cross-polarizations and the cavity model prediction.

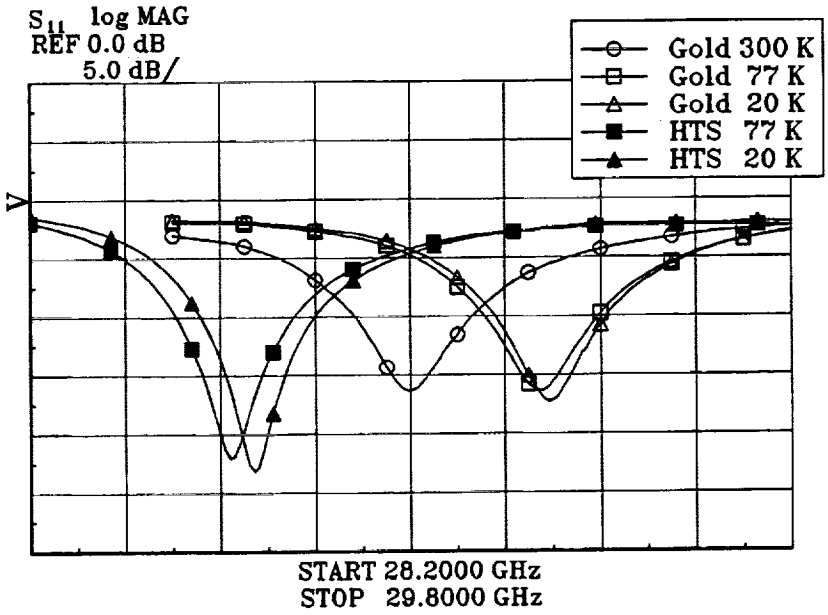

Figure 4-6: Measured return loss of the gold and HTS single patch antennas.

at 77 K for the HTS single patch. Assuming the current density distribution on the patch to be uniform in the y-direction (along the width of the patch) and sinusoidal in the x-direction (along the patch length), the radiated power has been shown to be given by[10]

$$P_r = \frac{V_0^2}{Z_0^2}\frac{60}{\pi}\epsilon_{eff}\int_0^{2\pi}\int_0^{\pi/2}\frac{\cos^2\left(\pi\sin\theta\,\cos\phi/2\sqrt{\epsilon_{eff}}\right)}{\left(\sin^2\theta\,\cos^2\phi - \epsilon_{eff}\right)^2}A(B + C)\sin\theta\,d\theta\,d\phi \quad (4\text{-}15)$$

where

$$A = sinc^2(Wk_0\sin\theta\,\sin\phi/2) \quad (4\text{-}16)$$

$$B = \frac{\cos^2\theta\sin^2\phi}{(\epsilon_r-\sin^2\theta)\cot^2(hk_0\sqrt{\epsilon_r-\sin^2\theta})+\cos^2\theta} \tag{4-17}$$

and

$$C = \frac{\cos^2\theta\ \cos^2\phi(\epsilon_r-\sin^2\theta)}{(\epsilon_r-\sin^2\theta)+\epsilon^2_r\cos^2\theta\ \cot^2(hk_0\sqrt{\epsilon_r-\sin^2\theta})} \tag{4-18}$$

The total stored energy in the antenna is given by[3]

$$\mathrm{E}_s = \frac{1}{2}\int_V \epsilon_r\epsilon_0 \mid E_z \mid^2 dv \tag{4-19}$$

Substituting Eqn. (4-1) into Eqn. (4-19), replacing E_0 by the voltage at the edge of the patch, V_0/h, and integrating over the volume of the patch, the total stored energy is

$$\mathrm{E}_s = \frac{V_0^2}{4h}\pi f_r\epsilon_r\epsilon_0 WL \tag{4-20}$$

The power lost in the dielectric is

$$P_d = \frac{1}{2}\int_V \sigma_d \mid E_z \mid^2 dv = \frac{\sigma_d\ \mathrm{E}_s}{\epsilon_r\epsilon_0} = \frac{V_0^2}{2h}\pi f_r\ WL\epsilon_r\epsilon_0\ \tan\delta \tag{4-21}$$

where σ_d has been written in terms of the dielectric loss tangent, $\sigma_d = 2\pi f_r\epsilon_r\epsilon_0\tan\delta$. The power lost in the conductor is

$$P_c = \int_A \mid I \mid^2 R_s\, da = \frac{2R_s}{\mu_0}\frac{\mathrm{E}_s}{h} = \frac{\epsilon_r\epsilon_0 WL}{h^2\mu_0}R_s \tag{4-22}$$

where R_s is the surface resistance of the conductors. The input resistance, then, is simply $R_o = V_0^2/2P_T$ where $P_T = P_r + P_d + P_c$. This analysis gives a patch edge resistance R_o of 1500 Ω. Since the patch feed position is inset into the patch, the value of the input resistance should decrease according to

$$R = R_0 \cos^2(\frac{\pi \delta}{L}) \qquad (4\text{-}23)$$

where δ is the amount of inset. Thus to produce an input impedance of 100 Ω, an inset of 41.7% or 390 μm is required. A method of moments simulation[11] agreed closely with this analysis, showing an inset of 400 μm, or 42.8 % to be necessary. Using Eq. (4-23) this translates to an edge impedance of 1980 Ω. The measured data, though, suggests that the inset of 400 μm used was slightly greater than optimum. The measured Z_{in} of 74 Ω for the gold patch and 85 Ω for the HTS patch at 77 K implies patch edge resistances of 1690 Ω and 1470 Ω respectively. It should be noted that the input impedance is quite sensitive to variations both in the patch length and the inset δ. For the dimensions used,

$$\frac{dZ_{in}}{d\delta} = -2.5\Omega/\mu m \quad \text{and} \quad \frac{dZ_{in}}{dL} = 1.1\Omega/\mu m \ .$$

4.3.5 Bandwidth and Q

Both the HTS and gold antennas suffer from very narrow bandwidths of between 0.80 % and 1.0% (VSWR < 2) because of the high frequency, high

dielectric constant, and low substrate height. The bandwidth can be obtained from the Q of a circuit according to the relation

$$B.W.(\%) = \frac{100}{Q\sqrt{2}} \tag{4-24}$$

The Q of the circuit is defined by

$$Q = \frac{2\pi E_S f_r}{P} \tag{4-25}$$

where E_s is the total stored energy given by Eqn. (4-19) and P is the dissipated power. Thus, the radiation Q is $Q_r = 2\pi f_r E_s/P_r$, the dielectric Q is $Q_d = 2\pi f_r E_s/P_d$, and the conductor Q is $Q_c = 2\pi f_r E_s/P_c$. The total Q, Q_T, is

$$\frac{1}{Q_T} = \frac{1}{Q_r} + \frac{1}{Q_d} + \frac{1}{Q_c} \tag{4-26}$$

The Q was calculated analytically from the expressions for E_s, P_r, P_d, and P_c given above. To do this, the surface resistance of YBCO films as reported by Miranda *et. al.*[8] was used to find the conductor loss in the HTS antenna, while the measured conductivity of gold as a function of temperature was used to calculate the conductor loss in the gold antenna. The dielectric loss was taken to be a constant 5×10^{-5} for both antennas. In each case, the change in permittivity with respect to temperature was accounted for. The calculated Q's are slightly higher than the measured Q's, and thus the calculated bandwidths are slightly lower than the measured ones. This can be explained by the shortcomings in the model, which assumes a perfect magnetic wall. The measured and calculated bandwidths

as a function of temperature are shown in Figure 4-7. In this figure, the measured curves for both antennas show a decreasing bandwidth with temperature. This is because the conductivity of the metallization improves with decreasing temperature. In the case of the modeled curve for the gold antenna, though, the slope is slightly negative (increasing bandwidth with decreasing temperature). This is because the effect of the conductivity is outweighed by the effect of the decreasing dielectric constant in the model. The modeled curve for the HTS antenna also shows a negative slope at temperatures much lower than T_c.

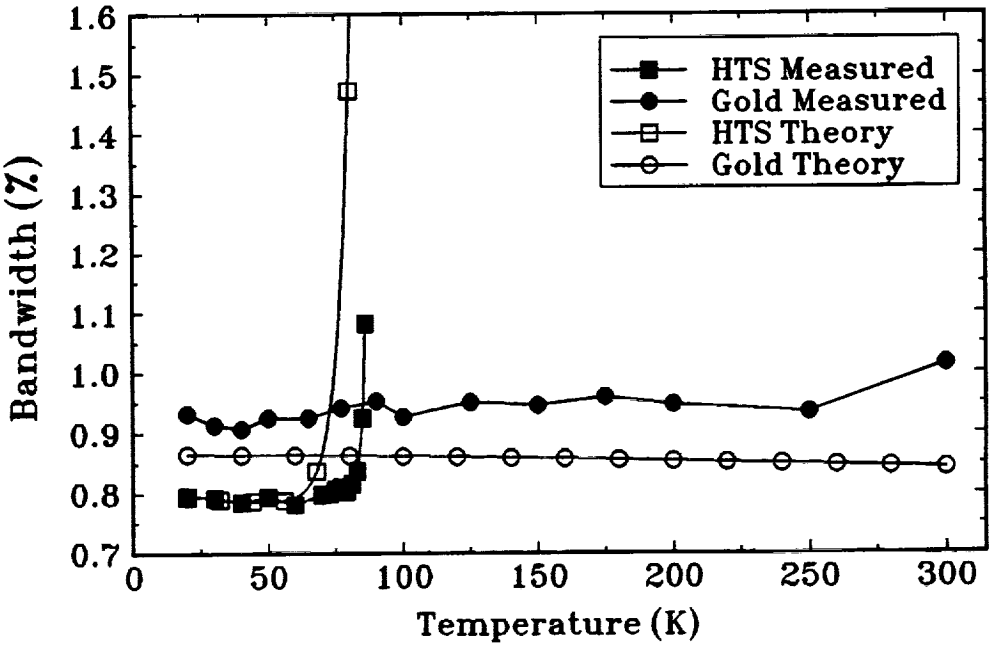

Figure 4-7: Measured and calculated bandwidths of the HTS and gold single patch antennas.

4.3.6 Efficiency

The efficiency of each single patch antenna was measured using the Wheeler Cap method as described in Chapter 3. The measured efficiencies of the single patch antennas are shown in Figure 4-8. The HTS antenna demonstrated a few percent increase in efficiency over the equivalent gold antenna. To model the efficiency of the gold antenna, the power dissipated in the conductors, dielectric, and radiation were calculated from the equations given above. The efficiency of the patch is calculated by

$$\eta_{patch} = \frac{P_r}{P_r+P_d+P_c} \tag{4-27}$$

The attenuation in the microstrip transmission line was calculated from Pucel's equations as given in Chapter 2. The efficiency of the antenna, including the feed line, is then given by

$$\eta_{antenna} = \frac{P_r}{P_r+P_d+P_c} 10^{-(\alpha_c+\alpha_d)/10} \tag{4-28}$$

where α_c is the attenuation of the transmission line due to conductor losses and α_d is the attenuation of the transmission line due to dielectric losses.

The efficiency of the HTS antenna was also modeled using the efficiency of the calculated efficiencies of the patch from previously given equations. However, instead of using reported surface resistance values to find the loss in the HTS feed line, the attenuation coefficient of the transmission line was assumed to be the same as that measured by Chorey *et. al.*[12]. This assumption

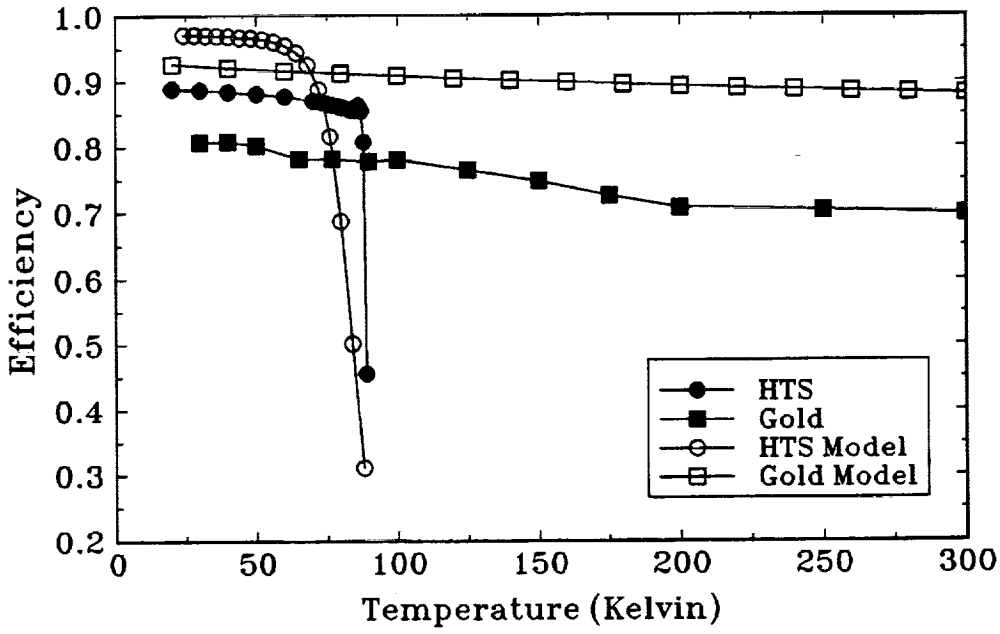

Figure 4-8: Measured efficiencies of the gold and HTS single patch antennas using the Wheeler cap method. Also shown are modeled efficiencies.

is obviously not entirely accurate because of variations in substrate parameters, film surface resistance and critical temperature, and a 20 % difference in operating frequency. Chorey's data was shifted in temperature to account for the difference in T_c between the films. Both modeled curves exhibit efficiencies that are approximately 10 % higher than the measured curves. This is due to losses that are unaccounted for in the models, including the losses in the coax-to-microstrip transition and substrate surface roughness.

4.4 Four Element Arrays

Using the direct coupled microstrip patch as the radiating element, a four element array was constructed. By studying the response of a four element array, the advantages of using HTS can be seen more clearly because of the losses in

a microstrip feed network fabricated using normal metals. The array, shown in Figure 4-9, is a two-dimensional square (2 x 2) array. The feed network is designed so that the path length to each element is exactly the same. This causes the elements to radiate in-phase and produces a broadside radiation beam, meaning that the main lobe of the radiation pattern is perpendicular to the plane of the substrate. The feed network is constructed from 50 Ω microstrip transmission lines. At each junction, a 71 Ω quarter wave transformer is employed for impedance matching. The element are spaced $\lambda_0/2$, or 5.06 mm apart at the resonant frequency of 29 GHz.

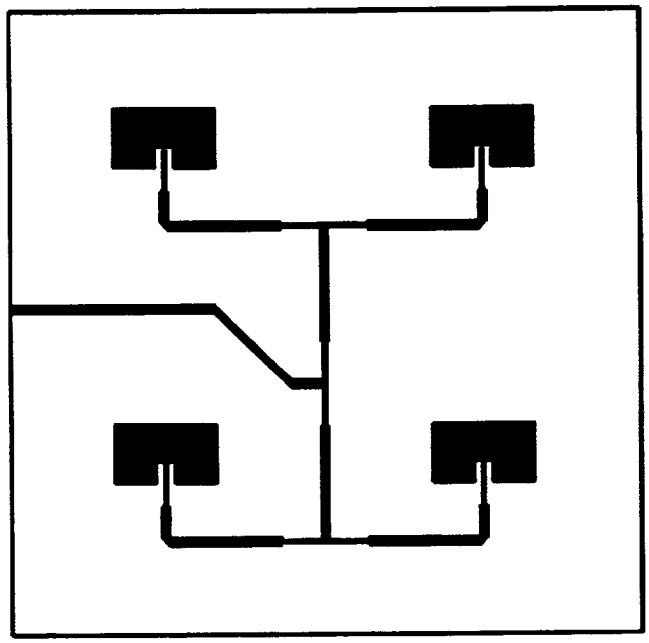

Figure 4-9: Physical layout of the direct coupled four element array antenna.

The resonant frequency and bandwidth for the four element arrays are shown in Figure 4-10. The shift in resonant frequency occurs as it did for the single element cases. However, the bandwidth is narrowed slightly due to the effect of the feed network. Both the HTS and gold arrays showed excellent impedance match characteristics over their respective operating temperature ranges. The gold array had a VSWR of less than 1.3, while the HTS array had a VSWR of less than 1.1 at temperatures below 82 K. This is shown in Figure 4-11. The change in VSWR with temperature can be attributed to several factors including improved conductivity of the metallization and change in patch edge impedance.

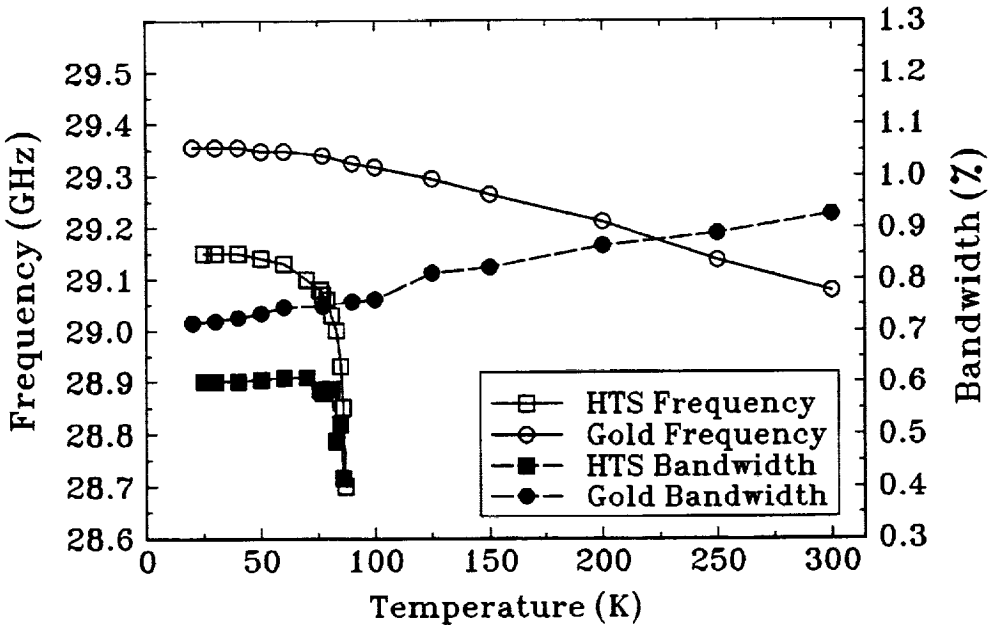

Figure 4-10: Resonant frequencies and bandwidths for the HTS and gold four element arrays.

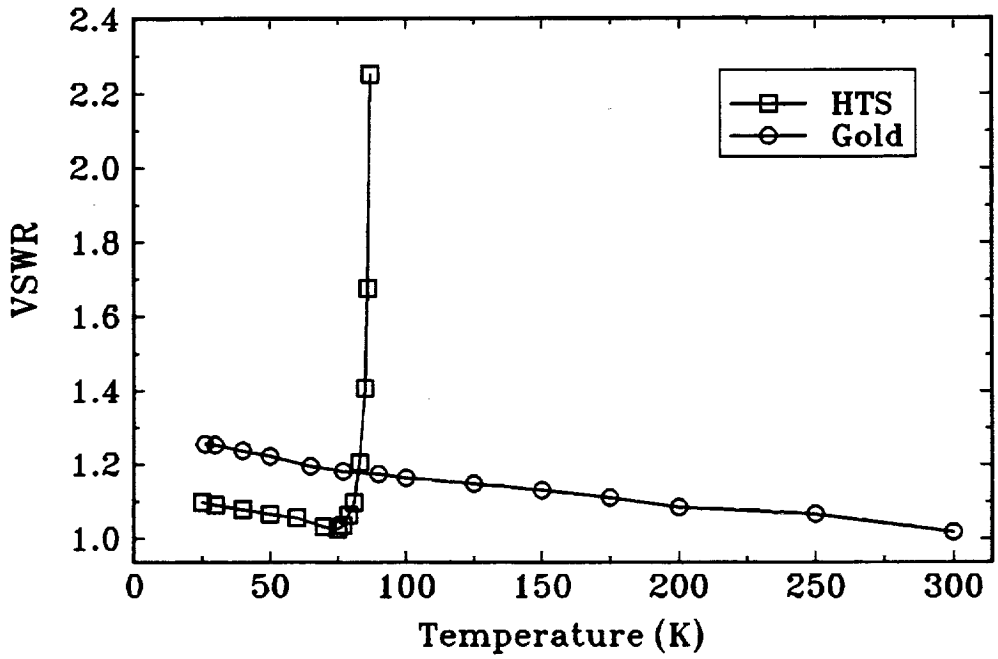

Figure 4-11: Measured VSWR of the four element arrays as a function of temperature.

Despite the severe disturbances in the E-plane pattern of the single patch antenna, the far field radiation patterns of the four element array are quite clean in both the E and H-plane, although some disturbances are evident at the extreme angles. In each case the cross polarization is more than 15 dB below the co-polarization peak, indicating very little feed line or other spurious radiation. These patterns are shown in Figures 4-12 and 4-13.

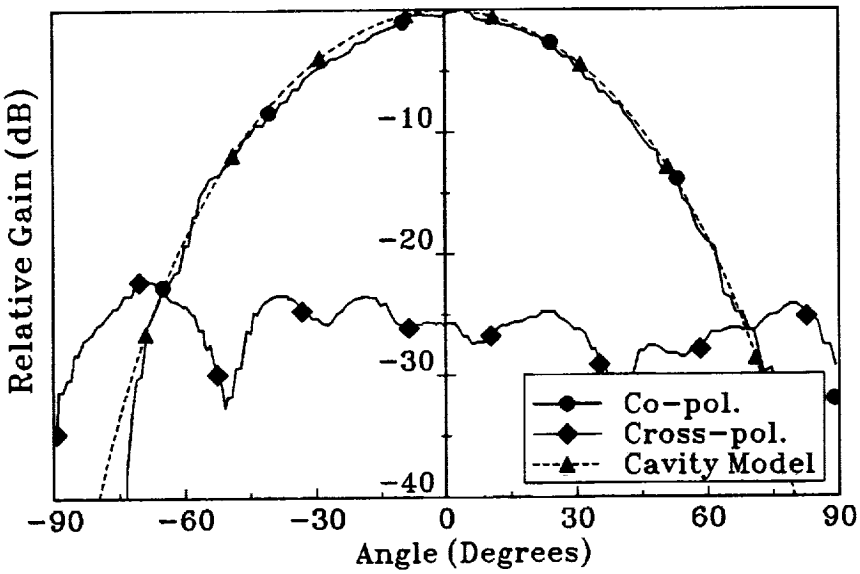

Figure 4-12: H-plane radiation patterns of the four element arrays. Co- and cross-polarization data is shown along with the pattern predicted by the cavity model.

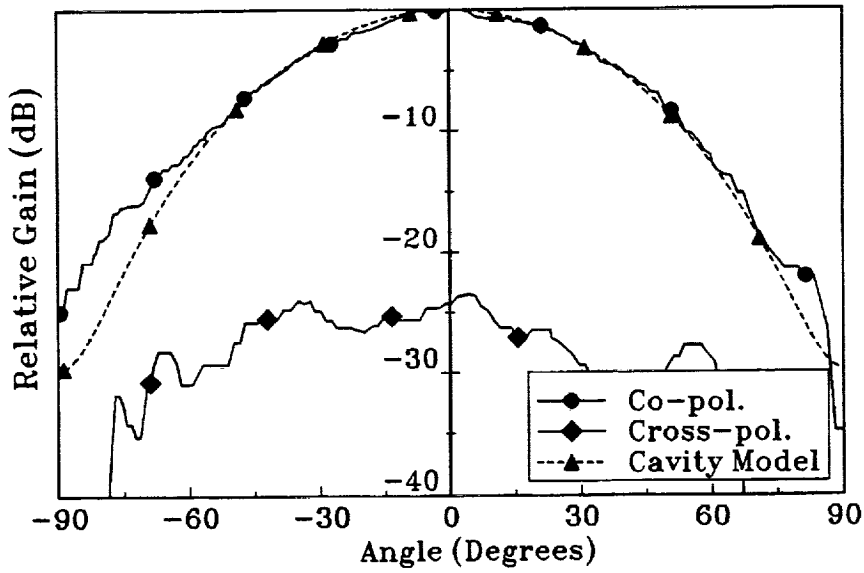

Figure 4-13: E-plane Radiation patterns of the four element arrays. Co- and cross-polarization data is shown along with the pattern predicted by the cavity model.

The gain of the gold 4-element array was measured at room temperature using a horn substitution method with a calibrated standard gain horn. The gain of the gold antenna was found to be 9.0 dB. As described in Chapter 3, the gain of the HTS array relative to the gold array was found by measuring the power received at boresight and applying the Friis transmission formula. The measured gain of the HTS antenna relative to the gold antenna is shown in Figure 4-14, while the absolute gain of each antenna is shown in Figure 4-15. The HTS array showed a gain of 9.9 dB at 77 K, increasing to 10.5 dB at 25 K. The half-power beam widths (HPBW) were used to calculate the directivities, or the maximum possible gain. With an E-plane beam width of 60 degrees and an H-plane beam width of 46 degrees, the directivity is estimated to be 11.7 dB.

The losses in each antenna due to metallization were also estimated analytically. From a moment method calculation, the attenuation coefficients for a 50 Ω and a 71 Ω transmission line on $LaAlO_3$ were found and multiplied by the path length in the feed network for one element. This loss was added to the loss of a patch, calculated in Section 4.3.6. This information is summarized in Table 1. The expected loss of the gold array was found to be 1.1 dB at room temperature and 0.72 dB at 77 K, while the expected loss of the HTS array was found to be 0.88 dB at 77 K. The modeled loss of the HTS patch is high because of the surface resistance values used to model the patch are from a film with a lower T_c, and thus the modeled patch efficiency at 77 K is 83 % as opposed to 97 % at 60 K. The experimental data indicates that the patch loss is

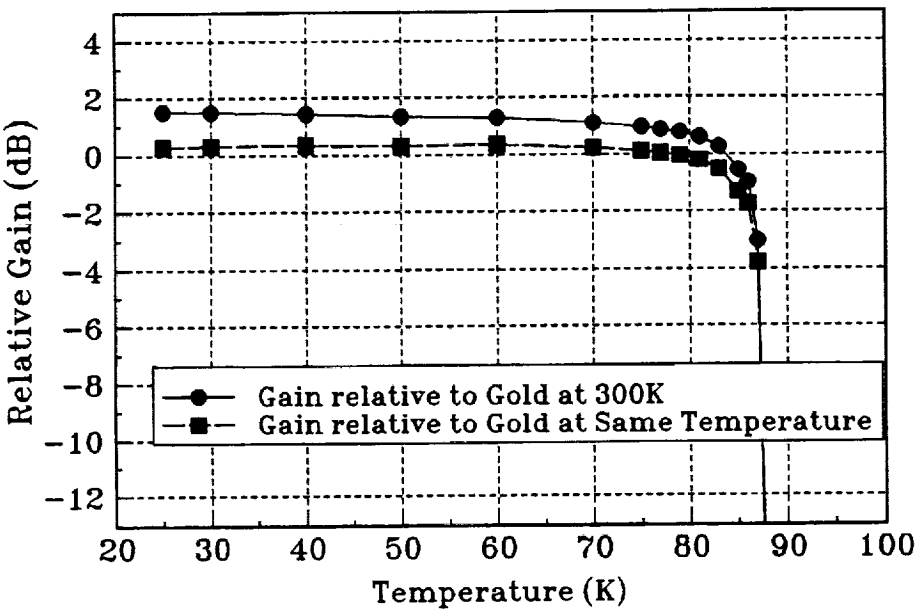

Figure 4-14: Gain of the HTS array relative to the gold array at room temperature (circles) and relative to the gold array at the same temperature as the HTS array (squares).

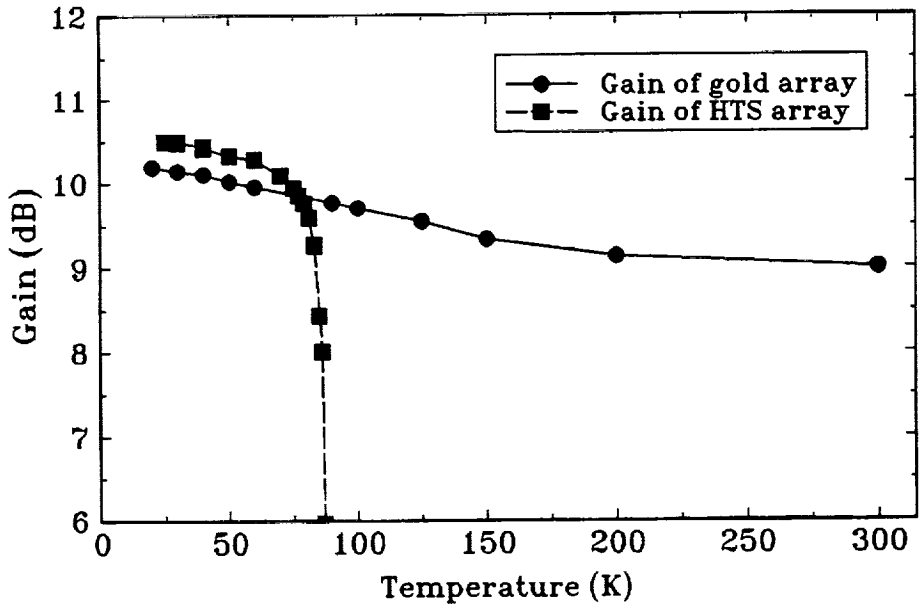

Figure 4-15: Absolute gains of the HTS and gold antennas as a function of temperature.

significantly lower than the calculated 0.88 dB. It is important to note that the HTS antenna at 77 K has a gain within 1.8 dB of the estimated directivity the direct coupled. This remaining loss can be attributed to losses in the ground plane, dielectric, the coax-to-microstrip transition, and surface wave scattering.

Table 4-1: Array Loss Budget

	Line Loss	Patch Loss	Total Loss	Measured Gain	Implied Loss
Gold 300K	0.88	0.22	1.10	9.0	2.7
Gold 77K	0.51	0.21	0.72	9.8	1.9
HTS 77K	0.07	0.81	0.88	9.9	1.8

4.5 A 30 GHz HTS 64 Element Array Antenna

It is difficult to clearly demonstrate the advantages of HTS over normal metals in single element antennas or even in four element arrays. Thus, a 64 element 30 GHz microstrip antenna array was designed and fabricated on a 254 μm thick $LaAlO_3$ substrate using a TlCaBaCuO superconductor. This antenna, together with an identical antenna fabricated using gold metallization, allowed a clear demonstration of the advantages that HTS poses in antenna arrays.

4.5.1 Antenna design

The array was designed at Ball Communications System Division under a NASA contract. The array, shown in Figure 4-16, is a corporate fed, 64 element

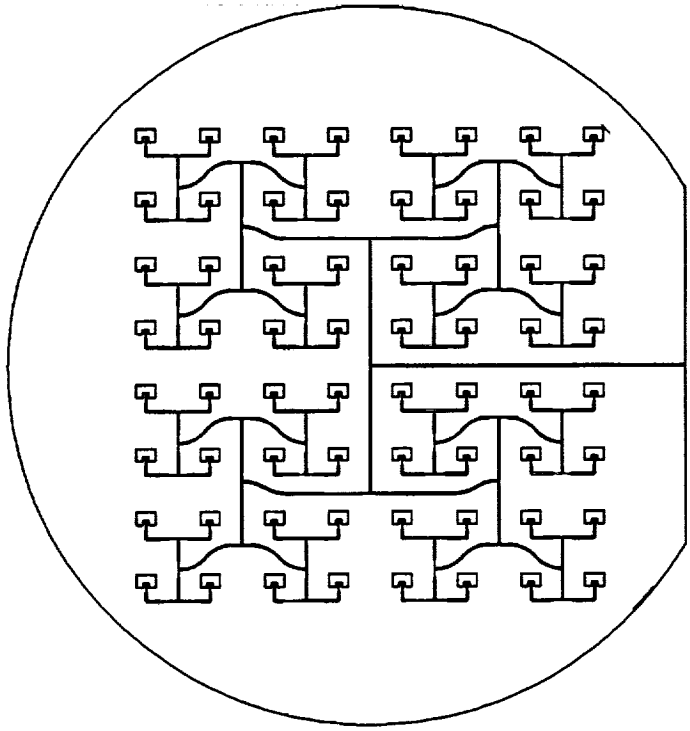

Figure 4-16: Physical layout of the 30 GHz 64 element array antenna.

2-dimensional square array of patches. An element spacing of 4500 μm was used for two reasons. First, this spacing allows the entire array to fit onto a 2 inch diameter wafer of $LaAlO_3$. Secondly, in theory this spacing causes the surface waves component of the radiation to destructively interfere while the space wave component constructively interferes. This is possible because the propagation constant of the surface wave component, k_{sw} is given by

$$k_{sw} = \frac{2\pi}{\lambda_g} \tag{4-29}$$

where λ_g is the wavelength in the dielectric, while the propagation constant of the space wave component is given by

$$k_{sw} = \frac{2\pi}{\lambda_0} = \frac{2\pi f}{c} \qquad (4\text{-}30)$$

For a high permittivity substrate, the guided wavelength, λ_g, is much smaller than the freespace wavelength, λ_0. In practice, though, it is very difficult to predict the exact propagation constant of the surface waves because of the presence of the feed network.

Each patch had a resonant length of 900 μm and a width of 1350 μm. The feedpoint was inset by 337 μm to provide an input impedance of 100 Ω. This input impedance was matched to a 50 Ω transmission line through a quarter-wave transformer. The 63 power dividers in the corporate feed network also used 71 Ω quarter wave transformers for impedance matching.

Fabrication of the HTS and gold arrays was done at Superconductor Technologies, Inc. One array was formed using 3 μm thick gold film while second array was fabricated using a $Tl_2CaBa_2Cu_2O_8$ HTS thin film. Both antennas had a 3 μm thick gold ground plane on the reverse sides. The antennas were mounted onto two identical test fixtures using an indium allow solder. Each array was then wire bonded to a 1 cm long 50 Ω transmission line fabricated on $LaAlO_3$. These short transmission lines separated the actual array from the coax-to-microstrip transitions. K-sparkplug launchers provided RF connection to each feedline.

4.5.2 Performance

The measured input reflection coefficient (S_{11}) data is shown in Figure 4-17. The gold antenna has resonances at 30.4 GHz and 31.0 GHz at room temperature and at 30.5 GHz at 77 K, while the HTS antenna has resonances at 30.0 GHz and at 30.3 GHz. From this data, the impedance bandwidth (VSWR < 2) is seen to be 2.3% for the gold antenna and 1.7% for the HTS antenna. The multiple resonances are due to reflections on the feed network and from variations in the actual patch sizes.

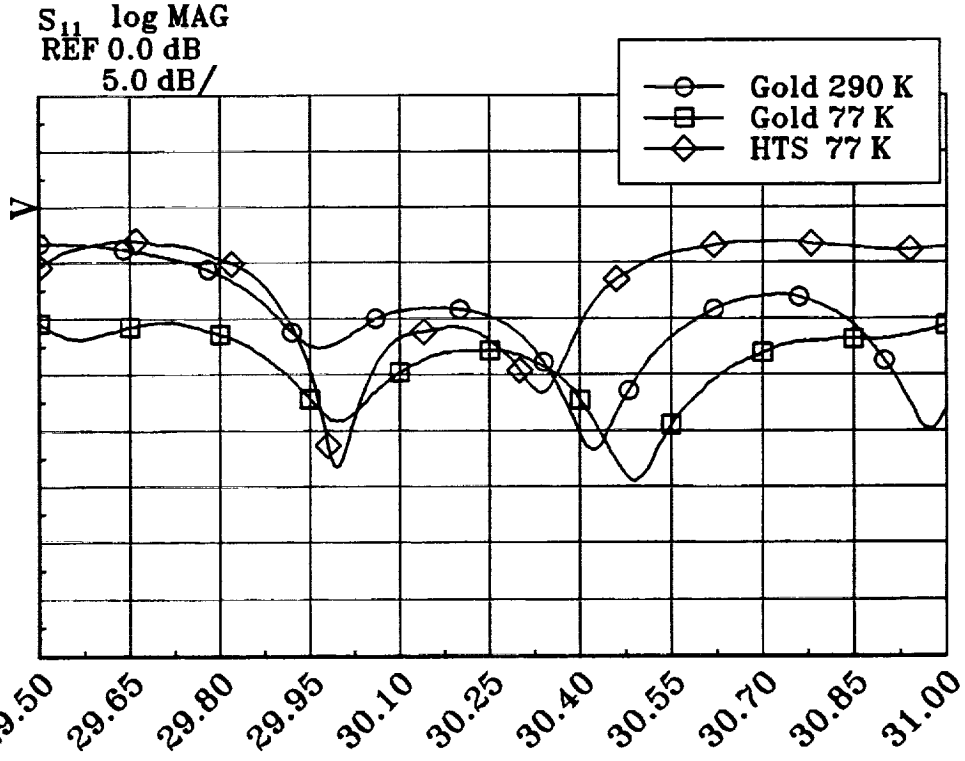

Figure 4-17: Measured reflection coefficient (S_{11}) data for the 64 element arrays.

The measured radiation patterns of the HTS antenna are shown in Figures 4-18 and 4-19. The patterns follow the cavity model predictions very closely. The E-plane pattern shows the first sidelobe level at the expected 13 dB below the main lobe while the H-plane pattern has shows sidelobe levels that are slightly higher than expected, at 10 to 11 dB below the main lobe. The slight skewing in the main lobe of both patterns is due to either asymmetry in the test fixture or to a slight miscalibration in the exact boresight position.

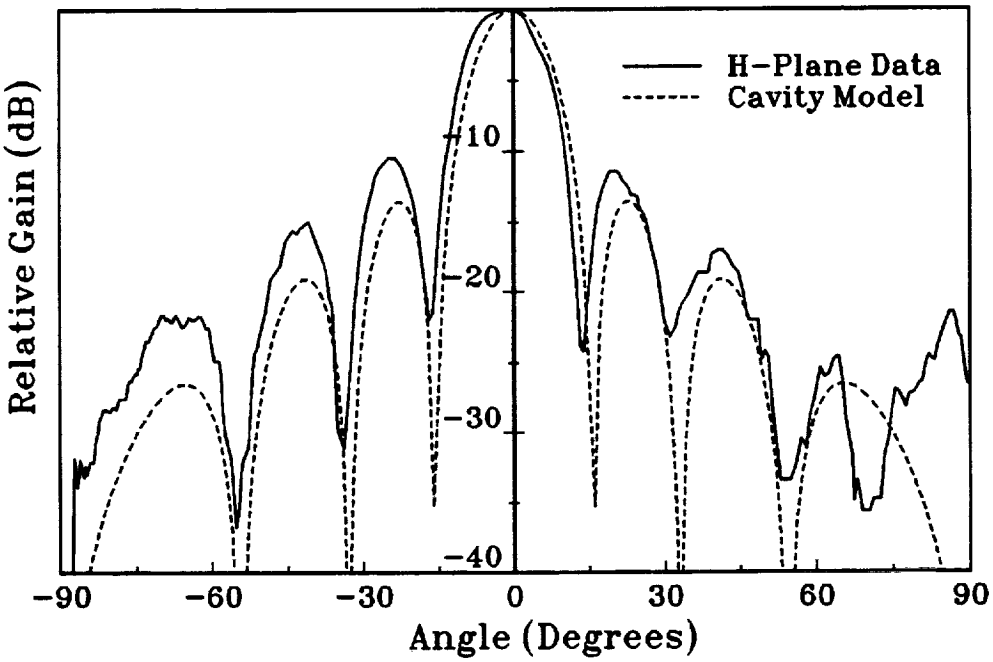

Figure 4-18: H-plane patterns of the 64 element HTS array.

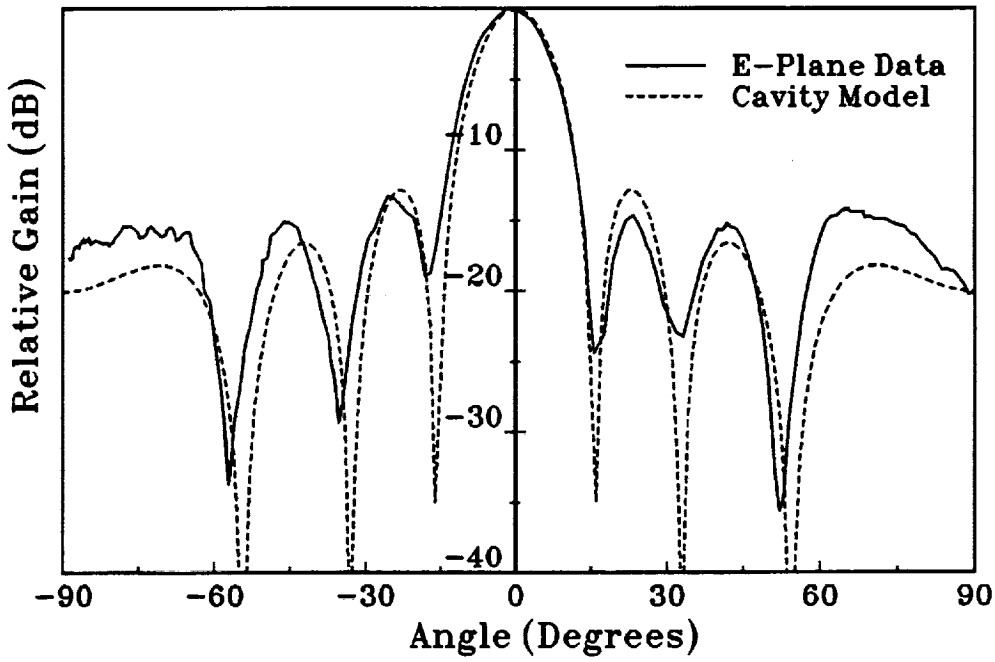

Figure 4-19: E-plane patterns of the 64 element HTS array.

The gain of the gold antenna was measured at resonance and on boresight and found to be 15.6 dB, with a 3 dB beamwidth of 13 degrees. From this, the gain of the HTS antenna was found by measuring transmission coefficient (S_{21}) in a transmission link as described in Chapter 3. At 77 K, the HTS antenna was found to have a gain 4.7 dB higher than the gold antenna at room temperature, for a gain of 20.3 dBi. From the half-power beam widths, the maximum directivity of the antenna was found to be 22.2 dBi. Thus, the HTS array has a total loss of 1.9 dB. This loss can be explained by the attenuation in the 1 cm gold feedline, losses in the gold ground plane, and surface wave losses. From the attenuation in the feed network, we would expect the gold loss to have about 3.8 dB more loss than the HTS antenna. Thus, the measured gains agree quite

well with the loss models. The gain of the HTS array relative to the gold array is shown in Figure 4-20.

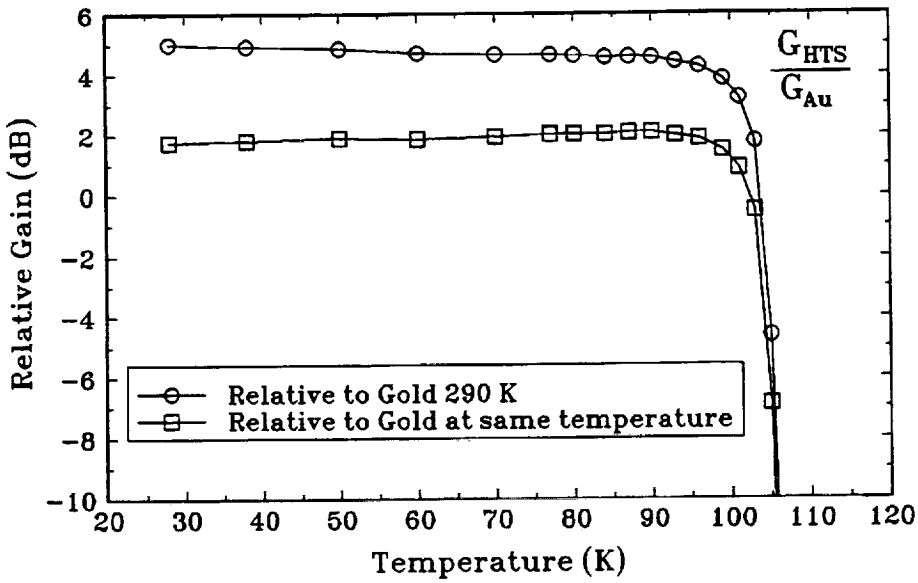

Figure 4-20: Gain of the HTS antenna relative to the gold antenna.

The superb performance of this array demonstrates clearly the advantages that HTS may have for microwave or millimeter wave antennas. Despite the high permittivity substrate, excellent radiation patterns and gain characteristics were obtained.

4.6 Summary

A direct coupled microstrip antenna architecture has been investigated for HTS antennas. Measurements on a single patch antenna showed a good match and reasonable radiation patterns although the E-plane pattern suffered from surface wave scattering. A slight improvement over an identical gold antenna was noted in the efficiency. A four element array constructed using the same

radiating element design showed excellent radiation pattern and gain characteristics. The gain of the HTS antenna at 77 K was found to be 0.9 dB higher than the gold antenna. A 64 element HTS array was also measured and at 77 K was found to have a gain 4.7 dB higher than an identical gold array at room temperature.

4.7 References

1. Y.T. Lo, D. Solomon, and W.F. Richards, "Theory and Experiment on Microstrip Antennas," *IEEE Trans. Antennas and Propagat.*, vol. AP-27, no. 2, pp. 137-145, Mar. 1979.

2. William F. Richards, Y.T. Lo, and Daniel D. Harrison, "An Improved Theory for Microstrip Antennas and Applications," *IEEE Trans. Antennas and Propagat.*, vol. AP-29, no. 1, pp. 38-46, Jan. 1981.

3. J.R. James, P.S. Hall, and C. Wood, *Microstrip Antenna Theory and Design*, Peter Peregrinus Press, 1981.

4. I.J. Bahl and P. Bhartia, *Microstrip Antennas*, Artech House, MA, 1980.

5. Tsuneo Konaka, Makoto Sato, Hidefumi Asano, and Shugo Kubo, "Relative Permittivity and Dielectric Loss Tangent of Substrate Materials for High-Tc Superconducting Film," *J. Superconductivity*, vol. 4, no. 4, pp. 283-288, 1991.

6. Felix A. Miranda, William L. Gordon, Vern O. Heinen, Ben T. Ebihara, and Kul B. Bhasin, "Measurements of Complex Permittivity in the 20 to 300 K Temperature Range from 26.5 to 40.0 GHz," NASA TM #102123, 1989.

7. C.J. Gorter and H.B.G. Casimir, "The Thermodynamics of the Superconducing State," *Physik. Z.* vol. 35, pp. 963-966, 1934.

8. F.A. Miranda, W.L. Gordon, K.B. Bhasin, V.O. Heinen, and J.D. Warner, "Microwave properties of $YBa_2Cu_3O_{7-\delta}$ high-transition-temperature superconducting thin films measured by the power transmission method," *J. Appl. Phys.*, vol. 70, no. 10, pp. 5450-5462, 15 Nov. 1991.

9. Daniel H. Schaubert and K. Sigfrid Yngvesson, "Experimental Study of a Microstrip Array on High Permittivity Substrate," *IEEE Trans. Antennas and Propagat.*, vol. AP-34, no. 1, pp. 92-97, Jan. 1986.

10. P. Perlmutter, S. Shtrikman, and David Treves, "Electric Surface Current Model for the Analysis of Microstrip Antennas with Application to Rectangular Elements," *IEEE Trans. Antennas and Propagat.*, vol. AP-33, no. 3, pp. 301-311, Mar, 1985.

11. *em*, Sonnet Software, 1990.

12. C.M. Chorey, Keon-Shik Kong, K.B. Bhasin, J.D. Warner, and Tatsuo Itoh, "YBCO Superconducting Ring Resonators at Millimeter-wave Frequencies," *IEEE Trans. on Microwave Theory and Tech.*, vol 39, no. 9, pp. 1480-1486, Sept. 1991.

CHAPTER V.

GAP COUPLED ANTENNA

5.1 Introduction

In the previous chapter, a direct coupled antenna was investigated. In this chapter, a second planar architecture is considered. Instead of having a microstrip transmission line directly contact the edge of the patch, a coupling gap was employed. In this chapter, the performance of a 26 GHz HTS circular disk microstrip antenna that is gap coupled to a microstrip transmission line is discussed. The chapter begins with the motivations for using such an architecture, and then presents the design and performance of an HTS single patch antenna. Performance parameters include patterns, input impedance, bandwidth, and efficiency. These results are compared with results that are expected from the cavity model. Following this, the performance of a four element array is presented. The chapter concludes with an investigation of a gap coupled annular ring antenna. In each case, the results are compared to those of an identical antenna fabricated using gold metallization.

5.2 Motivation

The gap coupled microstrip antenna was chosen for performance evaluation because of the high edge impedance of patch antennas fabricated on $LaAlO_3$. The gap allows for a impedance match that is rather simple. Instead of using impedance transformers such as a quarter wave transformer, or insetting the feedpoint into the patch interior, all that is required is a gap between the end of the transmission line and the patch antenna. In addition, it also has the fabrication and analytical advantages associated with the simplicity of a planar architecture.

A circular patch was chosen for the gap coupled antenna. Although the properties of rectangular and circular patches are quite similar, the rectangular patch antenna has the property that the edge impedance increases as the width is decreased. For gap coupling, a high edge impedance is desirable so that a wider gap may be used. Looking at this conceptually, for a given gap size, a smaller patch area can be coupled more strongly to a transmission line than can a larger patch area. However, the radiation efficiency of a rectangular patch decreases with decreasing width. Thus, for a rectangular patch, the coupling is achieved at the expense of radiation efficiency. A circular patch, on the other hand, eliminates this degree of freedom since only the radius may be changed. In addition, for a given frequency, the area of a circular patch is less than the area of a rectangular patch unless $W \leq L$.

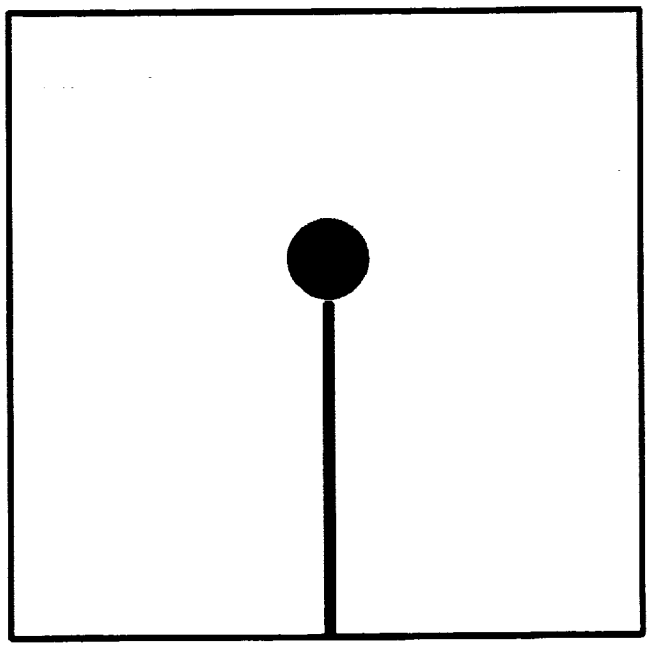

Figure 5-1: Physical layout of the gap coupled microstrip antenna on a 1 cm x 1 cm $LaAlO_3$ substrate.

5.3 Single Element Antennas

5.3.1 Design

The gap coupled antenna design used in this study is shown in Figure 5-1. It is a circular patch with a radius of 610 μm and is coupled to the 50 Ω transmission line via a 15 μm wide capacitive gap. The antenna is designed for a lanthanum aluminate substrate 1 cm x 1 cm square by 254 μm (10 mil) thick. The dielectric thickness used is the minimum practical substrate thickness and was chosen to reduce the generation of surface waves, while the size was chosen because larger area HTS films were not available. A YBCO superconducting thin film was used for the circuit metallization, while an evaporated copper ground plane of 1.6 μm in thickness was used. The HTS film used for this antenna was

deposited using a pulsed-laser deposition (PLD) method and had a relatively low T_c of 84.5 K. An identical circuit was also fabricated using silver and gold metallization.

5.3.2 Resonant Frequency

The resonant frequency of the circular patch can be found analytically from the dimensions of the cavity comprised of the disk and ground plane using the cavity model. The discussion below follows the work of Bahl and Bhartia[1]. Assuming the cavity to be free of current sources, the Helmholtz equation is $\nabla^2\mathbf{E} + k_{nm}^2\mathbf{E} = 0$, where k_{nm} is the propagation constant, $k_{nm} = 2\pi f_{nm}(\mu\epsilon)^{1/2}$. Applying the boundary condition of the perfect magnetic wall, the electric field is found to be

$$E_z = E_0 J_n(k_{nm} r)\cos n\phi \qquad (5\text{-}1)$$

In this equation, J_n are Bessel functions of order n. In accordance with the assumptions of the cavity model, the remaining components of the electric field, E_r and E_ϕ are assumed to be zero. The H-fields can be found by a simple application of Maxwell's curl equation and an integration over time,

$$\bar{H} = \frac{j}{\mu\omega}\nabla \times \bar{E} \qquad (5\text{-}2)$$

so that

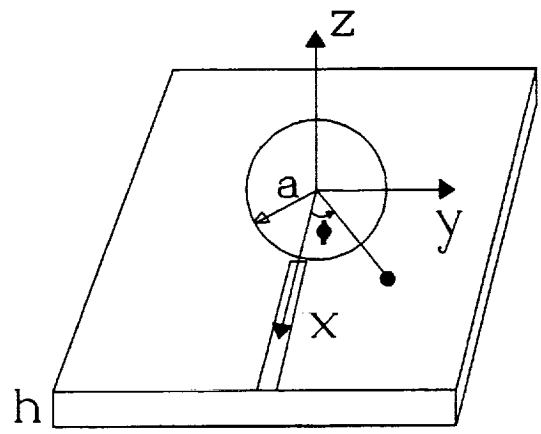

Figure 5-2: Coordinate system for the antenna.

$$H_r = \frac{j}{\omega\mu r}\frac{\partial E_z}{\partial \phi} = -\frac{jn}{\omega\mu r}E_0 J_n(k_{nm}r)\sin n\phi \tag{5-3}$$

and

$$H_\phi = -\frac{j}{\omega\mu}\frac{\partial E_z}{\partial r} = -\frac{jk_{nm}}{\omega\mu}E_0 J_n(kr)\cos n\phi \tag{5-4}$$

At the boundary of the disk the radial component of the surface current,

$$K = \hat{n} \times H \tag{5-5}$$

must go to zero, which implies

$$J'_n(k_{nm}a) = 0 \tag{5-6}$$

This is the condition for resonance. The integer m represents the m'th zero of Eqn. (5-6). Thus, the resonant frequency is then given by

$$f_{mn} = \frac{X_{nm}}{2\pi a\sqrt{\epsilon_r}} \tag{5-7}$$

where ϵ_r is the permittivity of the dielectric inside the cavity and X_{nm} are the roots of $J'_n(x) = 0$. For a patch antenna, a is the radius of the patch and ϵ_r is the permittivity of the substrate. The first root of this equation corresponds to the lowest order mode (TM_{11}), and is $X_{11} = 1.841$. The current distribution on the patch surface for the lowest order mode is shown in Figure 5-3.

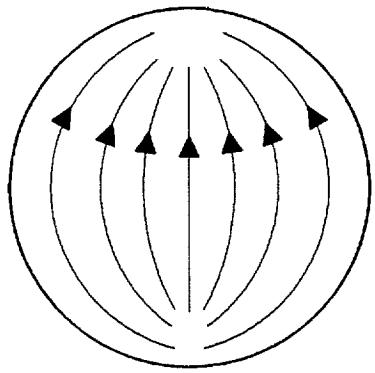

Figure 5-3: Current distribution on the circular patch for the TM_{11} mode.

As in the case of the rectangular patch, this expression predicts frequencies substantially higher than measured frequencies because the model does not account for the fringing fields. Several expressions for a modified, "effective" radius have been proposed to account for the fringing fields. The most common expression is the one given by Shen *et. al.*[2],

$$a_e = \left[1 + \frac{2h}{\pi a \epsilon_r}\left(\ln\frac{\pi a}{2h} + 1.7726\right)\right]^{1/2} \qquad (5\text{-}8)$$

A slightly more involved expression has been given by Chew *et. al.*[3],

$$a_e = a\left[1+\frac{2h}{\pi a \epsilon_r}\left(\ln\frac{a}{2h}+(1.41\epsilon_r+1.77)+\frac{h}{a}(0.268\epsilon_r+1.65)\right)\right]^{1/2} \qquad (5\text{-}9)$$

For this work the latter equation was deemed necessary since the parameters of the antenna used do not meet the criterion given by Shen of $h/a \ll 1$. The antenna used in this work has $h/a = 0.416$.

The gold antenna was found to have a room temperature resonance (TM_{11} mode) of 25.88 GHz, while the HTS has its fundamental resonance at 26.61 GHz. The difference in the measured resonant frequencies of the two antennas is attributable to variations in the dielectric height between samples and also to the fabrication process; over-etching of the HTS antenna caused its radius to be 600 μm instead of the desired 610 μm. This over-etching also caused the coupling gap to be almost twice the intended 15 μm width, causing a rather severe mismatch. Variations in substrate permittivities may also account for some of the difference in resonant frequency. The resonant frequency data for the gold and HTS antennas are shown in Figure 5-4.

The permittivity of gold antenna's substrate was extracted from the resonant frequency data using Eqns. (5-7) and (5-9) and is shown in Figure 5-5 as a function of temperature along with data from Konaka *et. al.*[4], and from Miranda

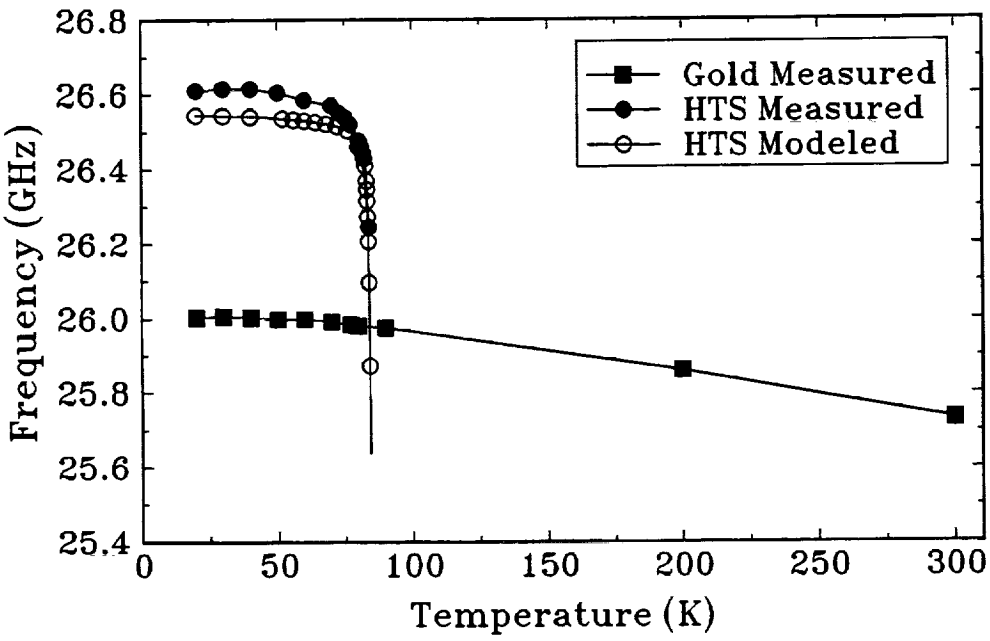

Figure 5-4: Resonant frequencies of the HTS and gold gap coupled antennas as a function of temperature.

et. al.[5] The permittivity was found to be 22.2, decreasing to 21.73 at 20 K. The permittivity extracted in this case differs by 7% from that reported by Konaka[4]. However, as in the case of the direct coupled antenna, the slope of the extracted permittivity curve closely resembles that of Konaka. Using the permittivity extracted from the gold antenna, the resonant frequency of the HTS antenna was calculated using Eqns. (5-7) and (5-9) and Eqns. (5-9) and (5-10) from Chapter 4 to account for the effect of the magnetic penetration depth. In this case, the film's T_c of 84.5 K and thickness of 350 mm, and an estimated zero temperature penetration depth, λ_{po}, of 200 nm was used. This modeled resonant frequency curve is also plotted in Figure 5-4.

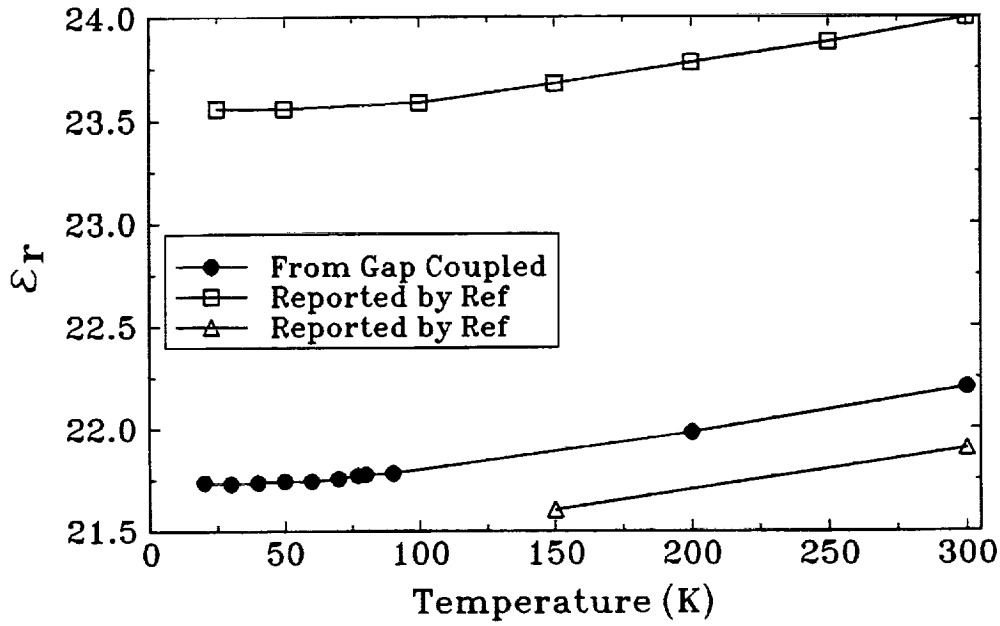

Figure 5-5: Permittivity of lanthanum aluminate extracted from the resonant frequency data of the gold antenna.

5.3.3 Antenna Patterns

The radiated fields from a rectangular patch can be evaluated by integrating the equivalent magnetic current, $\mathbf{M} = 2E_z \phi$ over the aperture of formed between the disk and ground plane. The far field patterns in the TM_{11} mode are then given by[6]

$$E_\theta = -j^n \frac{\pi V_0 a}{\lambda_0} \frac{e^{-jk_0 r}}{r} \left[J_0(A) - J_2(A)\right] \cos n\phi \qquad (5\text{-}10)$$

and

$$E_\theta = -j^n \frac{\pi V_0 a}{\lambda_0} \frac{e^{-jk_0 r}}{r} \left[J_0(A) + J_2(A)\right] \cos\theta \cos n\phi \qquad (5\text{-}11)$$

where $A = k_0 a \sin\theta$. In the E-plane, $\phi = 0°$ and the far field is just E_θ, while in the H-plane, $\phi = 90°$ and the far field is E_ϕ. The measured E- and H-plane patterns for the antennas are shown in Figures 5-6 and 5-7. As demonstrated in the case of the direct coupled antenna, the H-plane data shows good agreement with the cavity model while dramatic deviations from the model result in the E-plane. A considerable amount of effort was expended attempting to trace the effects of the perturbations in the E-plane. Shielding tape and radar absorbing material at the substrate edges did not change the pattern. To verify that radiation from and around the coupling gap was not causing these disturbances, a gold ribbon bond wire of the same width as the microstrip feedline was connected across the coupling gap, effectively shorting it out. This did not substantially change the E-plane pattern either.

5.3.4 Input Impedance, Q, and Bandwidth

The return loss characteristics of the gap-coupled antennas are shown in Figure 5-8. The gold single patch shows an excellent match with a VSWR of less than 1.1 (0.2 % reflected power), while the HTS patch was severely under-coupled because of the wider than expected coupling gap. The HTS had a VSWR of 2.3, or 16 % reflected power. Because of the presence of the coupling gap, the input resistance of the patch could not be ascertained directly. However, it may be estimated quite well using the measured Q. The loaded Q of the antenna is found by curve fitting the measured reflection coefficient data, as described in Chapter 2. By finding the return loss at resonance and at

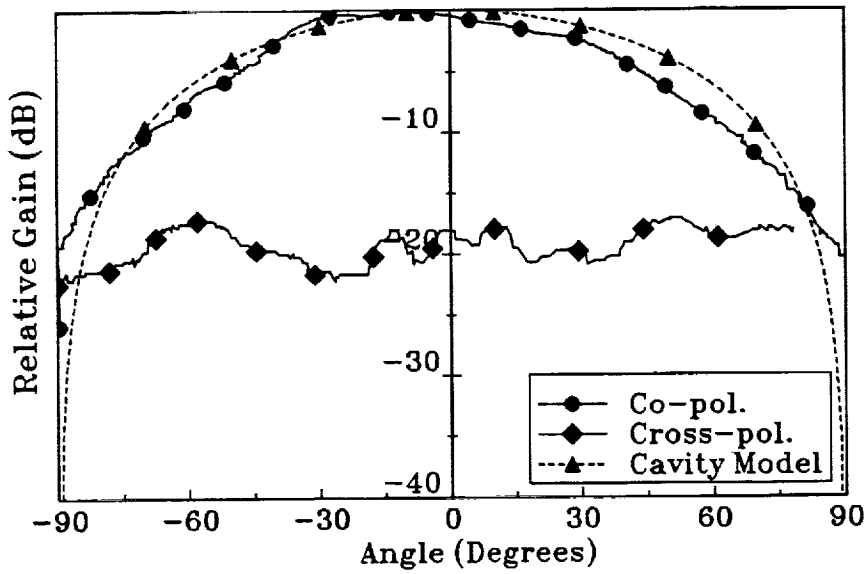

Figure 5-6: H-plane radiation patterns of the circular gap coupled single patch antenna. Co- and cross-polarization data is shown along with the cavity model prediction.

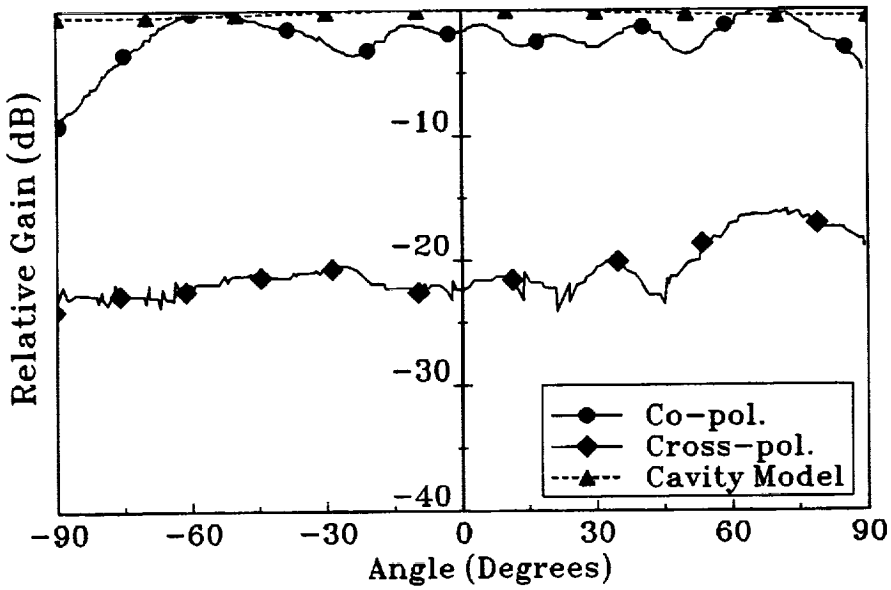

Figure 5-7: E-plane radiation patterns of the circular gap coupled single patch antenna. Co- and cross-polarization data is shown along with the cavity model prediction.

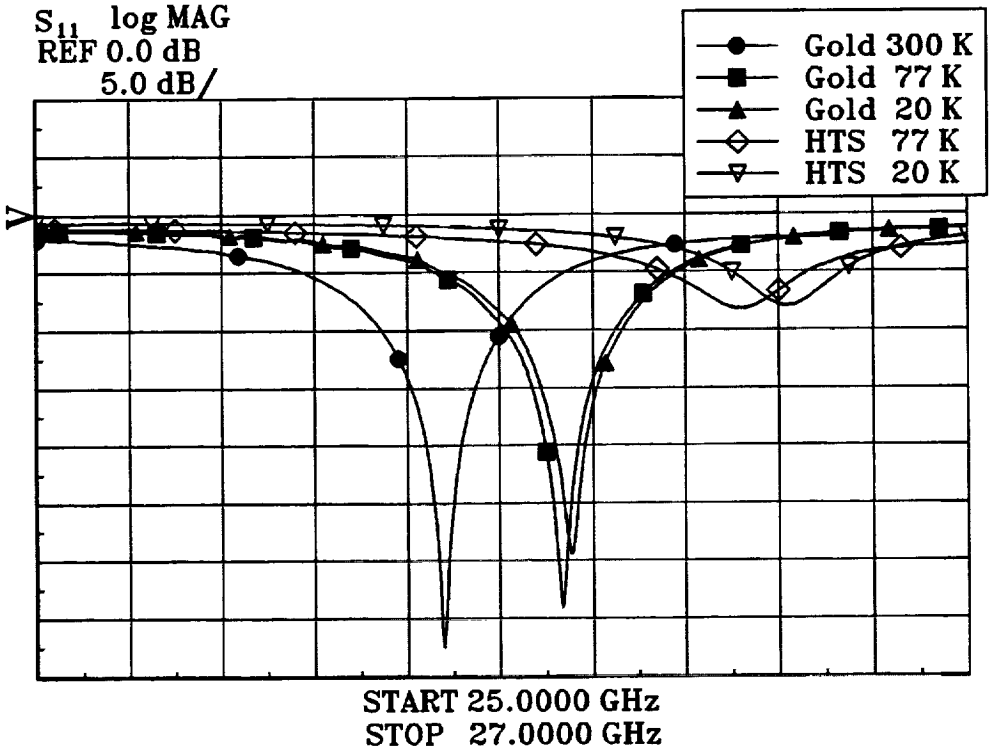

Figure 5-8: Measured return loss of the gap coupled single patch antennas.

frequencies far from resonance, the series coupling loss σ and coupling coefficient κ can be calculated so that the Q of the patch independent of the feed line and coupling gap may be found. Modeling the patch as a parallel RLC circuit, the unloaded Q of the patch can be expressed in terms of the model parameters as

$$Q_T = R\sqrt{\frac{C}{L}} \tag{5-12}$$

while the resonant frequency is given by

$$f_r = \frac{1}{2\pi\sqrt{LC}} \tag{5-13}$$

Substituting Eqn. (5-12) into Eqn. (5-13) and eliminating the inductance L, the input resistance can be found as

$$R_{in} = \frac{Q_T}{2\pi f_r C} \tag{5-14}$$

The expression for the capacitance of a microstrip disk, given by Chew *et. al.*[3],

$$C \approx \frac{a_e^2 \pi \epsilon_r \epsilon_0}{h} \tag{5-15}$$

where a_e is given by Eqn. (5-9), was used along with the measured Q and the substrate permittivity values extracted from the resonant frequency data. The input resistance of the gold patch was found to be 329 Ω at 300 K increasing to 383 Ω at 20 K while the HTS antenna was found to have an input impedance of 340 Ω at 77 increasing to 393 Ω at 20 K. Using Eqn. (5-13) and the calculated capacitance values, the inductance of the equivalent circuit can also be found so that all parameters of the equivalent circuit are known, save the series loss. These values are summarized in Table 5-1.

The cavity model may also be used to approximate the Q of the patch analytically, and thus the input resistance. The expressions given below are those presented by Bahl and Bhartia[1]. The total Q of the patch is defined as

Table 5-1: Equivalent Circuit Parameters			
Circuit	R (Ω)	C (pF)	L (pH)
Gold, 300 K	329	1.28	30.0
Gold, 20 K	383	1.25	29.9
HTS, 77 K	340	1.22	29.6
HTS, 20 K	393	1.22	29.4

$$Q_T = \frac{2\pi f_r \, E_T}{P_T} \tag{5-16}$$

where $P_T = P_r + P_d + P_c$ is the total power dissipated in the antenna by radiation, dielectric loss, and conductor loss, and E_T is the total stored energy. The total stored energy is given by

$$E_T = \frac{\varepsilon}{2} \int_V |E|^2 dV = \frac{hE_0^2}{8\omega f \mu} J_1^2(ka)\left[(ka)^2 - 1\right] \tag{5-17}$$

The radiated power is one-half the integral of the complex Poynting vector since power is radiated through the upper half-space only. Thus,

$$P_r = \frac{1}{4}\int_S (\bar{E} \times \bar{H}^*) dS = \frac{1}{4\eta_0} \int_0^{2\pi} \int_0^{\pi} \left(|E_\theta|^2 + |E_\phi|^2 \right) r^2 \sin\theta \, d\theta \, d\phi \tag{5-18}$$

where E_θ and E_ϕ are given by Eqns. (5-10) and (5-11). This expression must be evaluated numerically. The power lost in the patch and ground plane conductors is given by $I^2R/2$, or

$$P_c = 2\frac{R_s}{2}\int_S |K|^2 dS \qquad (5\text{-}19)$$

where **K** is the surface current density and R_s is the surface resistance. The integral can be evaluated to give

$$P_c = R_s \frac{0.40456\pi E_0^2}{(\omega\mu)^2} \qquad (5\text{-}20)$$

The dielectric loss is given by the integral of the electric field inside the cavity, or

$$P_d = \frac{\omega\epsilon\tan\delta}{2}\int_V \bar{E}\cdot\bar{E}^* dV = 8.05x10^{-5} h\tan\delta E_0^2/f \qquad (5\text{-}21)$$

Using these equations, the Q and input resistance of each patch was calculated and is shown in Figure 5-9. As in the case of the direct coupled antenna, the surface resistance of YBCO films as reported by Miranda *et. al.*[10] was used to find the conductor loss in the HTS antenna, while the measured conductivity of gold as a function of temperature was used to calculate the conductor loss in the gold antenna. The dielectric loss was taken to be a constant 5×10^{-5} for both antennas. The change in permittivity and operating frequency with respect to temperature was also accounted for. The modeled resistances show values that are two to three times higher than the measured values. This is mostly the result of two factors, namely the cavity model assumes a perfect

magnetic wall (no fringing) which is clearly not the case in this instance and, secondly, it makes no provisions for the power lost as surface waves.

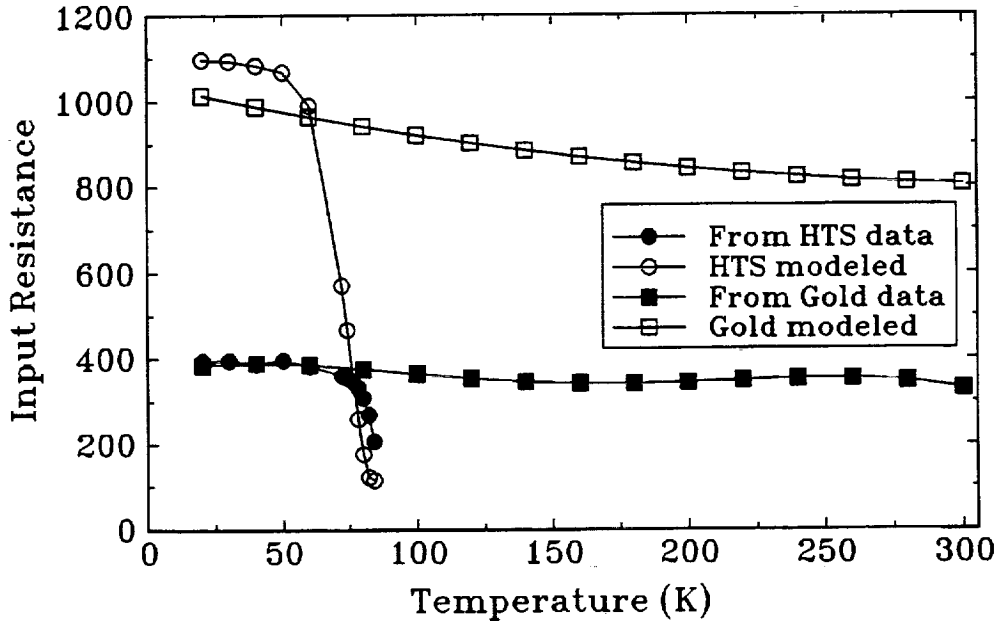

Figure 5-9: Measured and modeled input resistance of the gold and HTS single patch antennas.

Both the HTS and gold antennas suffer from very narrow bandwidths of between 0.80 % and 1.1% (VSWR < 2) because of the high frequency, high dielectric constant, and low substrate height. In the case of the gold antenna, the bandwidth was measured directly from the return loss data. This could not be done for the HTS antenna because of the mismatch; the return loss never dipped below VSWR = 2. Thus, the bandwidth was obtained from the Q according to the relation

$$B.W.(\%) = \frac{100}{Q\sqrt{2}} \qquad (5\text{-}22)$$

The bandwidths of the antennas were also calculated analytically. As described in the previous section, the modeled Q's are significantly higher than the measured Q's, and thus the calculated bandwidths are significantly lower than the measured ones. The measured and calculated bandwidths as a function of temperature are shown in Figure 5-10. In both the modeled and measured bandwidth curves, the bandwidth decreases as a function of temperature because of the reduced losses in the antenna.

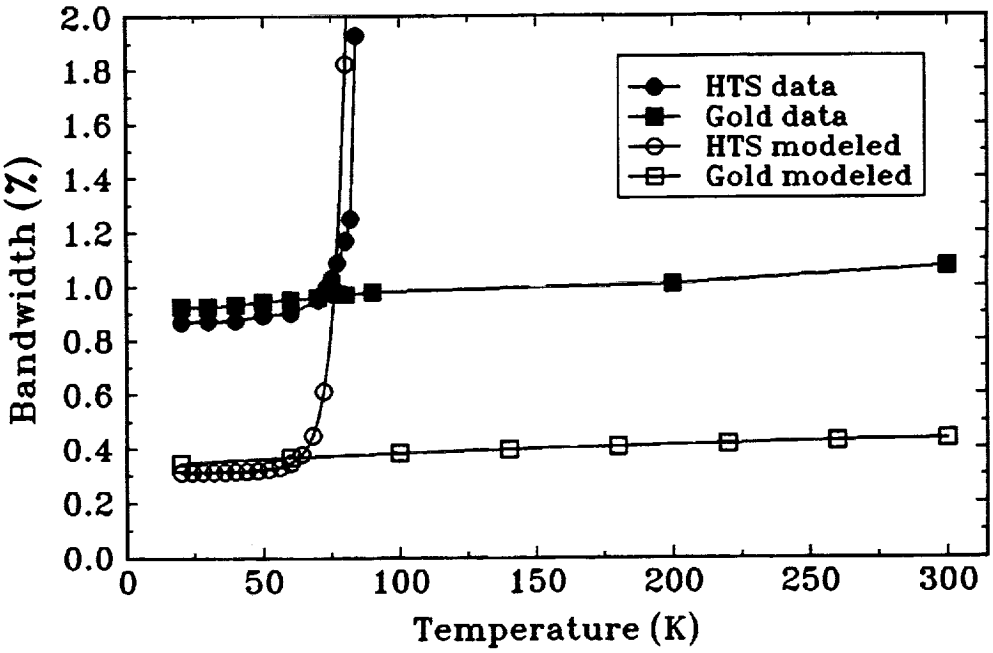

Figure 5-10: Measured and modeled bandwidths of the gap coupled single patch antennas. The bandwidth of the HTS antenna was obtained from the measured Q.

5.3.5 Efficiency

The efficiency of each single patch antenna was measured using the Wheeler Cap method as described in Chapter 3. The measured efficiencies of the single patch antennas are shown in Figure 5-11. The HTS antenna demonstrated a few percent increase in efficiency over its equivalent gold antenna. The efficiencies of both the gold and the HTS antenna were found to be quite low. The HTS antenna had a maximum efficiency of 71 % while the gold antenna showed a maximum of 63 %. To model the efficiency of the gold antenna, the power dissipated in the conductors, dielectric, and radiation were calculated from the equations given above. The efficiency of the patch is calculated by

$$\eta_{patch} = \frac{P_r}{P_r + P_d + P_c} \tag{5-23}$$

The attenuation in the microstrip transmission line was calculated from Pucel's equations as given in Chapter 2, using the measured conductivity of evaporated gold. The efficiency of the antenna, including the feedline, is then given by

$$\eta_{antenna} = \frac{P_r}{P_r + P_d + P_c} 10^{-(\alpha_c + \alpha_d)/10} \tag{5-24}$$

where α_c is the attenuation, in dB, of the transmission line due to conductor losses and α_d is the attenuation of the transmission line in dB due to dielectric losses.

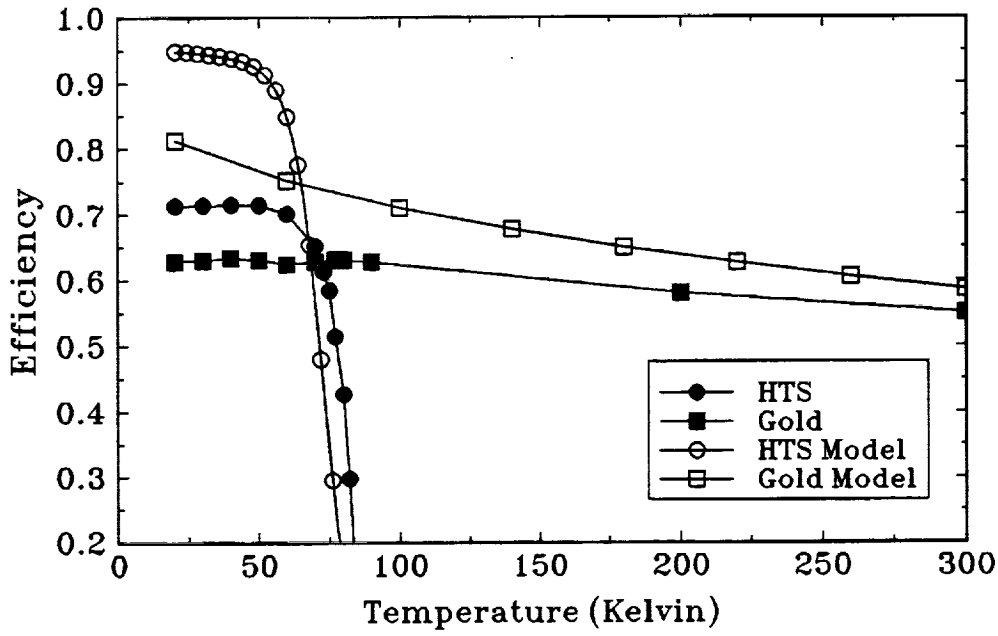

Figure 5-11: Measured and modeled efficiencies of the single patch gap coupled antennas.

The efficiency of the HTS antenna was also modeled using the calculated efficiencies of the patch from previously given equations. However, instead of using reported surface resistance values to find the loss of the HTS feedline, the attenuation coefficient of the transmission line was assumed to be the same as that measured by Chorey *et. al.*[7]. This assumption is obviously not entirely accurate because of variations in substrate parameters and film surface resistance and critical temperature, and a 25 % difference in operating frequency. Chorey's data was shifted in temperature to account for the difference in T_c between the films. Both modeled curves exhibit efficiencies that are significantly higher than the measured curves. The differences shown seem to be too large to be accounted for by losses such as those in the coax-to-microstrip transition and

substrate surface roughness, indicating that the models used may not accurately characterize the losses. It is not clear how surface wave efficiency affects the efficiency of the patches. Because the surface wave component is diffracted at the substrate edges to become radiated power, the efficiency measured by the Wheeler cap method should not measure the degradation due to surface wave losses.

5.4 Four Element Arrays

A four element array was constructed using the gap coupled circular patch as the radiating element. The array, shown in Figure 5-12, has all four elements fed in-phase to produce broadside radiation. The elements are spaced 5.8 mm apart, or $\lambda_0/2$ at the resonant frequency of 26 GHz. Fabrication tolerances were controlled more tightly than in the case of the single patch antennas, so that the gap sizes are quite uniform at 15 μm. The feed network is constructed from 50 Ω microstrip transmission lines, and 71 Ω quarter wave transformers are employed for impedance matching at each junction.

The resonant frequency and bandwidth for the four element arrays are shown in Figure 5-13. The shift in resonant frequency occurs as it did for the single element cases. However, the bandwidth is narrowed slightly due to the effect of the feed network. Both the HTS and gold arrays showed good return loss characteristics over their respective operating temperature ranges. The gold array had a VSWR of less than 1.42 (3.0 % reflected power) over the entire operating temperature range, while the HTS array had a VSWR of less than 1.18

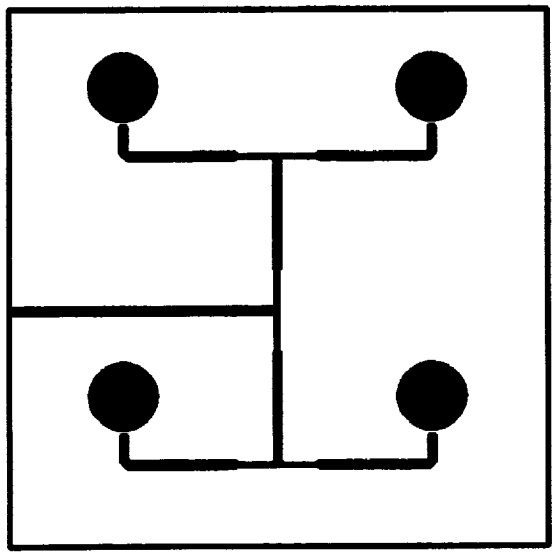

Figure 5-12: Physical layout of the gap coupled four element array.

(0.7 % reflected power) at temperatures below 85 K. This data is shown in Figure 5-14.

As in the case of the direct coupled antenna, the far field radiation patterns of the four element array are quite clean in both the E and H-plane, despite the disturbances in the single element E-plane pattern. Minor variations from the predicted patterns are evident at the extreme angles. In each case the cross polarization is more than 13 dB below the co-polarization peak, indicating very little feedline or other spurious radiation. These patterns are shown in Figures 5-15 and 5-16.

The gain of the gold 4-element array was measured at room temperature using a horn substitution method with a calibrated standard gain horn. The gain of the gold antenna was found to be 9.0 dB. As described in Chapter 3, the gain

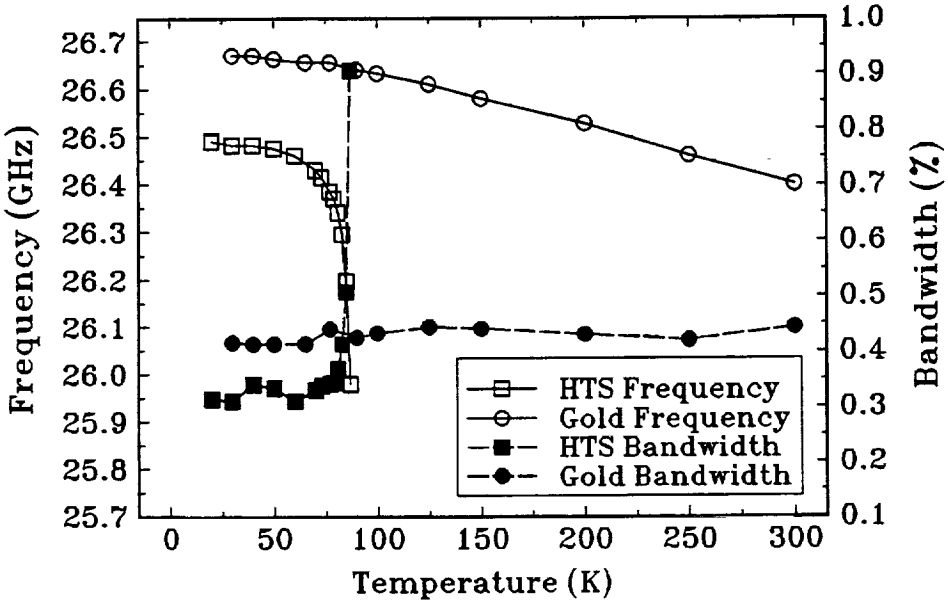

Figure 5-13: Resonant frequency and bandwidth for the four element arrays.

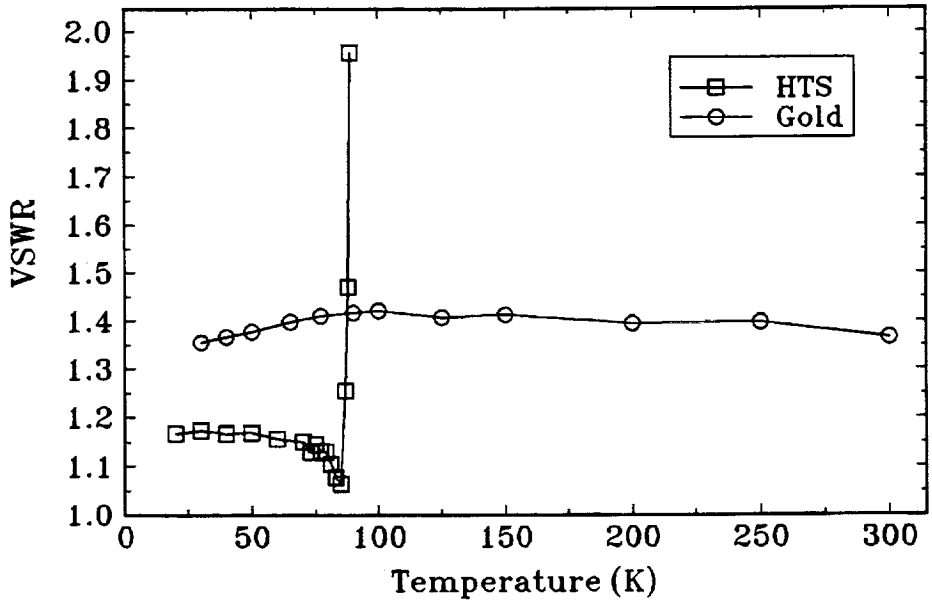

Figure 5-14: Measured VSWR of the gold and HTS four element array antennas.

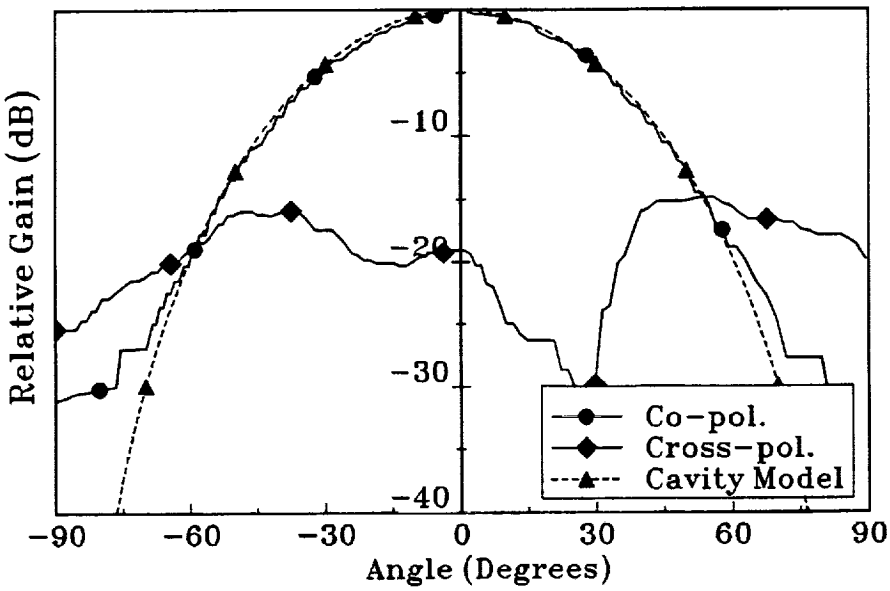

Figure 5-15: H-plane radiation patterns of the gap coupled four element arrays, showing co- and cross-polarization data and the cavity model prediction.

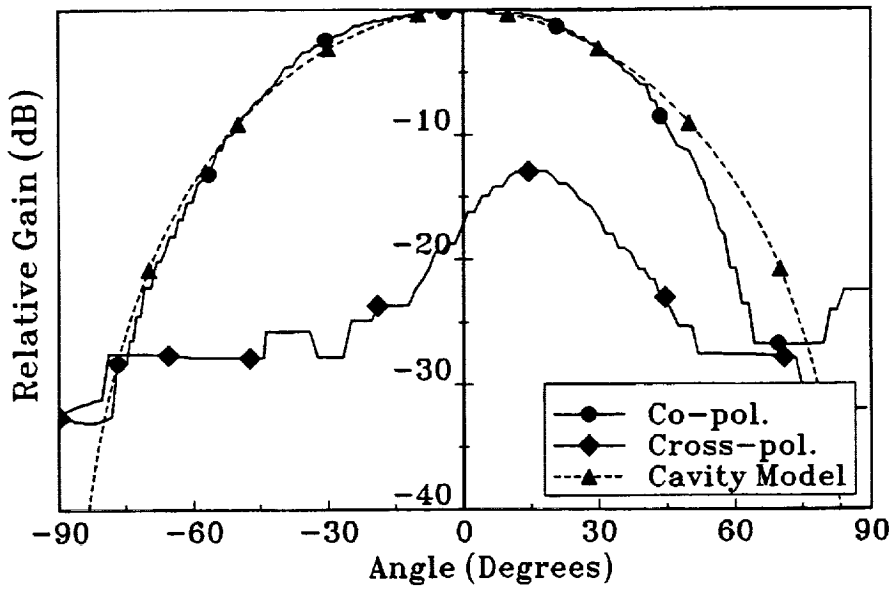

Figure 5-16: E-plane radiation patterns of the gap coupled four element arrays, showing co- and cross-polarization data and the cavity model prediction.

of the HTS array relative to the gold array was found by measuring the power received at boresight and applying the Friis transmission formula. The measured gain of the HTS antenna relative to the gold antenna is shown in Figure 5-17, while the absolute gain of each antenna is shown in Figure 5-18. The HTS array showed a gain of 10.7 dB at 77 K, increasing to 11.1 dB at 20 K. The gain of gold array increased from 9.0 dB at room temperature to 9.85 dB at 77 K and 10.13 dB at 20 K. The half-power beam widths (HPBW) were used to calculate the directivities, or the maximum possible gain. With an E-plane beam width of 59 degrees and an H-plane beam width of 50 degrees, the directivity is estimated to be 11.5 dB.

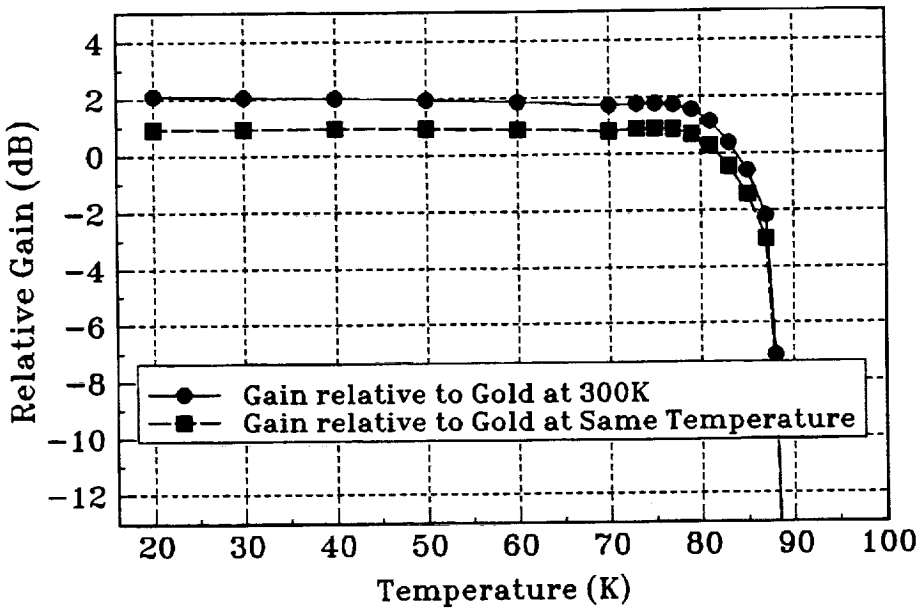

Figure 5-17: Gain of the HTS array relative to th e gold array when the gold array is at room temperature and at the same temperature as the HTS array.

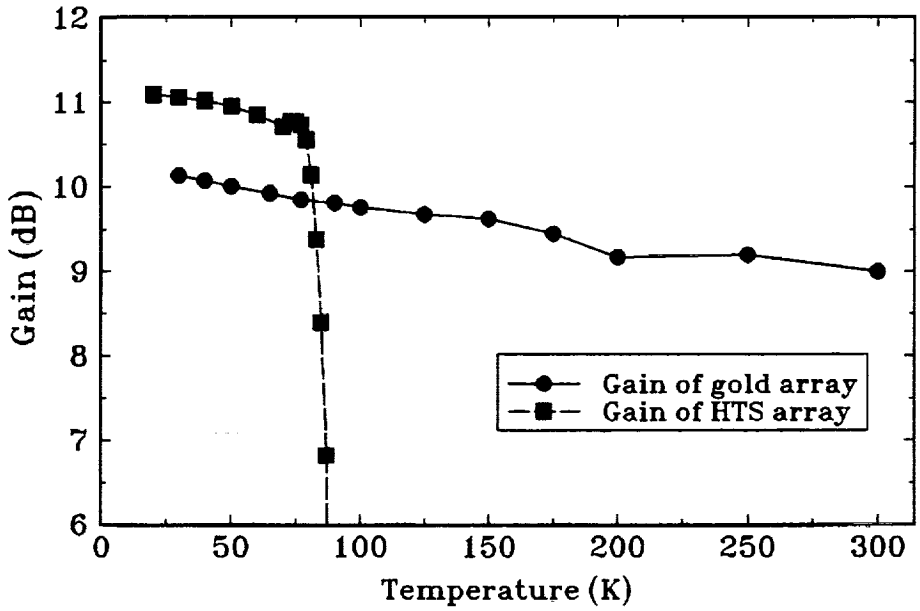

Figure 5-18: Absolute gain of the HTS and of the gold array.

In addition to the experimental data, the losses in each antenna due to metallization were also estimated analytically. From a moment method calculation, the attenuation coefficients for a 50 Ω and a 71 Ω transmission line on $LaAlO_3$ at 25 GHz were found and multiplied by the path length in the feed network for one element. This loss was added to the loss of a patch, calculated in Section 5.3.5. This information is summarized in Table 1. The expected loss of the gold array was found to be 2.75 dB at room temperature and 1.63 dB at 77 K, while the expected loss of the HTS array was found to be 5 dB at 77 K. In the case of the HTS antenna, the loss is substantially more than the measured loss because the surface resistance value used to model the HTS patch was quite high at 77 K, resulting in a modeled patch efficiency of 30 %. Measurements of

high at 77 K, resulting in a modeled patch efficiency of 30 %. Measurements of the HTS four element array show a loss (Directivity - Gain) of 0.8 dB at 77 K.

Table 5-2: Array Loss Budget

Circuit	Line Loss	Patch Loss	Total Loss	Measured Gain	Implied Loss
Gold 300K	0.75	1.99	2.0	9.0	2.7
Gold 77K	0.44	1.19	1.6	9.8	1.9
HTS 77K	0.035	5.0	5.0	10.7	0.8

5.5 A K-Band Superconducting Annular Ring Antenna

Annular ring antennas have been investigated by many researchers as an alternative to the typical rectangular or circular shaped antennas[8,9,10]. In the TM_{11} mode, the ring has a very narrow bandwidth. However, in the higher-order TM_{12} mode, the ring antenna has been shown to have a significantly higher bandwidth and a slightly higher gain than a circular disk or rectangular microstrip antenna[10,11]. The mode excited on the ring is dependent upon the choice of annulus radii.

The geometry of the annular ring microstrip antenna used in this investigation is shown in Figure 5-19. The antenna substrate is lanthanum aluminate. The inner radius a is 1.36 mm and the outer radius b is 2.64 mm. These dimensions were chosen for a TM_{12} mode operation in the K-band. The substrate thickness, h, was chosen to be the minimum practical thickness of 254 μm to

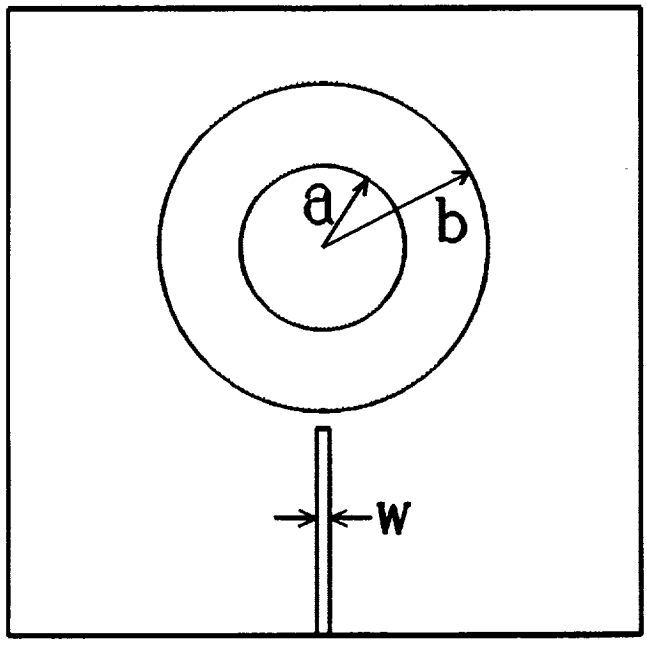

Figure 5-19: Geometry of the annular ring antenna. Parameters are a = 1.36 mm, b = 2.64 mm, w = 0.1 mm, and gap size g = 15 μm.

reduce surface wave generation. The antenna is capacitively gap-coupled to a 100 μm wide 50 Ω microstrip line via a 15 μm wide gap. The HTS thin film was deposited by a laser ablation process[12] and had a transition temperature (T_c) of 89 K. Standard photolithography and "wet" etching process were used for fabrication, as described in Appendix A. A silver contact of 2500 Å was deposited at the end of the microstrip feedline as a bonding pad. An identical antenna was fabricated with 1.6 μm of silver for comparison purposes. Both circuits used 1.6 μm of evaporated silver as ground planes.

The antennas had a fundamental (TM_{11} mode) resonance at 5.52 GHz and the higher-order TM_{12} mode resonance at 21.65 GHz. The resonant frequencies of annular rings are found by solving[13]

$$J'_n(ka)Y'_n(ka) - J'_n(kb)Y'_n(ka) = 0 \qquad (5\text{-}25)$$

where k = $2\pi/\lambda$. It has been shown[14] that good agreement between predicted and experimental values can only be obtained by using an effective dielectric constant ϵ_{eff} and modified radii of:

$$a_e = a - (3/4)h$$
$$b_e = b + (3/4)h$$

For this work, a value of 20 for ϵ_{eff} gave agreement within 2% for all measured resonances. The computed and measured resonant frequencies of the first few resonances are given in Table 5-3.

Table 5-3: Measured and Calculated Resonant Frequencies

Mode	F_{meas}	F_{calc}	% Error
TM_{11}	5.52	5.46	1.10
TM_{21}	10.61	10.65	0.38
TM_{31}	15.35	15.44	0.58
TM_{41}	19.79	19.89	0.50
TM_{51}	24.08	24.14	0.25
TM_{12}	21.65	21.70	0.23

For pattern measurements, the antennas were mounted in a brass test fixture with a 2 cm long microstrip line on alumina separating the K-connector launcher from the antenna. Wire bonds provided RF connections. The H-plane antenna pattern for the TM_{12} mode is shown in Figure 5-20 while the E-plane antenna pattern is shown in Figure 5-21. These patterns compare quite well with the patterns predicted by the cavity model as given by Lee and Dahele[14] (also

shown in Figures 5-20 and 5-21). Deviations of the experimental data from the predicted patterns in the H-plane are due to the finite ground plane, surface waves, and scattering from the test fixture, while deviations in the E-plane are due mainly to surface waves.[15]

The efficiency of these antennas were measured using the Wheeler Cap method as described in Chapter 3. The measured efficiencies are shown in Figure 5-22 as a function of temperature. The HTS antenna is seen to surpass the performance of the metal antenna at temperatures below 80 K, reaching a peak efficiency of 74%. A 5% increase in performance of the HTS antenna is seen over the silver at 77 K, and 10% is seen at 20 K, due to the lower conductor losses of the HTS. A substantial portion of the lost power is dissipated as surface waves; Pozar[16] showed that about 23% of the power is dissipated as surface waves at 20 GHz due to the high permittivity of the substrate.

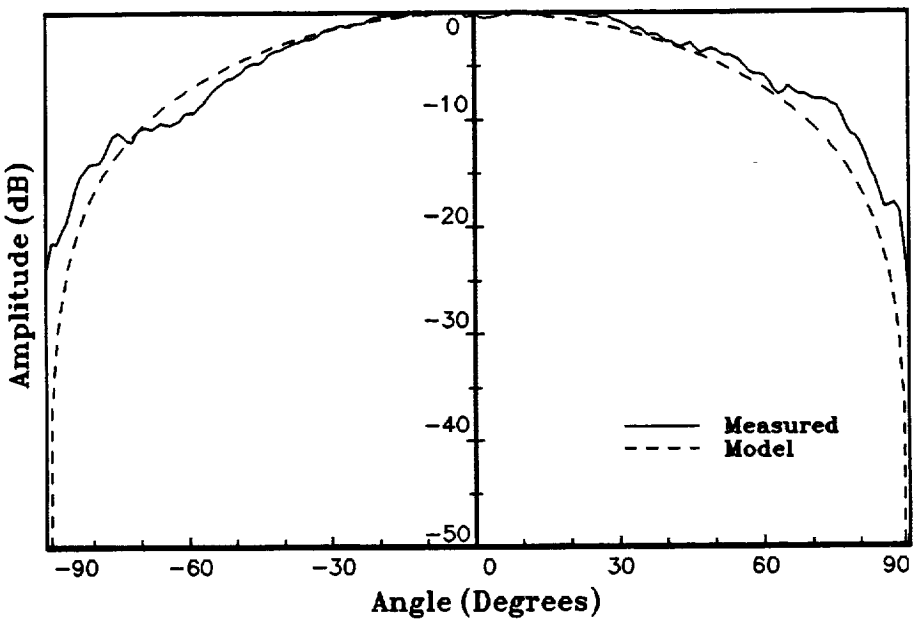

Figure 5-20: Measured and modeled H-plane patterns of the annular ring in the TM_{12} mode.

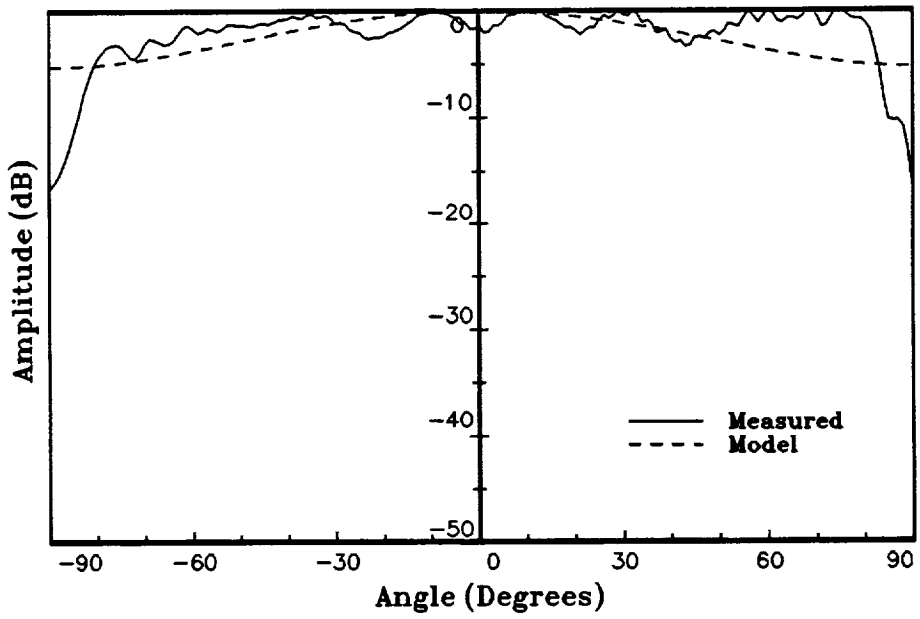

Figure 5-21: Measured and modeled E-plane patterns of the annular ring antenna in the TM_{12} mode.

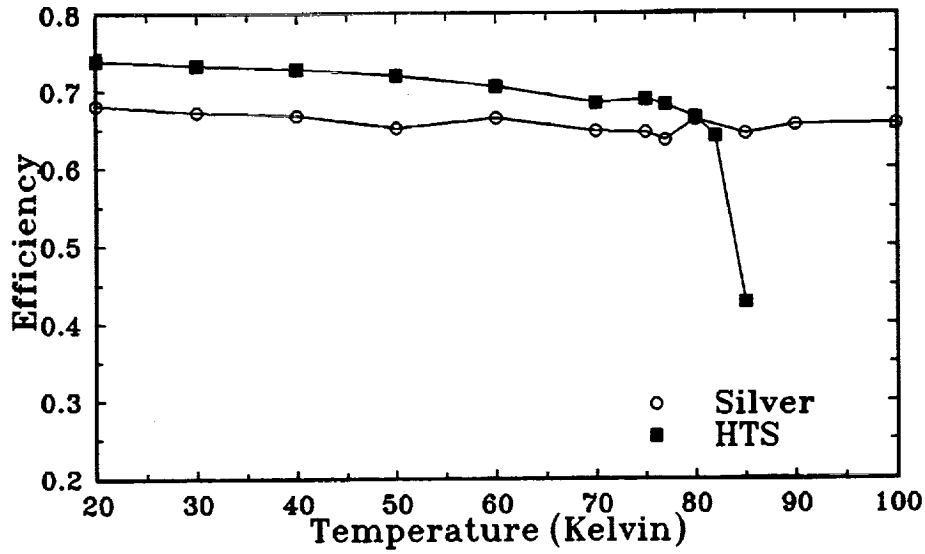

Figure 5-22: Efficiency of the annular rings measured using the Wheeler-cap method.

5.6 Summary

A gap coupled microstrip antenna architecture has been investigated for HTS antennas. Measurements on a single patch antenna showed a good match is possible if a narrow (15 μm) gap is used. Reasonable radiation patterns were obtained although the E-plane pattern suffered from surface wave scattering. A slight improvement over an identical gold antenna was noted in the efficiency. A four element array constructed using the same radiating element design showed excellent radiation pattern and gain characteristics. The gain of the HTS antenna at 77 K was found to be 1.7 dB higher than the gold antenna at room temperature and 0.9 dB higher than the gold antenna at 77 K.

5.7 References

1. I.J. Bahl and P. Bhartia, *Microstrip Antennas*, Artech House, MA, 1980.

2. L.C. Shen, S.A. Long, M.R. Allerding, and M.D. Walton, "Resonant Frequency of a Circular Disc, Printed-Circuit Antenna," *IEEE Trans. Antennas and Propagat.*, vol. AP-27, No. 7, pp. 595-596, July 1977.

3. Weng Cho Chew and Jin Au Kong, "Effects of Fringing Fields on the Capacitance of Circular Microstrip Disk," *IEEE Trans. Microwave Theory Tech.*, vol. MTT-28, no. 1, pp. 98-103, Feb. 1988.

4. Tsuneo Konaka, Makoto Sato, Hidefumi Asano, and Shugo Kubo, "Relative Permittivity and Dielectric Loss Tangent of Substrate Materials for High-Tc Superconducting Film," *J. Superconductivity*, vol. 4, no. 4, pp. 283-288, 1991.

5. Felix A. Miranda, William L. Gordon, Vern O. Heinen, Ben T. Ebihara, and Kul B. Bhasin, "Measurements of Complex Permittivity in the 20 to 300 K Temperature Range from 26.5 to 40.0 GHz," NASA TM #102123, 1989.

6. Anders G. Derneryd, "Analysis of the Microstrip Disc Antenna Element," *IEEE Trans. Antennas and Propagat.*, vol. AP-27, No. 5, pp. 660-663, Sept. 1979.

7. C.M. Chorey, Keon-Shik Kong, K.B. Bhasin, J.D. Warner, and Tatsuo Itoh, "YBCO Superconducting Ring Resonators at Millimeter-wave Frequencies," *IEEE Trans. on Microwave Theory and Tech.*, vol 39, no. 9, pp. 1480-1486, Sept. 1991.

8. William F. Richards, Jai-Dong Ou, and Stuart A. Long, "A Theoretical and Experimental Investigation of Annular, Annular Sector, and Circular Sector Microstrip Antennas," *IEEE Trans. Antennas and Propagat.*, vol. AP-32, no. 8, pp. 864-867, Aug. 1984.

9. J.S. Dahele and K.F. Lee, "Characteristics of Annular-Ring Microstrip Antenna," *Electron. Letters*, vol. 18, no. 24, pp. 1051-1052, Nov. 25 1982.

10. Weng Cho Chew, "A Broad-Band Annular Ring Microstrip Antenna," *IEEE Trans. Antennas and Propagat.*, vol. AP-30, no. 5, pp. 918-922, Sep. 1982.

11. A. Das, S.K. Das, S.P. Mathur, "Radiation characteristics of higher-order modes in microstrip ring antenna," *IEE Proceedings*, vol 131, pt. H, no. 2, pp. 102-106, April 1984.

12. J.D. Warner, K.B. Bhasin, N.J. Varaljay, D.Y. Bohman, and C.M. Chorey, "Growth and Patterning of Laser Ablated Superconducting YBCO Films on $LaAlO_3$ Substrates," NASA TM-102336.

13. Y.S. Wu and F.J. Rosenbaum, "Mode chart for microstrip ring resonators," *IEEE Trans. Microwave Theory and Tech.*, vol. MTT-20, no. 7, pp. 487-489, July 1972.

14. K.F. Lee and J.S. Dahele, "Characteristics of microstrip antennas and some methods of improving frequency agility and bandwidth," *Handbook of Microstrip Antennas*, Ed. by J.R. James and P.S. Hall, Peter Peregrinus Ltd, London, 1989.

15. Daniel H. Schaubert and K. Sigfrid Yngvesson, "Experimental Study of a Microstrip Array on High Permittivity Substrate," *IEEE Trans. Antennas and Propagat.*, vol. AP-34, no. 1, pp. 92-97, Jan. 1986.

16. D.M. Pozar, "Rigorous closed-form expressions for the surface wave loss of printed antennas," *Electron. Lett.*, 1990, vol. 26, no. 13, pp. 954-956.

CHAPTER VI.

ELECTROMAGNETICALLY COUPLED ANTENNA

6.1 INTRODUCTION

In the previous two chapters, two methods for feeding a planar antenna architecture were discussed. Although these antennas had the advantages of simplicity in fabrication and understanding, they suffered from very narrow bandwidths of about 1 %. In this chapter a two layer feeding architecture with a greater bandwidth will be presented. This architecture, known as electromagnetic coupling, consists of a feed line on a lower substrate and a patch antenna on an upper substrate. Because most of the loss in a microstrip array antenna occurs in the feed network, the patch antennas can be printed on a lower permittivity substrate using non-superconducting metallization while the feed network uses HTS on $LaAlO_3$. For this work, three different substrates were used for the patch substrate: Duroid, quartz, and alumina. Both circular and rectangular patches were used. A four element array was also fabricated and tested using an alumina top layer. The performance of these antennas including patterns, input impedance, bandwidth, efficiency and gain are presented. Where possible, these results are compared with results that are expected from

appropriate models. In each case, the results are compared to those of an identical antenna which has the feed network fabricated using a gold metallization instead of HTS.

6.2 Motivation

There are several methods that may be employed to increase the bandwidth of a planar microstrip antenna. One method is to introduce losses in the antenna. This will decrease the Q of the resonant cavity and thus increase the bandwidth since the bandwidth is inversely related to the Q. Clearly, this is not a desirable method of increasing the bandwidth as the efficiency will be lowered.

A second method is to use a lower permittivity substrate. As discussed in Chapter 1, HTS can only be deposited on certain high permittivity substrates. Thus, this method of bandwidth extension is not feasible at this point in time.

A third method is to use a substrate with a greater thickness, h. However, a thicker substrate also causes an increased amount of power to be coupled into surface waves modes. In particular, at 30 GHz on $LaAlO_3$, a substrate thickness greater than 530 μm will cause the TM_1 and TE_1 modes to be generated in addition to the TM_0 mode[1]. A first order approximation of the bandwidth of a microstrip antenna is given by

$$BW(\%) = \frac{4 f_r h}{1.4 c \sqrt{\epsilon_r}} \qquad (6\text{-}1)$$

Thus, at best the bandwidth could be doubled through the use of a substrate with a thickness of 500 μm instead of the 250 μm that was used. Even then, the performance will be deteriorated because of surface wave generation.

When multi-layer antenna architectures are used, a thicker, lower permittivity substrate could be utilized without losing the advantages of using HTS. One such architecture that has been proposed[2] and investigated[3,4,5] is the aperture coupled microstrip antenna shown in Figure 6-1. In this architecture, a feed line on one substrate couples power through an aperture in the ground plane into a cavity formed by the ground plane and microstrip patch on the reverse side. If HTS was to be used in this architecture, it could be used only for the feed network. Thus, only the feed substrate would need to be a high permittivity material while the patch substrate could be a relatively thick, low permittivity substrate such as Duroid. This architecture was not pursued because of experimental difficulties: neither side of the antenna could rest against a metallic test fixture. Resting the feed line side on a test fixture would short the feed line to ground, wile resting the patch side on a test fixture would suppress all radiation. At room temperature, some type of test fixture that would hold only the edges of the substrate could well be utilized. However, when cryogenics

must be employed, this could not be easily accomplished. The problem is further complicated by the small size of the substrates (1 cm x 1 cm) that were used.

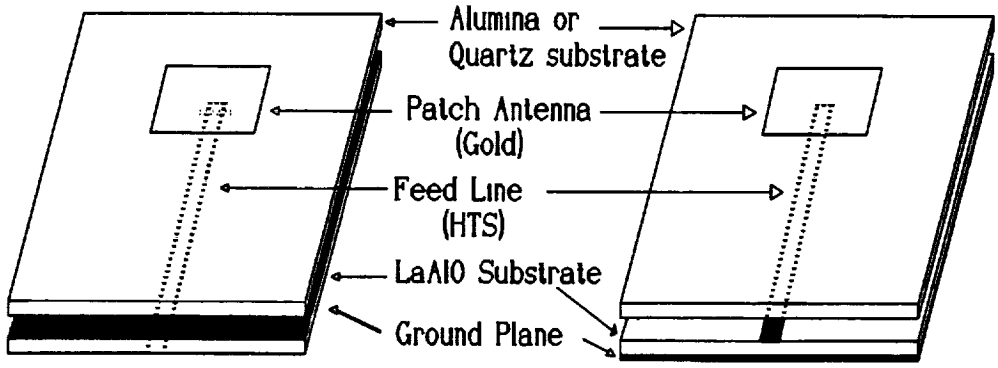

Figure 6-1: Aperture coupled (left) and electromagnetically coupled (right) antennas. The aperture coupled antenna has its ground plane between the two substrates while the electromagnetically coupled antenna has its feed line located there.

A second multi-layer structure utilizes electromagnetic coupling, also known as proximity coupling. This architecture is also shown in Figure 6-1. Like the aperture coupled antenna, this architecture also separates the feed substrate from the patch substrate. However, instead of having the substrate back-to-back with a common ground plane sandwiched between the two, the substrates are stacked on top of each other and the feed line is sandwiched between the two substrates. This method also allows the use of a lower permittivity substrate for the patch, but the patch will see a permittivity that is a composite of both the upper and lower substrates. This method of coupling was selected for experimental investigation because it is quite feasible to implement. Unlike aperture coupling,

this method has the advantage that the ground plane can be placed directly upon a metallic test fixture in the same way that conventional planar antenna can be.

Electromagnetic coupling was first used for microstrip dipole antennas rather than microstrip patch antennas[6]. Compared to the experimental research done on other microstrip antenna architectures, electromagnetic coupling has been investigated very little for use with microstrip patch antennas, although a number of theoretical papers have been published[7,8,9]. The experimental research reported to date has mostly been at frequencies below 5 GHz[10,11].

Two layer architectures which utilize a microstrip patch direct coupled to a transmission line on one substrate and a second patch electromagnetically coupled to the first patch on a second substrate have been researched by various investigators for conventional materials[12,13] and for HTS use[14]. These methods were not considered for this study.

6.3 Single Element Antennas

6.3.1 Design

A single patch electromagnetically coupled antenna using a 254 μm thick $LaAlO_3$ feed substrate (ϵ_r = 23) and a 127 μm thick alumina patch substrate (ϵ_r = 9.9) was first designed. The height of each substrate was kept to a minimum so as to reduce feed line radiation and dielectric height seen by the patch. A circular patch 760 μm in radius was used, as was a rectangular patch with a resonant length of 1200 μm and a width of 1800 μm. The feed line was made 6000 μm long and 100 μm wide. Although this width is the proper value

for a 50 Ω line on 254 μm thick $LaAlO_3$, the impedance of a microstrip line changes when the line is covered by an additional dielectric, as is the case for the electromagnetically coupled antenna. Work by Bahl and Stuchly[15] suggests that an appropriate line width can be calculated from the relation between capacitance and characteristic impedance Z_0 on a TEM line

$$Z_0 = Z/\sqrt{\epsilon_e} \tag{6-2}$$

$$Z = 1/C_0 c \tag{6-3}$$

$$\epsilon_e = C/C_0 \tag{6-4}$$

where ϵ_e is the effective dielectric constant, C and C_0 are the transmission line capacitances with and without the dielectrics,respectively, and c is the speed of light in free space. When the quasi-TEM mode is used, the capacitance is given by

$$\frac{1}{C} = \frac{1}{\pi \epsilon_0} \int_0^\infty \frac{A^2 d(\beta h_2)}{\left[\epsilon_{r1} \dfrac{\epsilon_{r1}\tanh(\beta h_1)+1}{\epsilon_{r1}+\tanh(\beta h_1)+\epsilon_{r2}\coth(\beta h_2)}\right]} \tag{6-5}$$

where

$$A = 1.6\left[\frac{\sin(\beta W/2)}{\beta W/2}\right] + \frac{2.4}{(\beta W/2)^2}\left[\cos(\beta W/2) - \frac{2\sin(\beta W/2)}{(\beta W/2)} + \frac{\sin^2(\beta W/4)}{(\beta W/4)^2}\right]$$

h_1 and h_2 are the thicknesses of the top and bottom dielectric layers, respectively, ϵ_{r1} and ϵ_{r2} are the relative permittivities of the top and bottom layers, and W is the width of the microstrip transmission line metallization.

Using the above relations for the material parameters used in this work, a 100 μm line was found to have a characteristic impedance of 45 Ω while a 50 Ω line was found to require a width of 70 μm. The 70 μm dimension was not used for three reasons. First, the upper dielectric layer could never entirely cover the microstrip transmission line because the excited end of the transmission line must remain uncovered to allow proper a proper connection of the coax-to-microstrip transition connector. Furthermore, the amount of transmission line left uncovered varies as the position of the patch over the transmission line is changed. Because the impedance of the transmission line changes at the point where the dielectric cover over the line begins, an impedance mismatch will occur regardless of whether the line width is 100 μm or 70 μm. Secondly, the center pin of the Wiltron K-connector which was used for input has a diameter of 300 μm. A line width which more closely matches the diameter of this pin creates a better electrical transition between the coax and microstrip. Finally, the use of the line width matched to the upper substrate layer would necessitate the use of a different width transmission line for each of the three upper substrates materials used. For these reasons, the wider line width was employed.

In addition to the alumina patch substrate, a 127 μm thick quartz substrate (ϵ_r = 3.8) and a 127 μm thick Duroid substrate (ϵ_r = 2.2) were used. With the

quartz substrate, a circular patch with a radius of 980 μm, and two rectangular patch with dimensions of L = 1680 μm, W = 2520 μm and L = 1680, W = 2100 μm were used. On the Duroid substrate only a circular patch with a radius of 1210 μm was used. These dimensions are summarized in Table 1.

Table 6-1: EM Coupled Patch Parameters

Substrate	Duroid	Quartz	Alumina
Permittivity	ϵ_r = 2.2	ϵ_r = 3.8	ϵ_r = 9.9
Radius (Circular)	1210 μm	980 μm	760 μm
Size (Rectangular)		1680x2520 1680x2100	1200x1800
Metallization	17 μm Cu	1.5 μm Au	1.5 μm Au

The patches were fabricated on the individual substrate materials using a normal metal. The quartz and alumina substrates used 12 nm of chrome for adhesion, followed by 1.5 μm of gold while the Duroid substrate used 17 μm thick copper. Both gold and HTS feed lines were fabricated. The quartz and alumina circular patches were tested using both feed lines, while the Duroid patch was tested only at room temperature. The rectangular patches were tested only with gold feed lines, but were tested at both cryogenic and room temperatures. The HTS films used for this portion of the work were deposited using an off-axis sputtering technique and were obtained commercially. The films had transition temperatures (T_c) of 89 K.

For an electromagnetically coupled antenna with the dimensions given in Table 1, it is important to that the patch be positioned accurately over the end of the feed line, and be held there tightly so that no movement of one substrate with respect to the other can occur. Thus, some type of material was needed to hold the two layers together. The holding compound, though, had to satisfy the following criteria. First, the material could not be conductive, since this would short the transmission line. Secondly, no material which is acidic or requires high temperature curing could be used. Either of these conditions would result in a degraded or destroyed HTS film. The material needed to be spread as a thin film so that maximum coupling between the feed line and patch antenna could occur. A minimal volume expansion coefficient was necessary so that very little contraction would occur as the antenna was cooled to cryogenic temperatures. Such changes could result in a cracked substrate. Finally, a compound which is removable was desired so that the circuits could be reassembled several times for further testing. A non-removable compound would necessitate the fabrication of new circuits for every test.

Fingernail polish was found to meet all of the above criteria. It established a firm bond between the layers that could be removed in acetone, was non-conductive, cured at room temperature, and did not harm the HTS thin film. Although the antennas tended to show some change in performance with decreasing temperature, the effects were reversible. That is, a gold antenna showed the same performance at room temperature before and after a cryogenic

cycle. As will be discussed in Section 6.3.2, it is important to note that the holding compound is not the sole source of such changes. The difference in volume expansion coefficients of the two layers could also contribute to this effect.

6.3.2 Resonant Frequency

The resonant frequency of an electromagnetically coupled microstrip patch has previously been found to be a function of the position of the patch relative to the feed line[6,9]. Thus, the resonant frequencies of the gold antennas were measured as a function of patch position. The measured resonant frequencies for the gold circular patches are shown in Figures 6-3 and 6-4 while those of the rectangular patches are shown in Figures 6-5 and 6-6. Figures 6-3 and 6-5 show frequency as a function of the patch overlap in the y-direction while Figures 6-4 and 6 show frequency as a function of patch overlap in the x-direction. In these plots, the quartz rectangular patch with the larger width is referred to as "Quartz 1" while the quartz rectangular patch with the smaller width is referred to as "Quartz 2". Directions and overlap are defined in Figure 6-2.

The measured data in the y-direction shows the resonant frequency increasing as the amount of feed line covered by the patch increases. This is consistent with results from a method of moments analysis as reported by Splitt and Davidovitz[9], and with measured data at lower frequencies on PTFE reported by Roy *et. al.*[11] In the x-direction, the frequency also increases as the feed is moved towards the center of the patch. As one would expect, the resonant

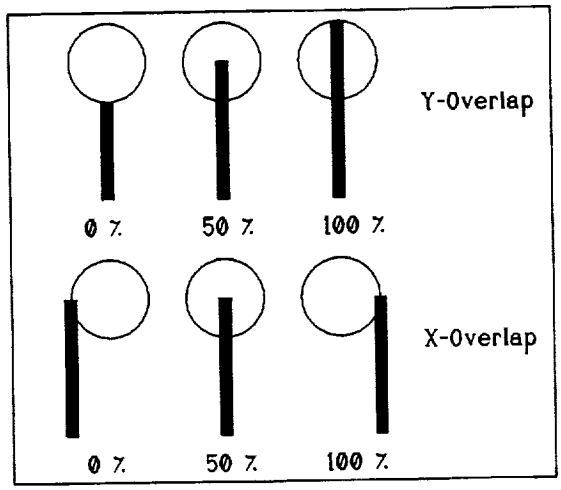

Figure 6-2: Definition of directions and overlap for the circular patches. The same definition applies for the rectangular patches with the resonant dimension in the y-direction.

frequency curve is symmetric around the center (y-axis). In either case, the frequency change is due to a perturbation of the field under the patch as a result of the presence of the feed line. The measured data for the circular patch on the alumina substrate shows a substantial amount of scatter. This is due to errors in accurately positioning the patch over the end of the feed line. Because the alumina patch is quite small, small deviations from proper position translate into a relatively large error in the percentage of overlap. To estimate the frequency of the two layer patch antennas analytically, the two dielectric layers were treated as a single dielectric layer with an equivalent permittivity, ϵ_{eq}. This equivalent permittivity was found using a static capacitor model based upon the relative permittivity and thickness of each layer,

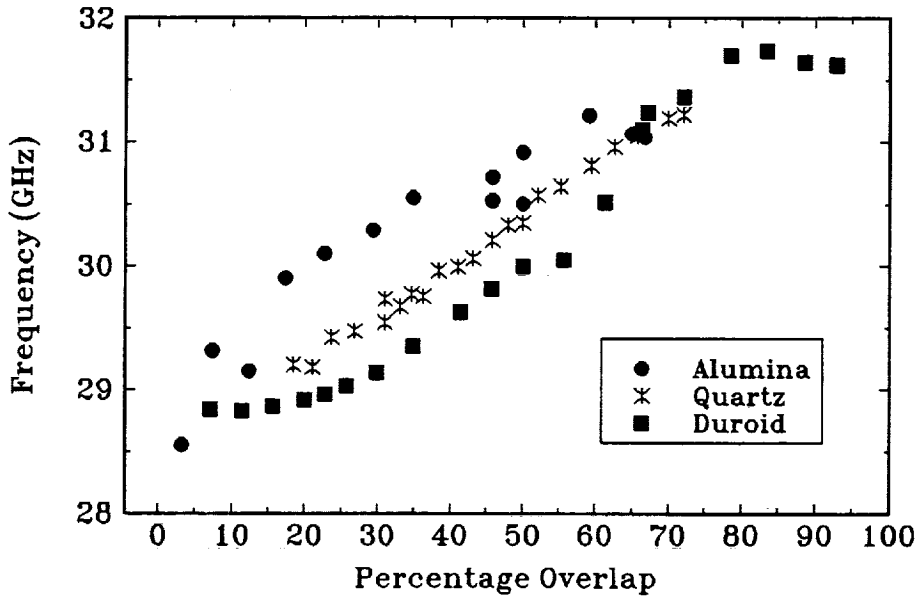

Figure 6-3: Resonant frequency of circular EM coupled patches as a function of patch position over the feedline in the y-direction.

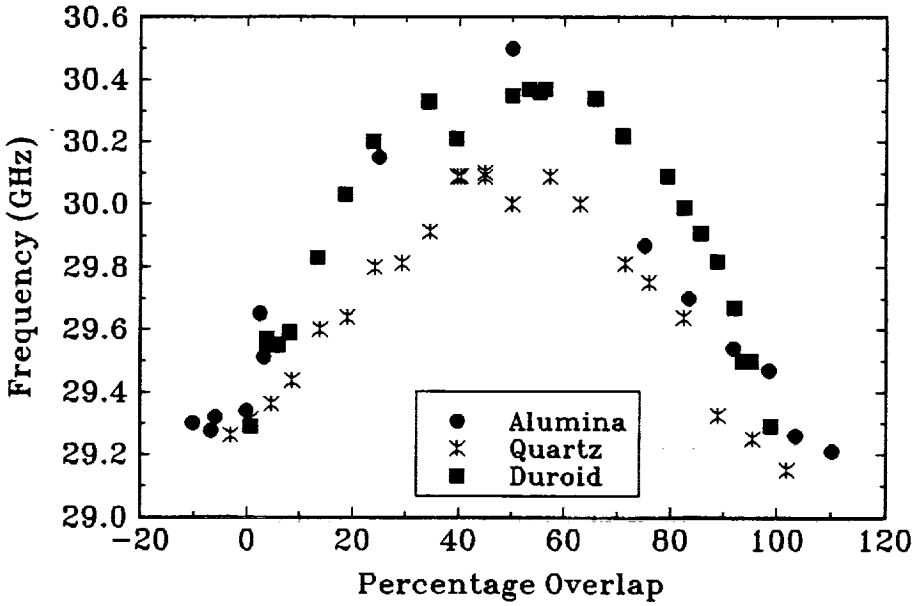

Figure 6-4: Resonant frequency of circular EM coupled patches as a function of patch position over the feedline in the x-direction.

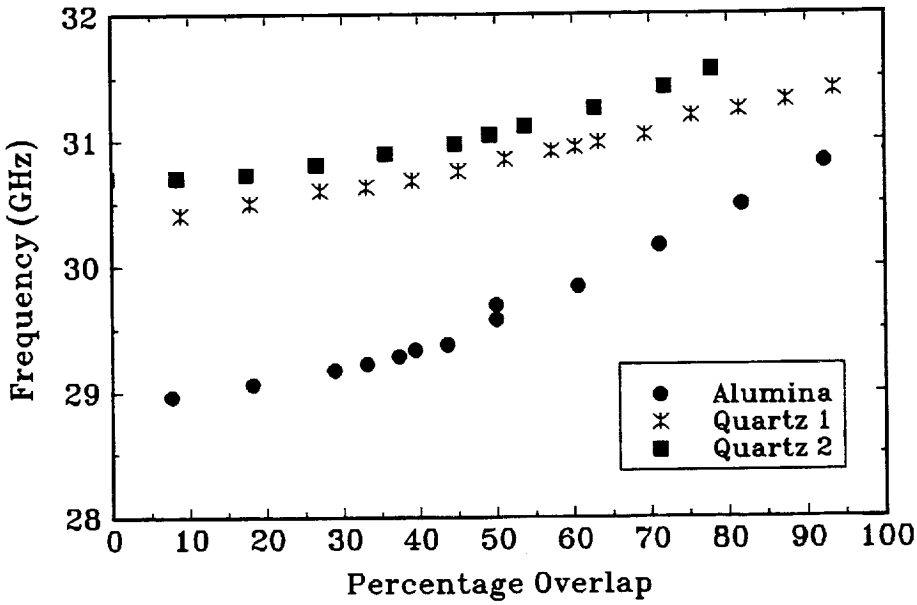

Figure 6-5: Resonant frequency of the rectangular EM coupled patches as a function of patch position over the feedline in the y-direction.

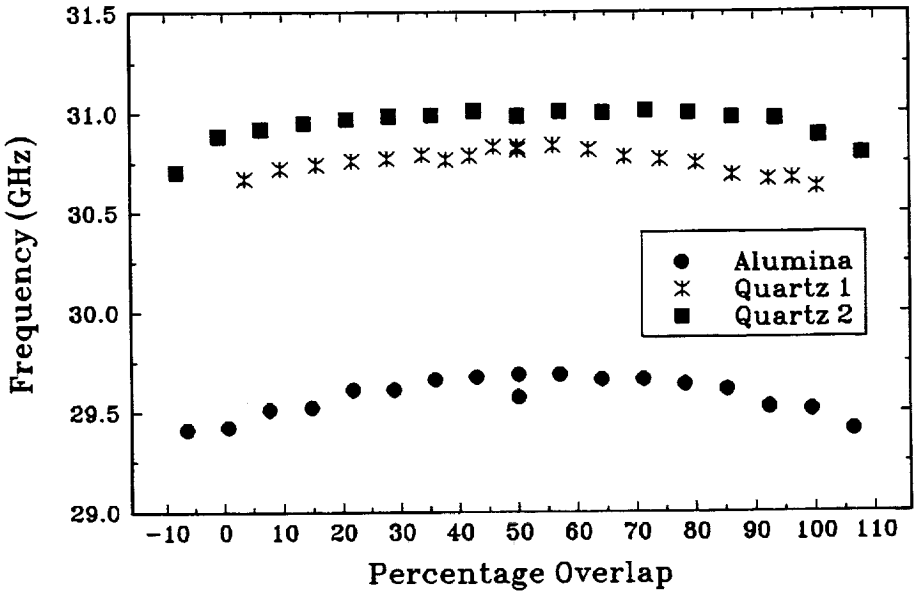

Figure 6-6: Resonant frequency of the rectangular EM coupled patches as a function of patch position over the feedline in the x-direction.

$$\epsilon_{eq} = \frac{3\epsilon_1\epsilon_2}{2\epsilon_1+\epsilon_2} \tag{6-7}$$

where ϵ_1 is the permittivity of the upper, patch substrate, and ϵ_1 is the permittivity of the lower, $LaAlO_3$, feed substrate. This model gives an equivalent permittivity of 5.5 for Duroid, 8.6 for quartz, and 16.0 for $LaAlO_3$. The resonant frequency of the patches is then found from cavity model expressions as given in Chapter 4 and 5 and repeated here. For rectangular patches,

$$f_r = \frac{c}{2(L+h/2)\sqrt{\epsilon_{eq}}} \tag{6-8}$$

while the resonant frequency of the circular patches were found from

$$f_r = \frac{1.841c}{2\pi a_e \sqrt{\epsilon_{eq}}} \tag{6-9}$$

where

$$a_e = a\left[1+\frac{2h}{\pi a\epsilon_{eq}}\left(\ln\frac{a}{2h} + 1.41\epsilon_{eq} + 1.77 + \frac{h}{a}(.268\epsilon_{eq}+1.65)\right)\right]^{1/2} \tag{6-10}$$

Using these models gave results which deviated from measured frequencies by as much as 23 %. This in not entirely unexpected. The cavity model assumes an electric field which is invariant in the z-direction. Clearly this condition does not hold true when two different dielectrics fill the cavity. The analytical results were found to be substantially closer to the measured values when no compensation (effective dimensions) for the fringing fields were used. These results are

summarized in Table 2. In this table, the measured values shown are those when the patch is centered over the end of the feed line (50 % overlap). It is important to note that a small air gap between the layers can also substantially change the effective permittivity seen by the patch radiators. In such a case, the effective permittivity seen by the three layer system is given by

$$\epsilon_{eq} = \frac{h\epsilon_1\epsilon_2\epsilon_3}{h_1\epsilon_2\epsilon_3 + h_2\epsilon_1\epsilon_3 + h_3\epsilon_1\epsilon_2} \qquad \textbf{(6-11)}$$

where h is the total dielectric height, h_1, h_2, and h_3 are the heights of the feed substrate, air gap, and patch substrates, respectively, and ϵ_1, ϵ_2, and ϵ_3 are the permittivities of the feed substrate, air gap, and patch substrates, respectively. If an air gap of 2 μm exists, the effective permittivity when an alumina patch substrate is used decreases from 16.0 to 14.8.

Table 6-2: Measured & Calculated Resonant Frequencies

Patch	$f_{meas.}$	$f_{calc.}$ Fringing	$f_{calc.}$ No Fring.
Rect. Alumina	29.63	27.34	30.45
Rect. Quartz 1	30.82	26.96	31.25
Rect. Quartz 2	31.04	26.96	31.25
Circular Alumina	30.70	23.73	28.91
Circular Quartz	30.00	25.78	30.59
Circular Duroid	30.35	26.52	30.98

The resonant frequency performance of the alumina and quartz based circular and rectangular patch antennas at cryogenic temperatures is shown in Figure 6-7. The Duroid patch could not be used at low temperatures because it could not be held flat over the feed substrate at low temperatures as the substrate tends to curl. The performance of the antennas using an HTS feed line was investigated only for the circular patches.

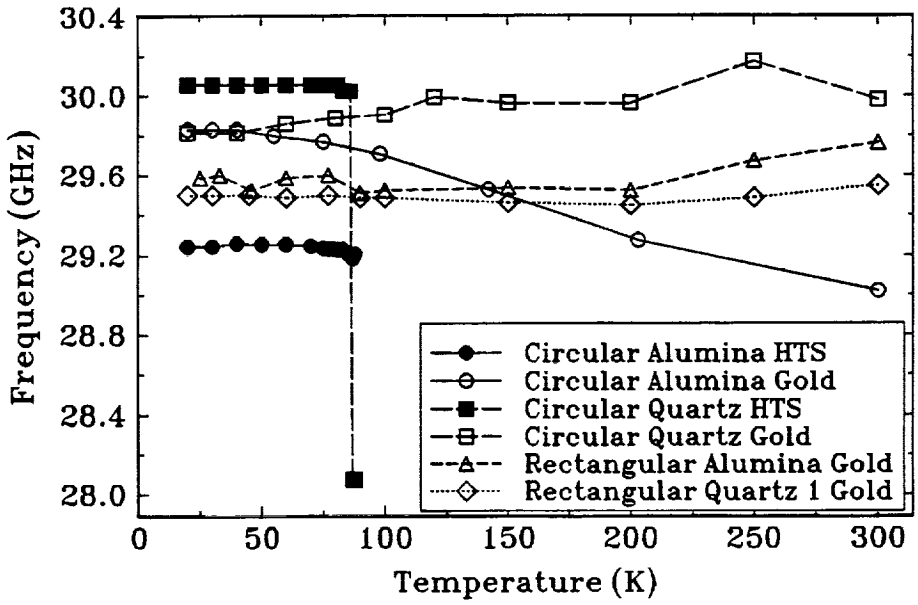

Figure 6-7: Resonant frequency of the EM coupled patches as a function of temperature. Data using circular patches with HTS feed lines are also shown.

Most of the resonant frequency curves of the gold antennas in Figure 6-7 are relatively flat with respect to temperature. The exception is the circular alumina patch, which changes by almost 3 %. This amount of change cannot be attributed to the change in permittivity of $LaAlO_3$ with temperature. Using Eqn. (6-9), a change of 11 % in the permittivity of $LaAlO_3$ would be required,

where as published reports[16] have shown a change of only 2 % over this temperature range. The shift in resonant frequency is more likely due to small shifts in the position of the two substrates relative to each other, which occur as a result of contraction with cooling. The antennas with HTS feed lines are also quite flat and show only a very small change in frequency at temperatures around T_c, unlike the direct and gap coupled antennas. This is because only the feed line, not the resonator (patch), is made from HTS.

6.3.3 Antenna Patterns

The E- and H-plane patterns of the alumina rectangular patch and of the three (alumina, quartz, and duroid) circular electromagnetically coupled patches were measured are shown in Figures 6-8 through 6-11. The expected radiated field patterns can be evaluated from the fields under each patch and have been given in Chapter 4 for the rectangular patch, and in Chapter 5 for the circular patch. The H-plane data shows good agreement with the cavity model and no substantial differences are seen between the H-plane patterns of the various antennas; all show similar deviations from the predicted curves. In each case, the cross polarization is at quite low levels of at least 10 dB below the peak. As demonstrated by other researchers[17] and shown in the case of the direct and gap coupled antennas, dramatic deviations from the model occur in the E-plane. The electromagnetically coupled antenna is no exception and the E plane patterns showed scallops in the patterns even for the antenna using the low permittivity Duroid as its top dielectric layer.

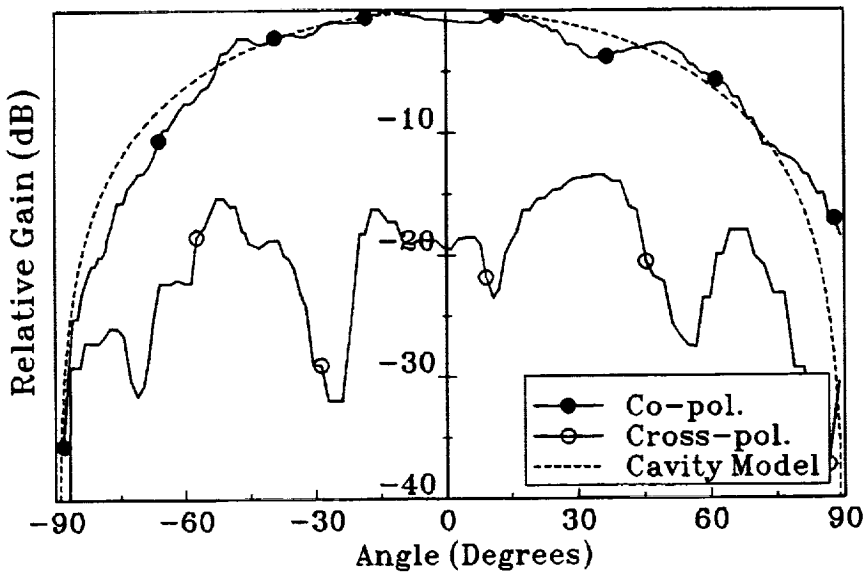

Figure 6-8: H-plane patterns of the EM coupled circular patch on alumina. Co- and cross polarization data is shown along with the pattern predicted by the cavity model.

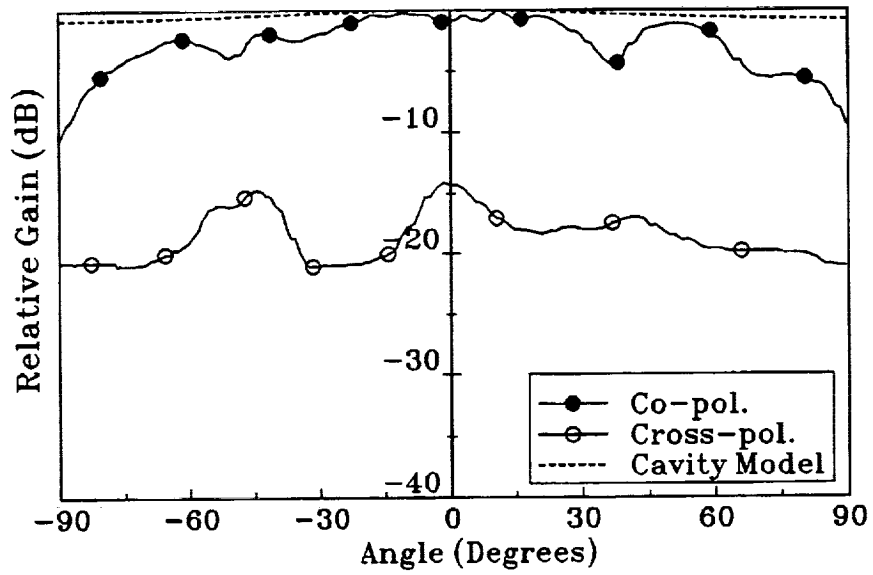

Figure 6-9: E-plane patterns of the EM coupled circular patch on alumina. Co- and cross-polarization data is shown along with the pattern predicted by the cavity model.

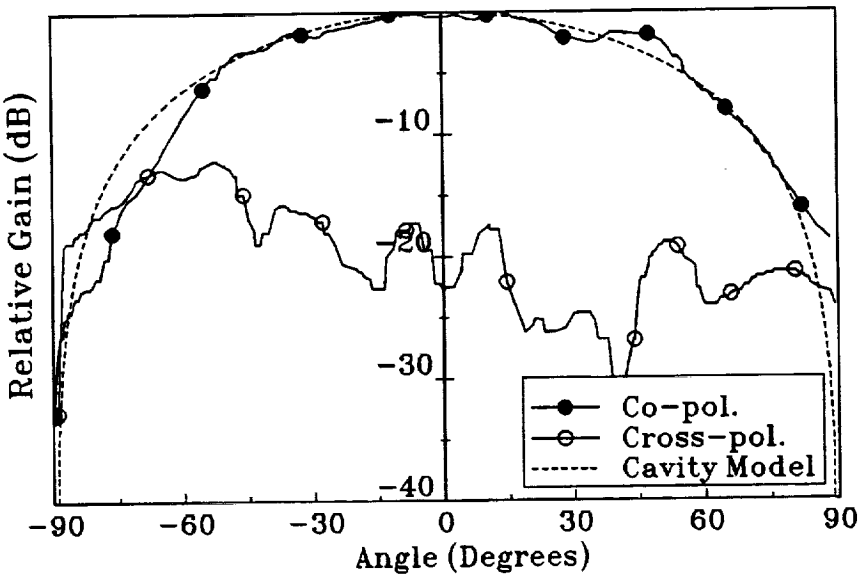

Figure 6-10: H-plane patterns of the EM coupled circular patch on quartz. Co- and cross polarization data is shown along with the pattern predicted by the cavity model.

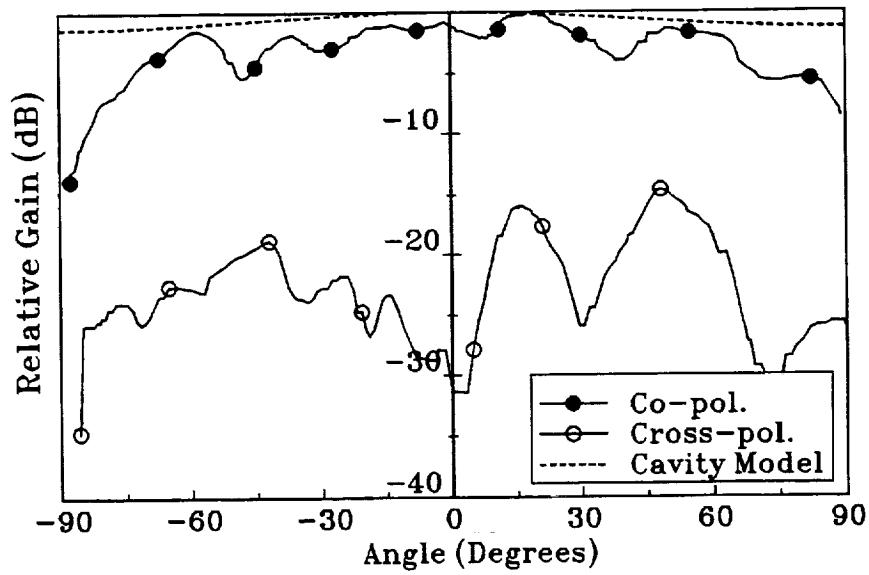

Figure 6-11: E-plane patterns of the EM coupled circular patch on quartz. Co- and cross polarization data is shown along with the pattern predicted by the cavity model.

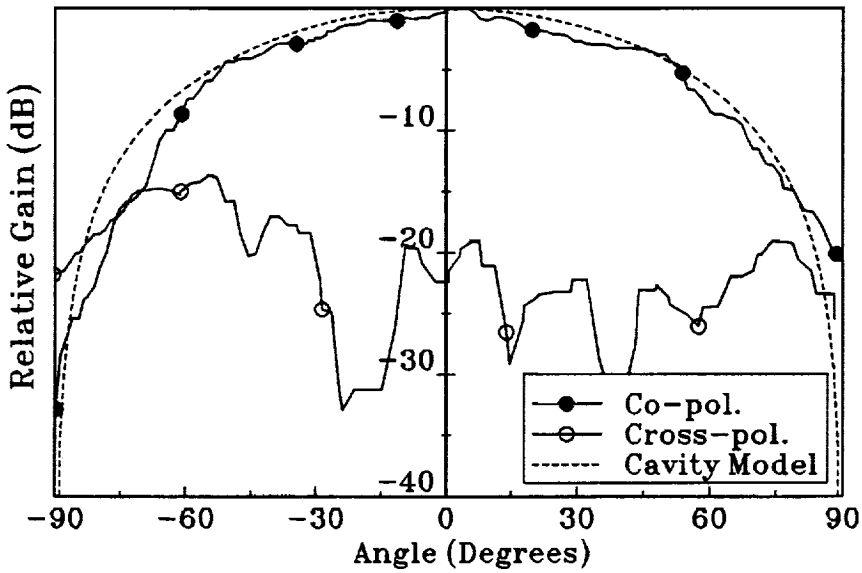

Figure 6-12: H-plane patterns of the EM coupled circular patch on Duroid. Co- and cross polarization data is shown along with the pattern predicted by the cavity model.

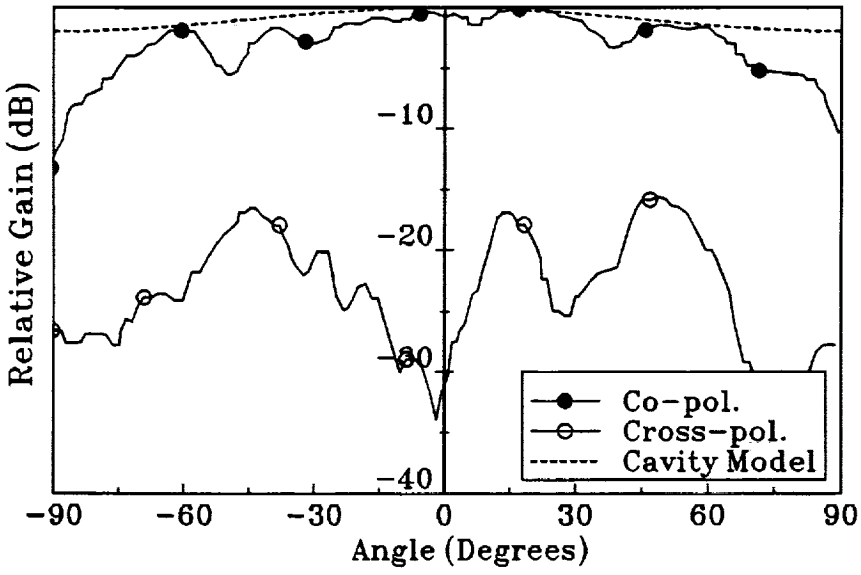

Figure 6-13: E-plane patterns of the EM coupled circular patch on Duroid. Co- and cross polarization data is shown along with the pattern predicted by the cavity model.

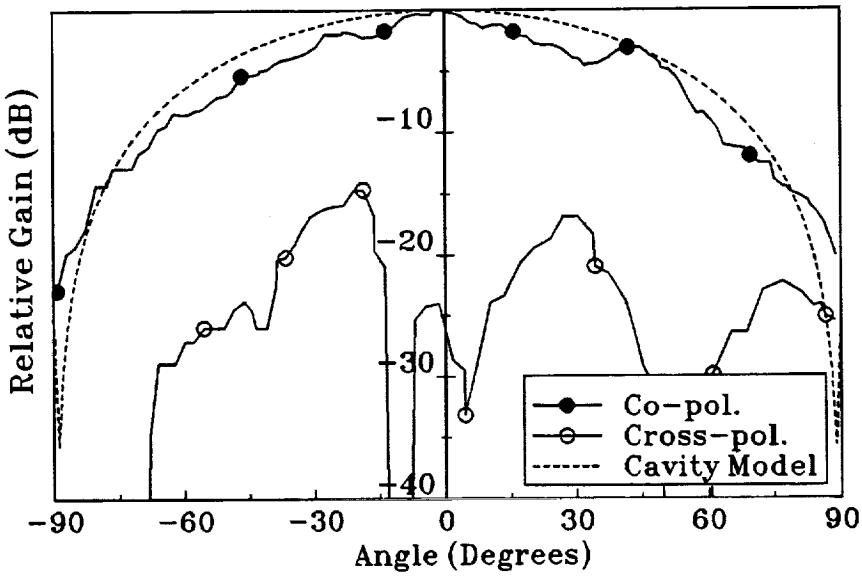

Figure 6-14: H-plane patterns of the EM coupled rectangular patch on alumina. Co- and cross polarization data is shown along with the pattern predicted by the cavity model.

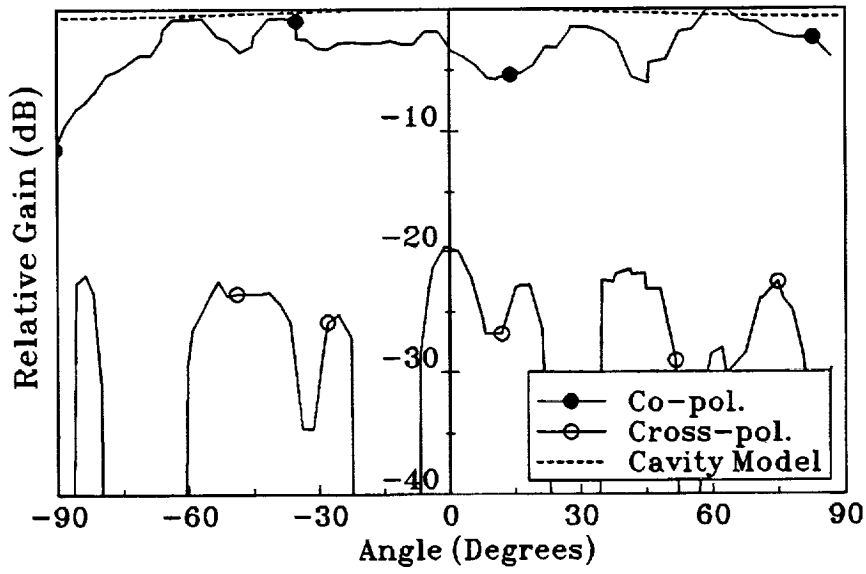

Figure 6-15: E-plane patterns of the EM coupled rectangular patch on alumina. Co- and cross polarization data is shown along with the pattern predicted by the cavity model.

6.3.4 Input Impedance

The input impedance of an electromagnetically coupled patch is a function of the patch position relative to the feed line. The cavity formed by the patch, ground plane, and magnetic walls is excited by the feed line, which functions as a probe. Thus, the coupling of the patch to the feed line can be adjusted to its optimum value by changing their relative position. The measured VSWR data for the circular patches are shown in Figures 6-16 and 6-17 as a function of patch position in x and y directions, respectively, while Figures 6-18 and 6-19 show the same for the rectangular patches.

Although at first glance the VSWR plots for the circular patches may appear to be randomly scattered, a closer inspection reveals the following definite trends. First, as the patch is moved from no overlap towards increased overlap, the VSWR increases from a high value towards 1.0. In this region, the patch is undercoupled, and increasing the amount of overlap increases the coupling coefficient. At some point around 5 to 20 % overlap, perfect coupling is achieved so that the VSWR is nearly unity. As the amount of overlap increases, the patch is overcoupled (coupling coefficient greater than 1.0) and thus the VSWR increases. As the overlap is moved past 50 to 60 %, the coupling begins to decrease again, until critical coupling is achieved and the VSWR goes to unity. Past this point, the patch is once again undercoupled and the VSWR begins to increase. In the case of x-direction movement, curves are symmetrical around the 50 % overlap position. This is to be expected since the field and current

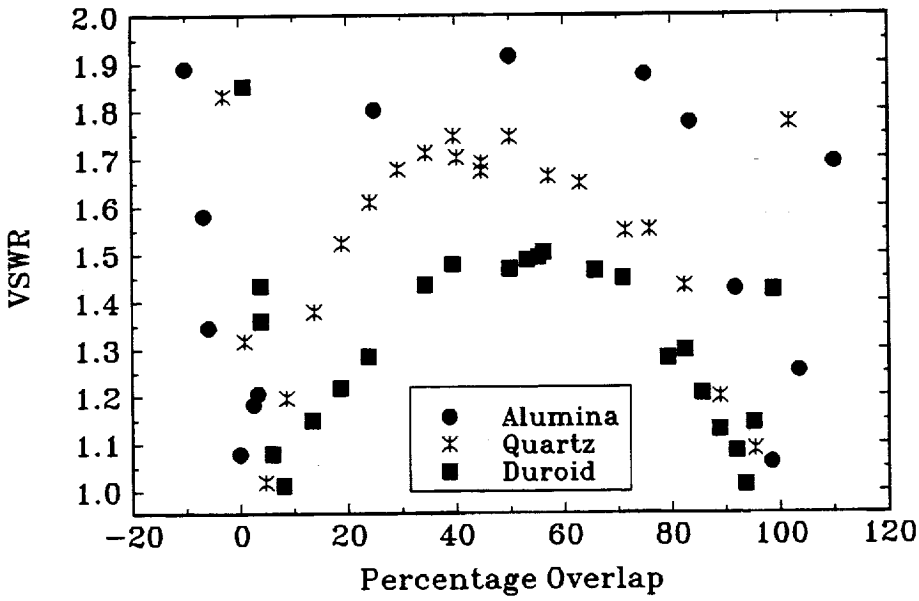

Figure 6-16: Measured VSWR as a function of patch movement in the x-direction for the circular patches.

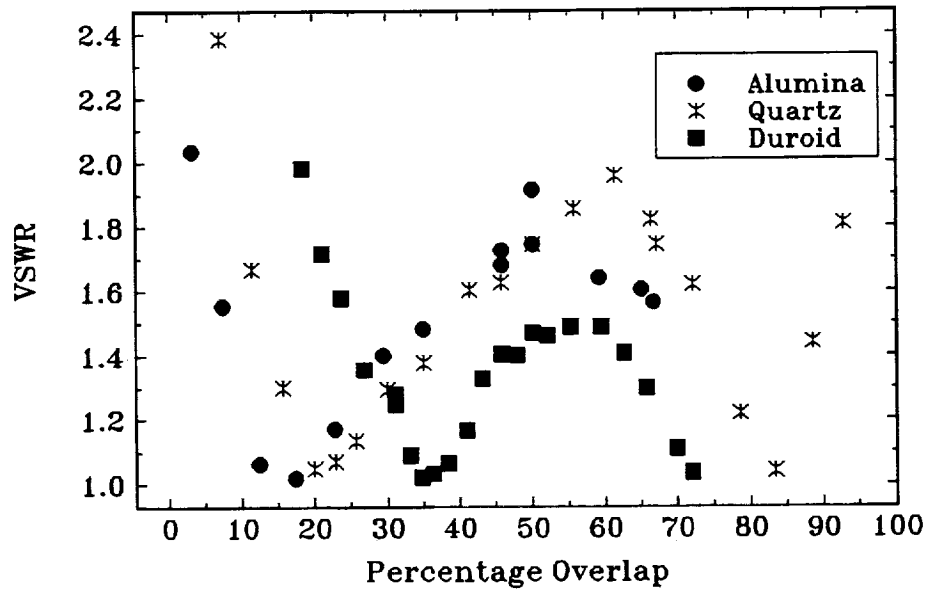

Figure 6-17: Measured VSWR as a function of patch movement in the y-direction for the circular patches.

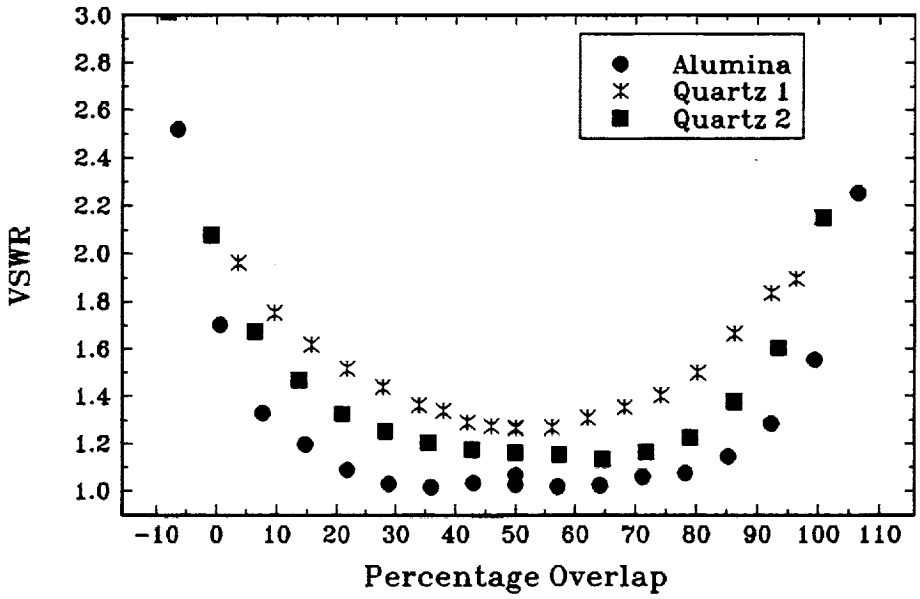

Figure 6-18: Measured VSWR as a function of patch movement in the x-direction for the rectangular patches.

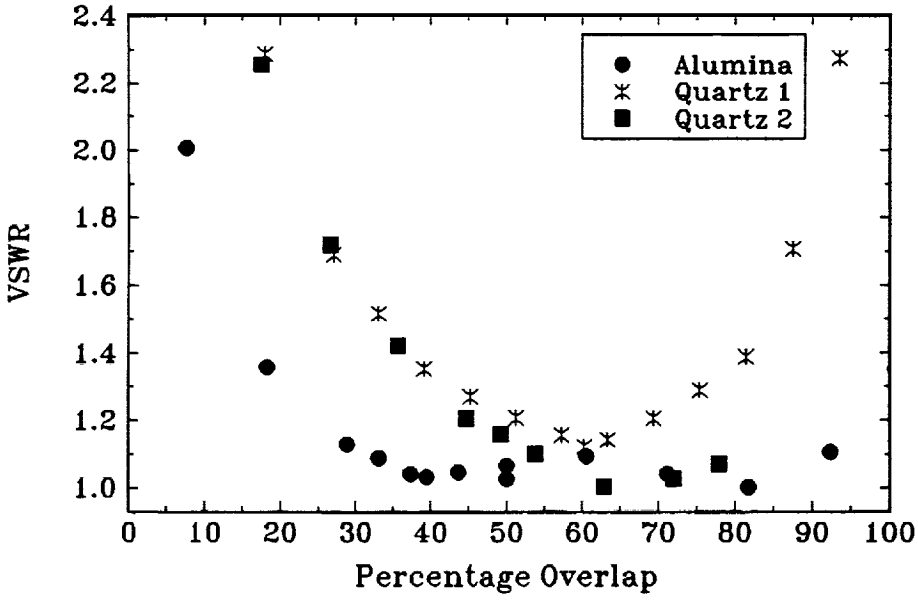

Figure 6-19: Measured VSWR as a function of patch movement in the y-direction for the rectangular patches.

distribution in the patch is symmetric about this axis. In the y-direction, maximum (over) coupling is achieved at around 60 %., meaning that slightly more than half of the patch must rest over the feed line to achieve maximum coupling.

A second trend that is apparent in the VSWR plots of the circular patches is in regards to the patch layer substrate material. It may be seen in Figure 6-16 that the alumina patch shows the highest VSWR's while the Duroid patch shows the lowest. This can be explained by the sizes of the three circular patches used. Because alumina has the highest permittivity, the patch fabricated on alumina has the smallest size at r = 760 μm. The patch on Duroid is the largest at r = 1210 μm because of the low permittivity of Duroid. For a given frequency, greater coupling can occur into a smaller cavity volume. The data in Figure 6-16 shows this effect distinctly, with the alumina patch showing maximum coupling and a VSWR of 1.9 at 50 %, the quartz with a VSWR of 1.75, and the patch on Duroid with a VSWR of 1.5. This effect is also seen in Figure 6-17, though not quite as clearly. In Figure 6-17, the alumina and Duroid data end at 70 % overlap. This is because the size of the substrates and test fixture used for this experiment prevented further movement in that direction.

In the VSWR plots of the rectangular patch antennas the over coupling is not apparent. In the case of the patch on alumina, Figure 6-18 shows the VSWR decreasing as the overlap increases and then increases slightly as the 50 % position is approached. The plot is symmetrical about the 50 % position. The patch on quartz with the larger width, labeled as Quartz 1, never dips below a

VSWR of 1.2 in this figure, while the patch with the smaller width, Quartz 2, does slightly better. Once again, the effect of the patch size is evident. In Figure 6-19 the VSWR's dip slightly lower with maximum coupling occurring at around 60% overlap. Thus, regardless of the patch shape, two points are evident:

1). The VSWR of an electromagnetically coupled antenna may be adjusted to the desired value by shifting the position of the patch relative to the feed line.

2). Any VSWR level may be obtained as long as the physical area of the patch is not too large.

The measured return loss performance of the rectangular patches using gold feed lines is shown in Figure 6-20, while the performance of the circular patch on alumina is shown in Figure 6-21 using both an HTS and gold feed line. The return loss performance of the electromagnetically coupled antenna as a function of temperature is rather unpredictable. For some antennas, a large change in frequency and return loss was noted, but this was not always true. The same return loss characteristics were obtained for repeated thermal cycling of each individual antenna. However, once the antenna was disassembled and reassembled, the characteristics changed substantially. This is because the position of the patch relative to the feed line changed when reassembled, both horizontally (x and y directions) and vertically.

Oltman and Huebner[6] noted that coupling occurs in a 3-dimensional ellipsoidal region around the end of the feed line and were able to demonstrate

sufficient coupling in microstrip dipoles even when separated from the feed substrate by an air gap. The use of an air gap did not succeed in this research. Gap sizes as small as 125 μm did not produce any detectable power coupling into the patch. This is due to the high permittivity of the feed substrate which tends to contain field lines very well, thus preventing significant coupling of the patch when separated from the feed line by an air gap.

6.3.5 Bandwidth and Q

The bandwidth of an electromagnetically coupled antenna is dependent upon the position of the feed line relative to the patch. Bandwidths of between 1.6 % and 4.9 % were measured. Figures 6-22 and 6-23 show the measured bandwidths of the circular patches as a function of patch position in the x and y directions, respectively, while Figures 6-24 and 6-25 show the bandwidth of two rectangular patches on quartz in the x and y directions, respectively. In general, the bandwidth curves of Figures 6-22 through 6-25 show the highest bandwidth in the areas of maximum coupling. No significant differences in bandwidth performance were noted between the antennas with the various patch substrates.

At cryogenic temperatures the antennas showed similar bandwidth performance. The circular patch on alumina using a gold feed line showed bandwidths of 1.65 % at room temperature and 1.91 % at 75 K while the same patch with an HTS feed line showed a bandwidth of 1.84 % at 77 K. The rectangular patch on quartz had a bandwidth of 4.35 % at room temperature and

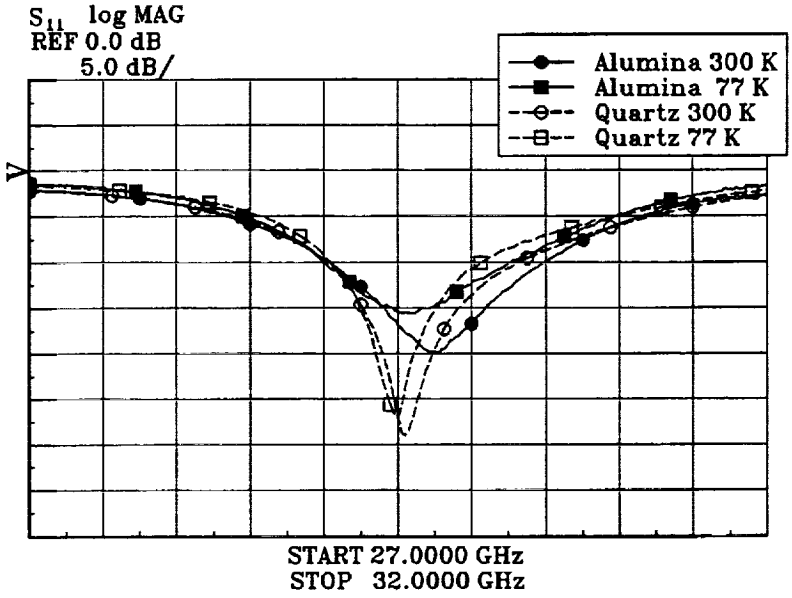

Figure 6-20: Return loss characteristics as a function of temperature for the rectangular electromagnetically coupled antennas using a gold feed line.

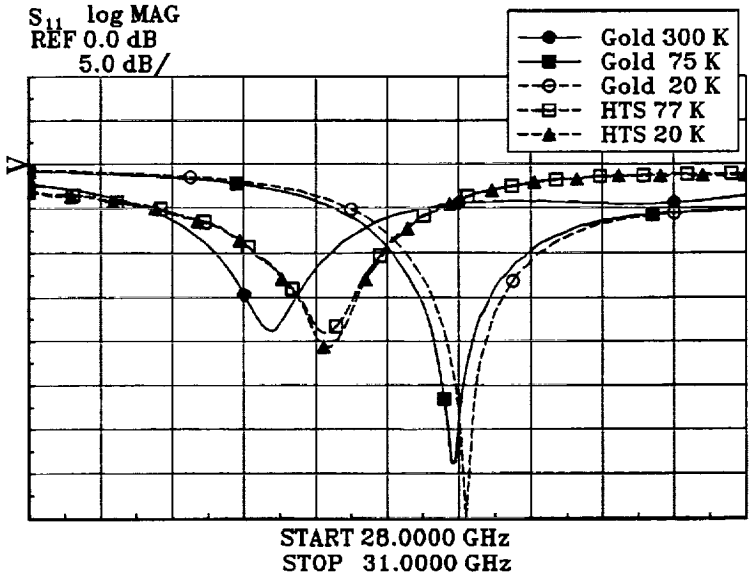

Figure 6-21: Return loss characteristics as a function of temperature for the circular electromagnetically coupled antennas with an alumina patch substrate using gold and HTS feed lines.

3.45 % at 77 K, while the rectangular patch on alumina had a bandwidth of 4.9 % at room temperature and 4.25 % at 77 K.

Analytically, the bandwidths can be calculated from the expressions given in Chapter 4 for the rectangular patches, and in Chapter 5 for the circular patches. The dielectric and conductor losses were assumed to be negligible in these calculations. The model for the circular patches gave values of 1.0 %, 1.5 %, and 2.2 % for the patches on alumina, quartz, and Duroid, respectively. For the rectangular patches, the model gave bandwidths of 2.2 % for the patch on alumina, 2.3 % for the wider patch on quartz (Quartz 1), and 2.1 % for the narrower patch on quartz (Quartz 2).

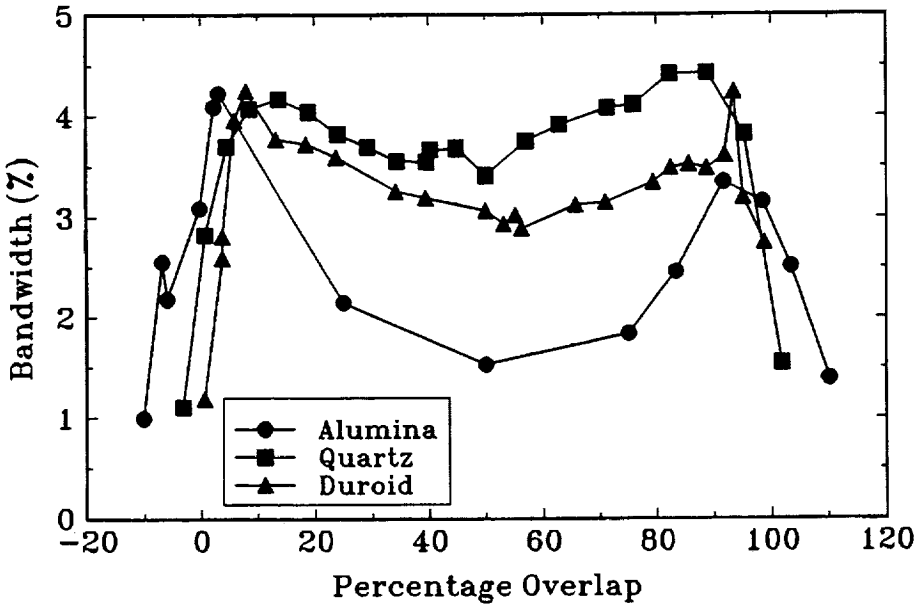

Figure 6-22: Measured bandwidths of the electromagnetically coupled circular patches as the patch position is varied in the x-direction.

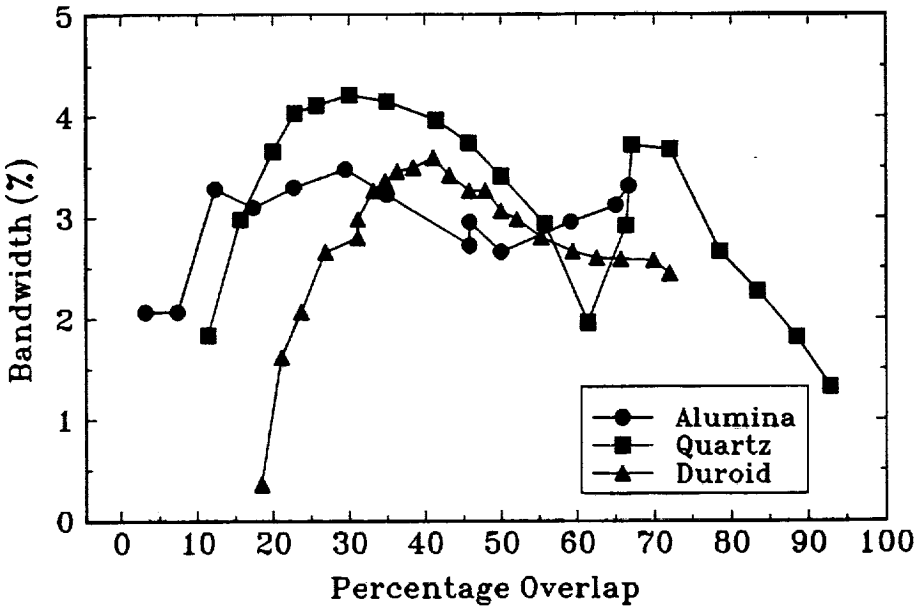

Figure 6-23: Measured bandwidths of the electromagnetically coupled circular patches as the patch position is varied in the y direction.

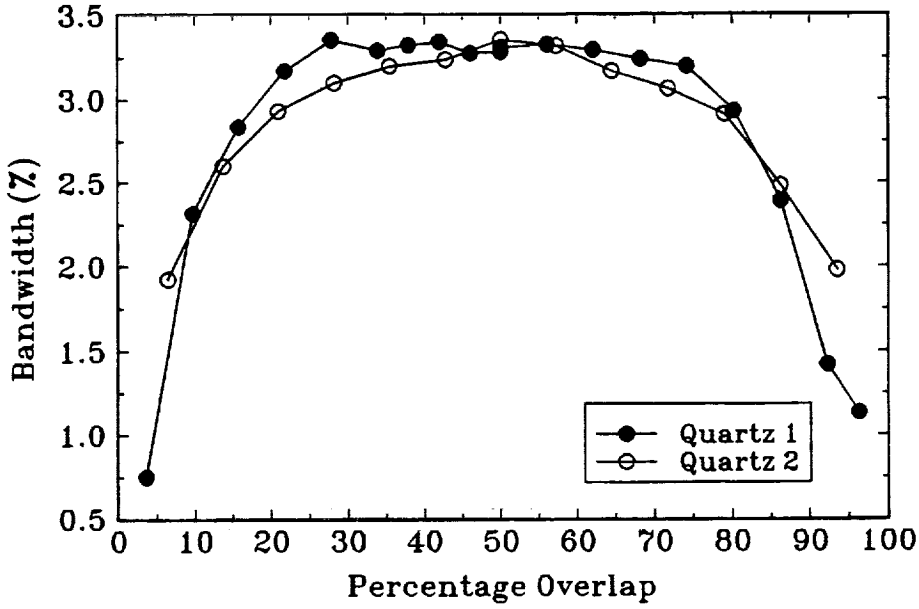

Figure 6-24: Measured bandwidths of the electromagnetically coupled rectangular patches as the patch position is varied in the x-direction.

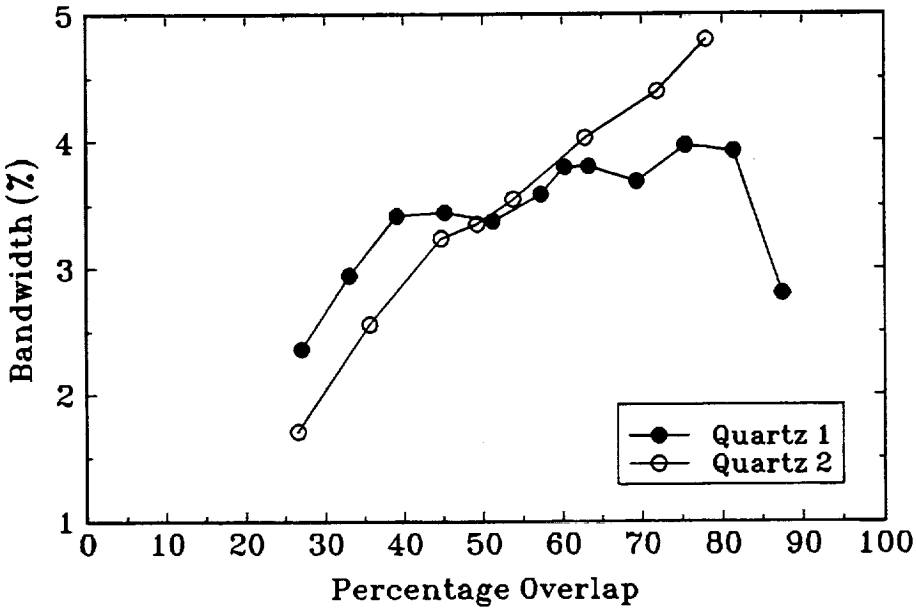

Figure 6-25: Measured bandwidths of the electromagnetically coupled rectangular patches as the patch position is varied in the y direction.

6.3.6 Efficiency

The efficiencies of several of the electromagnetically coupled patches were measured using the Wheeler Cap method as described in Chapter 3. Of the circular patches, the quartz and alumina based patches were measured with both gold and HTS feed lines, while the alumina and quartz based rectangular patches were measured with a gold feed line. The measured efficiencies of these antennas are shown in Figures 6-26 through 6-28. Each antenna with an HTS feed demonstrated a few percent increase in efficiency over its equivalent circuit fabricated with a gold feed. The patches on quartz were found to have a 5 % improvement in efficiency over the patches on alumina. To model the efficiency of the gold antenna, the power dissipated in the conductors, dielectric, and

radiation were calculated from the equations given in Chapter 4 for the rectangular patches and Chapter 5 for the circular patches. The attenuation in the gold microstrip transmission line was calculated from Pucel's equations as given in Chapter 2, while attenuation in the HTS transmission line was calculated based upon data reported by Chorey, *et. al.*[18]. In each case, the modeled curves exhibit efficiencies that are higher than the measured curves due to shortcomings in the models and losses that are unaccounted for in the models.

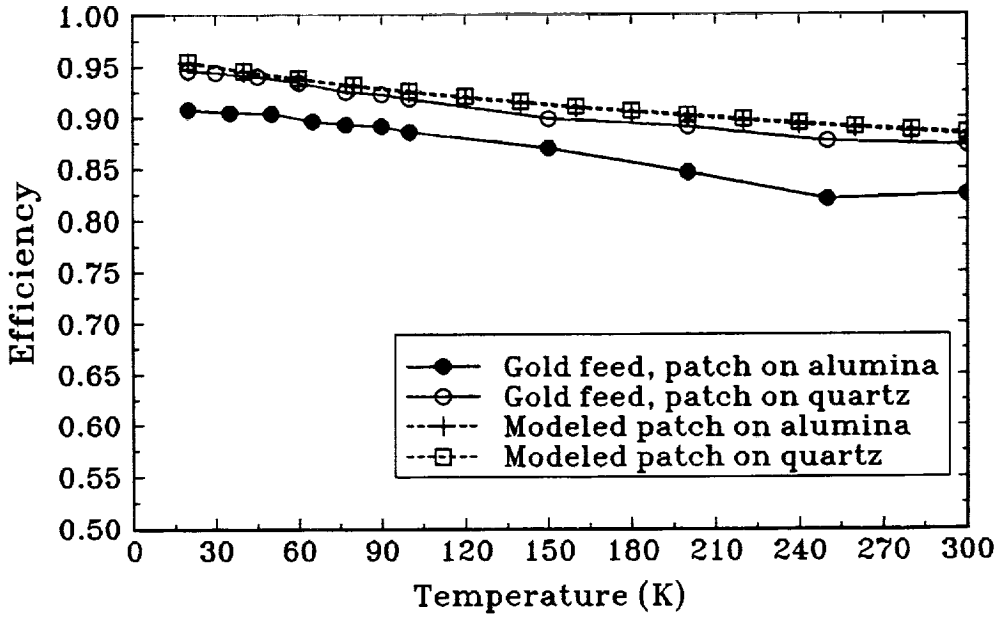

Figure 6-26: Measured efficiencies of the rectangular electromagnetically coupled patches using gold feed lines. Also shown are modeled efficiencies.

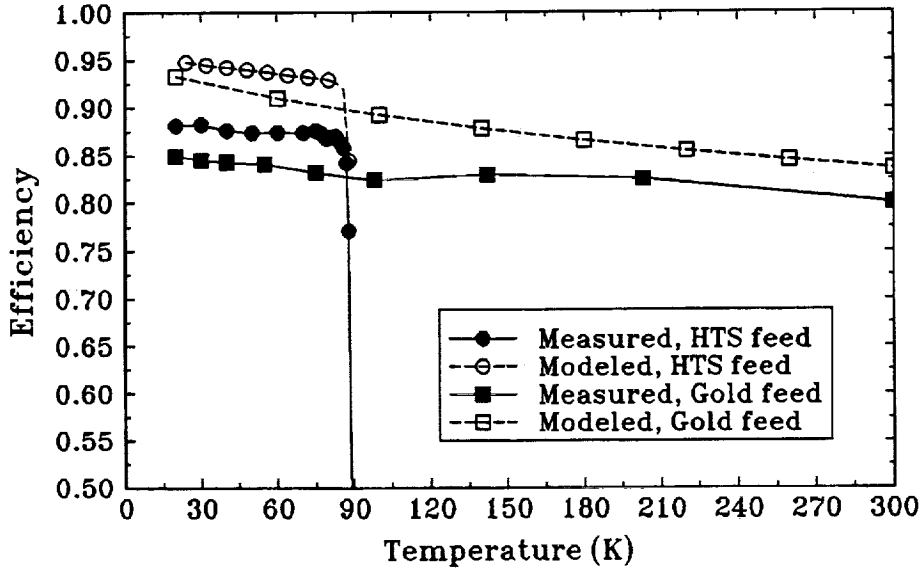

Figure 6-27: Measured efficiencies of the circular electromagnetically coupled patches on an alumina substrate with HTS and gold feed lines. Also shown are modeled efficiencies.

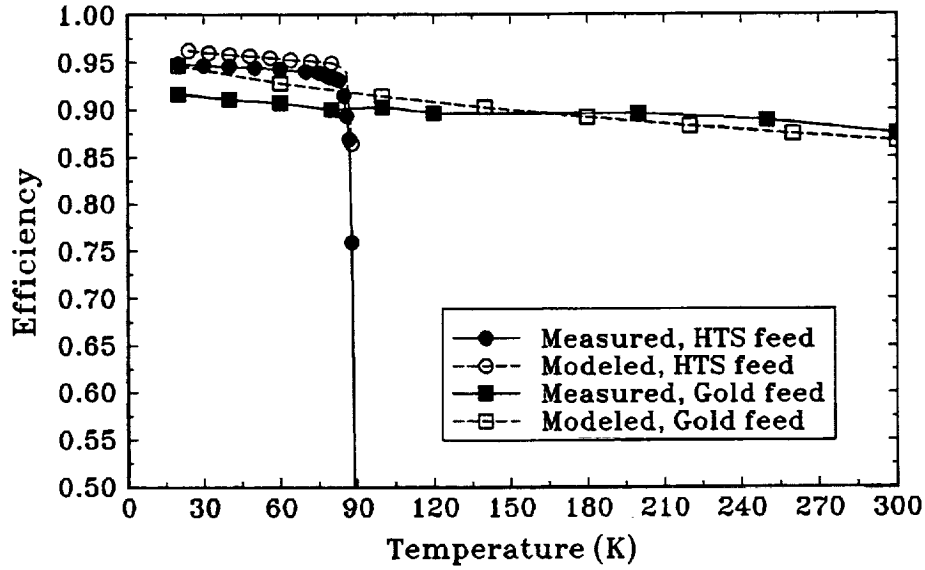

Figure 6-28: Measured efficiencies of the circular electromagnetically coupled patch on a quartz substrate with HTS and gold feed lines. Also shown are modeled efficiencies.

6.4 Four Element Arrays

A four element electromagnetically coupled array was constructed using a top dielectric layer of alumina. Initially, circular patches were used. However, rectangular patches were substituted when the performance of the circular patch array did not meet expectations, as will be discussed in Section 6.4.2. The array, shown in Figure 6-29, is a two-dimensional square (2 x 2) array. The feed network is designed so that the path length to each element is exactly the same, creating broadside radiation. The feed network is constructed from 50 Ω microstrip transmission lines, open circuited at the ends to allow coupling to the patch radiating elements on the upper dielectric layer. At each junction, a 71 Ω quarter wave transformer is employed for impedance matching. The element are spaced $\lambda_0/2$, or 5.0 mm apart at the resonant frequency of 30 GHz. Two arrays, identical in all aspects except for the feed network metallization, were fabricated. One feed network was fabricated using an HTS thin film, while the second was fabricated using 1.2 μm of gold.

The resonant frequency and VSWR for the four element arrays are shown in Figure 6-30. The change in frequency with temperature can be attributed to physical displacement of the substrates during the cool down cycle and factors such a change in the permittivity. Both the gold and HTS arrays showed excellent impedance match characteristics over their respective operating temperature ranges. The gold array had a VSWR of less than 1.2, while the HTS array had a VSWR of less than 1.1 at temperatures below 84 K. The bandwidth

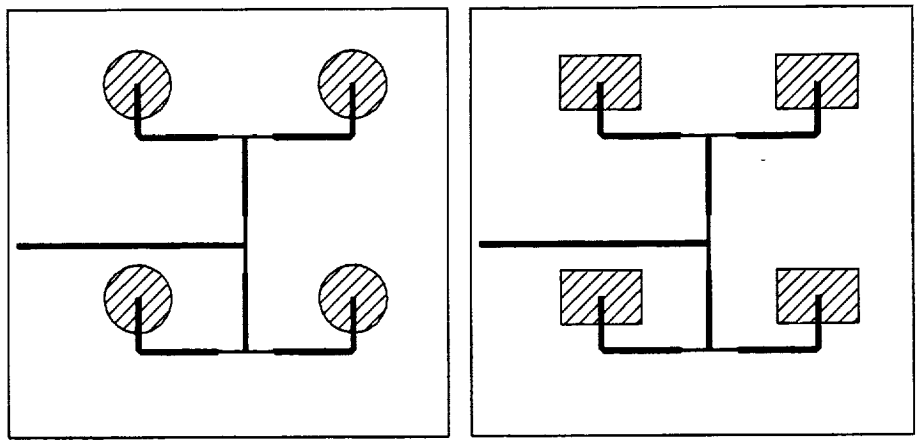

Figure 6-29: Layout of the electromagnetically coupled four element arrays with circular patches (left) and with rectangular patches (right).

of the gold array was a respectable 3.2 % at room temperature, 3.3 % at 77 K, and 3.2 % at 20 K, while the bandwidth of the HTS array was 2.0 % at 77 K and 3.0 % at 20 K.

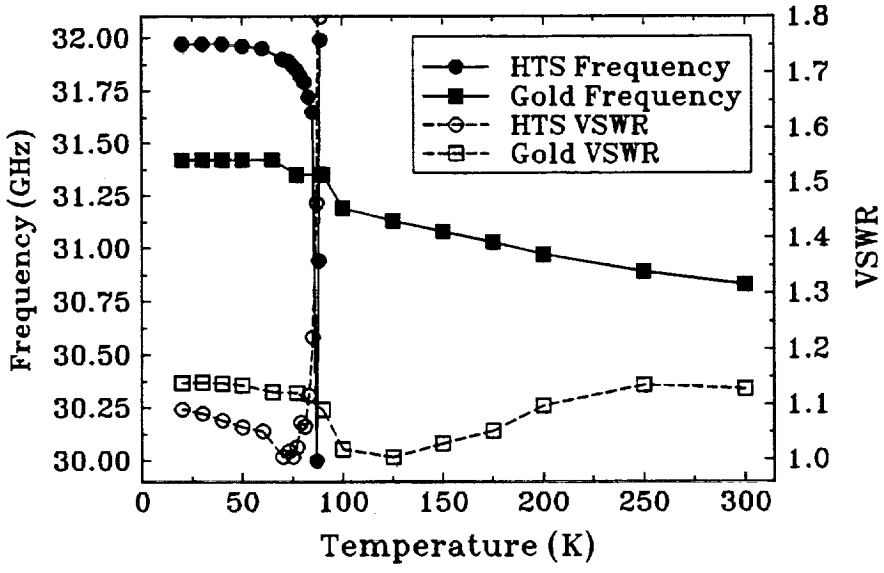

Figure 6-30: Resonant frequency and VSWR data for the four element arrays.

Initially, circular patches were used. However, no radiation patterns which agreed with published models could be obtained. Instead, E-plane data more characteristic of a single element array was measured as shown in Figure 6-31, indicating that unequal coupling from the feed network to the elements was occurring. However, repeated disassembly and reassembly of the array produced no improvement in the pattern. Thus, it was determined that the feed network was producing spurious coupling to the patch, causing the patch current to depart from the desired direction. This is possible in a circular patch because the current has no preferred direction other than the one induced by the source. As can be seen in Figure 6-29, feed lines which carry current at a right angle to the desired current direction lie in close proximity to the patches, and thus could distort the patch current.

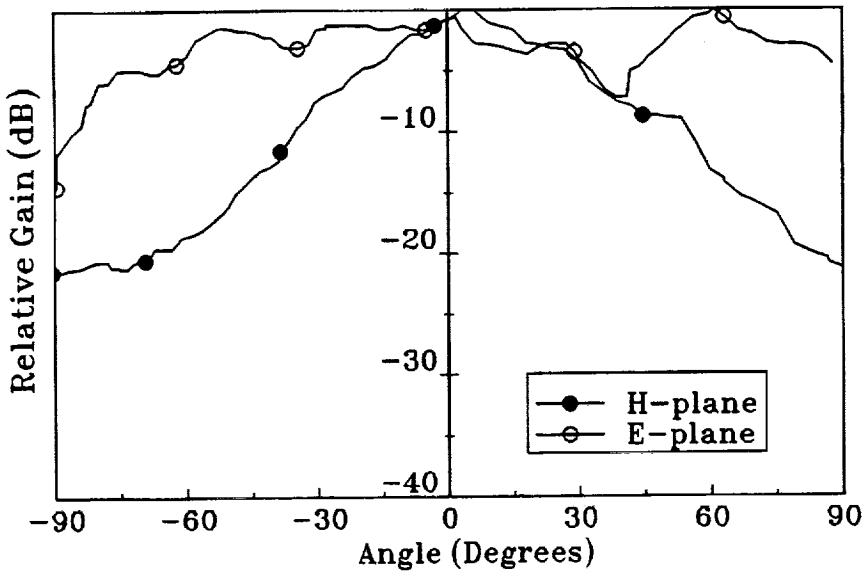

Figure 6-31: Radiation patterns of the four element array using circular patches.

To rectify this problem, the circular patches were abandoned in favor of rectangular patches, since a rectangular patch can support a resonance in only one direction at the desired frequency. The far field radiation patterns of the four element array using rectangular patches are shown in Figures 32 and 33. These patterns are quite clean in both the E and H-plane, although the E-plane pattern does show a departure from the model at the extreme angles. In each case the cross polarization is more than 20 dB below the co-polarization peak, indicating very little feed line or other spurious radiation.

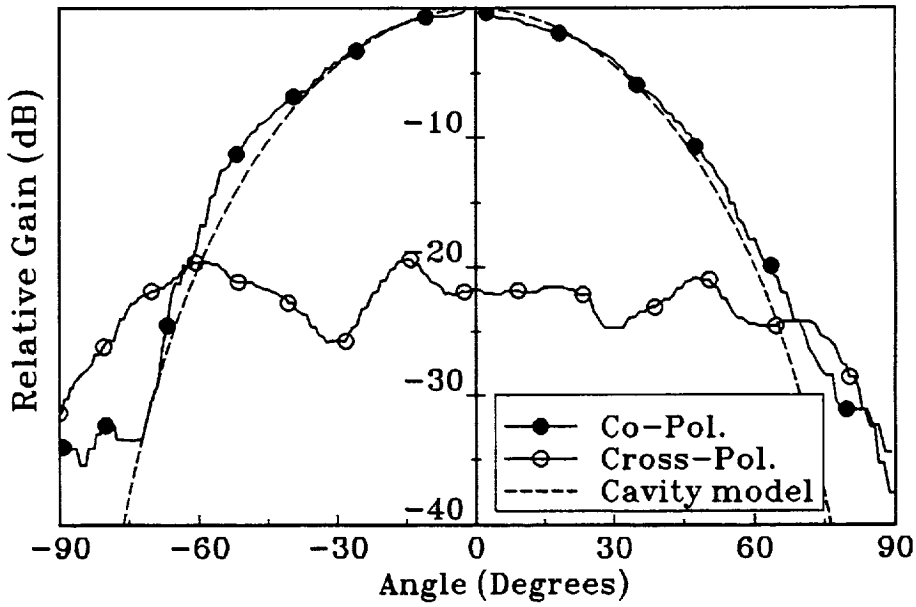

Figure 6-32: H-plane radiation patterns of the four element array using rectangular patches. Co- and cross-polarization data is shown along with the pattern predicted by the cavity model.

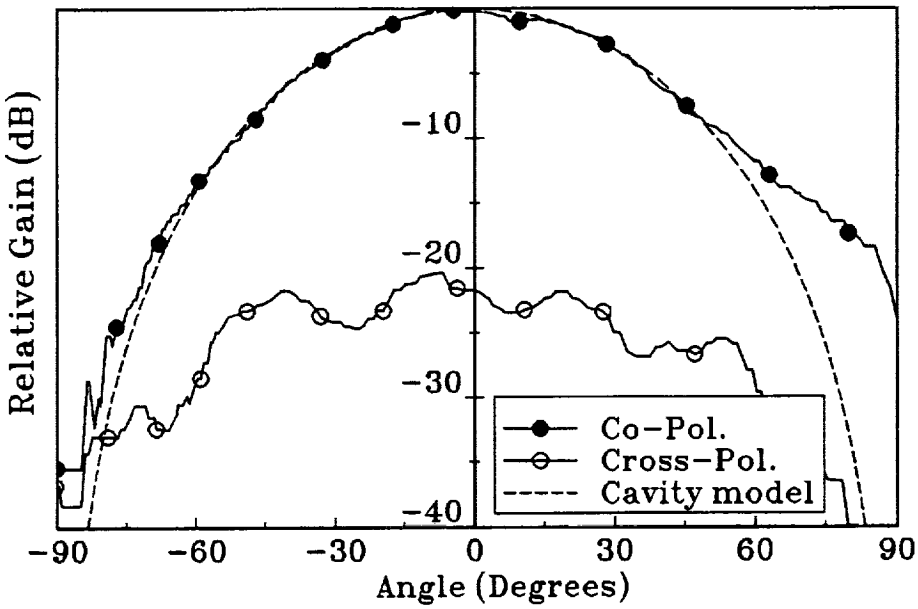

Figure 6-33: E-plane radiation patterns of the four element array using rectangular patches. Co- and cross-polarization data is shown along with the pattern predicted by the cavity model.

For gain measurement, a second set of arrays (HTS and gold) were fabricated and measured with the original pair. The gain of each gold 4-element array was measured at room temperature using a horn substitution method with a calibrated standard gain horn. The gain of gold array #1 was found to be 9.1 dB while gold array #2 had a gain of 9.3 dB. As described in Chapter 3, the gain of the HTS array relative to the gold array was found by measuring the power received at boresight and applying the Friis transmission formula. The measured gain of each HTS antenna relative to its gold antenna is shown in Figure 6-34, while the absolute gain of each antenna is shown in Figure 6-35. HTS array #1 showed a gain of 10.73 dB at 77 K and 10.66 dB at 20 K, while HTS array #2 showed a gain of 10.5 dB at 77 K and 10.55 dB at 20 K. The

half-power beam widths (HPBW) were used to calculate the directivities, or the maximum possible gain. With an E-plane beam width of 59 degrees and an H-plane beam width of 50 degrees, the directivity is estimated to be 11.5 dB.

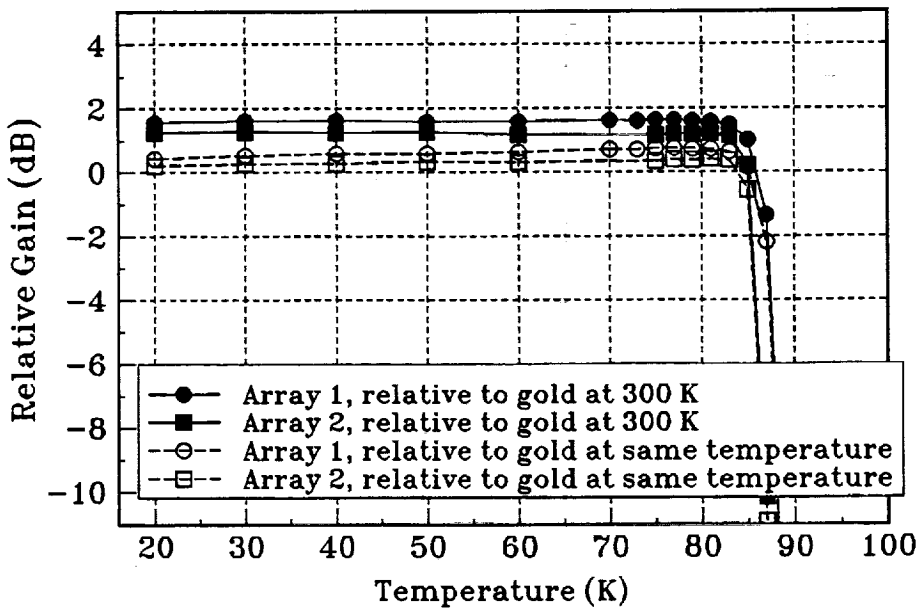

Figure 6-34: Gain of the HTS arrays relative to the gold arrays when the gold arrays are at room temperature and at the same temperature as the HTS arrays.

The losses in each antenna due to metallization were also estimated analytically. From a moment method calculation, the attenuation coefficients for a 50 Ω and a 71 Ω transmission line on $LaAlO_3$ were found and multiplied by the path length in the feed network for one element. This loss was added to the loss of a patch, calculated in Section 6.3.6. This information is summarized in Table 3. The expected loss of the gold array was found to be 1.26 dB at room temperature and 0.75 dB at 77 K, while the expected loss of the HTS array was

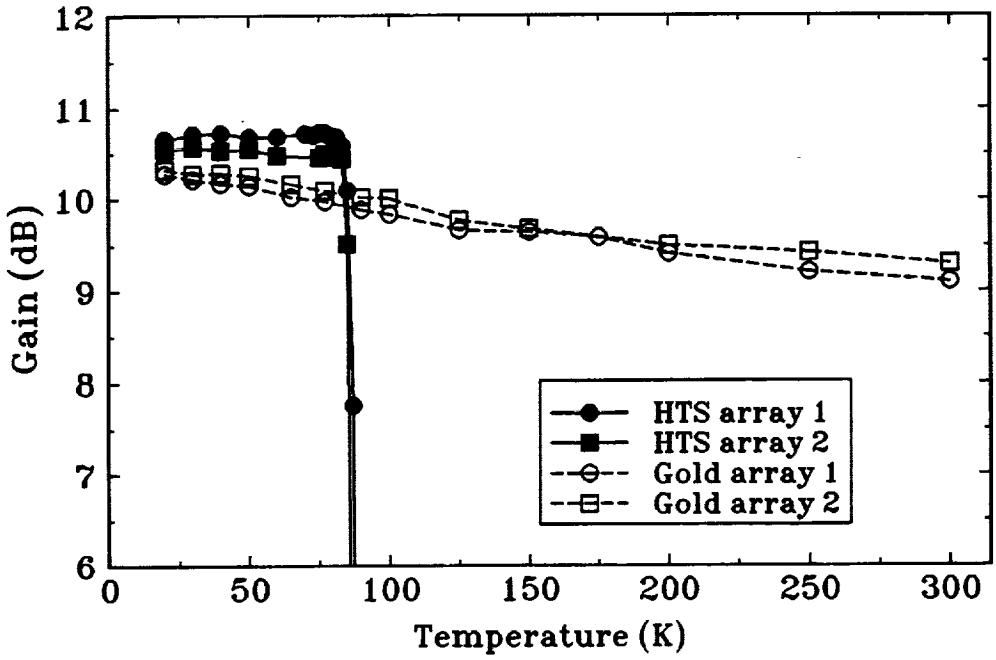

Figure 6-35: Absolute gains of the HTS and gold arrays.

found to be 0.33 dB at 77 K. The measured HTS antennas had a loss (directivity - gain) of 0.8 and 1.0 dB at 77 K. The differences between the modeled and measured losses can certainly be attributed to surface wave and connector losses.

6.5 Summary

An electromagnetically coupled microstrip antenna architecture has been investigated for HTS antennas. The antennas used HTS-compatible $LaAlO_3$ as the feed substrate. Measurements of single patch antennas were made using three different materials for the patch substrate. The resonant frequency, VSWR, and bandwidth were reported for these patches as a function of position. A

Table 6-3: Array Loss Budget					
	Line Loss	Patch Loss	Total Loss	Measured Gain	Implied Loss
Gold 300K	0.82	0.44	1.26	9.1 9.3	2.4 2.2
Gold 77K Gold 77K	0.48	0.27	0.75	9.9 10.1	1.6 1.4
HTS 77K HTS 77K	0.06	0.27	0.33	10.7 10.5	0.8 1.0

bandwidth of nearly 5 % was measured when the patch was positioned over the feed line in certain positions. Both rectangular and circular patches were investigated. Four element arrays were successfully designed using rectangular patches on alumina. Excellent radiation patterns and gain characteristics were measured.

6.6 References

1. R.E. Collin, *Field Theory of Guided Waves*, IEEE Press, New York, 1991, p. 713.

2. David M. Pozar, "Microstrip Antenna Aperture-Coupled to a Microstrip-line," *Elec. Letters,* vol. 21, no. 2, pp. 49-50, Jan. 17, 1985.

3. Peter L. Sullivan and Daniel H. Schaubert, "Analysis of an Aperture Coupled Microstrip Antenna," *IEEE Trans. Antennas and Propagat.*, vol. AP-34, no. 8, pp. 977-984, Aug. 1986.

4. G. Gronau and I. Wolff, "Aperture-Coupling of a Rectangular Microstrip Resonator," *Elec. Letters*, vol. 22, no. 10, pp. 554-555, May 8, 1986.

5. F. Croq and A. Papiernik, "Large Bandwidth Aperture-Coupled Microstrip Antenna," *Elec. Letters*, vol.26, no. 16, pp. 1293-1294, Aug. 2, 1990.

6. H. George Oltman and Donald A. Huebner, "Electromagnetically Coupled Microstrip Dipoles," *IEEE Trans. Antennas and Propagat.*, vol. AP-29, no. 1, pp. 151-157, Jan. 1981.

7. Marat Davidovitz and Y.T. Lo, "Rigorous Analysis of a Circular Patch Antenna Excited by a Microstrip Transmission Line," *IEEE Trans. Antennas and Progat.*, vol AP-37, No. 8, pp. 949-958, August 1989.

8. J.R. Herd, "Modelling of Wideband Proximity Coupled Microstrip Array Elements," *Elec. Letters,* vol. 26 no.16, pp. 1282-1284, Aug. 2, 1990.

9. Georg Splitt and Marat Davidovitz, "Guidelines for Design of Electromagnetically Coupled Microstrip Antennas on Two-Layer Substrates," *IEEE Trans. Antennas and Propagat.*, vol. AP-38 no. 7, pp. 1136-1140, July 1990.

10. D.M. Pozar and B. Kaufman, "Increasing the Bandwidth of a Microstrip Antenna by Proximity Coupling," *Electron. Letters*, vol. 23 no. 8, pp. 368-369, April 9, 1987.

11. J.S. Roy, S.K. Shaw, P. Paul, D.R. Poddar, and S.K. Chowdhury, "Some Experimental Investigations on Electromagnetically Coupled Microstrip Antennas on Two-Layer Substrates," *Microwave and Optical Technology Letters*, vol. 4, no. 6, pp. 236-238, May 1991.

12. R.Q. Lee, K.F. Lee, and J. Bobinchak, "Characteristics of a Two-Layer Electromagnetically Coupled Rectangular Patch Antenna," *Electon. Letters*, vol. 23 no. 20, pp. 1070-1072, Sep. 24, 1987.

13. J.P. Damiano, J. Bennegueouche, and A. Papiernik, "Study of Multilayer Microstrip Antennas with Radiating Elements of Various Geometries," *IEE Proc.*, vol 137, pt. H, no. 3, pp. 163-170, Jun. 1990.

14. J.S. Herd, J.P. Kenney, K.G. Herd, W.G. Lyons, Alfredo C. Anderson, P.M. Mankiewich, and M.L. O'Malley, "Experimental Results on a 12 GHz 16-Element Multilayer Microstrip Array with a High Temperature Superconducting Feed Network," *1992 IEEE Antennas and Propag. Symposium Digest*, pp. 974-977.

15. I.J. Bahl and Stanislaw Stuchly, "Analysis of a Microstrip Covered with a Lossy Dielectric," IEEE Trans. Microwave Theory Tech., vol. MTT-28, no. 2, pp. 104-109, Feb. 1980.

16. Tsuneo Konaka, Makoto Sato, Hidefumi Asano, and Shugo Kubo, "Relative Permittivity and Dielectric Loss Tangent of Substrate Materials for High-Tc Superconducting Film," *J. Superconductivity*, vol. 4, no. 4, pp. 283-288, 1991.

17. Daniel H. Schaubert and K. Sigfrid Yngvesson, "Experimental Study of a Microstrip Array on High Permittivity Substrate," *IEEE Trans. Antennas and Propagat.*, vol. AP-34, no. 1, pp. 92-97, Jan. 1986.

18. C.M. Chorey, Keon-Shik Kong, K.B. Bhasin, J.D. Warner, and Tatsuo Itoh, "YBCO Superconducting Ring Resonators at Millimeter-wave Frequencies," *IEEE Trans. on Microwave Theory and Tech.*, vol 39, no. 9, pp. 1480-1486, Sept. 1991.

CHAPTER VII.

A 10 GHZ ACTIVE PATCH ANTENNA

7.1 Introduction

In the previous chapters, the benefits of using HTS technology in phased-array antenna systems have been examined. However, for HTS to be useful in phased array antennas, active circuits such as oscillators, phase shifters and power amplifiers, will need to be integrated with radiating elements so that beam control and/or scanning may be realized. Because of the limited amount of available space in high frequency arrays, some authors have suggested the use of active patch antenna as the radiating element[1]. By using active patch antennas, the problem of rf distribution to each radiating element is minimized and space is made available for phase shifters and power amplifiers. Alternatively, phase control could be obtained by injection locking the oscillator.

A first demonstration of a HTS/GaAs hybrid active patch antenna consisting of a hybrid oscillator on one substrate[2,3], and a feedline proximity coupled to a circular microstrip patch antenna on a second substrate was carried out. The patch antenna was printed on alumina (ϵ_r = 9.9) to reduce the effective permittivity seen by the radiator. The performance of this active antenna was measured at 77 K.

7.2 Design

The S-parameters of the FET were first obtained by measurements at cryogenic temperatures for use in the design of the oscillator. The active device used in the oscillator was a low noise MESFET with a gate length of 0.25 μm (Toshiba GaAs MESFET, part # JS8830-AS). The S-parameters of the FET for the frequency range of 2 GHz to 26 GHz were measured over a range from room temperature (300 K) to 40 K. Of the S-parameters, the largest change in magnitude as a function of temperature occurred for the S_{21} values. This was due to an increase in the electron's mobility at the reduced temperatures. The variation in phase of S_{11} and S_{22} was the only other major change. The percent change of the magnitude and phase of the S-parameters at the design frequency of 10 GHz due to the change in the temperature from 300 K to 77 K is listed in Table 7-1.

Table 7-1: Percent change of S-parameters from 300 K to 77 K at 10 GHz

|S11|	∠S11	|S21|	∠S21	|S12|	∠S12	|S22|	∠S22
3.4%	16.2%	25.6%	8.4%	4.8%	6.2%	26.7%	27.1%

The oscillator was designed using simulations performed with a commercially available software package[4] under the assumption that the drain current would be held at I_d = 10 mA, and that the temperature would be held at 77 K. The design employed a parallel coupled ring resonator in the matching

network off the drain for the frequency stabilization. Using the small signal S-parameters that were measured at 77 K, the input reflection coefficient at the drain was made very large by varying the length of the transmission lines on the source and the gate. The selected lengths of the transmission lines from the source and gate were 1.57 mm and 2.79 mm, respectively. Both were open circuited lines. The ring resonator had with a fundamental resonant frequency of 10 GHz and was used to select the frequency of operation. It was placed $\lambda_g/4$ from the drain of the transistor and parallel coupled to the output transmission line using a 40 μm wide coupling gap. The matching network, including the ring resonator, was designed such that the magnitude of the real part of the impedance of the matching network was less than the magnitude of the real part of the impedance looking into the drain of the FET. The magnitude of the imaginary part of the impedance was equal to zero at the resonant frequency. With this criterion met, the 10 GHz oscillation will start upon proper biasing of the FET. The output of the oscillator was taken off the drain. The physical layout of this reflection mode oscillator is shown in Figure 7-1.

The antenna used for this investigation was a circular microstrip patch which was proximity coupled to a microstrip feedline. The feedline for the antenna was patterned on a second substrate for two reasons: this method allowed for the testing of both the oscillator and the antenna separately to determine their performance, and secondly, a HTS thin film with an area large enough to pattern the entire circuit was unavailable.

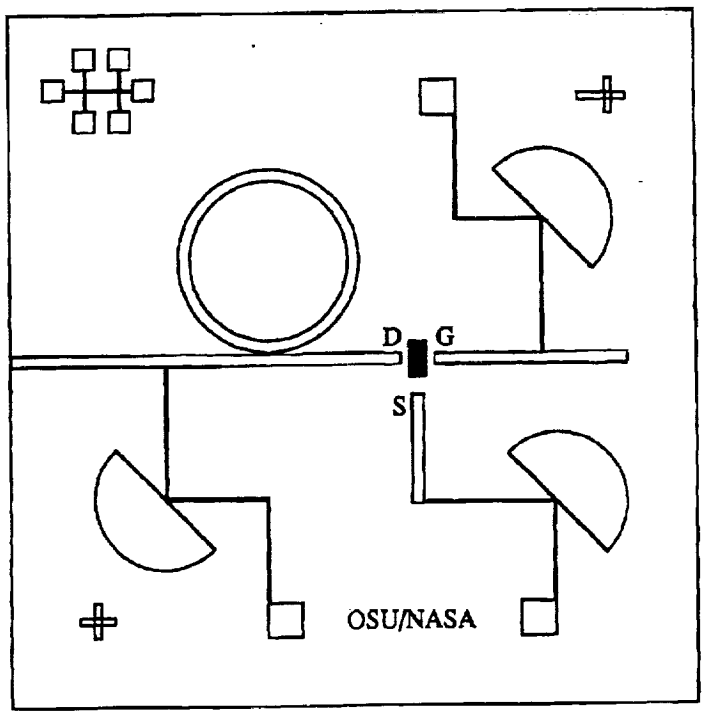

Figure 7-1: Physical layout of the hybrid 10 GHz superconductor/GaAs oscillator designed using the reflection method.

The resonant frequency of the circular antenna patch was found from the formula[5]

$$f = \frac{1.841c}{2\pi a_e \sqrt{\epsilon_{eq}}} \tag{7-1}$$

where a_e is the effective radius of the patch

$$a_e = a\left[1 + \frac{2d}{\pi a \epsilon_{eq}}\left(\ln\frac{a}{2d} + (1.41\epsilon_{eq} + 1.77) + \frac{d}{a}(0.268\epsilon_{eq} + 1.65)\right)\right]^{1/2} \tag{7-2}$$

Here, a is sum of the thickness of the two substrates between the patch and the ground plane and a is the physical radius of the patch. Because the patch was

printed on an alumina (ϵ_1 = 9.9) substrate with a thickness of 254 μm while the feedline and ground plane were on lanthanum aluminate (ϵ_2 = 23) with a thickness of 508 μm, the value for the net ϵ_{eq} of this dual layer substrate to use in Eqns. (7-1) and (7-2) was found using a static capacitor model

$$\epsilon_{eq} = \frac{3\epsilon_1\epsilon_2}{2\epsilon_1 + \epsilon_2} \qquad (7\text{-}3)$$

to be 16.0, resulting in the diameter of the patch equaling 4.02 mm. Measurements showed that a slightly larger diameter of 4.71 mm resulted in a resonance closer to the desired frequency of 10 GHz. The resonant frequency of the patch was tuned to match the output frequency of the oscillator by adjusting the position of the patch over the feedline.

7.3 Experimental Details

The film used for the oscillator was a commercially purchased film deposited using an off-axis sputtering technique and had a critical temperature of 88.6 K after patterning. Patterning was done as described in Appendix A. Contacts to the superconductor for the rf output and wire bonding pads were made of silver with a gold overlayer patterned by lift-off photolithography. Wire bonding pads were located at the bias pads as well as at the ends of the transmission lines near the FET. The GaAs FET was epoxied onto the substrate and wire bonds were made to the transmission lines with 0.7 mil gold wire by thermosonic bonding. A copper ground plane with a thickness of 2.4 μm was deposited on the backside of the substrate.

A second HTS thin film was used for the antenna feedline. A $YBa_2Cu_3O_{7-x}$ thin film was deposited by pulsed laser deposition onto this substrate[6]. The film had a critical temperature of 86 K. This film was patterned in the same way as the oscillator into a 50 ohm transmission line that was 160 μm wide and 5 mm in length. A silver/gold contact was deposited at the end of the feedline for ribbon bonding, and a 2 μm copper ground plane was evaporated on the backside of the substrate. An alumina substrate with the patterned antenna patch was placed on top of the feedline and held in place with small amounts of fingernail polish at the edges.

The performance of the oscillator was measured on a spectrum analyzer at 77 K by mounting the circuit in a sealed brass test fixture and submerging the fixture in liquid nitrogen. The efficiency of the antenna together with its HTS feedline was measured using the Wheeler Cap method as described in Chapter 3.

The oscillator and antenna circuits were then mounted with silver paint onto a brass test fixture. The rf connection between the two substrates was made by ribbon bonding to the contacts on the feedline of antenna and the output of the oscillator (Figure 7-2). The test fixture was then mounted in the closed-cycle gas refrigerator and covered with the high density polyethylene radome. An X-band horn attached to a pivoting arm served as the receive antenna to measure the radiation pattern of the active patch antenna in the far field as a function of angle.

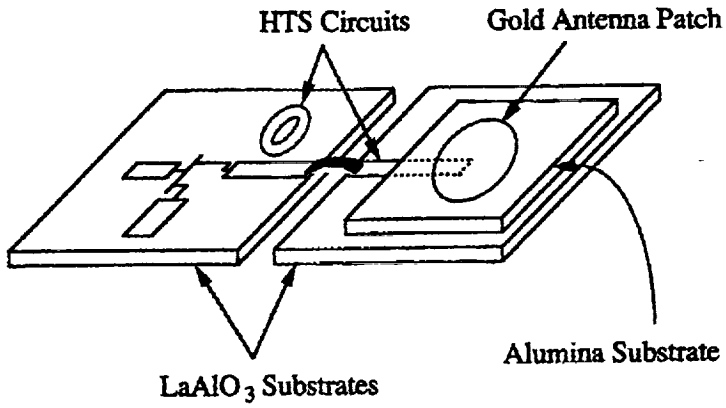

Figure 7-2: Physical layout of the active antenna. The gold patch was on an alumina substrate placed over a superconducting feedline on a $LaAlO_3$ substrate. The oscillator and patch antenna were ribbon bonded together.

7.4 Results and Discussion

The output power and frequency of operation of the hybrid oscillator were measured to verify its performance before bonding the oscillator to the antenna circuit. The maximum power attainable from the oscillator at 77 K was 11.5 dBm at a bias of V_{ds} = 4.0 V and V_{gs} = 0.0 V. The sensitivity of the frequency to temperature was -10 MHz/K at 77 K. For the active antenna measurements at 77 K, the FET was biased at V_{ds} = 0.5 V and V_{gs} = -0.5 V which gave a current of I_d = 12 mA. For this bias condition, the frequency of the signal was 10.082 GHz with an output power of -2.0 dBm. The efficiency of the oscillator was 10.5 %. The power of the second harmonic at 20.16 GHz was 35 dB less than the fundamental signal at 77 K.

The efficiency of the antenna was measured before bonding the antenna to the oscillator circuit. The efficiency as a function of temperature is shown in Figure 7-3. As expected, the efficiency rises dramatically as the HTS film becomes superconducting and then increases slowly as the temperature decreases, due to the increase in the conductivity of the HTS feedline. This trend was in agreement with the measured performance of HTS ring resonators. The efficiency reaches a maximum of 87.4 % at 30 K.

The measured antenna patterns with the superconducting oscillator driving the antenna are shown in Figures 7-4 and 7-5, along with the patterns predicted for the co-polarization by the cavity model[7]. The H-plane shows good agreement with the model, while the E-plane deviates substantially due to surface waves and the feedline, neither of which are accounted for in the model used. This is in agreement with results published by Schaubert *et. al.*[8] which demonstrated that antennas on high permittivity substrates are characterized by perturbations in the E-plane pattern. The 12 dB dip in the E-plane and the cross polarization patterns at an angle of 15 degrees is almost certainly due to radiation interference from the resonator and microstrip lines on the oscillator.

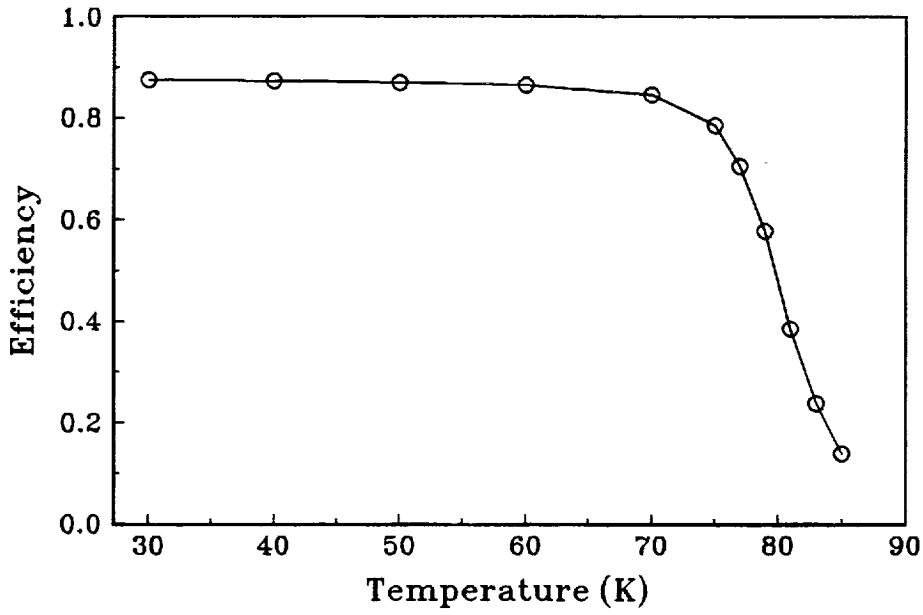

Figure 7-3: Efficiency of the patch antenna as a function of temperature measured from 30 K to 85 K. The efficiency at 77 K was 71 %.

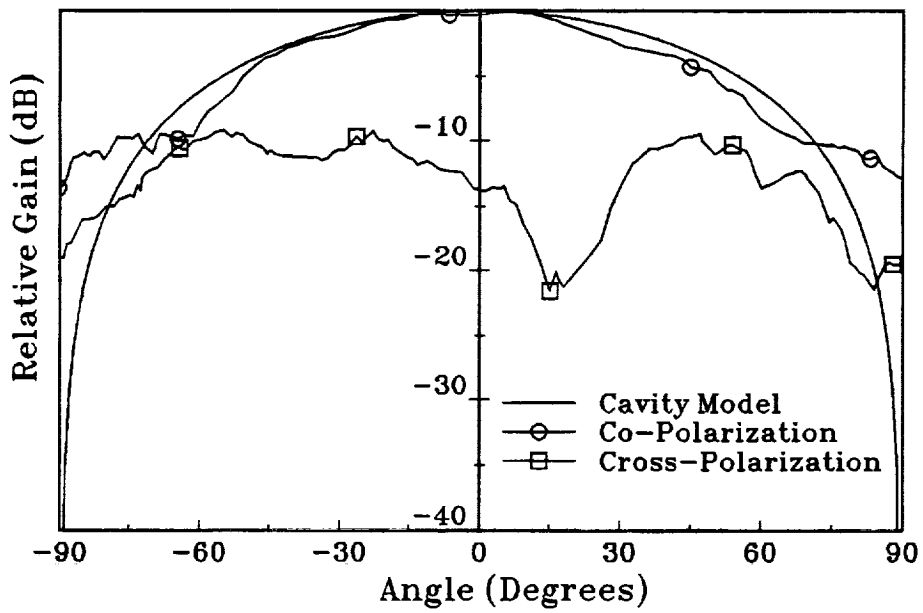

Figure 7-4: H-plane radiation patterns for the active patch at 77 K, including cavity model, co-polarization data, and cross polarization data.

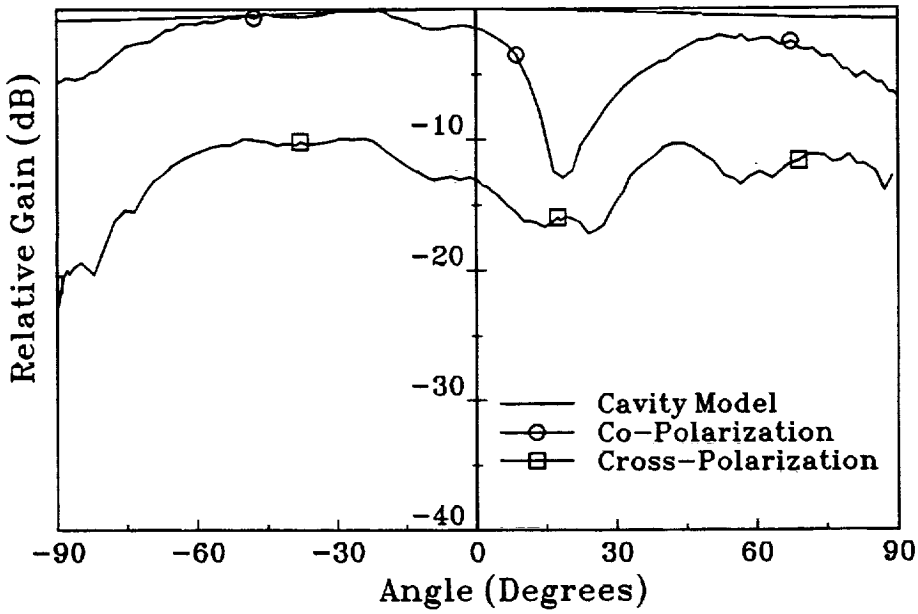

Figure 7-5: E-plane radiation patterns comparing the cavity model with the co-polarization and also showing the cross polarization data.

7.5 Conclusion

An active patch antenna has been designed using a circular patch proximity coupled to a 10 GHz HTS/GaAs hybrid oscillator. The performance of this Y-Ba-Cu-O superconducting active antenna, demonstrated for the first time, shows how superconducting antenna technology can be integrated with active components to form active antennas or arrays.

7.6 References

1. Kai Chang and Cheng Sun, "Millimeter-Wave Power-Combining Techniques," *IEEE Trans. Microwave Theory and Tech.*, vol. 31, no. 2, pp. 91-105, Feb. 1983.

2. *Touchstone*, EEsof, 1990.

2. N.J. Rohrer, G.J. Valco, and K.B. Bhasin, "Hybrid High Temperature Superconductor/GaAs 10 GHz Microwave Oscillator: Temperature and Bias Effects," To be published in *IEEE Trans. Microwave Theory and Tech.*

3 N.J. Rohrer, M.A. Richard, G.J. Valco, and K.B. Bhasin, "A 10 GHz YBCO/GaAs Hybrid Oscillator Proximity Coupled to a Circular Microstrip Patch Antenna," To be published in *IEEE Trans. Applied Superconductivity*.

4. *Touchstone*, EEsof, 1990.

5. W. C. Chew and J. A. Kong, "Effects of Fringing Fields on the Capacitance of Circular Microstrip Disks," *IEEE Trans. Microwave Theory and Tech.*, vol. 28, no. 2, pp. 98-104, Feb. 1990.

6. J.D. Warner, K.B. Bhasin, N.J. Varaljay, D.Y. Bohman, and C.M. Chorey, "Growth and Patterning of Laser Ablated Superconducting YBCO Films on $LaAlO_3$ Substrates," NASA TM-102336.

7. I.J. Bahl and P. Bhartia, *Microstrip Antennas*, Dedham, MA, Artech House, 1980.

8. Daniel H. Schaubert and K. Sigfrid Yngvesson, "Experimental Study of a Microstrip Array on High Permittivity Substrate," *IEEE Trans. Antennas and Propagat.*, vol. AP-34, no. 1, pp. 92-97, Jan. 1986.

CHAPTER VIII.

SUMMARY AND CONCLUSIONS

8.1 Summary

Although microstrip circuitry has many advantages such as small size and light weight, it has long been known to be quite lossy. With the advent of high temperature superconductors in 1986, there was a flurry of ideas on how superconductivity could be used in all type of microwave circuits to reduce these losses. The area of antennas was no exception, with several publications analyzing how HTS could prove advantageous for antenna systems. The research presented here was undertaken as a first experimental investigation of how superconductors could be used for high frequency microstrip antennas.

The implementation of HTS thin films for microstrip antennas is complicated by the high permittivity of the HTS compatible substrates. The permittivity of the substrate used in this research, $LaAlO_3$, is an order of magnitude higher than commonly used antenna substrates. This high permittivity makes traditional feed methods quite difficult, even for planar architectures. Coaxial feeding is difficult even at low frequencies because of the fragile nature of the crystalline HTS-compatible substrates, and impossible at K-band and

higher frequencies because of the small patch sizes. The traditional microstrip edge feed is possible, but the feedline must be inset into the patch edge substantially to match a 50 ohm transmission line.

The object of this research, then, was two fold. It was to first find practical ways of using superconductors in high frequency microstrip antennas. This was done by designing, fabricating, and testing microstrip antennas using three different feeding techniques. The second goal was to investigate experimentally the performance advantages of HTS antennas over antennas fabricated using conventional metals. This goal was met by measuring the gains and efficiencies of single patch and the four element array antennas and comparing them to both modeled data and identical antennas fabricated using normal metals. Each portion of this research demonstrated the performance of such a device for the first time.

To accomplish the stated goals, experimental procedures were first established. A cryogenic antenna test chamber was designed, and methods for measuring the microwave performance of the antennas were established. A way to measure the antenna patterns of superconducting antennas was devised, and a method to measure the efficiency of single patch antennas was researched and implemented. Gain measurement methods for the larger array antennas were also devised.

Three types of antenna architectures were investigated by fabricating single patch antennas and four element arrays. A direct coupled antenna operating at

30 GHz used a rectangular radiating element fed by a microstrip transmission line. The 50 Ω transmission line was matched to the patch impedance through the use of a quarter wave transformer and by insetting the feedpoint almost 43 % into the patch. The resonant frequencies of the HTS antenna was modeled to values within 2 % by the cavity model when the effects of the changing magnetic penetration depth of the superconductor were accounted for. The radiation patterns of the single element showed good correlation between measured and modeled data in the H-plane, and a rather poor correlation in the E-plane because of the high permittivity of the antenna. The patterns of the four element array followed the predicted patterns almost exactly, showing very effects due to the high permittivity.

The direct coupled antennas showed good VSWR characteristics, with return losses of 17 to 45 dB. The bandwidths of the antennas were found to be less than 1.0 %. The modeled bandwidths for the HTS and gold antennas showed good agreement with the measured bandwidths. Using the Wheeler Cap method, the efficiencies of the gold and HTS single element antennas were measured and found to be 0.7 to 0.8 for the gold antenna, and as high as 0.89 for the HTS antenna. The modeled efficiencies, though, were higher because of losses not accounted for in the models. The gain of the HTS array was found to be within 1.8 dB of the directivity at 77 K.

A gap coupled antenna operating at 26 GHz was the second architecture investigated. This antenna used a circular patch with a 15 μm gap between the

patch and the 50 Ω transmission line feeding it. Because of fabrication problems, the HTS antenna had a gap width of nearly twice the intended width. Therefore, while the gold antenna showed nearly critical coupling, the HTS antenna, was under coupled because of the wider gap. The resonant frequencies of the antennas were found to follow the predicted values quite well.

As in the case of the direct coupled antenna, the radiation patterns of the single element showed good correlation between measured and modeled data in the H-plane, and a rather poor correlation in the E-plane. The four element array followed the predicted patterns much better.

The input resistance of the single patch antenna was found by measuring the Q of the patch. Values between 330 Ω and 400 Ω were extracted. The bandwidths were measured to be less than 1.2 %. The cavity model did a poor job of predicting either the input resistance or the bandwidths of the circular patch because of shortcomings in the model.

Efficiency measurements showed radiation efficiencies of 60 % for the gold antenna and 70 % for the HTS antenna. The predicted efficiencies, though, were much higher. The gain of the HTS four element array was found to be 10.7 at 77 K as compared to the 9.8 dB gain of the gold array at 77 K. Modeled losses fell in line with the measured data for the gold array, but were much higher than measured for the HTS array. This was because the surface resistance value used to model the HTS patch was quite high at 77 K, resulting in a modeled patch loss of 5 dB.

The third architecture that was investigated was a two layer, electromagnetically coupled antenna. This antenna used a feed line on $LaAlO_3$ and a patch on second substrate resting directly over the feed line. This allowed the freedom to use a lower permittivity material for the patch substrate. The advantages of using HTS would not be lost, though, because the feed network could be made superconducting. Circular patches were fabricated on Duroid, quartz, and alumina substrates while rectangular patches were fabricated on quartz and alumina substrates.

Both the resonant frequency and the VSWR were found to be a function of the patch position in relation to the feed line and thus could be adjusted to the desired values. The bandwidths of the antennas were also position dependant, and were measured to be nearly 5 % in some instances.

The antenna patterns showed results similar to those of the direct and gap coupled antennas. No substantial differences were noted between the patterns of the antennas with different patch substrates.

Efficiency measurements were made on several of the antennas. The circular patches on quartz and alumina were measured using both gold and HTS feed lines, while the rectangular patches were measured only with the gold feed lines. Efficiencies ranged from 80 % to 95 %. The antennas fabricated using lower permittivity patch substrates showed slightly higher efficiencies than those with higher permittivity patch substrates while those with HTS feed lines showed a 4 to 10 % increase in the efficiency over their gold feed line counterparts.

Four element arrays were fabricated using rectangular patches. The radiation patterns were found to be quite clean in both the E- and the H-plane, although some departure from the modeled pattern was seen in the E-plane at extreme angles. The arrays were found to have bandwidths of 2 to 3 % and excellent gain characteristics. Gains of the two arrays using gold feed networks were found to be 9.1 dB and 9.3 dB at room temperature and 9.9 dB and 10.1 dB at 77 K, while the HTS arrays had gains of 10.5 dB and 10.7 dB at 77 K.

The performance of the four element arrays are summarized in Table 8-1. At 77 K, the direct coupled antenna showed the lowest gain of the HTS arrays. However, at lower temperatures the difference in gain between the architectures was much less pronounced, ranging from 10.5 dB for the direct coupled array to 10.6 and 10.7 dB for the electromagnetically coupled arrays, and 11.1 dB for the gap coupled array.

Table 8-1: Performance of Four Element Arrays

Antenna Architecture	Gain HTS 77K	Gain Gold 300K	Gain Gold 77K	Bandwidth
Direct	9.9 dB	9.0 dB	9.8 dB	0.7 - 1.1%
Gap	10.7 dB	9.0 dB	9.8 dB	0.4 - 1.0%
EM #1 EM #2	10.7 dB 10.5 dB	9.3 dB 9.1 dB	10.1 dB 9.9 dB	2 - 3 %

In addition to the comparison of antenna architectures, three related topics were investigated. A 21 GHz annular ring antenna operating in the TM_{12} mode

was fabricated using an HTS thin film on a 254 μm thick $LaAlO_3$ substrate. The antenna showed reasonable radiation pattern and efficiency characteristics.

An active patch antenna was designed using a 10 GHz HTS/GaAs hybrid oscillator. A circular patch was fabricated on alumina and electromagnetically coupled to a feed line driven by the oscillator. The efficiency of the patch and feed line was measured, as was the radiation patterns of the active antenna when driven by the oscillator. This demonstrated the performance of an HTS-semiconductor hybrid active antenna for the first time.

A 30 GHz 64 element array on a 2 inch diameter $LaAlO_3$ wafer was designed by Ball Aerospace Systems Division and tested by this researcher. The performance of this array demonstrated the advantages of HTS over normal metals, showing a 2 dB improvement over an identical array fabricated using gold metallization when both arrays were at 77 K. The HTS array at 77 K showed a 4 dB improvement over the gold array's room temperature performance. This experiment was the first demonstration of a large HTS array.

In any experimental research, the results are clouded by experimental uncertainties and errors. In this work, several steps were taken to minimize these. Some data were taken multiple times. This was done in the case of the electromagnetically coupled four element arrays and the position dependance data of the single patch electromagnetically coupled antennas. This allowed confirmation of the results. Secondly, the network analyzer was set in the step mode. In this mode, the analyzer phase locks on each frequency point for

maximum accuracy and repeatability. In addition, the analyzer was programmed to average the measured data. Thus at each frequency point the analyzer measured the data 32 times and then present the average of these measurements. Additionally, calibration standards were regularly cleaned and a calibration was performed after every cryogenic run (one to two hours). Using these techniques, the network analyzer has an accuracy within 0.1 dB.

8.2 Conclusions

From the research done, several conclusions can be drawn concerning superconducting microstrip antennas. First of all, as was evident from the start of this research, the high permittivity of the substrate complicates the design process. However, the research showed that this was not as large of a handicap as anticipated. Even though the single patch antennas showed scallops in the E-plane radiation patterns, the four element arrays had excellent pattern characteristics. In addition, the gain compared very favorably to the directivity for each architecture, indicating very little surface wave losses.

The main effect of the permittivity was seen in the bandwidth of the antennas. The two planar architectures had bandwidths of less than 1 %. The necessary bandwidth for a practical antenna depends upon the application. However, it is safe to assume that for applications other than radar, a bandwidth of less than 3 % will be insufficient. There are several way to increase the bandwidth of a microstrip antenna. One method, demonstrated in this research, is to use a multilayer architecture such as an electromagnetically coupled antenna.

The electromagnetically coupled antennas tested had bandwidths from 2 % to 5 %. This bandwidth could be extended by designing the antenna to accommodate an air gap between the layers, or by using parasitic elements. Alternatively, an aperture coupled antenna could be constructed. This would allow the patch, fabricated on a low permittivity substrate, to be isolated from the high permittivity feed substrate.

A second conclusion is that antennas designed on $LaAlO_3$ will need to be tuned experimentally because of variations in permittivity between samples. The effects of the permittivity differences between samples was seen repeatedly throughout this work. The effects of permittivity change with temperature was also pronounced, but in a practical application would not be as much of a problem. This is because the operating temperature would almost certainly be controlled within several degrees, either through the use of a refrigeration device or direct immersion in cryogens. To tune resonant circuits, some researchers report the use of lasers to locally destroy the HTS material, thereby shortening the resonator[1].

The choice of which architecture to use in a practical antenna, then, will be determined by the application. The two planar architectures had the advantage of simple fabrication, but were limited in bandwidth. The electromagnetically coupled antennas could be adjusted quite easily for optimum VSWR and had a bandwidth 2 to 5 times as high as those of the planar architectures. However, it was a difficult structure to work with experimentally because of unpredictable

shifts in resonant frequency and VSWR due to thermal contractions with temperature. In a larger array, though, these shifts could probably be reduced significantly by clamping the two layers together securely. This would eliminate the necessity of a bonding material as used in this research.

The actual application of HTS to future communication systems is still not clear. This research demonstrated that it is possible to make microstrip antennas and arrays using HTS, and that they have increased gain over normal metal antennas. It is clear that the four element arrays will not find practical applications because the increase in gain found through the use of HTS is too small to justify the additional complexity. However, it is a simple matter to extend the small arrays designed during the course of this work to larger arrays. In fact, the 64 element HTS array tested as part of this research showed a 4.7 dB improvement in gain over an identical gold array.

To justify the use of HTS antennas in a practical system, one of two criteria would have to be met. One scenario is the case where the power supply is limited. An example of this situation would be a lunar base of a Mars mission where only a small amount of power could be generated. In this case, it would be necessary to conserve power, and thus HTS could be employed to reduce the amount of wasted power. To do this, however, would necessitate the use of highly efficient cryocoolers so that the amount of power conserved in the communication system is not lost in the cooling equipment. Some studies have

shown that passive cooling would be possible in such missions, so that the cryocoolers could be dispensed with entirely[2].

A second scenario is the case where the incoming signal is very weak. In this case, the incoming signal is competing with the noise signal. Thus, it is necessary to have increased gain and decreased noise figures. An example of this is radio astronomy. Usually antennas for radio astronomy are too large to be replaced by HTS antennas or arrays. However, the feed horn could be replaced by an HTS array. In addition, the transmission lines and LNA circuitry could employ HTS for a lowered system loss and noise figure.

There may also be other cases where HTS antennas would be employed strictly because HTS components need to be used elsewhere in the system and thus no real penalty is incurred by using HTS in the antenna. An example of this situation is very high data rate communication systems where superconducting digital circuits need to be used.

8.3 Future Research Suggestions

Several areas of this research are suitable for further study. One relatively simple study would be to investigate the performance of larger arrays for any of the three coupling techniques investigated. This has already been done for the direct coupled antenna. A larger electromagnetically coupled array would eliminate some of the problems experienced in holding the two layer together for the four element arrays as clamps could be used.

In addition, alternative architectures could be investigated. One of the most promising such architecture is the aperture coupled antenna. This architecture was not investigated for this research because of the small size and extremely brittle nature of the substrates used. However, it may be possible to implement this architecture if larger substrates and special test fixtures are used.

In recent months, HTS thin films on sapphire substrate have become available. HTS microstrip antennas on sapphire would also be a worthy research topic. In addition to having a permittivity significantly less than $LaAlO_3$, sapphire is physically robust. Therefore, aperture coupled antennas may be quite feasible when sapphire is used. Of course circuit design on sapphire is complicated by the anisotropic nature of the substrate

Finally, a logical extension to this work would be to design an active HTS/semiconductor hybrid phased array. This could be done by designing HTS microstrip circuits such as power amplifiers or phase shifters which utilize discrete semiconductor components. These components would be integrated into the feed network of an antenna array to provide beam steering. As part of this work, a start in this direction was made through the demonstration of the active patch antenna. However, much more could be done in this field.

8.4 References

1. Katsumi Suzuki (private communication).

2. M.A. Shimko, C.J. Crowley, and P.N. Wallis, "Novel Concept for a Space Power Distribution Busbar Using HTS Materials and Passive Cooling," Presented at the Fifth Conference on Superconductivity and Applications, Buffalo, New York, Sept. 1991.

APPENDIX A.

CIRCUIT FABRICATION

To pattern an HTS thin film, first a 1:1 negative photomask of the desired circuit was made. The film was coated with a 2.1 μm thick coat of negative photoresist and baked in a 90 C° oven for 30 minutes. The photolithography was then done by exposing the coated film to a UV source through the pattern of the photomask. The photoresist was developed and rinsed in De-ionized H_2O, and baked in a 110 C° oven to harden the resist. With the photoresist patterned according to the mask, the film was then etched in 100:1:H_2PO_4 for 30 seconds, followed by a rinse in DI H_2O to stop the etching. On the films deposited by off-axis sputtering, a Q-tip dipped in ethanol was used to wipe off the haze of YBCO left after etching.

Because the phosphoric acid etches the YBCO isotropically, over-etching or undercutting of the film was a distinct possibility during the fabrication process (Figure A-1). Although this did occur on at least one of the early circuits used in the study, this was avoided during later fabrication procedures by careful control of the etching process.

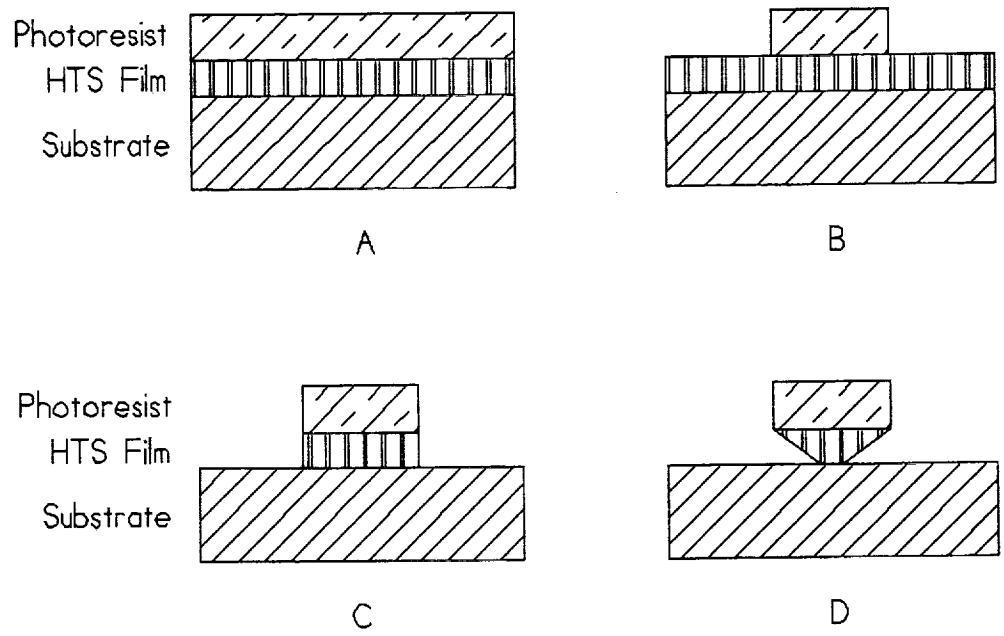

Figure A-1: Etch-back photolithography steps. 1a shows film coated with photoresist, 1b has photoresist patterned, 1c shows substrate after etching is completed. 1d shows substrate when the film is over-etched.

Silver contacts were placed on the patterned films. These contacts allowed wirebonds to be made to the HTS circuits without destroying the HTS material. Contacts were placed by using lift-off lithography. To do this, a 3.3 μm thick layer of photoresist was spun onto the patterned film and soft baked. The circuit was then exposed to a negative contact mask and developed, so that only the portion of the circuit where the contact was to be placed was stripped of photoresist. A membrane of 250 nm of silver followed by 700 nm of gold was evaporated onto the circuit. Lift off of the metal was then accomplished by dissolving the photoresist in acetone so that only the contact metal remained in place (Figure A-2).

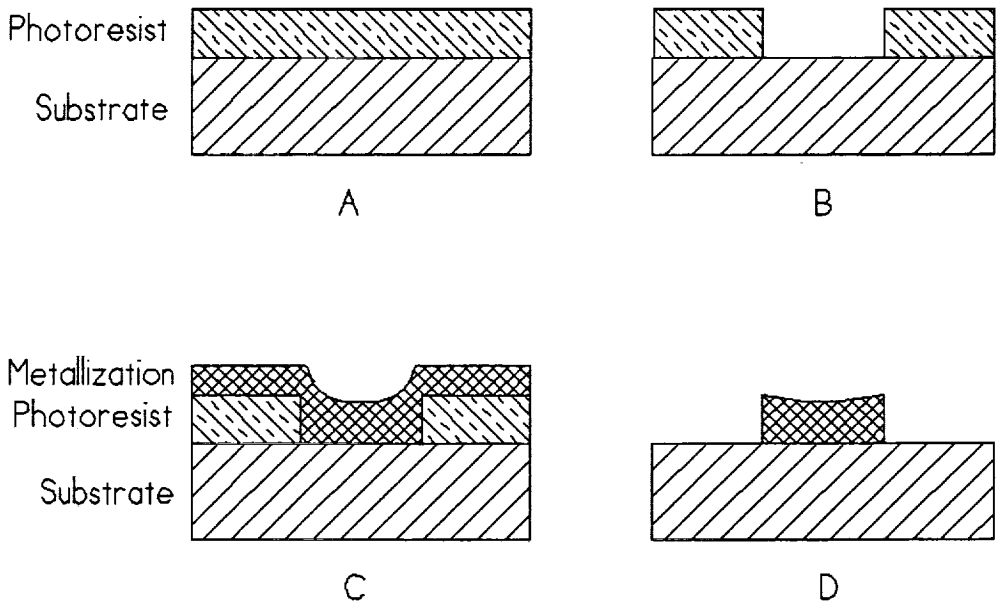

Figure A-2: Lift-off lithography. 2a shows substrate coated with photoresist, which is patterned into the desired pattern as in 2b. Metal is evaporated (2c), and the photoresist is dissolved to leave only the desired portion of the metal (2d).

To prepare for ground plane deposition, the circuit was cleaned in a bath of boiling acetone followed by boiling ethanol. The circuit was blow-dried with dry nitrogen. A protective layer of photoresist was spun on to the front side of the circuit and hard baked. The circuit was then placed in a oxygen plasma etcher to remove contaminants from the backside of the circuit. A 30 second etch in 10:1:H_20:HF acid completed the cleaning process. The ground plane was deposited by evaporating 20 nm of chromium followed by 1 to 2 μm of copper. The chrome layer facilitated the adhesion of the copper to the substrate.

The gold circuits used for comparison were, in general, fabricated using an etch-back procedure. To do this, a substrate was first coated with 1 to 2 μm of

gold. Photolithography was done in the manner described for the HTS films, and the gold was etched away so that only the circuit metallization remained. A ground plane of 1 to 2 μm of copper was then deposited. For circuits with very small dimensions (15 μm or less), lift-off lithography was used with gold metallization. This process eliminates the possiblity of overetching, but is more time consuming and difficult to implement sucessfully.

LITERATURE CITED

CHAPTER I.

1. Thomas A. Freeburg, "ALTAIR - True Wireless In-Building Networking," *IEEE Antennas and Propag. Symposium Digest*, p. 1269, 1992.

2. Raymond Leopold, "Motorola's IRIDIUM System: Low-Earth Orbit Global Cellular Communication Network," *IEEE Antennas and Propag. Symposium Digest*, p. 1270, 1992.

3. H. G. Booker, "Slot aerials and their relation to complementary wire aerials," *Journal of the IEE*, Pt. III A, vol. 93, p. 620, 1946.

4. G.A. Deschamps, "Microstrip Microwave Antennas," 3rd USAF Symposium on Antennas, 1953.

5. L. Lewin, "Radiation from discontinuities in stripline," *Proc. IEE*, vol. 107C, pp. 163-170, 1960.

6. *Proc. of the Workshop on Printed Circuit Antenna Technology*, October 17-19, 1979, New Mexico State University, Las Cruces, New Mexico.

7. *IEEE Trans. Antennas and Propag.*, Special Issue on Microstrip Antennas, vol. AP-29, no. 1, 1981.

8. L.C. Shen, "The elliptical microstrip antenna with circular polarization," *IEEE Trans. on Antennas and Propag.*, vol. AP-29, no. 1, pp. 90-94, Jan. 1981.

9. K. Luk, K.F. Lee, and J.S. Dahele, "Theory and experiment on equilateral triangular microstrip antenna," *Proc. 16th European Microwave Conference*, 1986.

10. Weng Cho Chew, "A Broad-Band Annular Ring Microstrip Antenna," *IEEE Trans. Antennas and Propagat.*, vol. AP-30, no. 5, pp. 918-922, Sep. 1982.

11. William F. Richards, Jai-Dong Ou, and Stuart A. Long, "A Theoretical and Experimental Investigation of Annular, Annular Sector, and Circular Sector Microstrip Antennas," *IEEE Trans. Antennas and Propagat.*, vol. AP-32, no. 8, pp. 864-867, Aug. 1984.

12. H.D. Weinschel, "Cyclindrical Array of Circularly Polarized Microstrip Antenna," *IEEE AP-S Int. Symposium Digest*, pp. 177-180, 1975.

13. Weng Cho Chew, "A Broad-Band Annular Ring Microstrip Antenna," *IEEE Trans. Antennas and Propagat.*, vol. AP-30, no. 5, pp. 918-922, Sep. 1982.

14. Y.T. Lo, D. Solomon, and W.F. Richards, "Theory and Experiment on Microstrip Antennas," *IEEE Trans. Antennas and Propagat.*, vol. AP-27, no. 2, pp. 137-145, Mar. 1979.

15. William F. Richards, Y.T. Lo, and Daniel D. Harrison, "An Improved Theory for Microstrip Antennas and Applications," *IEEE Trans. Antennas and Propagat.*, vol. AP-29, no. 1, pp. 38-46, Jan. 1981.

16. K.R. Carver, "Practical Analytical Techniques for the Microstrip Antenna," *Proc. Workshop on Printed Circuit Antennas*, New Mexico State University, Las Cruces, Oct. 1979, pp. 7.1-7.20.

17. Robert E. Munson, "Conformal Microstrip Antennas and Microstrip Phased Arrays," *IEEE Trans. Antennas and Propagat.*, vol. AP-22, no. 1, pp. 74-78, 1974.

18. A.G. Derneryd, "A Theoretical Investigation of the Rectangular Microstrip Antenna Element," *IEEE Trans. Antennas Propagat.*, vol. AP-26, no. 4, pp. 532-535, July 1978.

19. H. Pues and A. Van de Capelle, "Accurate Transmission-line Model for the Rectangular Microstrip Antenna," *IEE Proc.*, vol 131, pt. H, no. 6, pp. 334-340, Dec. 1984.

20. Pradeep K. Agrawal and M.C. Bailey, "An Analysis Technique for Microstrip Antennas," *IEEE Trans. Antennas and Propagat.*, vol. AP-25, no. 6, pp. 756-759, Nov. 1977.

21. V.H. Rumsey, "Reaction Concept in Electromagnetic Theory, *Physical Review*, vol. 94, pp. 1483-1491, June 15, 1954.

22. D.R. Poddar and J.S. Chatterjee, and S.K. Chowdhury, "On Some Broadband Microstrip Resonators," *IEEE Trans. on Antennas and Propag.* vol. AP-31, no. 1, Jan. 1983.

23. David M. Pozar, "Microstrip Antenna Aperture-Coupled to a Microstripline," *Elec. Letters,* vol. 21, no. 2, pp. 49-50, Jan. 17, 1985.

24. H. George Oltman and Donald A. Huebner, "Electromagnetically Coupled Microstrip Dipoles," *IEEE Trans. Antennas and Propagat.*, vol. AP-29, no. 1, pp. 151-157, Jan. 1981.

25. R.Q. Lee, K.F. Lee, and J. Bobinchak, "Characteristics of a Two-Layer Electromagnetically Coupled Rectangular Patch Antenna," *Electon. Letters*, vol. 23 no. 20, pp. 1070-1072, Sep. 24, 1987.

26. Richard E. Miller and Kai Chang, "Integrated Active Antenna Using Annular Ring Microstrip Antenna and Gunn Diode," *Microwave and Optical Technology Letters*, vol. 4, no. 2, pp. 72-75, Jan. 20 1991.

27. H.J. Thomas, D.L. Fudge, and G. Morris, "Gunn Source Integrated with a Microstrip Patch," *Microwaves and RF*, vol. 24, pp. 87-88, Feb. 1985.

28. J. Birkeland and T. Itoh, "Planar FET Oscillators Using Periodic Microstrip Patch Antennas," *IEEE Trans. Microwave Theory Tech.*, vol. MTT-37, no. 8, pp. 1232-1236, Aug. 1989.

29. E. H. Newman and J. E. Tehan, "Analysis of a Microstrip Array and Feed Network," *IEEE Trans. Antennas and Propagat.*, vol. AP-33, No. 4, pp. 397-403, Apr 1985.

30. David M. Pozar and Daniel H. Schaubert, "Comparison of Architectures for Monolithic Phased Array Antennas," *Microwave Journal*, pp. 93-104, Mar. 1986.

31. Barry J. Forman, "Directivity Characteristics of Scannable Planar Arrays, *IEEE Trans. Antennas and Propagat.*, vol. AP-20, no. 3, pp. 245-252, May 1972.

32. J.H. Cloete, and L.J. du Toit, "Linear Patch Array Pattern Degradation due to Corporate Feed Radiation," *IEEE Int. AP-S Symposium Digest*, pp. 466-469, 1988.

33. J. Ashkenazy, P. Perlmutter, and David Treves, "A Modular Approach for the Design of Microstrip Array Antennas," *IEEE Trans. Antennas and Propagat.*, vol. AP-31, No. 1, pp. 190-193, Jan. 1983.

34. Ely Levine, Gabi Malamud, Shmuel Shtrikman, and David Treves, "A Study of Microstrip Array Antennas with the Feed Network," *IEEE Trans. Antennas and Propagat.*, vol. AP-37, no. 4, pp. 426-434, Apr. 1989.

35. H.K. Onnes, "Disappearance of the Electrical Resistance of Mercury at Helium Temperatures," *Leiden Comm. Suppl.*, vol. 34, no. 122b, pp. 657-658, 1911.

36. W. Meissner and R. Ochsenfeld, *Naturwiss.*, vol. 21, p. 787, 1933.

37. J.G. Bednorz and K.A. Mueller, "Possible High-T_c Superconductivity in the Ba-La-Cu-O System," *Z. Physics B* vol. 64, pp. 189-193, 1986.

38. M.K. Wu, J.R. Ashburn, C.J. Torng, P.H. Hor, R.L. Meng, L. Gao, Z.J. Huang, Y.Q. Wang, and C.W. Chu, "Superconductivity at 93 K in a New Mixed-Phase Y-Ba-O Compound System at Ambient Pressure," *Phys. Rev. Lett.*, vol. 58, pp. 908-910, 1987.

39. H. Maeda, Y. Tanaka, N. Fukutomi, and T. Asano, *Jap. Journ. Appl. Phys. Lett.*, vol. 27, 1988.

40. S.S.P. Parkin, V.Y. Lee, E.M. Engler, A.I. Nazzal, T.C. Huang, G. Gorman, R. Savoy, and R. Beyers, *Phys. Rev. Lett.*, vol. 58, p. 908, 1987.

41. J.C. Gorter and H.B.G. Casimir, "The Thermodynamics of the Superconducting State," *Physik. Z.* vol. 35, pp. 963-966, 1934.

42. G.A. Samara and A.A. Giardini, "Pressure Dependence of the Dielectric Constant of Strontium Titanite," *Phys. Rev.* vol 140, p. A954-A957, 1965.

43. H.E. Weaver, "Dielectric Properties of Single Crystals of $SrTiO_3$ at Low Temperatures," *Pys. Chem. Solids*, vol. 11, pp. 274-277, 1959.

44. R.W. Simon, C.E. Platt, A.E. Lee, G.S. Lee, K.P. Daly, M.S. Wire, J.A. Luine, and M. Urbanik, *Appl. Phys. Lett.*, vol. 53, p. 2677, 1988.

45. F.A. Miranda, W.L. Gordon, V.O. Heinen, B.T. Ebihara, and K.B. Bhasin, "Measurements of Complex Permittivity of Microwave Substrates in the 20 to 300K Temperature Range from 26.5 GHz to 40.0 GHz," NASA TM-102123, 1989.

46. Tsuneo Konaka, Makoto Sato, Hidefumi Asano, and Shugo Kubo, "Relative Permittivity and Dielectric Loss Tangent of Substrate Materials for High-Tc Superconducting Film," *J. Superconductivity*, vol. 4, no. 4, pp. 283-288, 1991.

47. K.H. Young, G.V. Negrete, M.M. Eddy, J.Z. Sun, T.W. James, McD. Robinson, and E.J. Smith, "Comparisons of HTSC Thin films on various Substrates for Microwave Applications," Proc. ICFMCTF-91, San Diego, CA, 1991.

48. G.C. Liang, R.S. Withers, B.F. Cole, and W.G. Lyons, "High Temperature Superconductive Delay Lines and Filters on Sapphire and Thinned $LaAlO_3$ Substrates," Presented at the 1992 Applied Superconductivity Conference, Aug. 1992.

49. N.Newman, B. Cole, S. Garrison, K. Char, and R.C. Taber, "Double Gun Off-Axis Sputtering of Large Area $YBa_2Cu_3O_{7-\delta}$ Superconducting Films for Microwave Applications," *IEEE Trans. Magn.*, vol. 27, pp. 1276 - 1279, 1991.

50. D. Oates, A. Anderson, D. Sheen, and S. Ali, "Stripline Resonator Measurements of Z_s versus H_{rf} in $YBa_2Cu_3O_{7-x}$ Thin Films," *IEEE Trans. Microwave Theory and Tech.*, vol. 39, no. 9, pp. 1522-1529, 1991.

51. Erik Ekholm and Stephen McKnight, "Attenuation and Dispersion for High-Tc Superconducting Microstrip Lines," *IEEE Trans. Microwave Theory and Tech.*, vol. MTT-38, no. 4, pp. 387-394, Apr. 1990.

52. W.G. Lyons, R.R. Bonetti, A.E. Williams, P.M. Mankiewich, M.L. O'Malley, J.M. Hamm, Alfredo C. Anderson, R.S. Withers, A. Meulenberg, and R.E. Howard, "High-Tc Superconductive Microwave Filters," *IEEE Trans. on Magnetics*, vol. 27, no. 2, pp. 2537-2539, March 1991.

53. S.H. Talisa, M.A. Janocko, c. Moskowitz, J. Talvaccio, J.F. Billing, R. Brown, D.C. Buck, C.K. Jones, B.R. McAvoy, G.R. Wagner, and D.H. Watt, "Low and High-Temperature Superconducting Microwave Filters," *IEEE Trans. Microwave Theory and Tech.*, vol. 39, no. 9, pp. 1448-1454, Sept. 1991.

54. W. Chew, A.L. Riley, D.L. Rascoe, B.D. Hunt, M.C. Foote, T.W. Cooley, and L.J. Bajuk, "Design and Performance of a High-T_c Superconductor Coplanar Waveguide Filter," *IEEE Trans. Microwave Theory and Tech.*, vol. 39, no. 9, pp. 1455 - 2461, Sept. 1991.

55. J.H. Takemoto, F.K. Oshita, H.R. Fetterman, P. Korbin, and E. Sovoro, "Microstrip Ring Resonator Technique for Measuring Microwave Attenuation in High-T_c Superconducting Thin Films," *IEEE Trans. Microwave Theory and Tech.*, vol. 37, no. 10, pp. 1650-1652, Oct. 1989.

56. C.M. Chorey, Keon-Shik Kong, K.B. Bhasin, J.D. Warner, and Tatsuo Itoh, "YBCO Superconducting Ring Resonators at Millimeter-wave Frequencies," *IEEE Trans. on Microwave Theory and Tech.*, vol 39, no. 9, pp. 1480-1486, Sept. 1991.

57. C. Wilker, Z.Y. Shen, P. Pang, D.W. Face, W.L. Holstein, A.L. Matthews, and D.B. Laubacher, "5 GHz High-Temperature Superconductor Resonators with High Q and Low Power Dependence to 90 K," *IEEE Trans. Microwave Theory and Tech.*, vol. 39, no. 9, pp. 1462-1468, Sept. 1991.

58. G.B. Walker and C.R. Haden, "Superconducting Antennas," *Journal of Applied Physics*, vol. 40, no. 5, pp. 2035-2039, Apr. 1969.

59. V.A. Pavlyuk, E.F. Krivosheev, V.I. Mikhailov, A.V. Tarasov, "Superconducting Antenna," *Soviet Physics Technical Physics*, vol 4, no. 2, p. 80, Feb. 1978.

60. Saburo Adachi, Kazuhide Ashida, and Shigeo Ohnuki, "Superconducting Dipole Array Antenna," *Transactions of the IECE of Japan*, vol E 63, no. 9, pp. 683-684, Sep. 1980.

61. G.B. Walker, Clovis R. Haden, and O.G. Ramer, "Superconducting Superdirectional Antenna Arrays," *IEEE Trans. Antennas and Propagat.*, vol. AP-25, no. 6, pp. 885-887, Nov. 1977.

62. S.K. Khamas, M.J. Mehler, T.S. Maclean, C.E. Gough, "High Tc Superconducting Short Dipole Antenna," *Electron. Letters*, vol.24, no. 8, pp. 460-461, 1988.

63. R.C. Hansen, "Superconducting Antennas," *IEEE Trans. Aerospace and Electronic Systems*, vol 26, no. 2, pp. 345-354, Mar. 1990.

64. Robert J.Dinger, "Some Potential Antenna Applications of High Temperature Superconductors," *Journal of Superconductivity*, vol. 3, no. 3, pp. 287-296, Sep. 1990.

65. R.C. Hansen, "Fundamental Limitations in Antennas," *Proceedings of the IEEE*, vol. 69, pp. 170-182, Feb. 1981.

66. L.J. Chu, "Physical Limitations of Omni-Directional Antennas," *Journal of Applied Physics*, vol. 19, pp. 1163-1175, Dec. 1948.

67. R.F. Harrington, "Effects of Antenna Size on Gain, Bandwidth, and Efficiency," *Journal of Research of the National Bureau of Standards*, vol. 64D, pp. 1-12, Jan./Feb. 1960.

68. T. Moreno, *Microwave Transmission Design Data*, New York: Dover, 1948, Ch. 2.

69. Rogers Corp., Microwave Materials Division, 100 S. Roosevelt Ave., Chandler, AZ 85226.

70. Heinz Chaloupka, Norbert Klein, Michael Peiniger, Helmut Piel, Arndt Pischke, and Georg Splitt, "Miniaturized High-Temperature Superconductor Microstrip Patch Antenna," *IEEE Trans. Microwave Theory and Tech.*, vol. 39, no. 9, pp. 1513-1521, Sept 1991.

71. Robert J. Dinger, Donald R. Bowling, and Anna M. Martin, "A Survey of Possible Passive Antenna Applications of High-Temperature Superconductors," *IEEE Trans. Microwave Theory and Tech.*, vol. 39, no. 9, pp. 1498-1507, Sept. 1991.

72. Y.S. He, A.S. He, X.X. Zhang, C.S. Shi, N. Lu, B. Tian, D.R. Lu, M.L. Zhou, and W.G. Wang., "Progress in High Tc Superconducting Ceramic Antennas," *Superconductor Science Technology*, vol. 4 p. S124-S126, 1991.

73. J.S. Herd, J.P. Kenney, K.G. Herd, W.G. Lyons, Alfredo Anderson, P. M. Mankiewich, and M.L. O'Malley, "Experimental Results on a 12 GHz 16-Element Multilayer Microstrip Array with a High-T_c Superconducting Feed Network," *IEEE Antennas and Propag. Symposium Digest*, pp. 974-977, 1992.

CHAPTER II.

1. Harold A. Wheeler, "Transmission-Line Properties of a Strip on a Dielectric Sheet on a Plane, *IEEE Trans. Microwave Theory and Tech.*, vol. MTT-25, no. 8, p. 631-647, Aug. 1977.

2. M.V. Schneider, "Microstrip Lines for Microwave Integrated Circuits," *Bell System Tech. Journal*, vol. 48, pp. 1421-1444, May 1969.

3. M. Kirschning and R.H. Jansen, "Accurate Model for Effective Dielectric Constant of Microstrip with Validity up to Millimetre-wave Frequencies," *Electron. Letters*, vol. 18, no. 6, pp. 272-273, Mar. 18, 1982.

4. H.A. Wheeler, "Transmission-line Properties of Parallel Strips Separated by a Dielectric Sheet," *IEEE Trans. Microwave Theory Tech.*, vol. MTT-13, pp. 172-185, 1965.

5 Robert A. "Pucel, Daniel J. Masse, and Curtis P. Hartwig, "Losses in microstrip," *IEEE Trans. Microwave Theory and Tech.*, vol. MTT-16, no. 6, pp. 342-350, June 1968.

6. Robert A. "Pucel, Daniel J. Masse, and Curtis P. Hartwig, "Correction to 'Losses in microstrip,'" *IEEE Trans. Microwave Theory and Tech.*, vol. MTT-16, no. 12, pp. 1064, Dec. 1968.

7. F.A. Miranda, W.L. Gordon, K.B. Bhasin, V.O. Heinen, and J.D. Warner, "Microwave properties of $YBa_2Cu_3O_{7-\delta}$ high-transition-temperature superconducting thin films measured by the power transmission method," *J. Appl. Phys.*, vol. 70, no. 10, pp. 5450-5462, 15 Nov. 1991.

8. Hai-Young Lee and Tatsuo Itoh, "Phenomenological Loss Equivalence Model for Planar Quasi-TEM Transmission Lines with a Thin Normal Conductor or Superconductor," *IEEE Trans. Microwave Theory and Tech.*, vol. MTT-37, no. 12, pp. 1904-1909, Dec. 1989.

9. Erik Ekholm and Stephen McKnight, "Attenuation and Dispersion for High-Tc Superconducting Microstrip Lines," *IEEE Trans. Microwave Theory and Tech.*, vol. MTT-38, no. 4, pp. 387-394, Apr. 1990.

10. C.M. Chorey, Keon-Shik Kong, K.B. Bhasin, J.D. Warner, and Tatsuo Itoh, "YBCO Superconducting Ring Resonators at Millimeter-wave Frequencies," *IEEE Trans. on Microwave Theory and Tech.*, vol 39, no. 9, pp. 1480-1486, Sept. 1991.

11. L. Lewin, "Spurious radiation from microstrip," *IEE Proc.*, vol. 125, pp. 633-642, 1978.

12. David M. Pozar, "Considerations for Millimeter Wave Printed Antennas," *IEEE Trans. Antennas and Propagat.*, vol. AP-31, no. 5, pp. 740-747, Sept. 1983.

13. David M. Pozar and Daniel H. Schaubert, "Comparison of Architectures for Monolithic Phased Array Antennas," *Microwave Journal*, pp. 93-104, Mar. 1986.

14. R.E. Collin, *Field Theory of Guided Waves*, IEEE Press, New York, 1991, p. 713.

15. P. Perlmutter, S. Shtrikman, and David Treves, "Electric Surface Current Model for the Analysis of Microstrip Antennas with Application to Rectangular Elements," *IEEE Trans. Antennas and Propagat.*, vol. AP-33, No. 3, pp. 301-311, Mar, 1985.

16. B. Nauwelaers and A. Van de Capelle, "Surface Wave Losses of Rectangular Microstrip Antennas," *Electron. Letters*, vol. 25, no. 11, pp. 696-697, May 25, 1989.

17. David M. Pozar, "Rigorous Closed-Form Expressions for the Surface Wave Loss of Printed Antennas," *Elecron. Letters*, vol. 26, no. 13, pp. 954-956, Jun 21, 1990.

18. S.P. Morgan, "Effect of Surface Roughness on Eddy Current Losses at Microwave Frequencies," *J. Applied Physics*, vol. 20, pp. 352-362, Apr. 1949.

19. E.O. Hammerstad and F. Bekkadal, "Microstrip Handbook," ELAB report STF 44 A74169, The University of Trondheim, The Norwegian Institute of Technology.

20. Felix A. Miranda, "Microwave Response of High Transition Temperature Superconducting Thin Films," Ph.D. Dissertation, Case Western Reserve University, May 1991.

21. H. Sobol, "Technology and design of hybrid microwave integrated circuits," *Solid State Technol.*, pp. 49-57, Feb. 1970.

22. Robert R. Romanofsky, "Analytical and Experimental Procedures for Determining Propagation Characterisitics of Millimeter-Wave Gallium Arsenide Microstrip Lines," NASA Technical Paper 2899, 1989.

23. R.E. Collin, *Antennas and Radiowave Propagation*, McGraw-Hill, New York 1985.

CHAPTER III.

1. Conductus, Inc., 969 West Maude Ave., Sunnyvale, CA 94086.

2. J.D. Warner, K.B. Bhasin, N.C. Varaljay, D.Y. Bohman, and C.M. Chorey, "Growth and Patterning of the Laser Ablated Superconducting YBaCuO Films on $LaAlO_3$ Substrates," NASA TM #102346, 1989.

3. Karlheinz Seeger, "Microwave Measurement of the Dielectric Constant of High-Density Polyethylene," *IEEE Trans. Microwave Theory and Tech.*, vol. 39, no. 2, pp. 352-354, Feb. 1991.

4. Edward A. Wolff and Roger Kaul, *Microwave Engineering and Systems Applications*," John Wiley & Sons, New York, 1988.

5. J. Ashkenazy, E. Levine, and D. Treves, "Radiometric measurement of Antenna Efficiency," *Electron. Lett.*, vol. 21, no. 3, Jan. 31, 1985.

6. Harold A. Wheeler, "The radiansphere around a small antenna," *Proceedings of the IRE*, vol 47, pp. 1325-1331, Aug. 1959.

7. David M. Pozar, Barry Kaufman, "Comparison of Three Methods for the Measurement of Printed Antenna Efficiency," *IEEE Trans. Antennas and Propagat.*, vol. AP-36, no. 1, pp. 136-139 Jan. 1988.

8. E.H. Newman, Peter Bohley, and C.H. Walter, "Two methods for the measurement of antenna efficiency," *IEEE Trans. Antennas and Propagat.*, vol. AP-23, no. 4, pp. 457-461, July 1975.

9. David M. Pozar, Barry Kaufman, "Comparison of Three Methods for the Measurement of Printed Antenna Efficiency," *IEEE Trans. Antennas and Propagat.*, vol. AP-36, no. 1, pp. 136-139 Jan. 1988.

10. H.T. Friis, "A Note on a Simple Transmission Formula," *Proc. IRE*, vol. 34, pp. 254-256, May 1946.

CHAPTER IV.

1. Y.T. Lo, D. Solomon, and W.F. Richards, "Theory and Experiment on Microstrip Antennas," *IEEE Trans. Antennas and Propagat.*, vol. AP-27, no. 2, pp. 137-145, Mar. 1979.

2. William F. Richards, Y.T. Lo, and Daniel D. Harrison, "An Improved Theory for Microstrip Antennas and Applications," *IEEE Trans. Antennas and Propagat.*, vol. AP-29, no. 1, pp. 38-46, Jan. 1981.

3. J.R. James, P.S. Hall, and C. Wood, *Microstrip Antenna Theory and Design*, Peter Peregrinus Press, 1981.

4. I.J. Bahl and P. Bhartia, *Microstrip Antennas*, Artech House, MA, 1980.

5. Tsuneo Konaka, Makoto Sato, Hidefumi Asano, and Shugo Kubo, "Relative Permittivity and Dielectric Loss Tangent of Substrate Materials for High-Tc Superconducting Film," *J. Superconductivity*, vol. 4, no. 4, pp. 283-288, 1991.

6. Felix A. Miranda, William L. Gordon, Vern O. Heinen, Ben T. Ebihara, and Kul B. Bhasin, "Measurements of Complex Permittivity in the 20 to 300 K Temperature Range from 26.5 to 40.0 GHz," NASA TM #102123, 1989.

7. C.J. Gorter and H.B.G. Casimir, "The Thermodynamics of the Superconducing State," *Physik. Z.* vol. 35, pp. 963-966, 1934.

8. F.A. Miranda, W.L. Gordon, K.B. Bhasin, V.O. Heinen, and J.D. Warner, "Microwave properties of $YBa_2Cu_3O_{7-\delta}$ high-transition-temperature superconducting thin films measured by the power transmission method," *J. Appl. Phys.*, vol. 70, no. 10, pp. 5450-5462, 15 Nov. 1991.

9. Daniel H. Schaubert and K. Sigfrid Yngvesson, "Experimental Study of a Microstrip Array on High Permittivity Substrate," *IEEE Trans. Antennas and Propagat.*, vol. AP-34, no. 1, pp. 92-97, Jan. 1986.

10. P. Perlmutter, S. Shtrikman, and David Treves, "Electric Surface Current Model for the Analysis of Microstrip Antennas with Application to Rectangular Elements," *IEEE Trans. Antennas and Propagat.*, vol. AP-33, no. 3, pp. 301-311, Mar, 1985.

11. *em*, Sonnet Software, 1990.

12. C.M. Chorey, Keon-Shik Kong, K.B. Bhasin, J.D. Warner, and Tatsuo Itoh, "YBCO Superconducting Ring Resonators at Millimeter-wave Frequencies," *IEEE Trans. on Microwave Theory and Tech.*, vol 39, no. 9, pp. 1480-1486, Sept. 1991.

CHAPTER V.

1. I.J. Bahl and P. Bhartia, *Microstrip Antennas*, Artech House, MA, 1980.

2. L.C. Shen, S.A. Long, M.R. Allerding, and M.D. Walton, "Resonant Frequency of a Circular Disc, Printed-Circuit Antenna," *IEEE Trans. Antennas and Propagat.*, vol. AP-27, No. 7, pp. 595-596, July 1977.

3. Weng Cho Chew and Jin Au Kong, "Effects of Fringing Fields on the Capacitance of Circular Microstrip Disk," *IEEE Trans. Microwave Theory Tech.*, vol. MTT-28, no. 1, pp. 98-103, Feb. 1988.

4. Tsuneo Konaka, Makoto Sato, Hidefumi Asano, and Shugo Kubo, "Relative Permittivity and Dielectric Loss Tangent of Substrate Materials for High-Tc Superconducting Film," *J. Superconductivity*, vol. 4, no. 4, pp. 283-288, 1991.

5. Felix A. Miranda, William L. Gordon, Vern O. Heinen, Ben T. Ebihara, and Kul B. Bhasin, "Measurements of Complex Permittivity in the 20 to 300 K Temperature Range from 26.5 to 40.0 GHz," NASA TM #102123, 1989.

6. Anders G. Derneryd, "Analysis of the Microstrip Disc Antenna Element," *IEEE Trans. Antennas and Propagat.*, vol. AP-27, No. 5, pp. 660-663, Sept. 1979.

7. C.M. Chorey, Keon-Shik Kong, K.B. Bhasin, J.D. Warner, and Tatsuo Itoh, "YBCO Superconducting Ring Resonators at Millimeter-wave Frequencies," *IEEE Trans. on Microwave Theory and Tech.*, vol 39, no. 9, pp. 1480-1486, Sept. 1991.

8. William F. Richards, Jai-Dong Ou, and Stuart A. Long, "A Theoretical and Experimental Investigation of Annular, Annular Sector, and Circular Sector Microstrip Antennas," *IEEE Trans. Antennas and Propagat.*, vol. AP-32, no. 8, pp. 864-867, Aug. 1984.

9. J.S. Dahele and K.F. Lee, "Characteristics of Annular-Ring Microstrip Antenna," *Electron. Letters*, vol. 18, no. 24, pp. 1051-1052, Nov. 25 1982.

10. Weng Cho Chew, "A Broad-Band Annular Ring Microstrip Antenna," *IEEE Trans. Antennas and Propagat.*, vol. AP-30, no. 5, pp. 918-922, Sep. 1982.

11. A. Das, S.K. Das, S.P. Mathur, "Radiation characteristics of higher-order modes in microstrip ring antenna," *IEE Proceedings*, vol 131, pt. H, no. 2, pp. 102-106, April 1984.

12. J.D. Warner, K.B. Bhasin, N.J. Varaljay, D.Y. Bohman, and C.M. Chorey, "Growth and Patterning of Laser Ablated Superconducting YBCO Films on $LaAlO_3$ Substrates," NASA TM-102336.

13. Y.S. Wu and F.J. Rosenbaum, "Mode chart for microstrip ring resonators," *IEEE Trans. Microwave Theory and Tech.*, vol. MTT-20, no. 7, pp. 487-489, July 1972.

14. K.F. Lee and J.S. Dahele, "Characteristics of microstrip antennas and some methods of improving frequency agility and bandwidth," *Handbook of Microstrip Antennas*, Ed. by J.R. James and P.S. Hall, Peter Peregrinus Ltd, London, 1989.

15. Daniel H. Schaubert and K. Sigfrid Yngvesson, "Experimental Study of a Microstrip Array on High Permittivity Substrate," *IEEE Trans. Antennas and Propagat.*, vol. AP-34, no. 1, pp. 92-97, Jan. 1986.

16. D.M. Pozar, "Rigorous closed-form expressions for the surface wave loss of printed antennas," *Electron. Lett.*, 1990, vol. 26, no. 13, pp. 954-956.

CHAPTER VI.

1. R.E. Collin, *Field Theory of Guided Waves*, IEEE Press, New York, 1991, p. 713.

2. David M. Pozar, "Microstrip Antenna Aperture-Coupled to a Microstrip-line," *Elec. Letters*, vol. 21, no. 2, pp. 49-50, Jan. 17, 1985.

3. Peter L. Sullivan and Daniel H. Schaubert, "Analysis of an Aperture Coupled Microstrip Antenna," *IEEE Trans. Antennas and Propagat.*, vol. AP-34, no. 8, pp. 977-984, Aug. 1986.

4. G. Gronau and I. Wolff, "Aperture-Coupling of a Rectangular Microstrip Resonator," *Elec. Letters*, vol. 22, no. 10, pp. 554-555, May 8, 1986.

5. F. Croq and A. Papiernik, "Large Bandwidth Aperture-Coupled Microstrip Antenna," *Elec. Letters*, vol.26, no. 16, pp. 1293-1294, Aug. 2, 1990.

6. H. George Oltman and Donald A. Huebner, "Electromagnetically Coupled Microstrip Dipoles," *IEEE Trans. Antennas and Propagat.*, vol. AP-29, no. 1, pp. 151-157, Jan. 1981.

7. Marat Davidovitz and Y.T. Lo, "Rigorous Analysis of a Circular Patch Antenna Excited by a Microstrip Transmission Line," *IEEE Trans. Antennas and Progat.*, vol AP-37, No. 8, pp. 949-958, August 1989.

8. J.R. Herd, "Modelling of Wideband Proximity Coupled Microstrip Array Elements," *Elec. Letters*, vol. 26 no.16, pp. 1282-1284, Aug. 2, 1990.

9. Georg Splitt and Marat Davidovitz, "Guidelines for Design of Electromagnetically Coupled Microstrip Antennas on Two-Layer Substrates," *IEEE Trans. Antennas and Propagat.*, vol. AP-38 no. 7, pp. 1136-1140, July 1990.

10. D.M. Pozar and B. Kaufman, "Increasing the Bandwidth of a Microstrip Antenna by Proximity Coupling," *Electron. Letters*, vol. 23 no. 8, pp. 368-369, April 9, 1987.

11. J.S. Roy, S.K. Shaw, P. Paul, D.R. Poddar, and S.K. Chowdhury, "Some Experimental Investigations on Electromagnetically Coupled Microstrip Antennas on Two-Layer Substrates," *Microwave and Optical Technology Letters*, vol. 4, no. 6, pp. 236-238, May 1991.

12. R.Q. Lee, K.F. Lee, and J. Bobinchak, "Characteristics of a Two-Layer Electromagnetically Coupled Rectangular Patch Antenna," *Electon. Letters*, vol. 23 no. 20, pp. 1070-1072, Sep. 24, 1987.

13. J.P. Damiano, J. Bennegueouche, and A. Papiernik, "Study of Multilayer Microstrip Antennas with Radiating Elements of Various Geometries," *IEE Proc.*, vol 137, pt. H, no. 3, pp. 163-170, Jun. 1990.

14. J.S. Herd, J.P. Kenney, K.G. Herd, W.G. Lyons, Alfredo C. Anderson, P.M. Mankiewich, and M.L. O'Malley, "Experimental Results on a 12 GHz 16-Element Multilayer Microstrip Array with a High Temperature

Superconducting Feed Network," *1992 IEEE Antennas and Propag. Symposium Digest*, pp. 974-977.

15. I.J. Bahl and Stanislaw Stuchly, "Analysis of a Microstrip Covered with a Lossy Dielectric," IEEE Trans. Microwave Theory Tech., vol. MTT-28, no. 2, pp. 104-109, Feb. 1980.

16. Tsuneo Konaka, Makoto Sato, Hidefumi Asano, and Shugo Kubo, "Relative Permittivity and Dielectric Loss Tangent of Substrate Materials for High-Tc Superconducting Film," *J. Superconductivity*, vol. 4, no. 4, pp. 283-288, 1991.

17. Daniel H. Schaubert and K. Sigfrid Yngvesson, "Experimental Study of a Microstrip Array on High Permittivity Substrate," *IEEE Trans. Antennas and Propagat.*, vol. AP-34, no. 1, pp. 92-97, Jan. 1986.

18. C.M. Chorey, Keon-Shik Kong, K.B. Bhasin, J.D. Warner, and Tatsuo Itoh, "YBCO Superconducting Ring Resonators at Millimeter-wave Frequencies," *IEEE Trans. on Microwave Theory and Tech.*, vol 39, no. 9, pp. 1480-1486, Sept. 1991.

CHAPTER VII.

1. Kai Chang and Cheng Sun, "Millimeter-Wave Power-Combining Techniques," *IEEE Trans. Microwave Theory and Tech.*, vol. 31, no. 2, pp. 91-105, Feb. 1983.

2. N.J. Rohrer, G.J. Valco, and K.B. Bhasin, "Hybrid High Temperature Superconductor/GaAs 10 GHz Microwave Oscillator: Temperature and Bias Effects," To be published in *IEEE Trans. Microwave Theory and Tech.*

3 N.J. Rohrer, M.A. Richard, G.J. Valco, and K.B. Bhasin, "A 10 GHz YBCO/GaAs Hybrid Oscillator Proximity Coupled to a Circular Microstrip Patch Antenna," To be published in *IEEE Trans. Applied Superconductivity*.

4. *Touchstone*, EEsof, 1990.

5. W. C. Chew and J. A. Kong, "Effects of Fringing Fields on the Capacitance of Circular Microstrip Disks," *IEEE Trans. Microwave Theory and Tech.*, vol. 28, no. 2, pp. 98-104, Feb. 1990.

6. J.D. Warner, K.B. Bhasin, N.J. Varaljay, D.Y. Bohman, and C.M. Chorey, "Growth and Patterning of Laser Ablated Superconducting YBCO Films on $LaAlO_3$ Substrates," NASA TM-102336.

7. I.J. Bahl and P. Bhartia, *Microstrip Antennas*, Dedham, MA, Artech House, 1980.

8. Daniel H. Schaubert and K. Sigfrid Yngvesson, "Experimental Study of a Microstrip Array on High Permittivity Substrate," *IEEE Trans. Antennas and Propagat.*, vol. AP-34, no. 1, pp. 92-97, Jan. 1986.

CHAPTER VIII.

1. Katsumi Suzuki (private communication).

2. M.A. Shimko, C.J. Crowley, and P.N. Wallis, "Novel Concept for a Space Power Distribution Busbar Using HTS Materials and Passive Cooling," Presented at the Fifth Conference on Superconductivity and Applications, Buffalo, New York, Sept. 1991.

REPORT DOCUMENTATION PAGE

Form Approved
OMB No. 0704-0188

1. AGENCY USE ONLY (*Leave blank*)	2. REPORT DATE	3. REPORT TYPE AND DATES COVERED
	March 1993	Final Contractor Report

4. TITLE AND SUBTITLE

An Experimental Investigation of High Temperature Superconducting Microstrip Antennas at K- and Ka-Band Frequencies

5. FUNDING NUMBERS

WU-506-72-1B
NCC-3-99

6. AUTHOR(S)

Mark A. Richard

7. PERFORMING ORGANIZATION NAME(S) AND ADDRESS(ES)

Case Western Reserve University
Cleveland, Ohio 44106

8. PERFORMING ORGANIZATION REPORT NUMBER

E-7645

9. SPONSORING/MONITORING AGENCY NAMES(S) AND ADDRESS(ES)

National Aeronautics and Space Administration
Lewis Research Center
Cleveland, Ohio 44135-3191

10. SPONSORING/MONITORING AGENCY REPORT NUMBER

NASA CR-191089

11. SUPPLEMENTARY NOTES

Project Manager, Kul B. Bhasin, Space Electronics Division, NASA Lewis Research Center, (216) 433-3676. A similar version of this report was submitted by Mark A. Richard as a thesis in partial fulfillment of the requirements for the Degree of Doctor of Philosophy in Electrical Engineering and Applied Physics to Case Western Reserve University, Cleveland, Ohio.

12a. DISTRIBUTION/AVAILABILITY STATEMENT

Unclassified - Unlimited
Subject Category 33

12b. DISTRIBUTION CODE

13. ABSTRACT (*Maximum 200 words*)

The recent discovery of high temperature superconductors (HTS) has generated a substantial amount of interest in microstrip antenna applications. However, the high permittivity of substrates compatible with HTS results in narrow bandwidths and high patch edge impedances of such antennas. To investigate the performance of superconducting microstrip antennas, three antenna architectures at K and Ka-band frequencies are examined. Superconducting microstrip antennas that are directly coupled, gap coupled, and electromagnetically coupled to a microstrip transmission line have been designed and fabricated on lanthanum aluminate substrates using $YBa_2Cu_3O_7$ superconducting thin films. For each architecture, a single patch antenna and a four element array were fabricated. Measurements from these antennas, including input impedance, bandwidth, patterns, efficiency, and gain are presented. The measured results show usable antennas can be constructed using any of the architectures. All architectures show excellent gain characteristics, with less than 2 dB of total loss in the four element arrays. Although the direct and gap coupled antennas are the simplest antennas to design and fabricate, they suffer from narrow bandwidths. The electromagnetically coupled antenna, on the other hand allows the flexibility of using a low permittivity substrate for the patch radiator while using HTS for the feed network, thus increasing the bandwidth while effectively utilizing the low loss properties of HTS. Each antenna investigated in this research is the first of its kind reported.

14. SUBJECT TERMS	15. NUMBER OF PAGES
Microwave antennas, Superconductivity communications technology satellite	225
	16. PRICE CODE: A10

17. SECURITY CLASSIFICATION OF REPORT	18. SECURITY CLASSIFICATION OF THIS PAGE	19. SECURITY CLASSIFICATION OF ABSTRACT	20. LIMITATION OF ABSTRACT
Unclassified	Unclassified	Unclassified	